Cobos Sanchez, Clemente (2008) Forward and inverse analysis of electromagnetic fields for MRI using computational techniques. PhD thesis, University of Nottingham.

Forward and inverse analysis of electromagnetic fields for MRI using computational techniques

by

Clemente Cobos Sánchez.

Thesis submitted to
The University of Nottingham
for the degree of
Doctor of Philosophy

August 2008

Contents

Abstract

MRI has become an invaluable tool for diagnostic medicine. Its operation is based on the principles of electromagnetism that are dictated by Maxwell's equations. MRI relies on the existence of well defined, spatially and temporally controlled magnetic fields, which are usually generated by coils of wire. Human exposure to these fields has become a safety concern, especially with the increase in the strength of the magnetic fields used.

In this thesis, problems in electromagnetism relevant to different areas in MRI and involving the calculation of solutions to both forward and inverse problems are investigated using techniques derived for computational mechanics.

The first section of the work focuses on the development of an accurate technique for the solution of magnetostatic inverse problems using boundary element methods (BEM) with the aim of designing optimised gradient coils. This approach was found to be an extremely effective method which can be applied to a wide range of coil geometries and is particularly valuable for designs where the coil surface has low symmetry. BEM-based approaches to designing gradient coils that reduce the likelihood of peripheral nerve stimulation due to rapidly switched magnetic fields are also considered.

In the second section of the work, a novel BEM tool to allow the calculation of solutions to quasi-static forward problems has been developed, and used for the evaluation of the electric fields induced in the human body by temporally varying magnetic fields, due to either gradient switching or body movements in strong static magnetic fields. This approach has been tested by comparison with analytic solutions for simply shaped objects, exposed to switched gradients or moving in large static fields, showing good agreement between the results of numerical and analytical approaches. The BEM approach has also been applied to the evaluation of the electric fields induced in human body models.

This work involved the development of an appropriate theoretical framework for the study of conducting systems moving in magnetic fields. This involved correcting some misconceptions that had propagated in the literature and allowed the development of an efficient implementation of a BEM suited to this problem.

" A child of five would understand this.
Send someone to fetch a child of five ".

Groucho Marx

Acknowledgements

I would not be lying if I said that this thesis has been an exploration of boundaries, my own boundaries and the boundary element method. It has been a great opportunity that has allowed me to do "real" Physics and learn many new things.

Many people have helped me along the way and I would like to express my gratitude to them.

First and foremost I would like to thank **Professor Richard Bowtell**, for setting a fine example to me, as a researcher and moreover as a person, and **Professor Henry Power**, for his ideas, support throughout the duration of my PhD and for teaching me "to not be afraid of a dead tiger".

I would also like thank the rest of my supervisors and members of the research group; Professor Arthur Jones, Professor Adib Becker and Dr. Liviu Marin for giving me the opportunity to work with them on this project and for then guiding me through it; and Dr. Paul Glover, for his advices and his always brilliant intuition in solving problems.

I do not think I could have done it without the help of my friends in the Sir Peter Mansfield Magnetic Resonance Centre, especially all of the inhabitants and frequent visitors of the downstairs office, who created the perfect atmosphere to work in, with ingredients such as solidarity, affection and always a pinch of laughter and smiles.

I am especially grateful to Rosa Sánchez Panchuelo for making me not miss the Spanish sun too much and for being sweeter than any of the many cakes she made. I am also grateful to Michael Poole for showing me useful Matlab commands, such as "help mike", and for teaching me the meaning of some useful English words, such as *brilliant, coffee-time, friend, twopintsofale* and *mañana*.

Coincido con Carlos Cano en que *Granada es como una rosa, mas bonita que ninguna*, pero seguramente no seria tan bonita sin los rincones de Chari; las tertulias con mis amigos Ignacio y Pepe; y como no sin Trini, la única mujer capaz de aguantarme.

Especial agradecimiento va para mi familia, sobre todo a mis padres y mi hermana María, por haberme educado y apoyado en todo momento.

Chapter 1

Introduction

Magnetic resonance imaging (MRI) is a non-invasive technique for imaging the human body. MRI is based on a phenomenon called nuclear magnetic resonance (NMR). This was independently discovered by Purcell [1] and Bloch [2] in 1946, both of whom were awarded the Nobel Prize in 1952. In the following years NMR spectroscopy was then developed and used for chemical analysis, and in 1973 Lauterbur [4] and Mansfield [3] described the use of Nuclear Magnetic Resonance to form an image of a sample. For this work, they shared the Nobel Prize for Medicine in 2003. Magnetic Resonance Imaging has become an important diagnostic technique and an invaluable tool for investigating the structure and function of the human body.

MRI relies on the existence of well defined and controlled magnetic fields, which are generated by coils of wire which form the most important part of an MR scanner.

Nuclear Magnetic resonance is based upon the interaction between an applied magnetic field and the intrinsic angular momentum of nuclei, also known as spin. In the absence of an external magnetic field, the orientation of sample spins is random. When an external main magnetic field $\mathbf{B}_0$ is applied to the system, spins tend to align with the magnetic field, so that the bulk magnetization vector points along the positive direction of the magnetic field. A second resonant oscillating magnetic field perpendicular to the static field is applied to change the orientation of the magnetization. The variation with time of the magnetization vector is described by the Larmor equation. The resulting precession of the magnetization generates a radiofrequency signal which can be detected using an appropriate coil.

Gradient coils are used in MRI to encode the position of the magnetic resonance signal in the sample that is to be imaged. They generate a longitudinal magnetic field that varies linearly with position, so as to cause a linear variation in the Larmor frequency of the resonating nuclei within the sample. The gradient thus causes spins to precess at different

rates at different positions across the sample. The signals generated by different regions can therefore be discriminated by their frequencies and this discrimination forms the basis of MRI.

Large gradients are desirable for maximising the spatial resolution and they must also be rapidly switched, since short rise-times mean that less time is wasted in ramping up gradients in MR sequences, which often means faster image acquisition and improved signal to noise ratio.

The exposure of human subjects to these magnetic fields has become a safety concern, especially with the increase in the strength of the fields used in MRI. Any electromagnetic phenomenon in MRI can be understood by solving Maxwell's equations.

The boundary element method (BEM) is a numerical computational method of solving linear partial differential equations (PDEs). The basis of the method is to transform the original PDE into an equivalent integral equation by means of the corresponding Green's representation formula. The integrals are then numerically calculated over the boundaries, which are divided into boundary elements. If the boundary conditions are satisfied, a system of linear algebraic equations may be established for which a unique solution can be found. Boundary integral techniques have a long history, but with all numerical methods could not truly prosper until the invention of electronic computers in the early 1960s, when Jaswon, Ponter and Symm [5]-[6] presented the first implementations of this technique.

In this thesis, problems in electromagnetism relevant to different areas in MRI and involving the calculation of solutions to both forward and inverse problems are investigated using BEM.

1.1   Scope of this Thesis

The second chapter of this thesis reviews the literature describing the design of gradient coils for MRI, where the most relevant approaches, as well as the factors describing coil performance are described.

The problem in gradient coil design is an inverse problem of electromagnetic nature, which can hence be formulated using Maxwell's equations that provide a general description of electromagnetism.

The third chapter presents a new inverse boundary element method for the design of gradient coils, BESFM (Boundary Element Stream Function Method).

By using the BEM mathematical framework we develop a general technique for obtaining a divergence-free current density over a given surface. Subsequently BESFM for coil design is described as a magneto-static constrained optimization problem, whose formulation is

based on this divergence-free current.

The characterization of the the current density is locally based, so the resulting formulation is completely geometry-independent; and thus can be applied to any current carrying shape. In addition we investigate an extension of the BESFM, which can be used to minimize the modulus of the vector potential generated by the coil, and hence the electric field induced in conducting systems.

Chapter four details some numerical examples of the application of the BESFM to coil design. The reduction of the electric field induced by a coil which has been designed to minimize the modulus of the vector potential in a prescribed region inside the coil is also described.

Chapter five investigates the induced currents that exposure to time-changing magnetic fields and natural movements in and around high field MRI systems can produce. This chapter includes a literature review of these two areas, as well as a full electromagnetic theory valid for both cases, where special emphasis is placed in the description of Faraday's Law for a moving system.

The differences in the results obtained when using the formalism described here and other approaches that do not use Faraday's Law for moving systems is shown for some examples of moving conductors with simple geometries.

Chapter six describes an integral formulation of the problem of calculating the induced current by exposure to a changing magnetic field or movements in large magnetic fields together with the associated boundary conditions and its posterior solution using a constant BEM.

The validity of this BEM approach is demonstrated for simple geometries with known analytical solutions and it is also applied to the evaluation of the induced fields in more realistic and complicated meshed models of the human body in chapter seven.

Chapter eight discusses the findings of this work, and presents some areas that are worthy of further study.

Statement about the gauge used in thesis

It is known that the magnetic field, $\mathbf{B}$, and electric field, $\mathbf{E}$, can be defined in terms of the magnetic vector potential, $\mathbf{A}$, and the scalar potential, ϕ [25]. The invariance under gauge transformation of the fields $\mathbf{E}$ and $\mathbf{B}$ leads to some arbitrariness in the way that the potentials are defined. In this thesis all the studied problems are posed in the static and quasi-static regime, so unless it is stated, we found that the optimum gauge for the vector potential was the so-called Coulomb gauge.

Chapter 2

Coil Design

2.1 Introduction

Magnetic Resonance Imaging (MRI) is a non-invasive technique, that relies on the principles of nuclear magnetic resonance (NMR), and is used for imaging the inside of the human body. MRI is based on the use of well defined and controlled magnetic fields:

(A) A strong uniform static main field, capable of polarizing the sample.

(B) Magnetic field gradients, used to encode spatially the signals from the sample.

These field gradients are generated by coils of wire, usually placed on cylindrical surfaces, although as will see other geometries can be employed.

The main magnetic field strength is usually of the order of a few Tesla (T), whereas the magnetic field gradient produced by a typical whole body gradient coil is of the order of 30mT/m.

The problem in gradient coil design is to find optimal positions for the multiple windings of coils so as to produce fields with the desired spatial dependence and properties (low inductance, high gradient to current ratio, minimal resistance, and good field gradient uniformity). Therefore coil design is an obviously electromagnetic inverse problem which can be formulated in the magneto-static regime, and described as a constrained optimization problem.

In this chapter, we first review the electromagnetic formalism needed to set up the problem and list some of the most relevant performance parameters and requirements in coil design. A summary of the different and most important coil design methods for MRI is then presented.

4

2.2   Magneto-statics

The Maxwell's equations that describe magnetic phenomena in the static regime are Gauss'
Law

$$\nabla \cdot \mathbf{B} = 0, \tag{2.1}$$

and Ampère's Law

$$\nabla \times \mathbf{H} = \mathbf{J}. \tag{2.2}$$

where $\mathbf{J}$ is the current density, that is the source of the magnetic field, $\mathbf{H}$, which can be
related to the magnetic induction, $\mathbf{B}$, through the constitutive equation

$$\mathbf{B} = \mu\mathbf{H}. \tag{2.3}$$

Here μ is a characteristic of the medium known as the magnetic permeability. For non-
magnetic material Eq. 2.2 reduces to[1]

$$\nabla \times \mathbf{B} = \mu_0\mathbf{J}. \tag{2.4}$$

and in this case μ_0 represents the permeability of free space. It is easy to see from the above
equation that in the static regime the current density must be divergence-free

$$\nabla \cdot \mathbf{J} = 0. \tag{2.5}$$

The form of Eq. 2.1 allows us to introduce the magnetic vector potential $\mathbf{A}$, such that

$$\mathbf{B} = \nabla \times \mathbf{A}, \tag{2.6}$$

and substitution of the above expression into Eq. 2.4, yields

$$\nabla(\nabla \cdot \mathbf{A}) - \nabla^2\mathbf{A} = \mu_0\mathbf{J}. \tag{2.7}$$

With the choice of the Coulomb gauge, $\nabla \cdot \mathbf{A} = 0$, we obtain

$$\nabla^2\mathbf{A} = -\mu_0\mathbf{J} \tag{2.8}$$

---

[1]In the future we will only use $\mathbf{B}$, which can be referred to as the magnetic field as well, since it is the
field that is of relevance for MRI.

that is, **A** satisfies Poisson's equation. This partial differential equation (PDE) can be reformulated into an integral equation by means of the Green's function [7]

$$\mathbf{A}(\mathbf{r}) = \frac{\mu_0}{4\pi} \int \frac{\mathbf{J}(\mathbf{r'})}{|\mathbf{r} - \mathbf{r'}|} \, dV(\mathbf{r'}). \tag{2.9}$$

An integral representation for **B** can be obtained by applying the curl to the above equation

$$\mathbf{B}(\mathbf{r}) = \frac{\mu_0}{4\pi} \int \mathbf{J}(\mathbf{r'}) \times \frac{\mathbf{r} - \mathbf{r'}}{|\mathbf{r} - \mathbf{r'}|^3} \, dV(\mathbf{r'}). \tag{2.10}$$

This is the well known Biot-Savart Law. Since the surface integral of the current density is the total current intensity, I, passing through a closed curve, C, the last equation can also be expressed as[2]

$$\mathbf{B}(\mathbf{r}) = \frac{\mu_0 I}{4\pi} \int_C \frac{d\mathbf{l'} \times (\mathbf{r} - \mathbf{r'})}{|\mathbf{r} - \mathbf{r'}|^3} \tag{2.11}$$

whose differential form is

$$d\mathbf{B}(\mathbf{r}) = \frac{\mu_0 I}{4\pi} \frac{d\mathbf{l'} \times (\mathbf{r} - \mathbf{r'})}{|\mathbf{r} - \mathbf{r'}|^3}. \tag{2.12}$$

This is one of the main expressions used in gradient coil design as it can be used to describe the magnetic field produced at one point $\mathbf{r}$, by a wire element, $d\mathbf{l}$, carrying a current at position $\mathbf{r'}$.

It is also worth noting that in a source-free volume, that is, through which no current flows, the magnetic induction **B** satisfies

$$\nabla \times \mathbf{B} = 0; \qquad \nabla \cdot \mathbf{B} = 0 \tag{2.13}$$

so by using the vector identity, $\nabla \times \nabla \times \mathbf{B} = \nabla(\nabla \cdot \mathbf{B}) - \nabla^2 \mathbf{B}$, it is straightforward to prove that

$$\nabla^2 \mathbf{B} = 0. \tag{2.14}$$

But since the Laplacian is a scalar operator, each Cartesian component of **B** (and hence in particular the axial component) has to satisfy Laplace's equation

$$\nabla^2 B_z = 0. \tag{2.15}$$

B_z can therefore be represented in terms of a basis of orthogonal solutions of the Laplace equation.

---

[2] This electromagnetic theory will be applied to current carrying wires, so the use of I instead of **J** is more convenient for these purposes.

2.3 Requirements and performance parameters

One key concept in the MRI process is the generation of field gradients, whose z-component[3] is expected to vary linearly with position

$$B_z(\mathbf{r}) = G_x\ x, \qquad B_z(\mathbf{r}) = G_y\ y, \qquad B_z(\mathbf{r}) = G_z\ z \tag{2.16}$$

where G_i is the gradient proportionality constant, and $i = x, y, z$ the Cartesian coordinates. Hence three gradients are required, G_x, G_y and G_z in order to develop the spatial encoding; G_x and G_y are known as transverse and G_z as longitudinal gradients. Due to common cylindrical geometry (and hence axial symmetry) the y-gradient coil arrangement can be generated by a rotation of the x-gradient by 90° about the z-axis.

Next we list some of the most important parameters that describe the performance of a gradient coil, as well as the most important requirements and issues to consider when designing a coil to achieve the desired functionality and image quality.

Uniformity

The quality of the images will depend on how linear the variation of the field is with position. This uniformity can be assessed through the local deviation of the field from the desired value

$$E_B(\mathbf{r}) = \frac{B_z(\mathbf{r}) - G \cdot x_i}{G \cdot x_i}. \tag{2.17}$$

Equivalently a local error of the gradient can be defined as

$$E_G(\mathbf{r}) = \frac{dB_z(\mathbf{r})}{dx_i} - G. \tag{2.18}$$

An alternative but equally valid expression can also be used to describe the uniformity

$$E_B(\mathbf{r}) = \frac{B_z(\mathbf{r}) - G \cdot x_i}{B_z^{max}}, \tag{2.19}$$

where B_z^{max} is the maximum value of B_z in the imaging region.

---

[3]In MRI it is the variation of the z-component of the magnetic field, parallel to the strong polarising field, B_0, which is important.

Homogeneity

A related parameter which informs us how the actual field deviates from the ideal gradient within the imaging volume, V, can be defined as

$$\frac{1}{V} \int_V \left(\frac{B(\mathbf{r})}{G \cdot x_i} - 1 \right)^2 d^3 r \tag{2.20}$$

Efficiency

This is a quite significant performance value in the coil design that characterizes the gradient strength per unit of current drawn

$$\eta = \frac{G}{I}, \tag{2.21}$$

it has units of $Tm^{-1}A^{-1}$ for gradient coils and its amplitude varies with the radius or characteristic length of the coil, defined by a, as $\eta \sim a^{-2}$. When designing a coil the value of η should be made as large as possible, but as we are going to see this requirement may be in conflict with the need to optimize other performance parameters.

Inductance and Resistance

The inductance, L, can be related to the stored magnetic energy, W, in the coil

$$W = \frac{1}{2} \cdot L \cdot I^2, \tag{2.22}$$

and controls the maximum rate of change of current in the coil and hence the maximum possible rate of change of gradient per unit time

$$\frac{dG}{dt} = \frac{\eta \cdot v}{L}, \tag{2.23}$$

and the switching time (gradient rise time) τ

$$\tau = \frac{G \cdot L}{\eta \cdot v} = \frac{L}{R}, \tag{2.24}$$

where v is the voltage applied to the coil and R is the coil resistance, which is also related to the amount of power dissipated in the coil by

$$P = I^2 R. \tag{2.25}$$

Hence minimum inductance is one of the main requirements in any coil design method in order to reduce this rise-time, and so improve the image formation process, similarly ideal coils should have a minimum R in order to reduce the unwanted heating of the gradient coils.

This can be illustrated with a simple example [9]: in a RL-circuit (Fig. 2.1(a)) the current in the circuit satisfies the following differential equation

$$L\frac{dI(t)}{dt} + RI(t) = v(t). \tag{2.26}$$

(a)   (b)
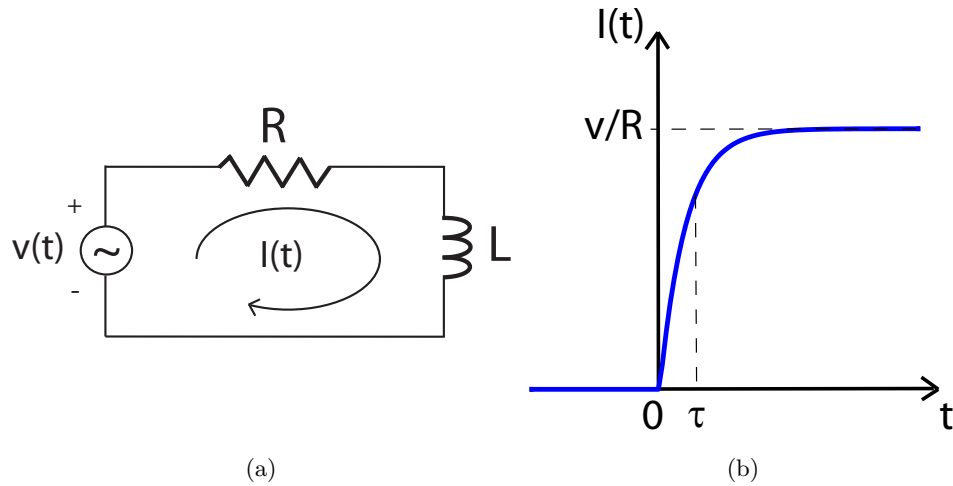
Figure 2.1: *(a) RL-circuit; (b) Evolution of the current intensity in a RL-circuit with the time.*

If the voltage is switched on at $t = 0$, with no current present in the electric circuit before this moment, then the current will rise exponentially

$$I(t) = \frac{v}{R}\left[1 - e^{(-R/L)t}\right]. \tag{2.27}$$

The intensity does not rise to its maximum value, $I_{max} = \frac{v}{R}$, instantaneously; in fact it shows an asymptotic behavior, and the rate at which this maximum current is reached is controlled by the relaxation time

$$\tau = \frac{L}{R}. \tag{2.28}$$

τ represents the time it takes for the current to rise 63% of its full value. So to reduce the

rise time we have to either increase R (but this will increase the undesired power dissipation) or reduce L.

Figure of Merit (FOM)

For any coil the inductance varies as $L \propto n^2$, where n is the number of turns; so by decreasing n, lower values of L are obtained. However as $\eta \propto n$, it is worth defining a new figure of merit which is independent of n

$$FOM = \frac{\eta^2}{L}. \tag{2.29}$$

For all the coils in this work, we consider L to be proportional to the characteristic length or radius a, hence the figure of merit just defined grows as $FOM \propto a^{-5}$.

It can also be shown that the FOM is inversely proportional to the power of the gradient coil amplifier needed to generates a fixed maximum gradient at a fixed rise time.

Another important figure of merit, suggested by Turner [8], which combines efficiency and homogeneity, is

$$\beta = \frac{\eta^2/L}{\sqrt{\frac{1}{V} \int_V \left(\frac{B(\mathbf{r})}{G \cdot x_i} - 1 \right)^2 d^3 r}}. \tag{2.30}$$

It is worth noting that some of the parameters may be in conflict, in the sense that the increase of one causes the reduction in another. This trade-off is a basic element in the coil design process, always directed towards producing the best coil performance.

Torque balancing

It is known that a current flowing in an external magnetic field experiences a force, $\mathbf{F}$, given by

$$\mathbf{F} = \int_V \mathbf{J} \times \mathbf{B} \; d^3 r \tag{2.31}$$

and hence a torque, $\mathbf{M}$, given by

$$\mathbf{M} = \int_V \mathbf{r} \times (\mathbf{J} \times \mathbf{B}) \; d^3 r. \tag{2.32}$$

So in designing gradient coils, it is important to consider the force and torque experienced by the coil windings when carrying current in the presence of the main field.

In general if the coil geometry has axial symmetry it will experience no net torque in the presence of a z-directed field, but for asymmetric coils it is necessary to balance the torque

deliberately to avoid damage or changes in the coil structure due to excessive torques.

Eddy Currents

When designing a gradient coil we aim to minimise its interaction with any other equipment present in the MRI system. The switching on/off of the gradient fields corresponds to a time-dependent magnetic field, and hence according to Faraday's Law an electric field, **E** will be induced in nearby conductors. Then the situation is no longer purely magneto-static and the resulting electric field can induce current flow, J in conducting media[4].

Consequently the switching of gradient coils generates an undesired electric field in nearby conducting objects (even in the human conducting tissues), and hence leads to the generation of electric currents which can affect the main magnetic field and degrade the gradient homogeneity producing a loss of image quality.

Turner et al. [11] investigated these undesirable reflected currents and proposed the use of a conducting shield positioned between the gradient coils and surrounding structures. Another solution to this problem was given by Mansfield [12] which is based on an active magnetic screening technique that allows the production of gradient coils which are magnetically decoupled from their surroundings.

Peripheral Nerve Stimulation (PNS)

Eddy currents not only occur in the scanner itself, but they can also be induced in the conducting tissue of the patient. These induced currents can lead to Peripheral Nerve Stimulation (PNS) [14, 15]. Although the process of nerve stimulation is not fully understood it can be related to a depolarisation of nerve or muscle cell membranes; being able to produce important bio-effects, including a feeling of a tingling or twitching, and at higher levels of stimulation even pain.

A solution to this problem was presented by Harvey [16], in which the approach results in an actively shielded whole-body gradient coil designed to reduce the peripheral nerve stimulation in its modes of operation by reduction of the length of the gradient coils region of uniformity. This technique is referred as modular gradient coil design and its basic principle is that the size of the volume of gradient field linearity, and consequently the gradient performance, is variable depending upon the application. Unfortunately it has the obvious drawback of reducing the extent of the region over which imaging can be carried out.

---

[4]Note that so far we have established the coil design within a magneto-static framework, but now there exist a time-dependence in the gradient fields. Nevertheless the switching frequencies, ω, for an MR scanner are usually below 10 kHz so the magnetic fields still dominate at these low frequencies, and the use of a quasi-static approximation is completely valid.

Acoustic noise

The forces induced by the flow of electric current through the gradient coils inside the static magnetic field produce physical movements in the conducting windings, these mechanical oscillations when coupled to the surrounding air can generate acoustic noise [18]-[19]. The levels of noise can be higher than 100 dB. This disturbing sound can produce undesired activation in brain regions involved in auditory processing, as well as anxiety [20] and other interferences with stimulus presentation in fMRI (functional Magnetic Resonance Imaging). Some engineering modifications in the hardware [21]-[23] have been suggested as a way of reducing the acoustic noise in gradient coils for MRI. These include active acoustic screening for quiet gradient coils. Vacuum technology [24] and other forms of isolation were also proposed for this purpose.

2.4 Coil design methods

Coil design methods are here divided into three groups. The first two categories, discrete wires and current density techniques, are considered classical methods, in the sense that these are the approaches described early in the development of gradient technology [8]. The remaining techniques are included in a third group termed as new methods.

A common feature of most of the methods is the characterization of the current density in term of specific functions. These methods therefore rely entirely on the properties of the functions used to describe the problem, and the solutions are therefore limited to the specific domain where the functions are defined.

2.4.1 Coils with discrete windings

Helmholtz coil

A circular loop of radius, a, carrying a current I, produces a magnetic field, $\mathbf{B}$. If it lies in the xy-plane the axial component of the magnetic induction along the z-axis will be given by [25]

$$B_z(\mathbf{r}) = \frac{\mu_0 I a^2}{2\big[a^2 + (z - z_0)^2\big]^{3/2}}. \tag{2.33}$$
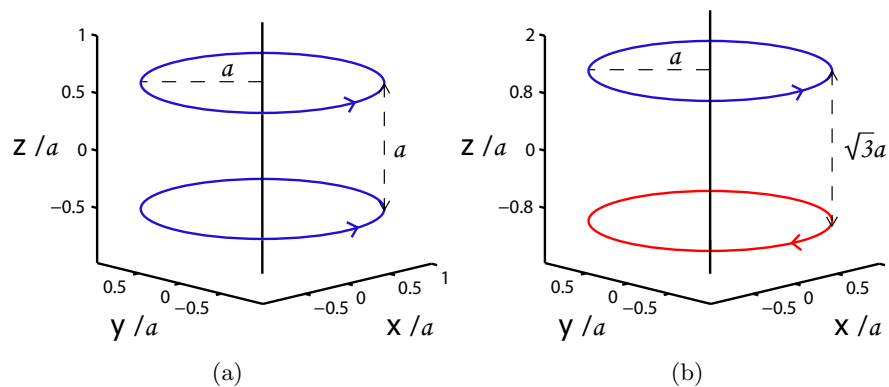
Figure 2.2: *(a) Helmholtz and (b) Maxwell coil configurations.*

The first attempts to produce a tailored field were made employing combinations of basic coil elements such as loops, whose magnetic profiles were well known. One of the simplest coil design is the Helmholtz pair or coil, which consists of two coaxial circular loops with the same radius and carrying the same current as shown in Fig. 2.2. The z-component of

the field produced on axis by this arrangement of two hoops placed at $z_0 = \pm a/2$ is

$$B_z(\mathbf{r}) = \frac{\mu_0 I a^2}{2\left[a^2 + (z - \frac{a}{2})^2\right]^{3/2}} + \frac{\mu_0 I a^2}{2\left[a^2 + (z + \frac{a}{2})^2\right]^{3/2}}. \tag{2.34}$$

The symmetry of the arrangement eliminates all odd orders of field variation with z, so that the separation distance between loops is then chosen to be equal to the radius, in order to cancel the second order term in a Taylor expansion of B_z on axis such that

$$B_z(\mathbf{r}) = B_0 + O(z/a)^4, \tag{2.35}$$

therefore B_z on the axis is constant up to a term of order z^4, and the Helmholtz coil generates a uniform constant field of magnitude, $B_0 = \frac{\mu_0 I}{a}$, around the origin (see Fig. 2.3(a)).
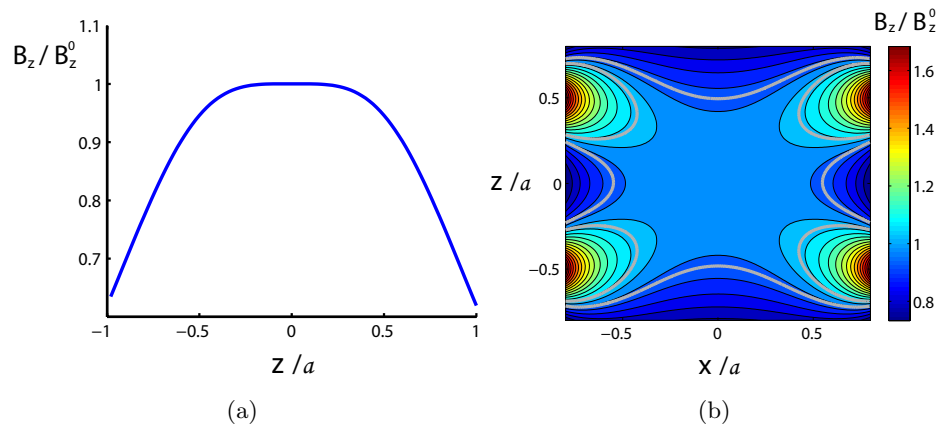
Figure 2.3: a) B_z on z-axis for a Helmholtz coil; (b) shows the contour lines of this field in the central xz-plane, the grey line delimits the region where the field deviates less than 5% from its value at the center, B_0.

Maxwell Coil

As we have seen the Helmholtz coil design relies on the combination of discrete wire loop elements with a spacing chosen to cancel undesired orders of B_z. This idea can also be applied to the design of a longitudinal gradient coil. The most elemental example is the Maxwell coil, consisting of two coaxial circular loops of radius a, but this time carrying currents circulating in opposite directions and with a slightly larger separation of the loops 2.2(b). This is an antisymmetric configuration, in which B_z and all its even derivatives

vanish at the origin. When the loops are spaced by a distance of $\sqrt{3}a$ the third order term is also zero, so that

$$B_z(\mathbf{r}) = B'_z(0)z + O(z/a)^5. \tag{2.36}$$

The Maxwell coil produces a z-gradient field that deviates by less than 5% within a sphere of radius 0.5a, Fig. 2.4(b), and has an efficiency of

$$\eta = \frac{8.058 \times 10^{-7}}{a^2} Tm^{-1}A^{-1} \tag{2.37}$$

per turn.

(a)   (b)
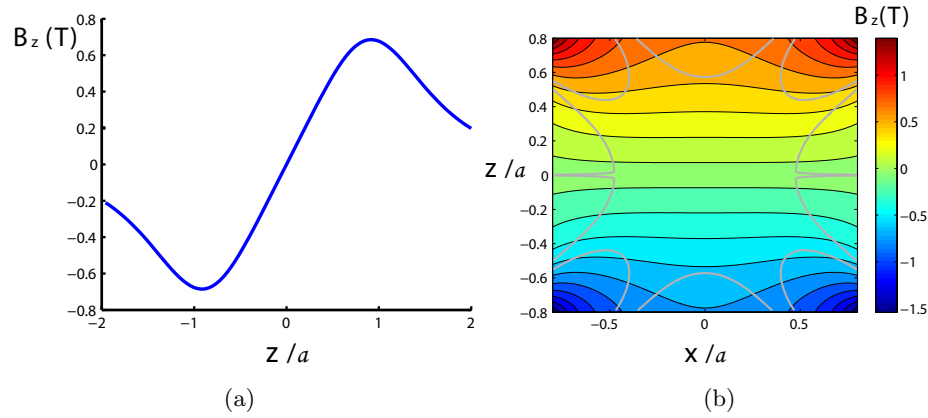
Figure 2.4: *(a) B_z on the z-axis for a Maxwell coil; (b) shows the contour lines of this field on a xz-plane, the grey line encloses the region where the field deviates less than 5% from an ideal longitudinal gradient.*

Golay Coil

Transverse field gradients can also be produced by combination of basic wire elements. In this case saddle units are employed. An important example is the so-called Golay [26] or double-saddle coil, consisting of four sets of symmetrically placed saddle coils as depicted in Fig. 2.5.

To understand how saddle positions are chosen we have to recall the harmonic nature of the magnetic field in a source free region, Eq. 2.15; which means B_z can be expanded in a series of appropriate orthonormal functions [10]

$$B_z(r, \theta, \phi) = \sum_{n=0}^{\infty} \sum_{m=0}^{n} r^n P_n^m(\cos\theta)(A_{nm}\cos m\phi + B_{nm}\sin m\phi) \tag{2.38}$$

where $P_n^m(\cos\theta)$ are the associated Legendre polynomials. This is the general solution for B_z, and A_{nm} and B_{nm} are unknown coefficients that can be determined from the coil's wire paths.

The strategy for obtaining the desired transverse gradient field coil is equivalent to that applied with Helmholtz and Maxwell coils, but now the expansion used for B_z of every wire unit is given by Eq. 2.38 instead of the simple Taylor approach.
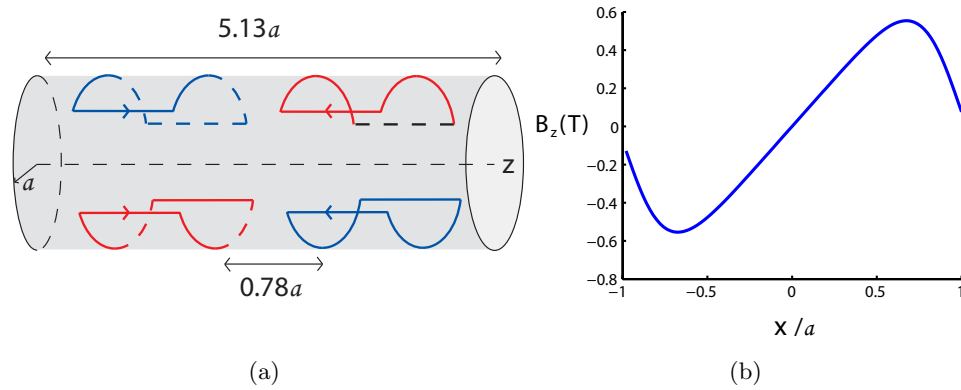
Figure 2.5: *(a) Golay Coils (b) B_z on x-axis produced by this Golay Coil.*

The saddle coil's axial extents positions and the angle subtended by each of the arc segments are chosen to eliminate unwanted terms in the field expansion, leaving the term corresponding to the desired field gradient, which in the Golay coil case is that whose axial component linearly increases in the transverse direction.

It can be shown [9] that the optimal configuration possesses four inner and four outer arcs, all subtending an angle of 120° with the saddle coil positions as shown in Fig. 2.5. The transverse field gradient deviates by less than 5% from linearity within a sphere of radius $0.6a$, and the coil has an efficiency of

$$\eta = \frac{9.2 \times 10^{-7}}{a^2} Tm^{-1}A^{-1} \tag{2.39}$$

per turn. The main disadvantage of this type of coil is its large size; the performance of the coil can be improved by employing more arcs with different arc lengths whose localization has to be chosen to null more undesired higher-order terms in the field expansion [27], [28].

2.4.2 Coils with distributed windings

This type of coil is based on the idea of wire arrangements wound so as to approximate continuous current distributions. This leads to a distribution of the windings over the whole coil surface which means less concentration of current density and consequently lower inductance values at fixed efficiency, as well as a larger region of uniformity than is provided by coils composed of more discrete windings. Before describing the different coil design techniques that belong in this group, we introduce some useful concepts to provide a better understanding of these approaches.

Generally all these methods rely on the cylindrical shape of the coil. Therefore at this point, it is worth introducing cylindrical coordinates (ρ, ϕ, z) as this coordinate systems suits the geometry of the problem. The current density $\mathbf{J}$ can be written

$$\mathbf{J}(\rho, \phi, z) = \mathbf{J}(\phi, z) \; \delta(\rho, a) \tag{2.40}$$

where the delta functions restrict current flow to the cylindrical surface of a coil of radius, a. Since there is no radial component of $\mathbf{J}$, the current density can be written as

$$\mathbf{J}(\phi, z) = J_\phi \hat{\boldsymbol{\varphi}} + J_z \hat{\boldsymbol{k}}. \tag{2.41}$$
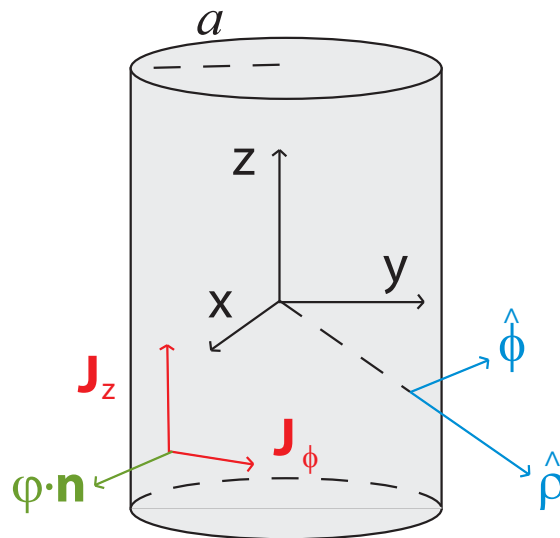
Figure 2.6: *Cylindrical Coordinates*

In cylindrical coordinates the continuity equation, Eq. 2.4, can be written as

$$\frac{1}{a}\frac{\partial J_\phi}{\partial \phi} = -\frac{\partial J_z}{\partial z} \tag{2.42}$$

which links both components of the current density vector.

As **J** is a divergence-free vector, it can be expressed as the curl of a vector perpendicular to the surface where the current flows

$$\mathbf{J}(\mathbf{r}) = \nabla \times \left[\varphi(\mathbf{r})\, \mathbf{n}(\mathbf{r}) \right], \tag{2.43}$$

where $\mathbf{n}(\mathbf{r})$ is a unit vector normal to the surface, that is, for a cylindrical surface the radial unit vector; then the components of the current can be written as

$$J_\phi = \frac{\partial \varphi}{\partial z}; \qquad J_z = -\frac{1}{a}\frac{\partial \varphi}{\partial \phi} \tag{2.44}$$

φ is usually referred to as the stream function. The introduction of the idea of the stream function for current density in coil design was an important improvement, as it provides an alternative representation of the problem, as well as, a realistic description of the current density, as **J** defined through Eq. 2.43 is automatically divergence-free and lies on the surface.

A final step, common to all the following methods, is finding the best approximation of discrete wires to a continuous current distribution. This can be achieved using the concept of a stream function, as the wire paths can be considered as stream lines of φ, that is, the lines where this function takes a constant value, which can be proved to be locally parallel to the current density vector [30]. The final wire arrangement can therefore be obtained from the contours of this function.

Some approaches apply the stream function indirectly such as the one proposed by Schenck *et al.* [31] who developed a method that uses a scalar function φ, to calculate the shape of the wires. Unfortunately this approach lacks an end-coil correction. More details about coils designed using this mathematical tool and its implementation will be found in the following sections.

Finally we now describe the different methods in this group, most of them rely upon on an analytic representation of the problem; for example, Fourier-Bessel expansion (instead of the harmonic one performed for discrete coils with discrete windings).

Target field method

The target field method developed by Turner [32], relies on representation of the field in terms of the Fourier-Bessel expansion.

The starting point for this representation is the Poisson equation (Eq. 2.8), the Green's function for the partial differential equation in cylindrical coordinates, which can be expressed as [25]

$$\frac{1}{|\mathbf{r} - \mathbf{r'}|} = \frac{1}{\pi} \sum_{m=-\infty}^{+\infty} \int_{-\infty}^{+\infty} dk \; e^{im(\phi-\phi')} e^{ik(z-z')} I_m(k\rho^<) K_m(k\rho^>) \tag{2.45}$$

where $\rho^<(\rho^>)$ is the lesser (greater) of ρ (radial coordinate of the field point) and ρ' (radial coordinate of the source point). $I_m(k\rho^<)$ and $K_m(k\rho^>)$ are the mth-order modified Bessel functions [11].

By using Eq. 2.10 the z-component of the magnetic field inside the cylinder of radius, a, can also be written as a Fourier-Bessel series

$$\mathbf{B}_z(\rho, \phi, z) = -a\frac{\mu_0}{2\pi} \sum_{m=-\infty}^{+\infty} \int_{-\infty}^{+\infty} dk e^{im\varphi} e^{ikz} ka I_m(k\rho) K'_m(ka) J_\phi^m(k) \tag{2.46}$$

where $J_\phi^m(k)$ is the Fourier transform of the azimuthal component of the current density

$$J_\phi^m(k) = \frac{1}{2\pi} \int_{-\pi}^{+\pi} d\phi \int_{-\infty}^{+\infty} dk e^{im\varphi} e^{ikz} J_\phi(\phi, z). \tag{2.47}$$

It is worth noting, once more, that in order to be confined to the cylindrical surface, the current lacks a radial component, and that the ϕ- and z-components of the current density are related by the continuity equation, which in this case can be reduced to

$$J_\phi^m(k) = -\frac{ka}{m} J_z^m(k). \tag{2.48}$$

Now that the mathematical formalism has been established let us introduce the target field method. It starts from Eq. 2.46, which shows the relationship between flowing currents and magnetic field generated. This can be inverted, so that given a prescribed B_z (target field) over a cylindrical surface inside the coil, the current density required to create it may be determined. Evaluating Eq. 2.46 on a second cylinder of radius $r = c < a$ and
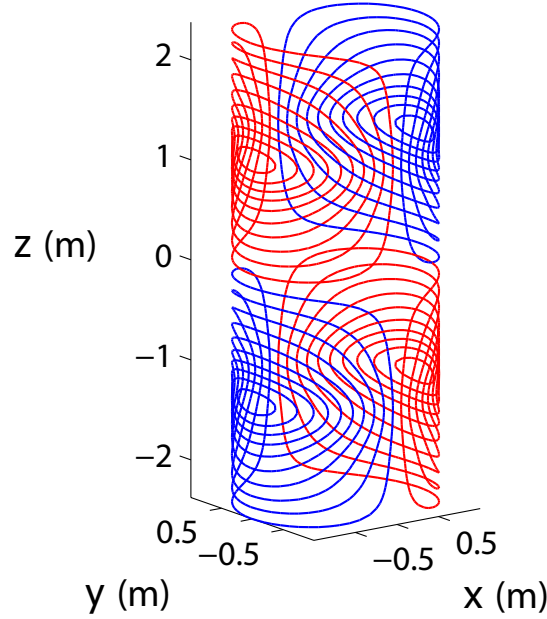
Figure 2.7: *Transverse gradient coil designed using the target field method.*

performing the inverse Fourier transform of both sides of the equation, yields

$$J_\phi^m(k) = -\frac{B_z^m(c,k)}{\mu_0 ka I_m(kc) K_m'(ka)} \tag{2.49}$$

where

$$B_z^m(c,k) = \frac{1}{2\pi} \int_{-\pi}^{+\pi} d\phi \int_{-\infty}^{+\infty} dz\, e^{-im\phi} e^{-ikz} B_z(c,\phi,z). \tag{2.50}$$

Thus if B_z is known everywhere on a cylinder of radius c, the current density can be found from a Fourier transformation of $J_\phi^m(k)$ (note that $J_z^m(k)$ can be deduced from Eq. 2.48). It can be proved that for other values of r, inside the coil, the magnetic field behaves in a similar fashion to the target field. This is based on approximations and convergence conditions of the modified Bessel functions.

This inversion of an integral equation finds a powerful tool in its computational implementation in the Fast Fourier Transformation (FFT) algorithm [34].

Minimum inductance method

The minimum inductance method developed by Turner [35], is an extension of the target field approach leading to an improved ability to design coils with optimum inductance,

which was one aspect not considered in the original target field approach and which is consistent with the initial requirements related to the coil performance.

An expression based on the Fourier-Bessel expansion can be achieved by applying Eq. 2.48 to the definition of inductance

$$L = -\frac{\mu_0 a^2}{I^2} \sum_{m=-\infty}^{+\infty} \int_{-\infty}^{+\infty} dk |J_\phi^m(k)|^2 I_m'(ka) K_m'(ka), \qquad (2.51)$$

where I is the current in each turn of the coil.

A functional $U(J_\phi^m(k))$ can be built using the set of Lagrange multipliers λ_n

$$U(J_\phi^m(k)) = L + \frac{1}{I} \sum_{n=1}^{N} \lambda_n (B_n - B_z(r_n, \phi_n, z_n)), \qquad (2.52)$$

where $\mathbf{r} = (r_n, \phi_n, z_n)$ is the set of points in the target region, B_n is the desired field at the points and B_z the actual field values at these positions.

The minimization of this functional, followed by the constraint

$$B_z(r_n, \phi_n, z_n) = B_n \qquad (2.53)$$

leads us to an expression for the current distribution and an analogous approach can be followed in order to derive a minimum resistance (power dissipation) coils [36].

Apodisation

Coils designed to have minimum inductance, power or coil length can show a spatial oscillatory behavior of the current density (see Fig. 2.8(a)), which increases the power dissipation of the coil and reduces coil efficiency.

These oscillations can be removed by using the technique termed as apodisation, which involves in multiplying the calculated Fourier transform of J_z by a Gaussian function so as to smooth it.

$$j_\phi^A(\phi, z) = j_\phi(\phi, z) e^{-2h^2 k^2} \qquad (2.54)$$

where h is the apodisation length.

Coils of restricted length

A technique developed by Carlson *et al.* [37] incorporates constraints on the length of the gradient coil, which is a characteristic that was not considered in the previously described
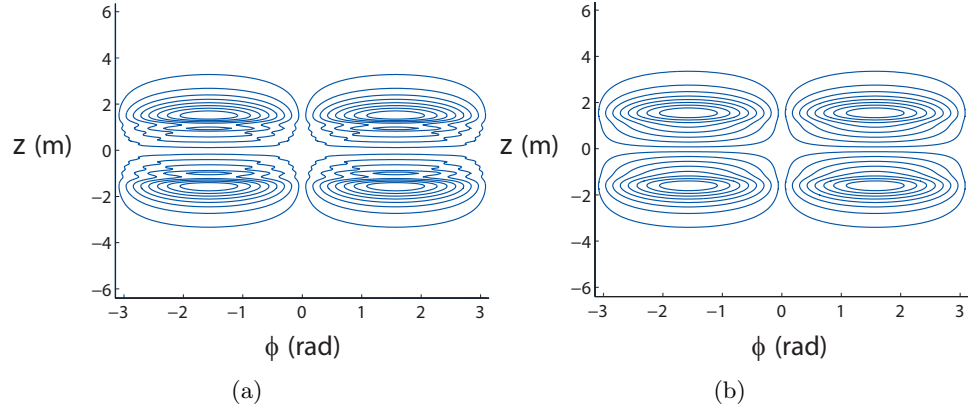
Figure 2.8: *(a) Unapodised minimum inductance x-gradient contour lines and (b) the same coil contour lines after apodisation.*

methods and which is very important when designing coils of reduced size. This length constraint is set in the definition of the current distribution, which is written in terms of a Fourier series. For a z-gradient coil we can write

$$J_\phi(\phi, z) = \sum_n^N a_n sin\frac{\pi z}{L} \tag{2.55}$$

for an x-gradient coil

$$J_\phi(\phi, z) = \sum_n^N b_n cos\frac{\pi z}{L} cos\phi \tag{2.56}$$

with the Fourier coefficients as unknowns, $|z| < L$ while $J_\phi(\phi, z) = 0$ for both cases when $|z| > L$. In this way, it can be seen that the finite length current distribution is formed. From this definition, expressions for the coil inductance, resistance or field in terms of the Fourier coefficients can be obtained. The following functional is then formed

$$U = \alpha L + \beta R + \sum_{p=1}^{P} [B_z(\mathbf{r}_p) - B_p]^{2,} \tag{2.57}$$

where the $\mathbf{r}_p$ represents a set of points of the region of interest inside the coil, where B_z is the actual field and B_n is the desired field. The weights α and β are chosen to allow a degree of flexibility in the trade-off between coil homogeneity, inductance and resistance. By finding the Fourier coefficients that minimize this functional, an expression for the current density can be formed.

A modification to this approach is the Slack, Finite-Length Coil Design [38], in which the functional is not differentiated to obtain the parameters that define the current density. Rather, an inequality relationship is constructed that describes the error in the magnetic field uniformity Eq. 2.18 at each of the P target points.

Matrix Inverse Method

This method suggested by Hoult [29], whose first application was to design solenoid coils to produce a uniform field, is based on a matrix description of the current density for the coils and the magnetic field at N different locations, where the current in the loops can be related to the field. If N such points are well chosen, the magnetic field matrix can be invertible, but in general it may be a singular matrix and the solution may require large variations of the current from one turn to another, which will increase the power dissipation of the coil. This problem can be overcome by using a Moore-Penrose inversion or pseudo inversion technique, which yields the current distribution able to generate the prescribed magnetic field with minimum power dissipation.

This technique has also been applied to coils with discrete windings. In general, the field can be decomposed into a set of orthogonal basis functions, such as spherical harmonics, and instead of specifying the field at a small number of points on axis, the field can be specified in terms of a small number of spherical harmonics.

2.4.3 New methods

Simulated Annealing

Simulated Annealing (SA) is an iterative optimization technique which is based on a modified Monte Carlo approach. It was introduced by Metropolis *et al.* [128], and as its name implies, it exploits an analogy between the way in which a metal cools and freezes into a minimum energy crystalline structure (the annealing process) and the search for a minimum in a more general system.

This technique finds a solution to an optimization problem by trying random variations of the current solution. A worse variation is accepted as the new solution with a probability that decreases as the computation proceeds. The slower the cooling schedule, or rate of temperature decrease, the more likely the algorithm is to find an optimal or near-optimal solution.

In applying the SA algorithm to coil design an error function for minimisation is chosen, whose terms correspond to the coil's linearity, efficiency, inductance or other factors such as shielding or power dissipation.

A initial guess is selected as a starting point for the coil configuration and then the initial error is calculated,. Aa small random move in either wire positions or current in the wires, is then performed. The iterations finish when a global minimum of the specified gradient error function is located. This technique has been shown capable of producing useful field gradient coils [39]-[41].

Planar Coils

Planar gradient coil designs can have a number of advantages over cylindrical coils as objects to be imaged can sometimes be inserted more easily, the distance from the current path to the image region can be reduced; coils may be easier to manufacture and even the claustrophobia experienced by some patients during MRI scans may be reduced. The disadvantage of this type of assembly is that it is difficult to control field homogeneity with planar coils.

The use of this alternative coil geometry has been the subject of considerable research [45]-[51], where most of the methods explained before can be applied for the design of planar coils.

Analytic Approaches for Other Coil Geometries

Most of the methods so far described are based on a current carrying surface with a cylindrical shape. The symmetry properties of this geometry make it relatively simple to form mathematical descriptions of the coil characteristics. In the same way, other shapes offer suitable form geometries where an analytic formalism can be developed.

The most clear case is the sphere, where the Green's function associated with the Poisson equation can be expressed in terms of a linear combination of spherical harmonics [25]. This property has been used by Liu. *et al* [42] to present a Lagrange multiplier technique for design of a minimum inductance gradient coil with a spherical shape. This type of coil shows a high efficiency as the imaging region is completely surrounded by the coil, but in general closed geometries suffer the significant disadvantage of offering no natural aperture for sample access.

Another relevant approach introduced by Green *et al.* [43] deals with spherical geometries employing a similar mathematical formalism, although in this work the main emphasis is placed on gradient coils with hemispherical shape. This is an open geometry, which is well matched to the head for imaging the brain and which provides improved performance compared with cylindrical coils.

Whereas symmetric coils are torque-balanced, removing the axial symmetry of a transverse
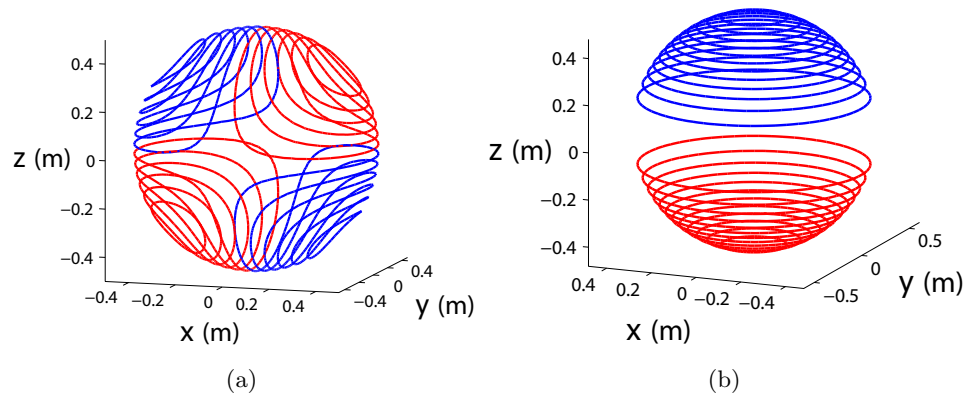
Figure 2.9: *(a) Longitudinal and (b) transverse spherical gradient coils.*

gradient coil means that it is no longer naturally torque-balanced. In the case of a transverse gradient coil this problem is overcome by including a zero net torque constraint in the approach to coil design.

It was also shown by Legget *et al.* [44] how the addition of a short, cylindrical coil section to the open end of the hemisphere, helps overcome the problem of torque-balancing in the design of transverse hemispherical coils.
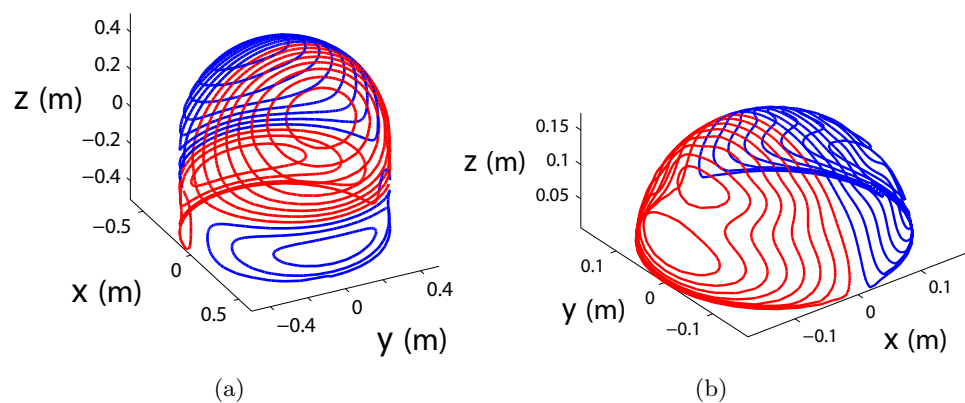
Figure 2.10: *(a) Transverse dome and hemispherical gradient coils.*

Using this approach, a full three-axis, dome head gradient coil set was designed, where the current was characterized in term of Fourier harmonics for the cylindrical portion of the coil, and spherical harmonics on the hemispherical surface; with the corresponding match-

ing condition between the two parts. This type of coil presents significant advantages for brain imaging as a result of the large increase in gradient performance that is achieved as the coil size is reduced.

Wave Equation Method

In designing dome structures correct interfacing of current densities at the boundary between the hemispherical and cylindrical parts is one the main difficulties, as the analytical boundary restrictions can impose limitations on the achievable coil design. Iterative techniques such as the wave equation method (WEM) [52] that do not use a strict boundary condition can be used to remove this restriction and to allow the wire windings to freely form over these two domains.

The WEM has also been used to design planar x-, y-, and z-gradient wire windings to produce required magnetic fields within a certain domain [52].

Stream Function Methods

The stream function of a current density, φ, is a widely employed idea, but as it has already been stated, its major application has been oriented to determining the coil wire paths once an optimal current distribution has been identified. There have also been some approaches using φ indirectly, such as [54] in which the stream function is used in a hybrid technique that combines SA and the target field method.

Stream function methods are here understood as being those approaches that model the stream function directly so as to find the wire paths, after determining the surface current density, from which the stream function is constructed. Due to the essential relation with the next chapter, we pay special interest to this group of methods here, which can be interpreted as constant inverse boundary element methods (IBEM).

All methods described so far rely entirely on the properties of the functions used to describe the global current distribution and related magnitudes. Stream function methods are based on the use of a local characterization of the current. Because these functions are locally based, the resulting formulation is completely geometry-independent.

The pioneer of this approach is Pissanetzky [55], who introduced the idea in 1992. It was recovered by Lemdiasov [56] for the design of single- and multi-surface gradient coils. Pissanetzky's method is now described using Lemdiasov's notation, which in the opinion of the author, shows more clarity.

As in previous techniques, the goal of this method is to find an optimal current distribution with length constraints so as to achieve a desired magnetic field in the Region Of Interest

(ROI) and to minimize the stored magnetic energy.

Pissanetzky achieves his improvement in the way that a divergence free current distribution that minimizes this cost function is specified. In order to develop such a current distribution the surface of the coil is discretized into triangular patches, whose vertices are called nodes. The starting point is the approximation of the stream function of the problem, which here is written as S, by a linear combination of linear basis functions

$$S(\mathbf{r}) \approx \sum_{n=1}^{N} I_n \varphi_n(\mathbf{r}) \tag{2.58}$$

where N is the number of nodes on the surface, and I_n unknown coefficients; so applying

$$\mathbf{J}(\mathbf{r}) = \nabla \times [S(\mathbf{r}) \ \mathbf{n}(\mathbf{r})] \tag{2.59}$$

where $\mathbf{n}(\mathbf{r})$ is the outward normal surface vector in the point $\mathbf{r}$, yields

$$\mathbf{J}(\mathbf{r}) \approx \sum_{n=1}^{N} I_n \nabla \times [\varphi_n(\mathbf{r})\mathbf{n}(\mathbf{r})] = \sum_{n=1}^{N} I_n \mathbf{f}_n(\mathbf{r}) \tag{2.60}$$

In order to describe the $\mathbf{f}_n(\mathbf{r})$ functions, *triangular meshing* of the coil surface is needed. All triangles, that share a given node, n, form a current element. For any element we can define the vector $\mathbf{e}$, which forms the opposite edge of the mesh triangle to the node Fig. 2.11(a).

The $\mathbf{f}_n$ basis functions are then defined as

$$\mathbf{f}_n(\mathbf{r}) = \mathbf{v}_{ni} = \frac{\mathbf{e}_{ni}}{2A_{ni}}, \qquad if \ \mathbf{r} \in \triangle_{ni}, \tag{2.61}$$

where A_{ni} is the area of the ith-triangle containing the nth-node ($\triangle_{ni}$), and N is the number of triangles related to the same node. Imposing the convention that all the $\mathbf{e}$ vectors follow the same anticlockwise or clockwise direction, a divergence free current density that flows on the surface is produced (the divergence free condition for any point is straightforward to prove since $\mathbf{v}_{ni}$ are constants in any triangle).

It is worth remarking on the complete dependence of the current definition upon the geometry of the mesh.

Having defined the current distribution it is easy to form expressions for the required physical magnitudes involved in the functional to be minimized.

Unfortunately in Lemdiasov's [56] description there are two main drawbacks:
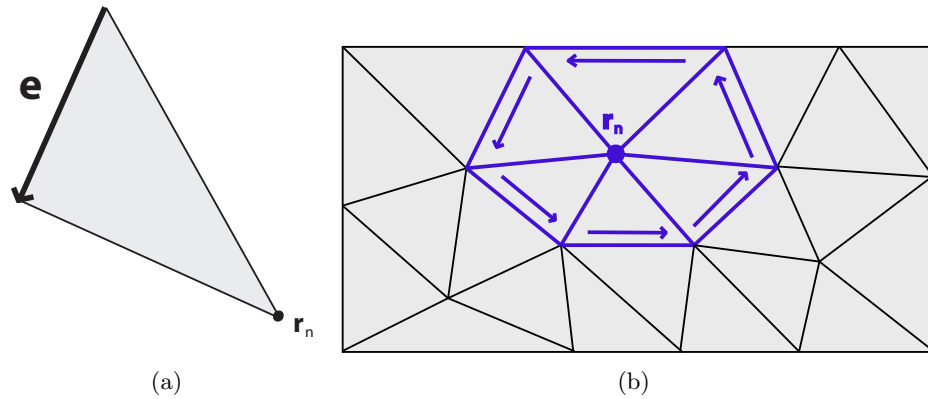
Figure 2.11: *(a) One of the triangles, and the vector **e** associated to the node **r_n**; (b) current element.*

(A) The definition of the stream function: the unknown coefficients I_n, as well as the basis functions φ_n are not perfectly identified. Pissanetzky explains with clarity that I_n can be related to the nodal values of the stream function, although he avoids the use of φ_n as he introduces the current basis functions directly.

(B) The treatment of singular integrals: in the calculation of the magnitudes involved in the functional to minimize, integrals over triangles must be computed. The calculation of these integrals is partially solved by using numerical integration procedures such as Gaussian quadrature, but there are other integrals that are approximated to sums. This allows shorter computational times but represents a potential source of error.

To summarise, Pissanetzky' stream function method is an efficient coil design technique of clear BEM nature, that can be applied to any arbitrary coil surface. Only recently Poole [59]-[60] has been able to take advantage of the full potential of this method, using it to produce coils with totally arbitrary geometry, for example, shielded head gradients with highly asymmetric surface geometry; very short, shielded gradient coils; bi-planar coils or an insertable set of head gradient coils with shoulder cutouts.

Poole integrates a mesh generating program and adds three modifications to improve the original method: i) minimization of power dissipation via inclusion of an extra term in the functional; ii) 3D Contouring Algorithm that allows the position of the wire-paths for any surface and iii) minimum wire spacing is considered in the algorithm, as it is an important engineering constraint.

Another work using Pissanetzky's method is from Moon *et al.* [61], who designed convex-surface gradient coils for interventional applications in vertical-field MRI.

Before finishing this section it is worth mentioning another excellent piece of work by Peeren [58], in which a formulation for quasi-static electromagnetic topological optimization problems involving good conductors only is presented. In this work, the required solution is a conductor shape, subject to geometrical and magnetic constraints. An approach that is well suited for applications such as coil design where a linear or quadratic functional, including terms such as the stored energy or power dissipation, has to be optimized. As an application of the stream function method Peeren [58] studied the design of cylindrical coils using a simple quadrilateral mesh, instead of triangular elements.

Chapter 3

Boundary Element Stream Function Method

3.1 Introduction

In the last chapter, a variety of approaches to coil design based on the stream function method were described, and it was stated that those techniques are, in essence, inverse boundary element methods (IBEM).

A BEM is a numerical method for solving partial differential equations (PDEs). The basis of this method is the reformulation of the PDEs into integral equations that are mathematically equivalent to the original PDEs and describe the same physical problem. In order to solve the integral equations the boundary has to be discretized, and in every mesh element approximations over the involved magnitudes are then applied. In IBEM some or all of the boundary values are unknown, while internal point data are known.

The aim of this chapter is to present a Boundary Element Stream Function Method (BESFM) for the design of gradient coils which is a generalization of the previous approaches [55]-[60] that are based on linear (flat) triangular boundary elements and constant current over the element. Extension to quadratic curved elements has been investigated previously by this author [62] and [67], so any reference to curved element can be found in this work. Here a valid method for any other higher order of element is proposed, although we only describe its application to flat elements.

First by using a BEM mathematical framework, and departing from the stream function we develop a general technique to obtain current density over a given surface which satisfies the continuity equation.

The characterization of the stream function and hence of the current density is given

in term of specific functions which are locally based, so that the resulting formulation is completely geometry-independent; and thus can be applied to any current carrying surface.

Subsequently a BESFM for coil design is described as a magneto-static constrained optimization problem, whose formulation is based on this divergence-free current. We provide an overview of this method and as a simple example, show its application to the design of a cylindrical transverse gradient coil.

Finally we illustrate an extension of this coil design method which can be used to minimize the modulus of the vector potential, and hence to reduce the electric field induced in conducting systems.

3.2   Divergence-free BEM

Let us consider a conductive surface on which an electric current density, $\mathbf{J}$, flows. This current density has to satisfy two conditions

(A) $\mathbf{J}$ must flow on the coil surface. That is

$$\mathbf{J} \cdot \mathbf{n} = 0, \tag{3.1}$$

where $\mathbf{n}$ is the local unit surface vector.

(B) The current density, $\mathbf{J}$, must be divergence-free

$$\nabla \cdot \mathbf{J} = 0, \tag{3.2}$$

so that it obeys the continuity equation over the coil surface.

In the following by making use of the stream function and the BEM framework, we describe how to produce a divergence-free current of any order.

3.2.1   Mesh

BEM requires discretization of the bounding surfaces, which are divided into small sections referred to as boundary elements. The conducting surface can be approximated using T triangular elements $S_t \equiv \triangle_t$ (not necessarily flat)

$$S = \bigcup_{t=1}^{T} S_t \tag{3.3}$$

with N nodes, $\{\mathbf{r}_n\}_{n=1}^{N}$. These nodes are the corners of the elements (plus the mid-point of each side for quadratic curved elements).

We can now define

N2T, which maps the nth-node, $\mathbf{r}_n$ to the set of elements

$$N2T(\mathbf{r}_n) = \{S_{ni}\}_{i=1}^{\Omega} \tag{3.4}$$

where Ω is the number of elements for which $\mathbf{r}_n$ is a node.

T2N, which maps a given element, S_t with its nodes

$$T2N(S_t) = \{\mathbf{r}_{ti}\}_{i=1}^{\Lambda} \tag{3.5}$$

where Λ is the number of nodes in the element.
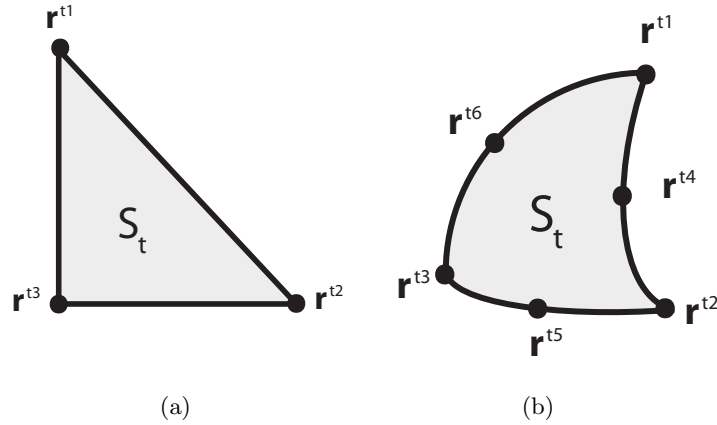
Figure 3.1: *(a) $T2N(S_t)$ for a linear flat element $(\Lambda = 3)$; (b) $T2N(S_t)$ for a quadratic element $(\Lambda = 6)$.*

3.2.2 Shape functions

Shape functions form a useful tool in BEM [63]-[64] as they allow us to express the position of a point placed at one element, $\mathbf{r} \in S_t$, in terms of the coordinates of the nodes of this element, $T2N(S_t) = \{\mathbf{r}_{ti}\}_{i=1}^{\Lambda}$

$$\mathbf{r} = \sum_{i}^{\Lambda} \mathbf{r}_{ti} N^{ti}(\mathbf{r}). \tag{3.6}$$

(a)   (b)
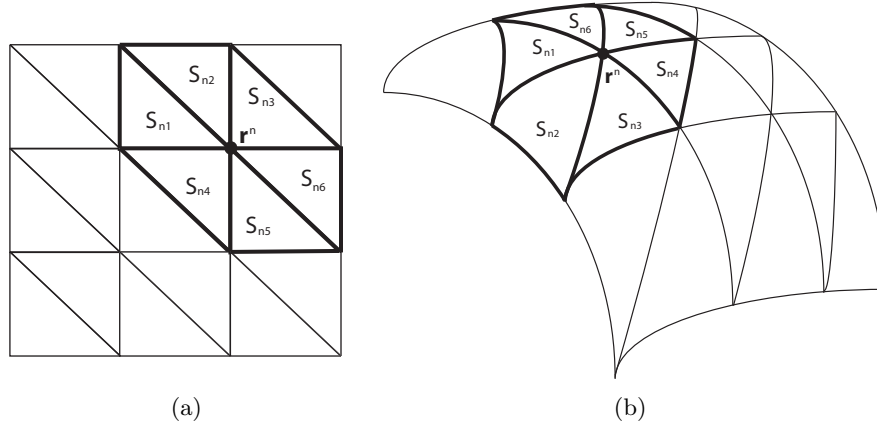
Figure 3.2: *The $N2T(\boldsymbol{r}_n)$ function relates a given node $\boldsymbol{r}_n$ with the elements to which it belongs; (a) flat linear element; (b) quadratic element ($\Lambda = 6$).*

Here each shape function, N^{ti}, is associated with one node $\mathbf{r}^{ti}$, and it must satisfy a interpolation condition: it takes the unit value when evaluated at this node and is zero at the other nodes

$$N^{ti}(\mathbf{r}_{tj}) = \delta_{i,j}. \tag{3.7}$$

Similarly to the representation of the geometry we can use the shape functions to describe the variation of functions defined within the element, in terms of their nodal values

$$\varphi(\mathbf{r}) = \sum_{i}^{\Lambda} \varphi_{ti} N^{ti}(\mathbf{r}) \tag{3.8}$$

where $\varphi_{ti} = \varphi(\mathbf{r}_{ti})$.

For example, the first order shape functions, that apply in the case of flat triangular elements ($\Lambda = 3$) or for linear evolution of the function, can be written in Cartesian coordinates as

$$N^{t1}(\mathbf{r}) = \frac{\mathbf{r} \cdot (\mathbf{r}_{t2} \times \mathbf{r}_{t3})}{\mathbf{r}_{t1} \cdot (\mathbf{r}_{t2} \times \mathbf{r}_{t3})}; \qquad N^{t2}(\mathbf{r}) = \frac{\mathbf{r} \cdot (\mathbf{r}_{t1} \times \mathbf{r}_{t3})}{\mathbf{r}_{t2} \cdot (\mathbf{r}_{t1} \times \mathbf{r}_{t3})}; \tag{3.9}$$

and

$$N^{t3}(\mathbf{r}) = 1 - N^{t1}(\mathbf{r}) - N^{t2}(\mathbf{r}). \tag{3.10}$$

Usually, however it is more convenient to work in parametric space, where the triangular element is mapped into the 2-D parametric (or oblique) representation

$$\mathbf{r} = \sum_{i}^{\Lambda} \mathbf{r}_{ti} N^{ti}(\xi, \eta).\tag{3.11}$$
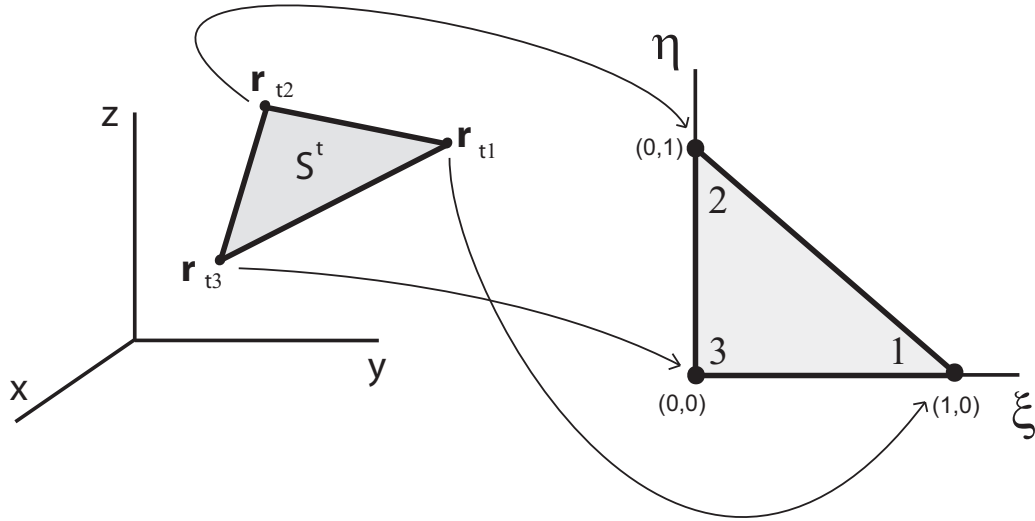
Figure 3.3: *Parametric transformation.*

In this representation the shape functions take a simpler form. For instance, the first order shape functions are

$$N^{t1}(\xi, \eta) = \xi; \qquad N^{t2}(\xi, \eta) = \eta; \qquad N^{t3}(\xi, \eta) = 1 - \eta - \xi.\tag{3.12}$$

with $\xi, \eta \in [0, 1]$. The position of any point inside the flat element is then given by

$$\mathbf{r} = \mathbf{r}_1 \eta + \mathbf{r}_2 \xi + \mathbf{r}_3 (1 - \xi - \eta).\tag{3.13}$$

Analogously we can use the shape functions to represent the linear evolution of a given function in the parametric space

$$\varphi(\xi, \eta) = \varphi_1 \eta + \varphi_2 \xi + \varphi_3 (1 - \xi - \eta),\tag{3.14}$$

where φ_i, i=1,2,3 are the nodal values of the function.

A quadratic evolution of the geometry ($\Lambda = 6$) or of any function can be obtained by using second order shape functions, which in the parametric space are given by

$$
\begin{aligned}
N^{t1}(\xi, \eta) &= \xi(2\xi - 1); & N^{t4}(\xi, \eta) &= 4\xi\eta; \\
N^{t2}(\xi, \eta) &= \eta(2\eta - 1); & N^{t5}(\xi, \eta) &= 4\zeta\eta; \\
N^{t3}(\xi, \eta) &= \zeta(2\zeta - 1); & N^{t6}(\xi, \eta) &= 4\xi\zeta,
\end{aligned}
\tag{3.15}
$$

where $\zeta = 1 - \eta - \xi$.

It is worth remarking that the approximations used to describe geometry and function variation (and hence the shape function used to described them) can be different for a given element. For instance, we can consider a six-node flat element (shape functions of the first order to represent the geometry) where φ has a quadratic variation, and hence we would use shape functions of second order to describe its evolution.

Isoparametric representations arise when the orders of the approximations used for geometry and function are the same.

3.2.3   Stream Function interpolation

Let us mesh the current carrying surface, S, into T triangular elements S_t with N nodes, $\mathbf{r}_n$. We saw in the last chapter that according to the condition described by Eq. 3.2, the current density on the surface can be associated to a stream function by

$$
\mathbf{J}(\mathbf{r}) = \nabla \times \big[\varphi(\mathbf{r})\,\mathbf{n}(\mathbf{r})\big].
\tag{3.16}
$$

If we denote the unknown values of the stream function at the mesh nodes as I_n, that is

$$
\varphi(\mathbf{r}_n) = I_n, \qquad \forall n = 1, ..., N
\tag{3.17}
$$

then we can define the value of the stream function for a given point $\mathbf{r}$ in the tth-element, $\mathbf{r} \in S_t$ as

$$
\varphi(\mathbf{r}) = \sum_{n=1}^{N} \mathcal{N}^n(\mathbf{r}) I_n
\tag{3.18}
$$

where $\mathcal{N}^n$ is a function related to the nth-node, which is defined as follows

$$
\mathcal{N}^n(\mathbf{r}) = \begin{cases} 0 & \text{if} \quad \mathbf{r}_n \notin S_t \\ N_t^n(\mathbf{r}) & \text{if} \quad \mathbf{r}_n \in S_t \end{cases}
\tag{3.19}
$$

and $N_t^n(\mathbf{r})$ is the shape function associated to the same node $\mathbf{r}_n$ in the element S_t. According to the definition above, for any $\mathbf{r}$

$$\mathcal{N}^n(\mathbf{r}) = 0, \qquad \text{unless} \qquad \mathbf{r} \in \{S_{ni}\}_{i=1}^{\Omega} = N2T(\mathbf{r}_n). \tag{3.20}$$

In the same way, if a given point $\mathbf{r}$ is in the tth-element, $\mathbf{r} \in S_t$, the nodes in this element are

$$T2N(S_t) = \{\mathbf{r}_{ti}\}_{i=1}^{\Lambda}. \tag{3.21}$$

The stream function at this point can be expressed as a linear combination of the nodal values of the element where the point is located

$$\varphi(\mathbf{r}) = \sum_{i=1}^{\Lambda} N_t^{ti}(\mathbf{r}) I_{ti}. \tag{3.22}$$

This is the usual expression that describes the function value at one point placed at one element using the shape functions, classical in BEM. Also it should be stressed that although I_n is a fixed value for a given node, the function $N_t^n(\mathbf{r})$ *depends on the element in which* $\mathbf{r}$ *lies.*

3.3 Divergence-free current interpolation

The stream function that has just been defined is continuous, so by using Eq. 3.16 we can express the current density as follows

$$\mathbf{J}(\mathbf{r}) = \sum_{n=1}^{N} I_n \nabla \times [\mathcal{N}^n(\mathbf{r}) \, \mathbf{n}(\mathbf{r})]. \tag{3.23}$$

If we introduce the *current basis vector* associated to the nth-node as

$$\jmath^n(\mathbf{r}) = \nabla \times [\mathcal{N}^n(\mathbf{r}) \, \mathbf{n}(\mathbf{r})], \tag{3.24}$$

then

$$\mathbf{J}(\mathbf{r}) = \sum_{n=1}^{N} I_n \, \jmath^n(\mathbf{r}), \tag{3.25}$$

where

$$\jmath^n(\mathbf{r}) = \begin{cases} 0 & \text{if} & \mathbf{r}_n \notin S_t \\ \nabla \times [N_t^n(\mathbf{r}) \, \mathbf{n}(\mathbf{r})] & \text{if} & \mathbf{r}_n \in S_t \end{cases} \tag{3.26}$$

so that

$$\boldsymbol{\jmath}^n(\mathbf{r}) = 0, \qquad \text{unless} \qquad \mathbf{r} \in N2T(\mathbf{r}_n). \tag{3.27}$$

It is also worth stressing that $\boldsymbol{\jmath}^n(\mathbf{r})$ varies depending on the element in which $\mathbf{r}$ lies. The set of all possible values that $\boldsymbol{\jmath}^n(\mathbf{r})$ can take in its associated elements $N2T(\mathbf{r}_n) = \{S_{ni}\}_{i=1}^{\Omega}$, is termed the **current element** (Fig. 3.5(b)).

This current density satisfies the required conditions specified in Eqs. 3.1- 3.2. It is seen clearly that $\mathbf{J}$ lies on the coil surface and also it is straightforward to prove its divergence-free nature

$$\nabla \cdot \mathbf{J}(\mathbf{r}) = \sum_{n=1}^{N} I_n \, \nabla \cdot \boldsymbol{\jmath}^n(\mathbf{r}) = 0 \tag{3.28}$$

since

$$\nabla \cdot \boldsymbol{\jmath}^n(\mathbf{r}) = \nabla \cdot \left[\nabla \times [\mathcal{N}^n(\mathbf{r}) \, \mathbf{n}(\mathbf{r})] \right] = 0. \tag{3.29}$$

The current density at $\mathbf{r}$ can be defined in terms of a linear combination where the weights are the stream function's nodal values

$$T2N(S_t) = \{\mathbf{r}_{ti}\}_{i=1}^{\Lambda} \tag{3.30}$$

so

$$\mathbf{J}(\mathbf{r}) = \sum_{i=1}^{\Lambda} I_{ti} \, \boldsymbol{\jmath}^{ti}(\mathbf{r}). \tag{3.31}$$
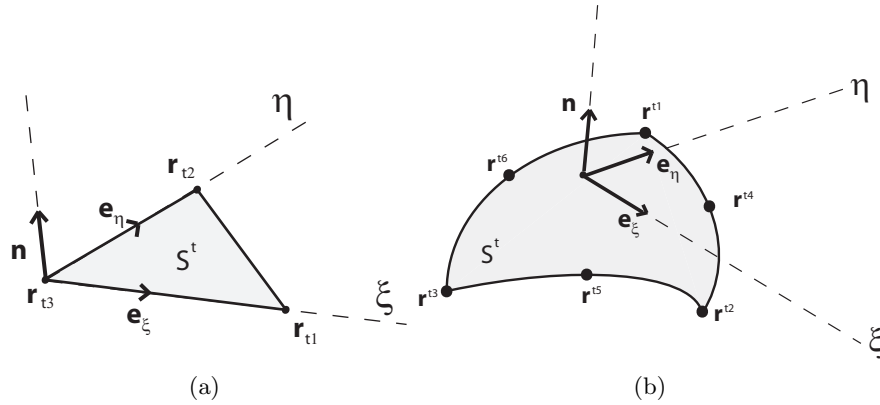
Figure 3.4: *Coordinates system (ξ, η).*

The current basis vectors are found by computation of the curl of the shape functions.

This can be done in Cartesian coordinates, but in general, the expression of the shape functions is simpler in the parametric space, as we have seen in the previous section, and therefore it is easier to work in this representation. Nonetheless evaluating this curl in the parametric space is not trivial, since it is a non-orthogonal coordinate system. Only for flat elements simple expression for the $\boldsymbol{\jmath}^n(\xi,\eta)$ can be achieved [58]

$$\boldsymbol{\jmath}^n(\xi,\eta) = \frac{1}{\mathcal{J}(\xi,\eta)}\left[\frac{\partial\big[\mathcal{N}^n(\xi,\eta)\big]}{\partial\eta}\frac{\partial\mathbf{r}}{\partial\xi} - \frac{\partial\big[\mathcal{N}^n(\xi,\eta)\big]}{\partial\xi}\frac{\partial\mathbf{r}}{\partial\eta}\right] \tag{3.32}$$

where the Jacobian of the coordinate transformation is

$$\mathcal{J}(\xi,\eta) = \left\|\frac{\partial\mathbf{r}}{\partial\xi}\times\frac{\partial\mathbf{r}}{\partial\eta}\right\|. \tag{3.33}$$

And the unit vector which is normal to the surface in the new representation can be expressed as

$$\mathbf{n}(\xi,\eta) = \frac{1}{\mathcal{J}(\xi,\eta)}\Big[\frac{\partial\mathbf{r}}{\partial\xi}\times\frac{\partial\mathbf{r}}{\partial\eta}\Big]. \tag{3.34}$$

Let now us study the current associated with different evolution of φ within the elements.

3.3.1 Linear elements and shape functions

Consider a flat linear element S_t, with nodes $\{\mathbf{r}_{ti}\}_{i=1}^{3}$. In this case, the normal vector is constant along the element, so

$$\boldsymbol{\jmath}^n(\xi,\eta) = \nabla\times[\mathcal{N}^n(\xi,\eta)\,\mathbf{n}]. \tag{3.35}$$

In this isoparametric linear approximation, the evolution of φ and the geometry of the element are defined employing the same linear shape functions

$$N^{t1}(\xi,\eta) = \xi; \qquad N^{t2}(\xi,\eta) = \eta; \qquad N^{t3}(\xi,\eta) = 1 - \eta - \xi. \tag{3.36}$$

The position vector of any point on the element can therefore be written as

$$\mathbf{r} = \xi\mathbf{r}_{t1} + \eta\mathbf{r}_{t2} + (1 - \eta - \xi)\mathbf{r}_{t3} \tag{3.37}$$

where the Jacobian is twice the area, A, of the element

$$\mathcal{J}(\xi,\eta) = \left\|\frac{\partial\mathbf{r}}{\partial\xi}\times\frac{\partial\mathbf{r}}{\partial\eta}\right\| = 2A. \tag{3.38}$$

Then Eq. 3.32 can be written as

$$\jmath^n(\xi, \eta) = \frac{1}{2A} \left[\frac{\partial \mathcal{N}^n(\xi, \eta)}{\partial \eta} (\mathbf{r}_{t1} - \mathbf{r}_{t3}) - \frac{\partial \mathcal{N}^n(\xi, \eta)}{\partial \xi} (\mathbf{r}_{t2} - \mathbf{r}_{t3}) \right]. \tag{3.39}$$

Figure 3.5: *(a) Current basis vectors in one element; (b) Current basis vector associated to the nth-node $\jmath^n(\mathbf{r})$ (its value depends on the particular element which $\mathbf{r}$ lies in) .*

Thus $\jmath^{ti}$ are (see Fig. 3.5(a))

$$\jmath^{t1} = -\frac{(\mathbf{r}_{t2} - \mathbf{r}_{t3})}{2A}; \qquad \jmath^{t2} = \frac{(\mathbf{r}_{t1} - \mathbf{r}_{t3})}{2A}; \qquad \jmath^{t3} = \frac{(\mathbf{r}_{t2} - \mathbf{r}_{t3})}{2A} - \frac{(\mathbf{r}_{t1} - \mathbf{r}_{t3})}{2A} \tag{3.40}$$

and according Eq. 3.31

$$\mathbf{J}(\mathbf{r}) = -\frac{I_{t1}}{2A}(\mathbf{r}_{t2} - \mathbf{r}_{t3}) + \frac{I_{t2}}{2A}(\mathbf{r}_{t1} - \mathbf{r}_{t3}) + \frac{I_{t3}}{2A}\left[(\mathbf{r}_{t2} - \mathbf{r}_{t3}) - (\mathbf{r}_{t1} - \mathbf{r}_{t3})\right]. \tag{3.41}$$

As we have already stated, the current basis vector associated with the nth-node, $\jmath^n(\mathbf{r})$, depends on the element where $\mathbf{r}$ lies, as it is shown in Fig. 3.5(b).

It should be mentioned that the use of isoparametric linear representation leads to a constant current over the element; which is an expected result, as the current is described by one order less than the stream function approximation.

In addition, we can see that this result is equivalent to Pissanetzky's [55] local description of the current.

The current basis can be derived in the Cartesian frame, but this in general implies more computational work. The shape functions in Cartesian coordinates can be expressed as

$$N^{t1}(\mathbf{r}) = \frac{(x-x_3)(y_2-y_3)-(y-y_3)(x_2-x_3)}{(x_1-x_3)(y_2-y_3)-(y_1-y_3)(x_2-x_3)} \tag{3.42}$$

$$N^{t2}(\mathbf{r}) = \frac{(x-x_3)(y_1-y_3)-(y-y_3)(x_1-x_3)}{(x_2-x_3)(y_1-y_3)-(y_2-y_3)(x_1-x_3)} \tag{3.43}$$

and $N^{t3}(\mathbf{r}) = 1 - N^{t1}(\mathbf{r}) - N^{t2}(\mathbf{r})$.

For example for the first current basis vector

$$\boldsymbol{J}^{t1}(\mathbf{r}) = \frac{1}{a}\Big[-n_z(x_2-x_3)\hat{\boldsymbol{i}} - n_z(y_2-y_3)\hat{\boldsymbol{j}} + (n_y(y_2-y_3)+n_x(x_2-x_3))\hat{\boldsymbol{k}}\Big] \tag{3.44}$$

where

$$a = (x_1-x_3)(y_2-y_3)-(x_2-x_3)(y_1-y_3);$$

but as

$$n_y(y_2-y_3)+n_x(x_2-x3) = -n_z(z_2-z_3) \tag{3.45}$$

then

$$\boldsymbol{J}^{t1} = -\frac{(\mathbf{r}_{t2}-\mathbf{r}_{t3})}{2A}. \tag{3.46}$$

The other current basis vectors can be obtained in the same fashion.

3.3.2 Linear elements and quadratic shape functions

As in the foregoing section we are dealing with linear flat elements so the normal vector is constant for every element

$$\boldsymbol{J}^n(\xi,\eta) = \nabla \times [\mathcal{N}^n(\xi,\eta)\,\mathbf{n}] \tag{3.47}$$

and the position vector of any point in the tth-element is

$$\mathbf{r} = \xi\mathbf{r}_{t1} + \eta\mathbf{r}_{t2} + (1-\eta-\xi)\mathbf{r}_{t3}. \tag{3.48}$$

But this time to describe a quadratic behavior of φ within the element we use second order shape functions $(\Lambda = 6)$

$$
\begin{aligned}
N^{t1}(\xi,\eta) &= \xi(2\xi-1); & N^{t4}(\xi,\eta) &= 4\xi\eta; \\
N^{t2}(\xi,\eta) &= \eta(2\eta-1); & N^{t5}(\xi,\eta) &= 4\zeta\eta; \\
N^{t3}(\xi,\eta) &= \zeta(2\zeta-1); & N^{t6}(\xi,\eta) &= 4\xi\zeta,
\end{aligned} \tag{3.49}
$$

where $\zeta = 1 - \eta - \xi$. Therefore although we only need the three triangle vertices to describe the geometry, to represent a quadratically varying stream function the mid-points must also be considered producing a six-node flat triangle.

Equation 3.32 for this case can then be written as

$$\mathbf{J}^n(\xi, \eta) = \frac{1}{2A} \left[\frac{\partial \mathcal{N}^n(\xi, \eta)}{\partial \eta} (\mathbf{r}_{t1} - \mathbf{r}_{t3}) - \frac{\partial \mathcal{N}^n(\xi, \eta)}{\partial \xi} (\mathbf{r}_{t2} - \mathbf{r}_{t3}) \right]. \tag{3.50}$$
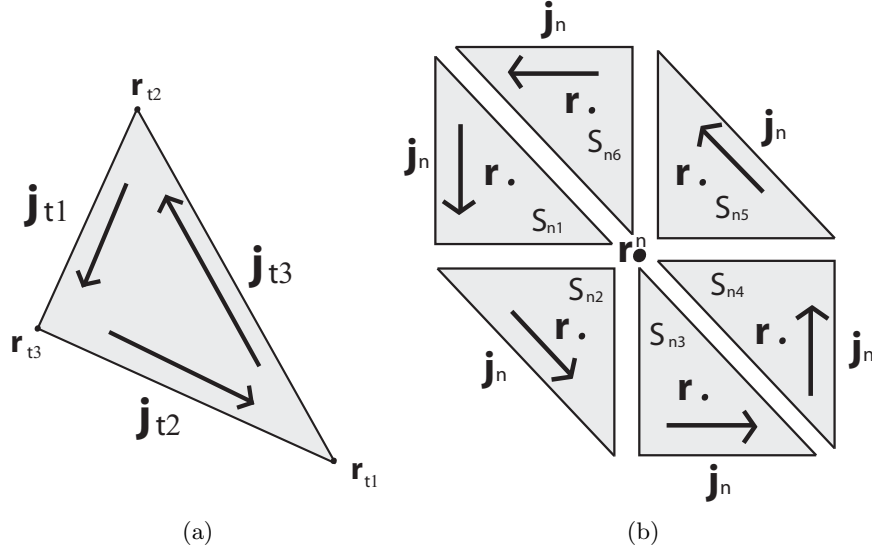
The current basis functions are therefore

$$\mathbf{J}^{t1}(\xi, \eta) = -(4\xi - 1)\frac{(\mathbf{r}_{t2} - \mathbf{r}_{t3})}{2A}; \tag{3.51}$$

$$\mathbf{J}^{t2}(\xi, \eta) = (4\eta - 1)\frac{(\mathbf{r}_{t1} - \mathbf{r}_{t3})}{2A}; \tag{3.52}$$

$$\mathbf{J}^{t3}(\xi, \eta) = (1 - 4\zeta)\left[\frac{(\mathbf{r}_{t1} - \mathbf{r}_{t3})}{2A} - \frac{(\mathbf{r}_{t2} - \mathbf{r}_{t3})}{2A}\right]; \tag{3.53}$$

$$\mathbf{J}^{t4}(\xi, \eta) = 4\xi \frac{(\mathbf{r}_{t1} - \mathbf{r}_{t3})}{2A} - 4\eta \frac{(\mathbf{r}_{t2} - \mathbf{r}_{t3})}{2A}; \tag{3.54}$$

$$\mathbf{J}^{t5}(\xi, \eta) = 4(\zeta - \eta)\frac{(\mathbf{r}_{t1} - \mathbf{r}_{t3})}{2A} + 4\eta \frac{(\mathbf{r}_{t2} - \mathbf{r}_{t3})}{2A}; \tag{3.55}$$

$$\mathbf{J}^{t6}(\xi, \eta) = -4\xi \frac{(\mathbf{r}_{t1} - \mathbf{r}_{t3})}{2A} - 4(\zeta - \xi)\frac{(\mathbf{r}_{t2} - \mathbf{r}_{t3})}{2A}. \tag{3.56}$$

Proof of the divergence free condition of these function can be easily see in parametric space

$$\nabla_{\xi, \eta} \cdot \mathbf{J}^{ti}(\xi, \eta) = 0, \tag{3.57}$$

or in a more complex way in the Cartesian representation, since by performing the transformation

$$\xi = \frac{(x - x_3)(y_2 - y_3) - (y - y_3)(x_2 - x_3)}{(x_1 - x_3)(y_2 - y_3) - (y_1 - y_3)(x_2 - x_3)} \tag{3.58}$$

$$\eta = \frac{(x - x_3)(y_1 - y_3) - (y - y_3)(x_1 - x_3)}{(x_2 - x_3)(y_1 - y_3) - (y_2 - y_3)(x_1 - x_3)}, \tag{3.59}$$

and then applying the divergence operator in Cartesian coordinates it can be seen that

$$\nabla \cdot \mathbf{J}^{ti}(\mathbf{r}) = 0. \tag{3.60}$$

3.4 The Inverse Problem

A general BEM for describing divergence-free and physically meaningful currents that flow on a conducting surface has been presented. The current distribution, **J** , is defined in terms of the nodal values of the stream function, I_n, and elements of the local geometry derived from the shape functions. We now proceed to describe the inverse problem for coil design and incorporate **J** into this framework.

3.4.1 Problem Description

Finding the optimal current distribution that produces a desired field is an ill-posed problem and it cannot be solved by direct methods, additional information about the desired solution has to be imposed. We pose the inverse problem as a constrained optimization, in which the goal is to find an optimal current distribution over a given conducting surface so as to achieve a desired magnetic field in a Region Of Interest (ROI), to balance the torque experienced by the current density in an applied static magnetic field and to minimize the magnetic stored energy.

According to these requirements we can define the following quadratic programming (QP) problem [129], in which a quadratic function (or Lagrangian) of several variables, which are subject to linear constraints, must be minimized

$$\mathcal{F} = \frac{1}{2}\sum_{k=1}^{K}[B_z(\mathbf{r}_k) - B_{des,z} + B_{off}]^2 + \alpha W_{magn} + \sum_{p=1}^{P}(\lambda_{px}M_{px} + \lambda_{py}M_{py} + \lambda_{pz}M_{pz}) \quad (3.61)$$

here $B_{des,z}$ is the z-component of the desired field over a set of K points in the ROI. B_z is the actual field, B_{off} is an offset magnetic field (in some geometries better performance can be obtained if the field is nonzero at the center of the ROI), α is the weight for the the magnetic energy, W_{magn}. The last term reflects the torque calculated with respect to a fixed point, and the $\lambda's$ are the Lagrange multipliers that allow the constrained optimization. The terms that depend on torque acquire more importance for non-symmetrical surfaces. Some other terms could also have been included taking care of different aspects, such as for example, minimization of power dissipation [60].

The coefficient α can be interpreted as a regularization parameter. The purpose of regularisation techniques is to introduce a smoothing norm to the solution, which is basically what we have imposed via the magnetic energy term. In fact, this procedure can be considered as a Tikhonov regularization method [65]; where if we set $\alpha = 0$ (and do not include the torque term) the problem reduces to least squares method.

In the following we use the divergence-free current density defined in the previous sections to characterize all the magnitudes involved in the problem. Then by approximating the functions using their discretized versions, the infinite-dimensional problem is then reduced to a finite-dimensional one, in which the functional of Eq. 3.61 can be minimized to produce the optimal set of stream function nodal values and therefore the most appropriate coil design.

3.4.2 Magnetic vector potential

The magnetic vector potential, $\mathbf{A}$, can be determined from

$$\mathbf{A}(\mathbf{r}) = \frac{\mu_0}{4\pi} \int_{S'} \frac{\mathbf{J}(\mathbf{r}')}{|\mathbf{r} - \mathbf{r}'|} \, dS' \tag{3.62}$$

and by applying Eq. 3.25, this yields

$$\mathbf{A}(\mathbf{r}) = \frac{\mu_0}{4\pi} \sum_{n=1}^{N} I_n \int_{S'} \frac{\boldsymbol{\jmath}^n(\mathbf{r}')}{|\mathbf{r} - \mathbf{r}'|} \, dS', \tag{3.63}$$

and if the conducting surface is approximated by the union of the T elements

$$\mathbf{A}(\mathbf{r}) = \frac{\mu_0}{4\pi} \sum_{n=1}^{N} I_n \sum_{t=1}^{T} \int_{S_t} \frac{\boldsymbol{\jmath}^n(\mathbf{r}')}{|\mathbf{r} - \mathbf{r}'|} \, dS', \tag{3.64}$$

but as

$$\boldsymbol{\jmath}^n(\mathbf{r}) = 0, \qquad \text{unless} \qquad \mathbf{r} \in N2T(\mathbf{r}_n) = \{S_{ni}\}_{i=1}^{\Omega} \tag{3.65}$$

then we can write

$$\mathbf{A}(\mathbf{r}) = \frac{\mu_0}{4\pi} \sum_{n=1}^{N} I_n \sum_{i=1}^{\Omega} \int_{S_{ni}} \frac{\boldsymbol{\jmath}^n(\mathbf{r}')}{|\mathbf{r} - \mathbf{r}'|} \, dS'. \tag{3.66}$$

To simplify the notation we can write $\mathbf{A}$ as a linear combination of the magnetic potentials produced by the current element associated with each node.

$$\mathbf{A}(\mathbf{r}) = \sum_{n=1}^{N} I_n \mathbf{a}^n(\mathbf{r}), \tag{3.67}$$

where $\mathbf{a}^n(\mathbf{r})$ is the magnetic potential produced by a unit stream function at the nth-node

$$\mathbf{a}^n(\mathbf{r}) = \frac{\mu_0}{4\pi} \sum_{i=1}^{\Omega} \int_{S_{ni}} \frac{\boldsymbol{\jmath}^n(\mathbf{r}')}{|\mathbf{r} - \mathbf{r}'|} \, dS'. \tag{3.68}$$
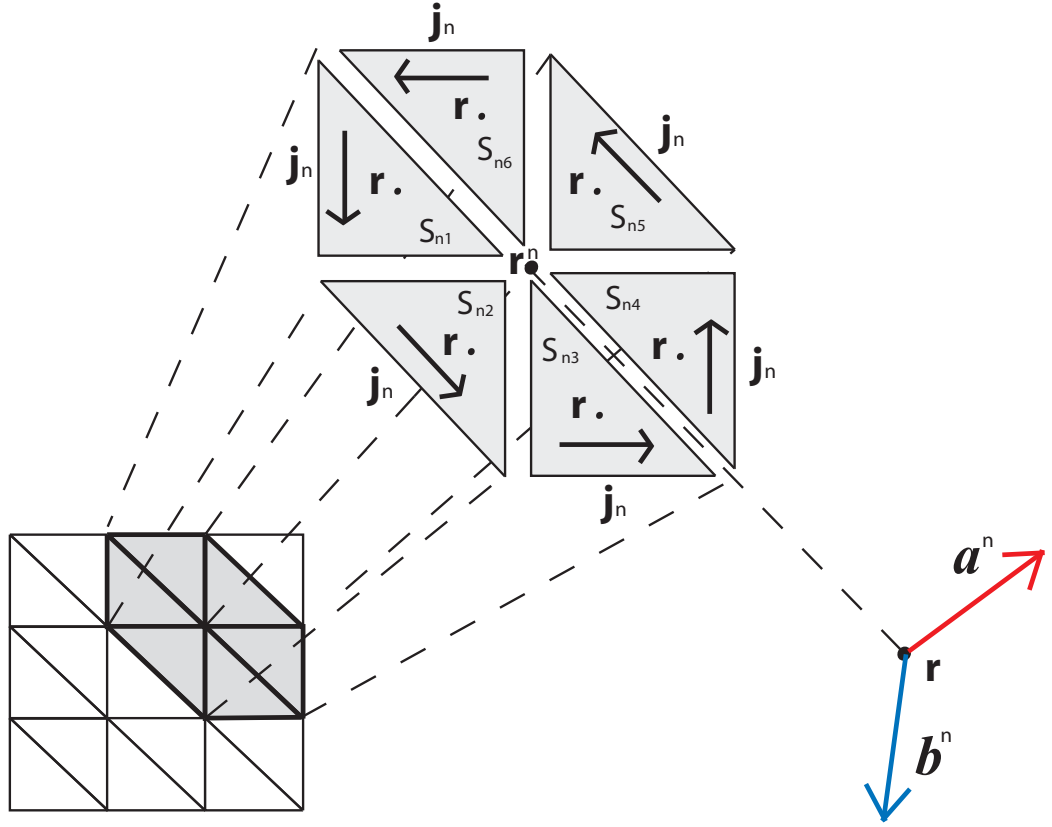
Figure 3.6: *Linear isoparametric current elements.*

3.4.3 Magnetic Induction

If we apply the curl operator to Eq. 3.66, an expression for the magnetic induction is then obtained

$$\mathbf{B}(\mathbf{r}) = \frac{\mu_0}{4\pi} \sum_{n=1}^{N} I_n \sum_{i=1}^{\Omega} \int_{S_{ni}} \nabla \times \frac{\boldsymbol{J}^n(\mathbf{r}')}{|\mathbf{r} - \mathbf{r}'|} \, dS'. \tag{3.69}$$

As we are mainly concerned with the axial component of $\mathbf{B}$, we focus on B_z which can be written as

$$B_z(\mathbf{r}) = \frac{\mu_0}{4\pi} \sum_{n=1}^{N} I_n \sum_{i=1}^{\Omega} \int_{S_{ni}} \frac{j_y^n(\mathbf{r}')(x - x') - j_y^n(\mathbf{r}')(y - y')}{|\mathbf{r} - \mathbf{r}'|^3} \, dS'. \tag{3.70}$$

Following the previous reasoning B_z can be approximated as a linear combination of terms

$$B_z(\mathbf{r}) = \sum_{n=1}^{N} I_n b_z^n(\mathbf{r}), \tag{3.71}$$

where b_z^n is the z-component of the magnetic induction produced by the current element associated to the nth-node

$$b_z^n(\mathbf{r}) = \frac{\mu_0}{4\pi} \sum_{i=1}^{\Omega} \int_{S_{ni}} \frac{\jmath_y^n(\mathbf{r}')(x - x') - \jmath_x^n(\mathbf{r}')(y - y')}{|\mathbf{r} - \mathbf{r}'|^3} \, dS'. \tag{3.72}$$

Both $\mathbf{a}^n(\mathbf{r})$ and $b_z^n(\mathbf{r})$ include integrals that usually cannot be solved analytically, so a numerical integration procedure has to be adopted. As the field point, $\mathbf{r}$, is never at the surface, the integrals involved are non-singular and can be easily computed using Gaussian quadrature [64].

3.4.4 Magnetic Energy: Inductance

Operating in a similar fashion the magnetic energy in the coil can be written as

$$W_{mag} = \frac{\mu_0}{8\pi} \int_S \int_{S'} \frac{\mathbf{J}(\mathbf{r})\mathbf{J}(\mathbf{r}')}{|\mathbf{r} - \mathbf{r}'|} dSdS' = \frac{1}{2} \sum_{n=1}^{N} \sum_{m=1}^{N} I_n I_m L_{mn} \tag{3.73}$$

where L_{mn} is the mutual inductance between the mth and n^{th} current elements

$$L_{mn} = \frac{\mu_0}{4\pi} \int_S \int_{S'} \frac{\jmath^n(\mathbf{r}) \cdot \jmath^m(\mathbf{r}')}{|\mathbf{r} - \mathbf{r}'|} \, dSdS', \tag{3.74}$$

so

$$L_{mn} = \frac{\mu_0}{4\pi} \sum_{i=1}^{\Omega} \sum_{j=1}^{\Omega} \int_{S_{ni}} \int_{S_{mj}} \frac{\jmath^n(\mathbf{r}) \cdot \jmath^m(\mathbf{r}')}{|\mathbf{r} - \mathbf{r}'|} \, dSdS'. \tag{3.75}$$

The double integral involved in the definition of the components, L_{mn}, of the inductance matrix shows a singular behavior when $m = n$. Analytical expressions for these singular double integrals have been presented by Eibert [57] for linear isoparametric elements, although a general approach for dealing with these type of double weak singular integrals is given by Marin *et al.* [67]. This is based on a transformation into a local polar coordinate system where the integration can be performed by avoiding the singularity.

3.4.5 Torque

We saw in the previous chapter the need to consider the torque, $\mathbf{M}$, experienced by the surface current in the presence of the axial main magnetic field, B_0

$$\mathbf{M} = \int_S \mathbf{r} \times (\mathbf{J} \times \mathbf{B}_0) \ dS. \tag{3.76}$$

The torque components can be written using the BEM approximation as

$$M_x = B_0 \int_S J_x z \ dS = B_0 \sum_{n=1}^{N} I_n \int_{S_{ni}} \jmath_x^n(\mathbf{r}) \ z \ dS \tag{3.77}$$

$$M_y = B_0 \int_S J_y z \ dS = B_0 \sum_{n=1}^{N} I_n \int_{S_{ni}} \jmath_y^n(\mathbf{r}) \ z \ dS \tag{3.78}$$

$$M_z = -B_0 \int_S (J_x x + J_y y) \ dS = -B_0 \sum_{n=1}^{N} I_n \int_{S_{ni}} (\jmath_x^n(\mathbf{r}) \ x + \jmath_y^n(\mathbf{r}) \ y) \ dS \tag{3.79}$$

3.4.6 Optimization. Matrix Equation.

If the discretized versions of the functions are incorporated into the problem, we obtain the functional $\mathcal{F}(\mathbf{I})$ (Eq. 3.61), where $\mathbf{I} = (I_1, I_2, ..., I_N)$ are the set of the stream function nodal values. For the sake of clarity the torque term and B_{off} offset magnetic field will be omitted in the following formulation, their inclusion being quite straightforward in any case [56].

The function $\mathcal{F}(\mathbf{I})$ can be minimized by finding the parameters which make

$$\frac{\partial \mathcal{F}(I)}{\partial I_p} = 0; \qquad p = 1, ..., N. \tag{3.80}$$

This procedure generates the following matrix equation

$$\mathbb{A}\mathbf{I} = \boldsymbol{\mathcal{B}} \tag{3.81}$$

where $\mathbb{A}$ is a $N \times N$ matrix whose coefficients are given by

$$\mathbb{A}_{pn} = \beta \sum_{k}^{K} b_z^p(\mathbf{r}_k) b_z^n(\mathbf{r}_k) + \alpha L_{pn}; \qquad p, n = 1, ..., N; \tag{3.82}$$

and $\boldsymbol{\mathcal{B}}$ is a N-dimensional vector with components

$$\mathcal{B}_p = \beta \sum_k^K b_z^p(\mathbf{r}_k) \, B_{des,z}(\mathbf{r}_k); \qquad p = 1, ..., N. \tag{3.83}$$

By solving this system of equations we obtain the optimal stream function values that optimise the functional. To remove physically meaningless solutions it is important to specify boundary conditions in order to generate feasible solutions. We impose the condition that there is no net flux of current flowing into or out of the coil surface. This is equivalent to setting a common value of the stream function for all nodes belonging to the same boundary.

This leads to a reduction of the dimensions of the matrices and vectors involved in the regularised system of equations, as all the nodal values of the stream function for a given edge give rise to only one unknown.

3.4.7 Selection of the regularisation parameter α

The regularisation parameter, α, is chosen so that the magnetic field deviates by less than a given value, usually $\Delta B_z(\mathbf{r}) \leq 5\%$ over the ROI.

This parameter, then, allows control of the coil properties, and illustrates the trade-off between coil features.

3.4.8 Contouring

The inverse problem finishes with the identification of the optimal nodal values of the stream function, which allow us to construct the discretized version of the current density over the surface, that produces the desired field variation and satisfies the other imposed constraints.

However, the final goal in coil design is to find the wire arrangement that approximates the continuous current distribution. As we know, the conversion of the current solution into a conductor pattern is achieved by contouring the stream function. Some symmetric coil geometries can be projected into a 2-D plane where the stream function can be contoured. But, in general, and since this coil design method is independent of the shape of the current-carrying surface a 3D contouring approach is needed. Here we employ an extension of the algorithm proposed by Poole *et al.* [60].

We choose a number of contour levels N_c that are equally spaced and separated by a step

$$\Delta \varphi = \frac{\max \varphi - \min \varphi}{N_c - 1} \tag{3.84}$$

where $\max \varphi$ ($\min \varphi$) is the maximum (minimum) value of the stream function on the coil surface.

Every element can then be seen as a hypersurface embedded in the 4-dimensional space (x, y, z, φ). The stream lines are the intersection of the element hypersurface with the set of hyperplanes of constant φ, that is, (x, y, z, φ^j), where

$$\varphi^j = \min \varphi + j \; \Delta\varphi; \qquad j = 0, ..., N_c - 1. \tag{3.85}$$

The intersection can then be a straight line for flat triangle or a parabolic line for curved triangles (for curved elements see [62]). To determine the direction of the current flow, we can evaluate the rate of change of the stream function by using $\nabla\varphi$, whose sign indicates the direction of the current flow.

3.5 Example of the Inverse Problem Solution

In this section we overview the solution of an inverse problem using the BESFM. This process is illustrated using the particular case of a transverse, cylindrical gradient coil design. The cylindrical surface has a radius of 0.5 m and a length of 2 m.

Once we select the desired coil geometry, the current carrying surface has to be discretized into T triangular elements S_t with N nodes, $\{\mathbf{r}_n\}_{n=1}^N$. Clearly, the more elements in the mesh, the higher the accuracy we obtain.

In case of open geometries, it is necessary to identify the nodes at the boundaries, at which the appropriate boundary conditions are going to be established. To define the functional fully we have to specify the desired region of gradient uniformity, ROI, where we define the target field (see Fig. 3.7). Here we consider a uniform distribution of 400 points spread over a sphere of radius 0.18 m.

Having meshed the coil surface it is easy to develop the divergence-free current technique that was described in the Section 3.3, and hence produce discretized versions of the functions involved in the problem.

Also in the construction of the functional we have imposed a linear variation of B_z with x (G=1 T m^{-1}) as the target field, and the optimal regularisation parameter was found to be $\alpha \sim 5.0 \times 10^{-8}$.

To obtain the final system of equations we need to produce the reduced version of the matrix equation by applying edge constraints. Figure 3.8(a) shows the colormap of the inductance matrix L; whereas Fig. 3.8(b) displays the same color map for the reduced L matrix, where all rows and columns for each of the edge nodes have been removed and replaced with a
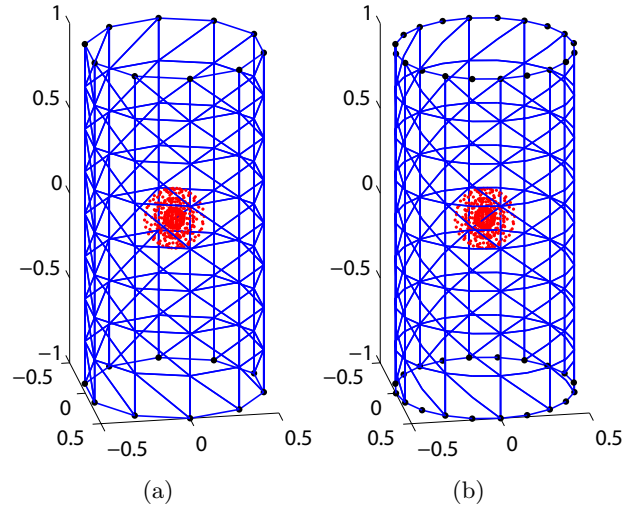
Figure 3.7: *Cylinder meshed using (a) 160 flat elements (b) and using 160 quadratic curved elements (see [62] and [67]). The ROI is formed from a spherical distribution of 400 points (in red); and the nodes at the edges are marked in black.*

single row and column for each edge, so all nodes belonging to the same boundary give rise to only one unknown.

Solving the reduced matrix equation yields the values of the stream function that minimize the functional. Figure 3.8(c) shows the conversion from the stream function over the coil surface to the wire arrangement (stream lines). We can see how the field produced by the wire pattern calculated via Biot-Savart integration over the coil, Fig. 3.8(d), is quite similar to that generated by the current distribution, Fig. 3.8(e), from Eq. 3.8(d). Integrating over the wire-paths the torque experienced by the coil can also be found. For this example it is less than 10^{-6} NmA^{-1}T^{-1}.

Using FastHenry © [68], a multipole impedance extraction tool, and assuming the coil wires have a 3 mm diameter, the value of the inductance is found to be 235 μH for this case, which yields the following performance parameter (FOM)

$$\frac{\eta^2}{L} = 9.6 \times 10^{-6} \; T^2 m^{-2} A^{-2} H^{-1}. \tag{3.86}$$
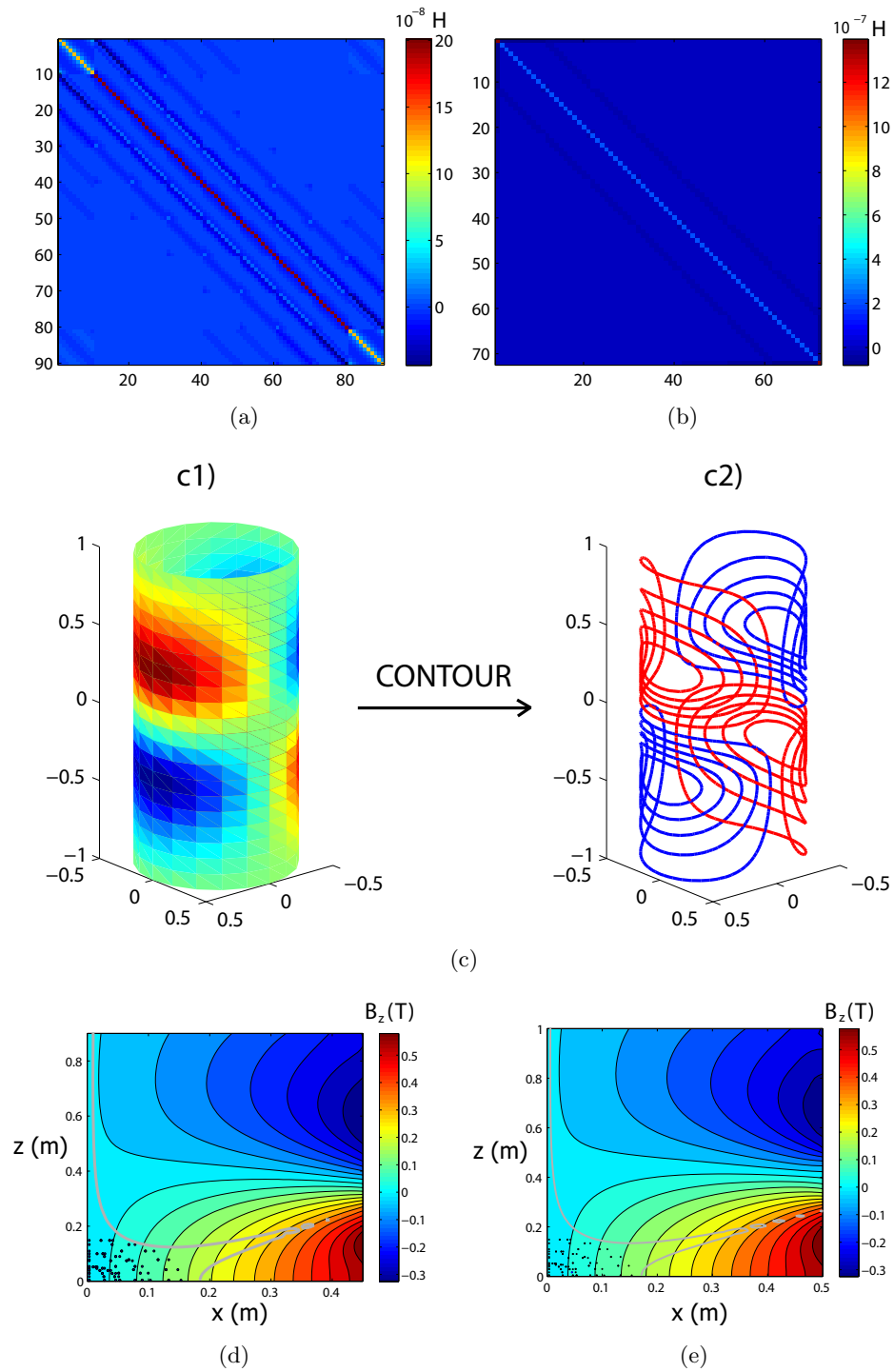
Figure 3.8: *Colormap of the (a) inductance matrix; (b) reduced inductance matrix; (c1) Stream function over the coil surface, (c2) wire arrangement (stream lines); Contours of the B_z field produced by (d) theoretical current density; (e) and the wire arrangement. The grey line delineates the region where the field deviates by less than 5% from linearity. The points where the field is evaluated in the ROI are shown in black.*

3.6 |A|-Coil

The inverse BEM problem allows the addition of new constraints (such as minimization of the power dissipation [60]), which involves modification of the functional (Eq. 3.61) by addition of new terms. It is worth noting that the inclusion of new conditions and hence the increase of a given property causes, in general, the reduction of another.

Temporally varying magnetic gradient fields induce electric fields, $\mathbf{E}$, and consequently electric currents in conducting tissues, which may cause PNS. There are two sources of $\mathbf{E}$, the first one of magnetic origin is the temporal derivative of the vector potential, $\mathbf{A}$, which is produced by current flowing in coils; $\mathbf{A}$ produces initially a redistribution of free charges, which accumulate at boundaries between regions of different conductivity and generate the second, conservative contribution to $\mathbf{E}$.

So although the local temporal derivative of $\mathbf{A}$ *is not a reliable indicator of* $\mathbf{E}$ [66], the two fields are intrinsically related. In the following we investigate the effect of including a new condition in the optimization problem by adding an extra term in the functional to minimize the modulus of the vector potential, $\mathbf{A}$, produced by the coil in a second region of interest (ROI2). The new Lagrangian is

$$\mathcal{F} = \frac{1}{2}\sum_{k=1}^{K}[B_z(\mathbf{r}_k) - B_{des,z} + B_{off}]^2 + \alpha W_{magn} + \frac{\gamma}{2}\sum_{m=1}^{M}|\mathbf{A}(\mathbf{r}_m)|^2$$
$$+ \sum_{p=1}^{P}(\lambda_{px}M_{px} + \lambda_{py}M_{py} + \lambda_{pz}M_{pz}) \tag{3.87}$$

where γ is a new optimization parameter that weights the contribution of the new term and $\mathbf{A}(\mathbf{r}_m)$ is the value of the vector potential in the set of M points of the ROI2.

The introduction of this new constraint must compromise other aspects of the coil performance as little as possible, especially gradient homogeneity, so choosing ROI2 as a different zone to ROI of the target field can help.

The new matrix equation is

$$\widetilde{\mathbb{A}}\mathbf{I} = \boldsymbol{\mathcal{B}} \tag{3.88}$$

where $\widetilde{\mathbb{A}}$ is a $N \times N$ matrix whose coefficients are given by

$$\widetilde{\mathbb{A}}_{pn} = \beta\sum_{k}^{K} b_z^p(\mathbf{r}_k)\, b_z^n(\mathbf{r}_k) + \gamma\sum_{m}^{M}\mathbf{a}^p(\mathbf{r}_m)\cdot\mathbf{a}^n(\mathbf{r}_m) + \alpha L_{pn}; \qquad p, n = 1, ..., N; \tag{3.89}$$

By imposing the boundary conditions we obtain a reduced version of the linear system

of equations, whose solution yields the optimal nodal values of the stream function that minimize $|\mathbf{A}|$ in the prescribed ROI2.

In the following chapter the results of using BESFM and its extension to produce coils that minimize the modulus of the vector potential are shown.

3.6.1   Plausibility of the |A|-Coil

In Chapter 6, a forward BEM approach is developed that allows the numerical solution of forward electromagnetic problems; by using this constant BEM approximation we could produce a representation of the gradient of the scalar potential in terms of the values of the magnetic vector potential at the boundary elements of the system, weighted by coefficients that only depend on the particular geometry of the discretized surfaces.

Therefore if we want to minimize the electric field induced at one point in a given conducting system exposed to a switched gradient, we must minimize the sum of the vector potential at that point, plus the values of the vector potential at the boundary of the system weighted by these geometric coefficients.

The A-Coil method can therefore be seen as first stage in the implementation of a proper inverse quasi-static approach.

Chapter 4

BESFM: Numerical Results

4.1 Window Coil

BESFM is as a powerful coil design approach which is independent of the geometry of the current-carrying surface. In this section it is used to design cylindrical head gradient coils, incorporating a rectangular window (from which wires are excluded) so as to allow visual interaction with the subject. Unless it is stated the coils produced in this chapter have been designed using a linear isoparametric BEM.

Cylindrical, transverse and longitudinal head gradient coils of radius 0.175 m and height 0.35 m incorporating a window of height 0.1 m and length 0.20 m, with a spherical ROI of radius 0.065 m, Fig. 4.1(a), were designed. The regularization parameter was adjusted to produce a coil of minimum inductance with less than 5% relative field error in the ROI.
The inclusion of the window in the surface removes the axial symmetry of the coils, and so they are no longer naturally torque-balanced. The use of the zero net force and torque condition is therefore vital in the design of these coils.
The coil layouts corresponding to the transverse and longitudinal cylindrical window coils are shown in Figs. 4.1(c)-4.1(d). The torques experienced by the coil windings are found in Table Fig. 4.1(b), where the FOM for window coils is also displayed and compared to ordinary cylindrical coils of the same size without windows. Although the ordinary cylindrical coils and window coils have the same region of homogeneity, a relatively small reduction of the performance due to the inclusion of the window is evident.
The Biot Savart law was used to calculate the B_z field produced by both coils as shown in Figs. 4.1(e)-4.1(f).

(a)

	L (µH)	η^2/L ($T^2 m^{-2} A^{-2} H^{-1}$)	M (N m $A^1 T^{-1}$)
X-Gradient	48	3.2×10^{-4}	2×10^{-4}
	(42)	(3.4×10^{-4})	$(< 10^{-4})$
Z-Gradient	124	6.5×10^{-4}	3×10^{-4}
	(102)	(8.2×10^{-4})	$(< 10^{-4})$

The values in brackets correspond to coils with no window.

(b)

(c)   (d)

(e)   (f)
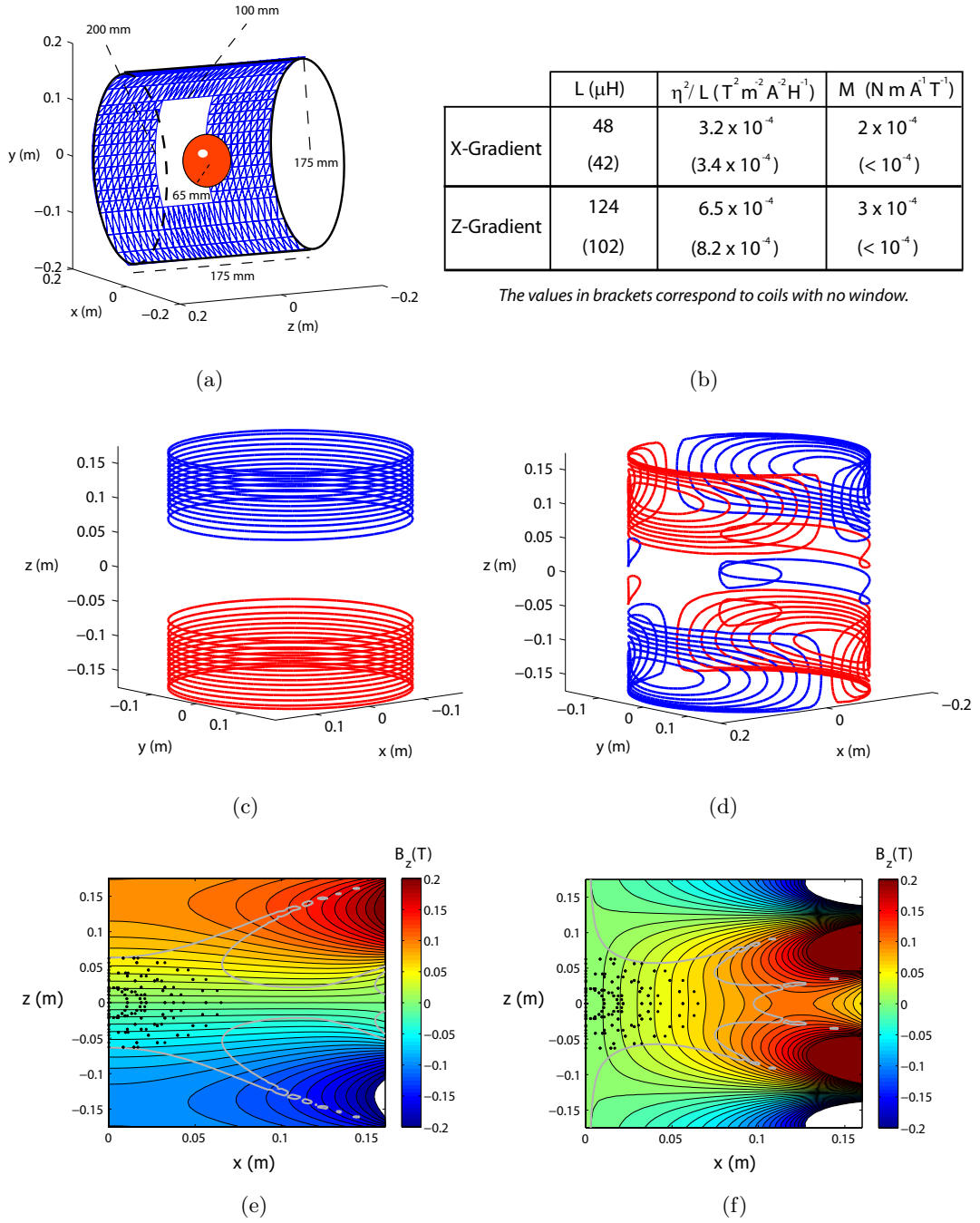
Figure 4.1: *(a) Geometry of the cylindrical gradient coils with a window; (b) coil properties of the transverse and longitudinal gradient coils with and without window; wire patterns for the (c) z-gradient and (d) x-gradient coils with a window; (e) and (f) contour plots of B_z produced by the gradient coils shown in (c) and (d) respectively.*
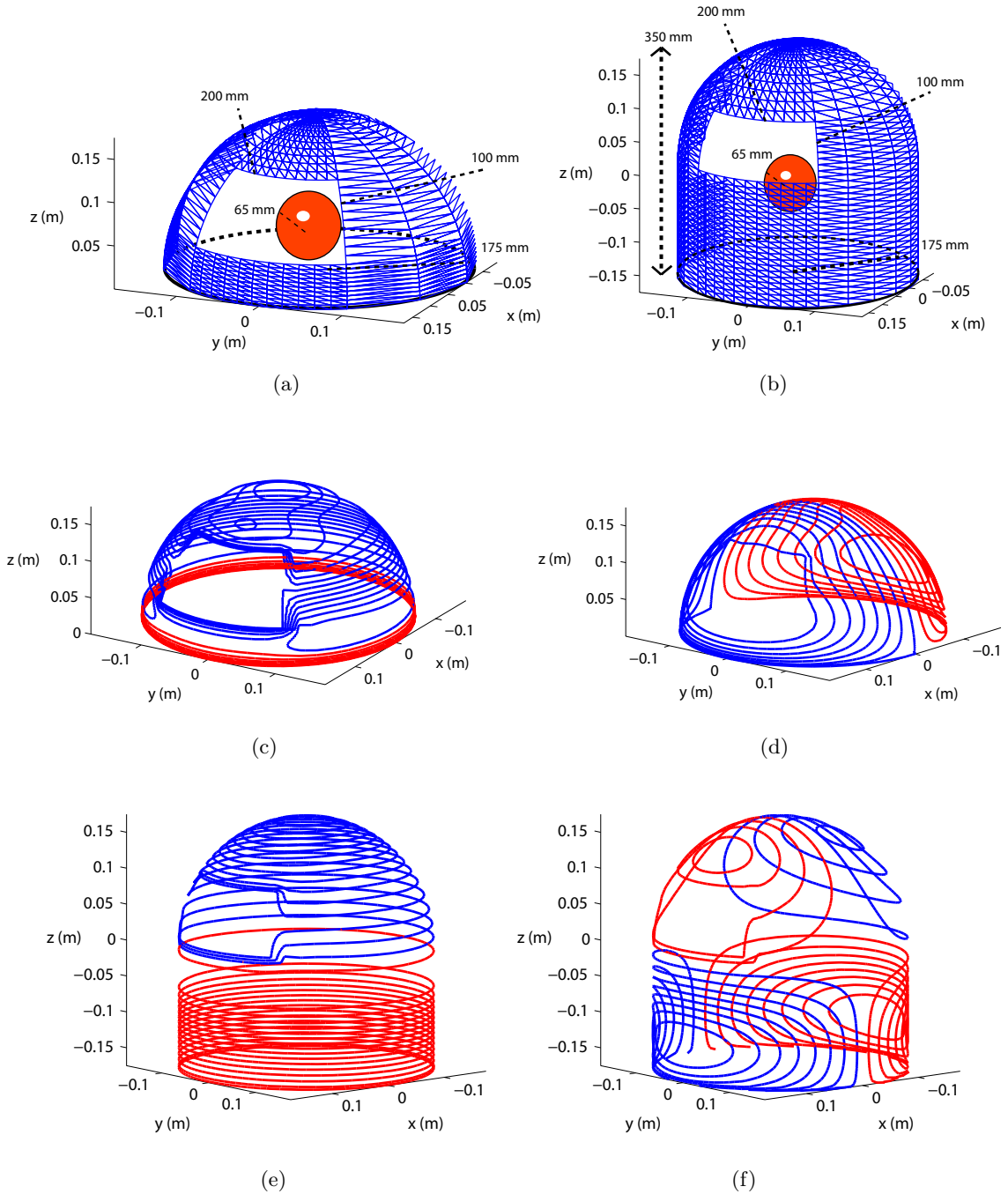
Figure 4.2: *Geometry of the hemispherical gradient coils with a window (a) without cylindrical extension and (a) with cylindrical extension; wirepaths of a hemispherical, (c) z-gradient window coil, (d) x-gradient window coil, (e) z-gradient window coil with cylindrical extension and (f) x-gradient window coil with cylindrical extension.*

The idea of including a window can be exported to other coil geometries. Hemispherical coils of radius 0.175 m with and without a cylindrical extension of height 0.175 m were also designed using BSFEM (Fig. 4.2) and with a window of height 0.10 m and length 0.20 m for both cases, where the target ROI region is a sphere of radius 0.065 m containing 400 points.
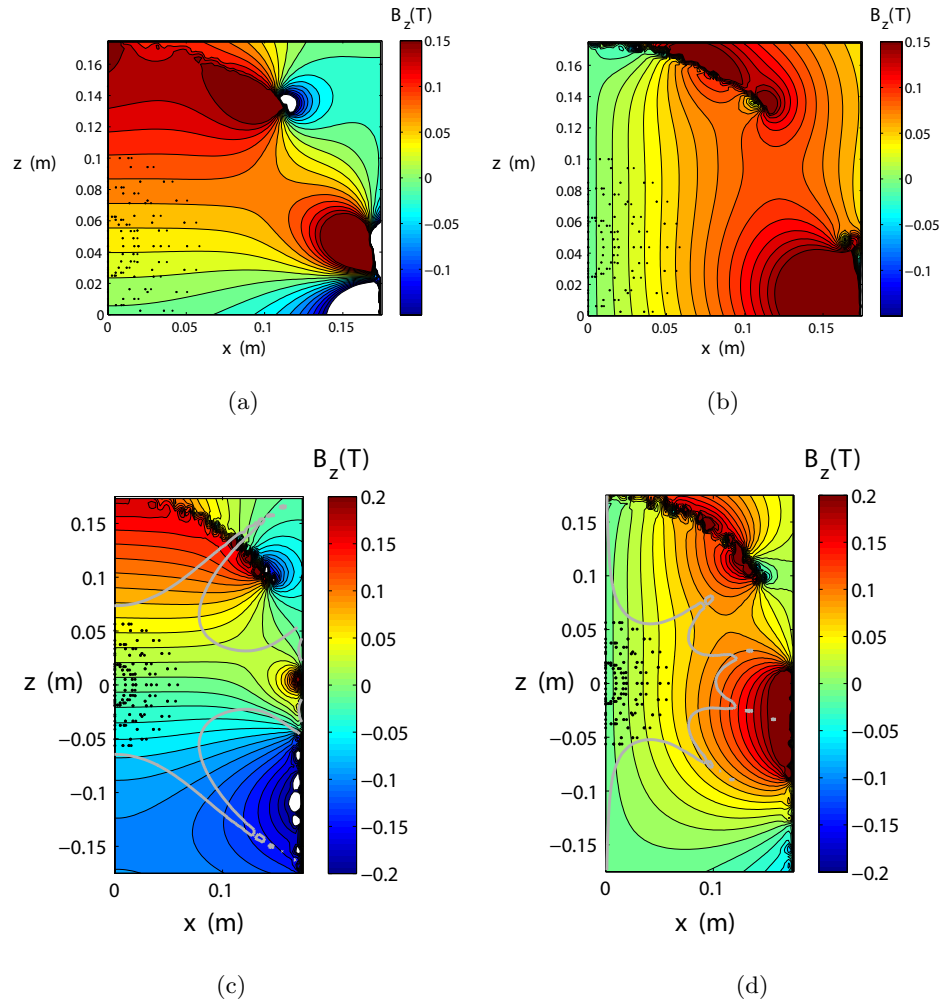
Figure 4.3: *(a) Contour plots of B_z produced by the gradient coils shown in Fig. 4.2(d), Fig. 4.2(c), Fig. 4.2(e) and Fig. 4.2(f) respectively.*

The FOM of the hemispherical, transverse and longitudinal gradient coils with (without) windows are respectively

$$\frac{\eta^2}{L} = 2.1 \ (4.3) \times 10^{-4} \ T^2 m^{-1} A^{-2} H^{-1};$$
$$\frac{\eta^2}{L} = 7.8 \ (20.0) \times 10^{-4} \ T^2 m^{-1} A^{-2} H^{-1}. \tag{4.1}$$

It can be appreciated from these numbers that there is a significant reduction of the FOM when a window is added. The situation is improved by the use of the cylindrical extension, yielding the following FOMs

$$\frac{\eta^2}{L} = 1.1 \ (1.69) \times 10^{-3} \ T^2 m^{-1} A^{-2} H^{-1};$$
$$\frac{\eta^2}{L} = 1.5 \ (1.70) \times 10^{-3} \ T^2 m^{-1} A^{-2} H^{-1}. \tag{4.2}$$

In this case the FOMs for coils including windows are quite similar to those without window. These are surprising results since the inclusion of the window reduces the performance only by 35% for the z gradient and less than 15% for the x-gradient coil.

4.1.1 Numerical implementation

Software was written in Fortran 90 to implement the BESFM. The calculations were run on a dual-Pentium PC III motherboard (2x850 MHz), and the finest meshes tackled were discretized using less than 5000 elements. The computation time varies from less than 5 minutes for 1000 elements to a bit more than 5 hours for the finest meshes. The calculation of the inductance matrix L_{mn} is the most time demanding process, the computation time for this step grows approximately as n^2.

The Fortran 90 software includes a subroutine that allows the testing of the coil designs, as it calculates the field produced by the wire pattern via Biot-Savart integration.

4.2 Study of the Convergence

All the coils presented so far could be designed by application of any of the different order of BEM approximation that were illustrated in the last chapter. The efficacy of employing curved rather than flat element geometry and linear rather than parabolic approximation of the stream function over the element is now explored by performing a mesh convergence study, that is, we study the solutions of every BEM approximation for different mesh densities (number of elements). The curved element approach is the one described in previous work of the authors [62] and [67].
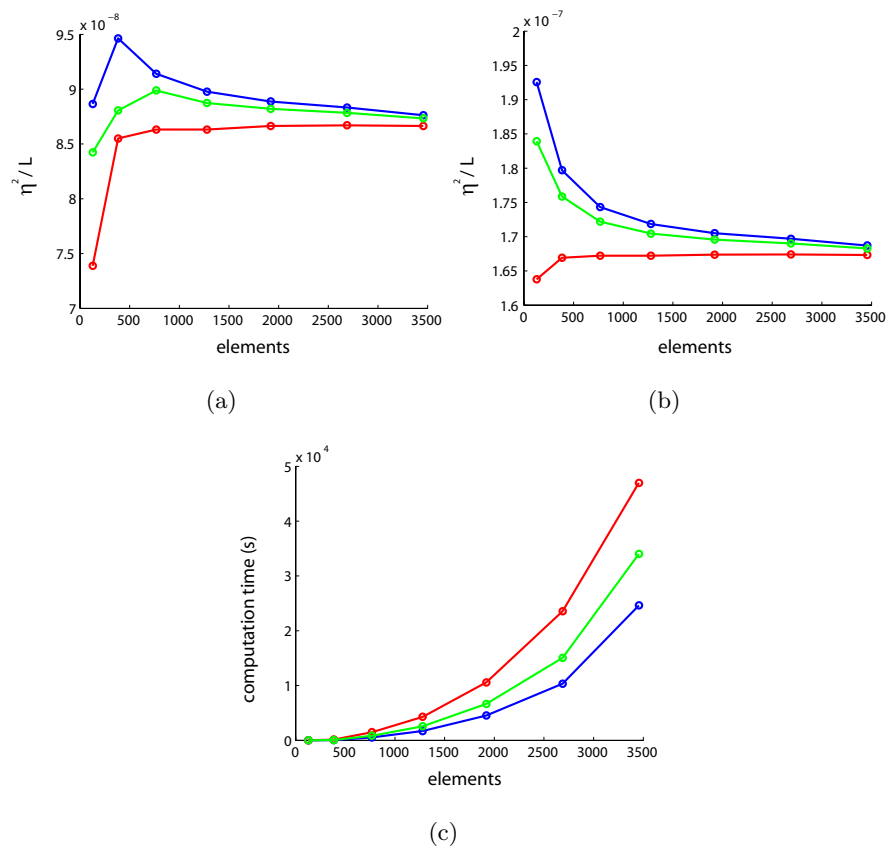
Figure 4.4: *(a) Convergence study in terms of the FOM $(a^{-5}T^2m^{-2}A^{-2}H^{-1})$ for a cylindrical transverse gradient coil (height=1.6 m and radius=0.4 m), the linear and quadratic isoparametric solutions are shown in blue and red respectively. The green line displays the solution for flat elements with quadratic evolution of φ; (b) convergence study for a cylindrical longitudinal gradient coil of similar geometry; (c) computation time for different numbers of surface elements.*

Figure 4.4(a) shows that the quadratic (red line) and linear (blue line) isoparametric solutions converge to the same value for the simple problem of a cylindrical transverse gradient coil. The convergence for the case of flat triangles with a parabolic stream function (green line), is faster than in the other two cases. Figure 4.4(b) displays another convergence plot in terms of the FOM for a longitudinal gradient coil. The parabolic isoparametric approximation exhibits a higher rate of convergence with increasing number of elements, that is, convergence occurs for a smaller number of elements. It is worth noting that for the two previous cases, there seems to be a residual error between the convergence of solutions using flat elements and curved elements.

For both problems, all the BEMs approximations produce effective solutions and a finer mesh results in a more accurate solution. However, as a mesh is made finer, the computation time increases as shown in Fig. 4.4(c). As expected the computation time grows with the number of elements and is always higher for curved triangles and parabolic approximations.

An equivalent study of the convergence can be performed with the use of the L^2-norm

$$L = \sum_{k}^{K} \frac{[B_z(\mathbf{r}_k) - B_{des,z}]^2}{K} \tag{4.3}$$

where B_z is the actual field produced by the coil and $B_{des,z}$ the z-component of the desired field over the set of K points in the ROI. Figure 4.5 depicts the convergence for linear and quadratic isoparametric elements for the problem of the cylindrical window coils described in the Section 4.1. It can be appreciated how the rate of convergence is higher for the linear solution for the transverse coil, whereas a parabolic description provides a better solution for the longitudinal window coil.

To summarize, the kind of BEM approximation for which convergence occurs at smaller numbers of elements will depend on the particular geometry of the coil design, but we must always balance accuracy and computing resources. The best choice of element type for very large number of mesh elements seems to be the linear isoparametric approximation, which produces effective solutions with a computation time that is significantly shorter than in other approximations.
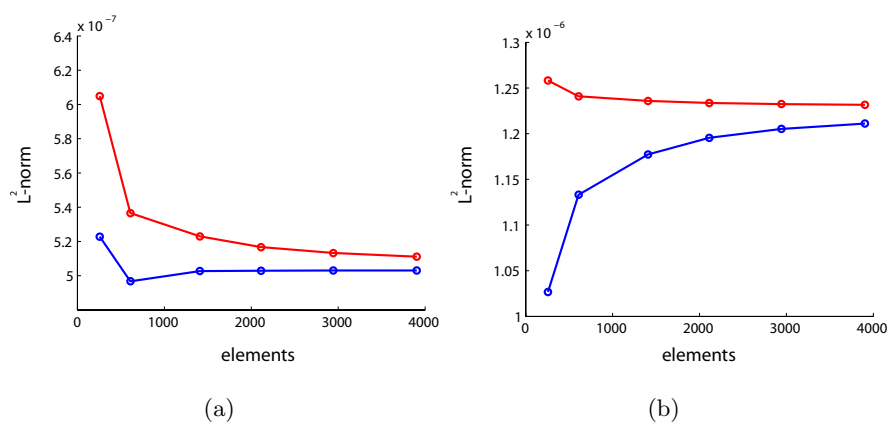
Figure 4.5:   *Convergence study for a cylindrical (a) transverse and (b) longitudinal gradient coils incorporating a window. Blue and red line represent the linear and quadratic isoparametric solution.*

4.3 |A|-Coil

The BESFM approach has also been used to design transverse gradient coils on a cylindrical former, in which the vector potential has been minimized over a second ROI. The radius of the coil cylinder was 0.40 m and its total length 1.60 m. Four coils have been produced that are referred to as **coil1, coil2, coil3 and coil4**; they are designed to produce a field gradient whose strength is specified to be 1.0 T/m and which deviates from linearity by less than 5% within a central, spherical region of 0.15 m diameter (ROI). These coils are also designed to have minimum inductance and to generate zero net torque.

Coil1 is not constrained to minimize $|\mathbf{A}|$, so the regularization parameter γ in Eq. 3.97 is equal to 0, and there is no need to define a second ROI (ROI2).

Coil2 is designed to minimize $|\mathbf{A}|$ in the prescribed volume of interest (ROI2), which is made up of two spherical regions of radius 0.4 m that are centred on the z-axis at $z = \pm 0.4$ m, as depicted in Fig. 4.6(a).

Coil3 is constructed to minimize $|\mathbf{A}|$ in a cylinder (ROI2) of length 1.6 m, diameter 0.6 m, that is co-axial with the coil.

Coil4 is designed to minimize $|\mathbf{A}|$ in the prescribed volume of interest (ROI2), which is made up of one spherical region of radius 0.4 m that is centred on the z-axis at $z = +0.4$ m.

By using the BESFM we can identify the optimal stream function for each case and then obtain the winding pattern. Figures 4.7(b)-(d) show the wire arrangements for each of the three coils, which when energized produced the B_z field and vector potential magnitude, $|\mathbf{A}|$, displayed in Fig. 4.8. Both field magnitudes were calculated using the elemental Biot-Savart expression applied directly to the wire paths.

(a)
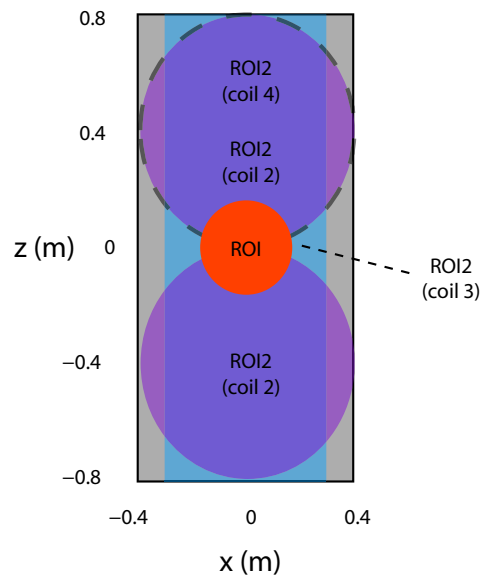
	L (µH)	η^2 / L ($T^2 m^{-2} A^{-2} H^{-1}$)	M ($N\,m\,A^{-1}\,T^{-1}$)
Coil 1	170	9.5×10^{-5}	2.4×10^{-5}
Coil 2	172	8.1×10^{-5}	5.3×10^{-4}
Coil 3	187	5.1×10^{-5}	1.5×10^{-4}
Coil 4	186	7.3×10^{-5}	1.1×10^{-4}

(b)

Figure 4.6: *(a) The geometry of coil1, coil2, coil3 and coil4, the red sphere is the ROI for all four coils; whereas the 2 purple spheres, the blue cylinder and the purple sphere with the dashed contour form the ROI2 for coil2, coil3 and coil4 respectively. (b) Coil performance parameters.*
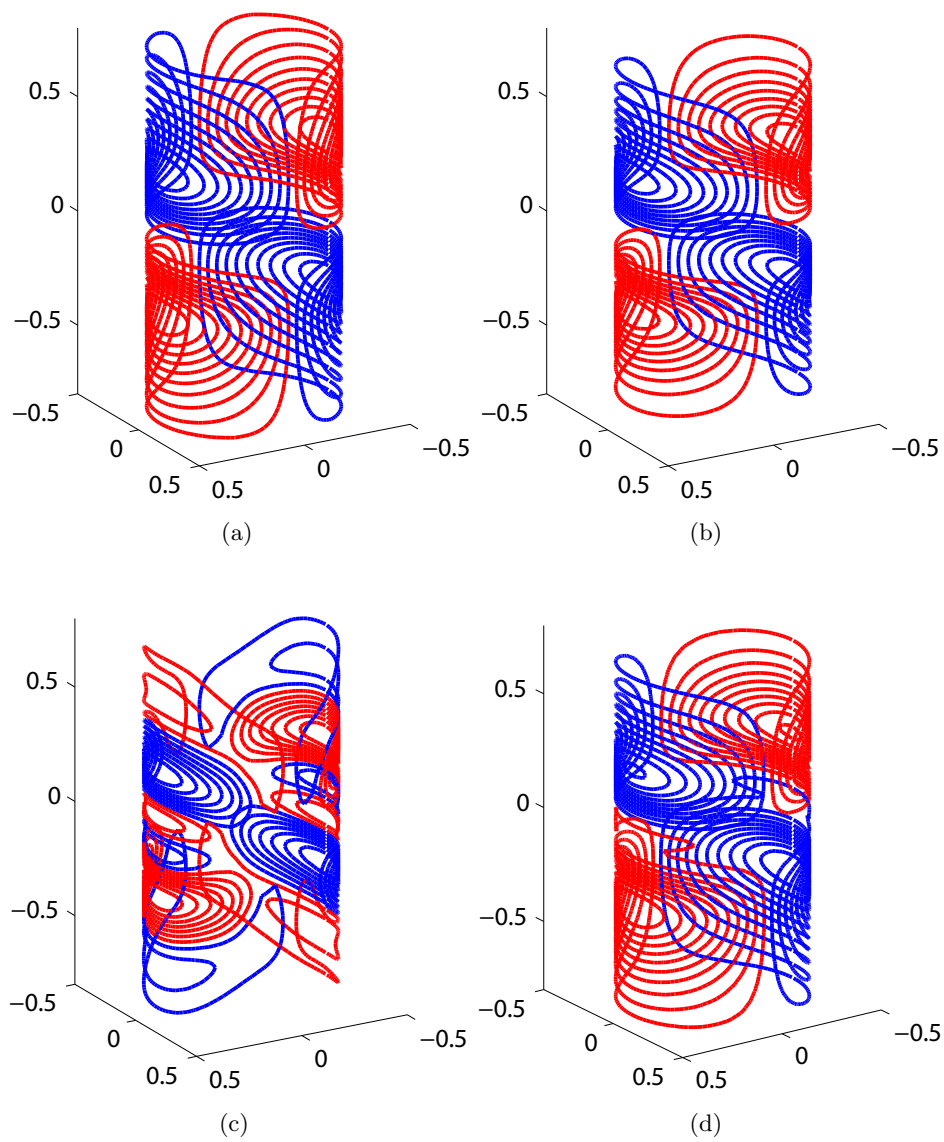
Figure 4.7: *Wire arrangements for (a) coil1, (b) coil2, (c) coil3 and (d) coil4.*
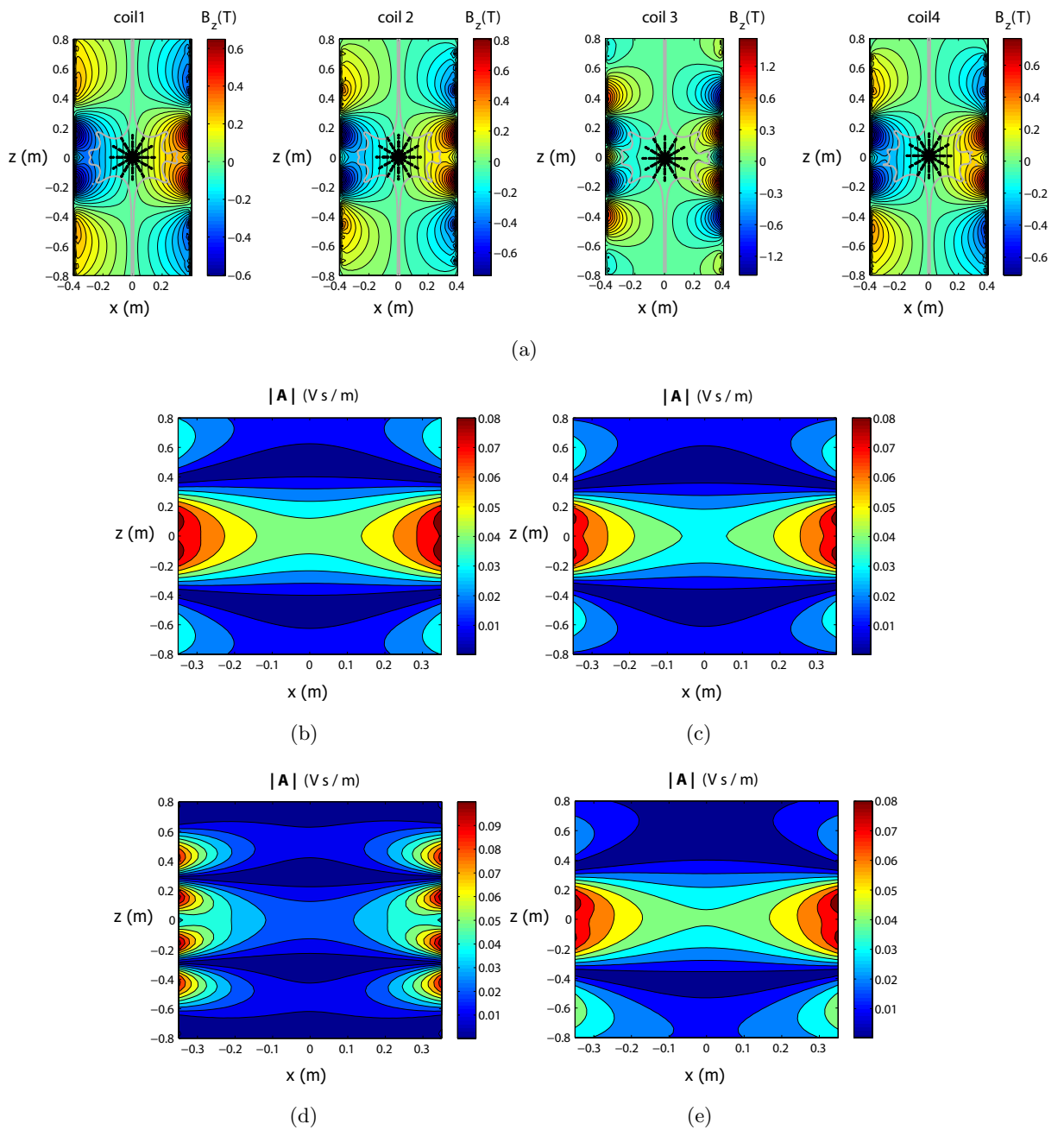
Figure 4.8: *(a) Contour plots of the axial field on a xz-plane calculated for the four transverse coil designs, overlaid with the 5% (grey line) deviation contour line. The ROI is formed from a spherical distribution of 400 points (in black). Variation of the modulus of $\boldsymbol{A}$ in the xz-plane at y=0 produced by (b) coil1, (c) coil2, (d) coil3 and (e) coil4 .*

Clearly, the four coils generate an axial magnetic field that satisfies the initial requirements. The vector potentials are slightly different in magnitude and spatial form for coil1, coil2 and coil4, whereas this difference increases significantly for coil3. These differences are also evident in the performance of the coils, Fig. 4.6(b).

Nevertheless, we cannot proffer any information about the electric field yet from these results, as the local temporal derivative of **A** is not a good indicator of **E**.
To acquire details of the induced **E**, we applied a direct BEM that will be explained in Chapter 6, which allows calculation of the electric field induced by gradient coils in conducting systems. We considered the case where the applied gradients vary at a frequency of 500 Hz, generating a gradient field of 1 T/m.
First this BEM approach is employed to investigate a homogeneous spherical volume conductor of radius 0.1 m which is described with a mesh of 360 elements and placed at the centre of the four coils. Figure 4.9(a) shows the modulus of the electric field induced at every spherical mesh element, the values obtained for coil1 (black) are quite similar to those for coil2 (red), slightly higher than in the case of coil3 (blue) and sometimes even lower than coil4 (green).
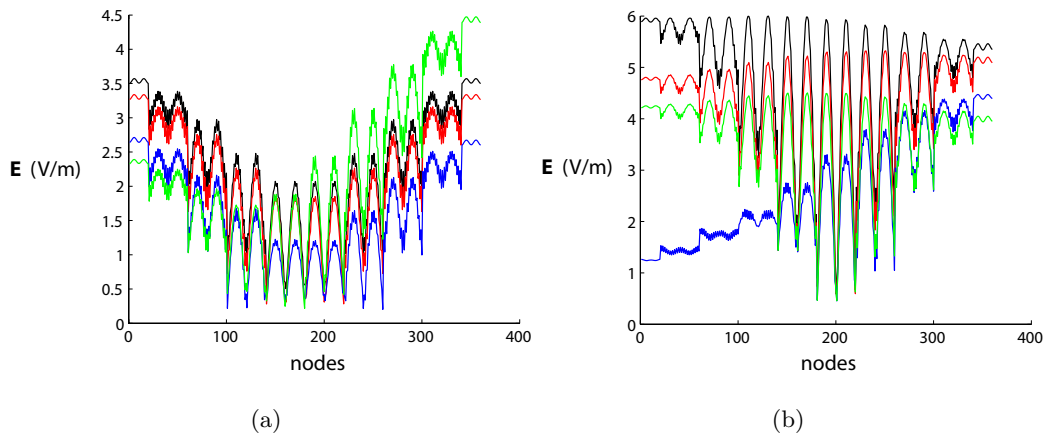
Figure 4.9: *(a) E-field induced at the surface of a spherical conductor of radius 0.1 m described using a mesh of 360 elements and located at the coil centre by coil1(black), coil2(red), coil3(blue) and coil4(green);(b) E-field induced for the same sphere when placed at z=0.4 m ($G = 1Tm^{-1}$, frequency = 500 Hz).*
The algorithm used to mesh each spherical surface starts at the top of the sphere where the polar angle $\theta = \arccos(z/r)$ is zero and ends at the bottom of the sphere where $\theta = \pi$. At each value of θ, elements are spread over the azimuthal angle ($\varphi = \arctan(y/x)$). In general, the number of elements, N, is given by $N = 2[n_\theta(n_\varphi - 1)]$, where n_θ and n_φ are the number of steps in θ and ϕ respectively.

The difference of the electric fields induced in the sphere by different coils becomes higher if the sphere is placed away from the origin. This can be seen in Fig. 4.9(b) where the spherical conductor is located on the z-axis at z=0.4 m. This fact can also be appreciated in Fig. 4.10(a) which shows the field at the surface of a conducting sphere of 0.2 m radius whose centre is shifted along the longitudinal axis by 0.6 m.

Numerical tests have also been run to calculate the electric field distribution induced inside a conducting cylinder of radius 0.2 m and 1.4 m height and co-axial with the coil, by each of the 4 gradient coils ($G = 1Tm^{-1}$ and frequency = 500 kHz).
The values of $|\mathbf{E}|$ close to the origin do not differ too much between coils, but away from the origin there is a substantial difference between coils. Figure 4.10(b) displays the E-field in the xz-plane with y=0.1 m inside the cylinder. It can be seen how the E-field induced by coil4 in the region that corresponds to the position of ROI2 is substantially smaller than the electric field produced by the other coil. Nonetheless the E-field induced by coil4 is significantly higher in other region where a minimum $|\mathbf{A}|$ was not imposed.

Finally we investigated the electric field induced in a human body model with homogeneous electric properties. Figure 4.11(a) depicts the human model with a colour-coded map of the scalar potential, ϕ generated at the body surface by the coil1 [1].
Once more, values of the E- field are similar for all the coils at the origin, also the electric field patterns in the xz-plane (with y=0) from different coils do not differ significantly Fig. 4.11(b)-4.11(e). The variation becomes significant when departing from the central planes (x,y,z=0).

It can be seen in Fig. 4.11(e) that the E-field induced by coil4 in the shoulder is less than the one produced by coil1, although the price we have to pay for this reduction is the increase of the E-field induced in other body parts. This redistribution can be used to allow larger rates of change of gradient to be achieved at stimulation threshold, without alteration of the imaging field of view, as proposed by Hidalgo in [69], where an additional uniform field switched synchronously with the gradient field is used for this purpose.

To summarize, we have introduced a new condition to minimize the modulus of the vector potential over a prescribed regions, ROI2, in the BSFEM for coil design. A suitable choice of ROI2 can significantly reduce the electric field induced, as the numerical simulations presented using a BEM have shown.

---

[1]The scalar potential is generated by charges accumulated at boundaries between regions of different conductivity, its computation is vital stage in the calculation of the induced E-field when using the BEM approach described in Chapter 6.

(a)

(b)
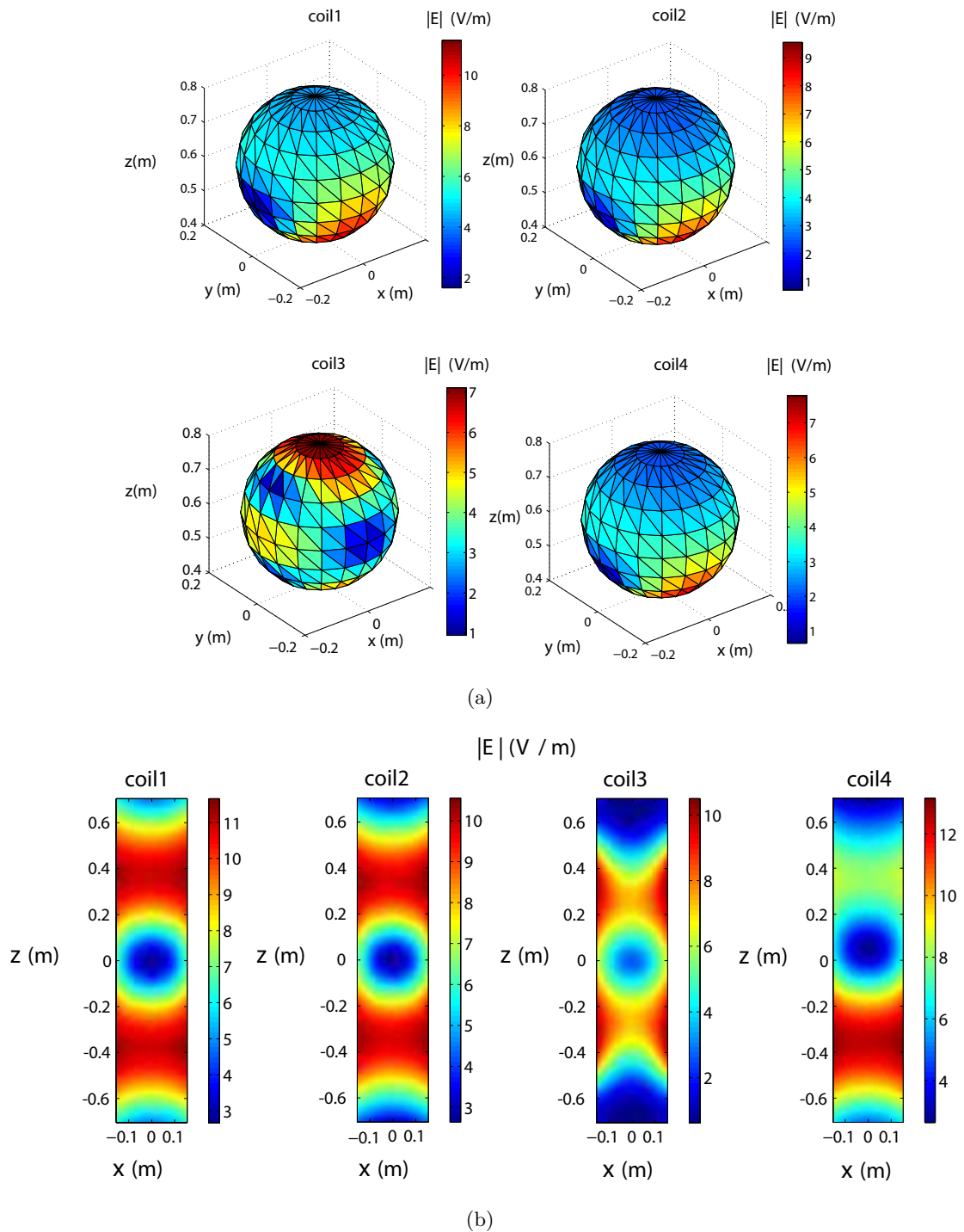
Figure 4.10: *(a) Three-dimensional plot of the colour-coded modulus of the E-field at the surface of the sphere of radius 0.2 m for the case where it was shifted along the z-axis by 0.6 m; (b) Colour-coded |E| maps on a xz-plane with y=0.1 m inside the cylinder exposed to each of the three time-varying x-gradients ($G = 1Tm^{-1}$, frequency = 500 kHz).*
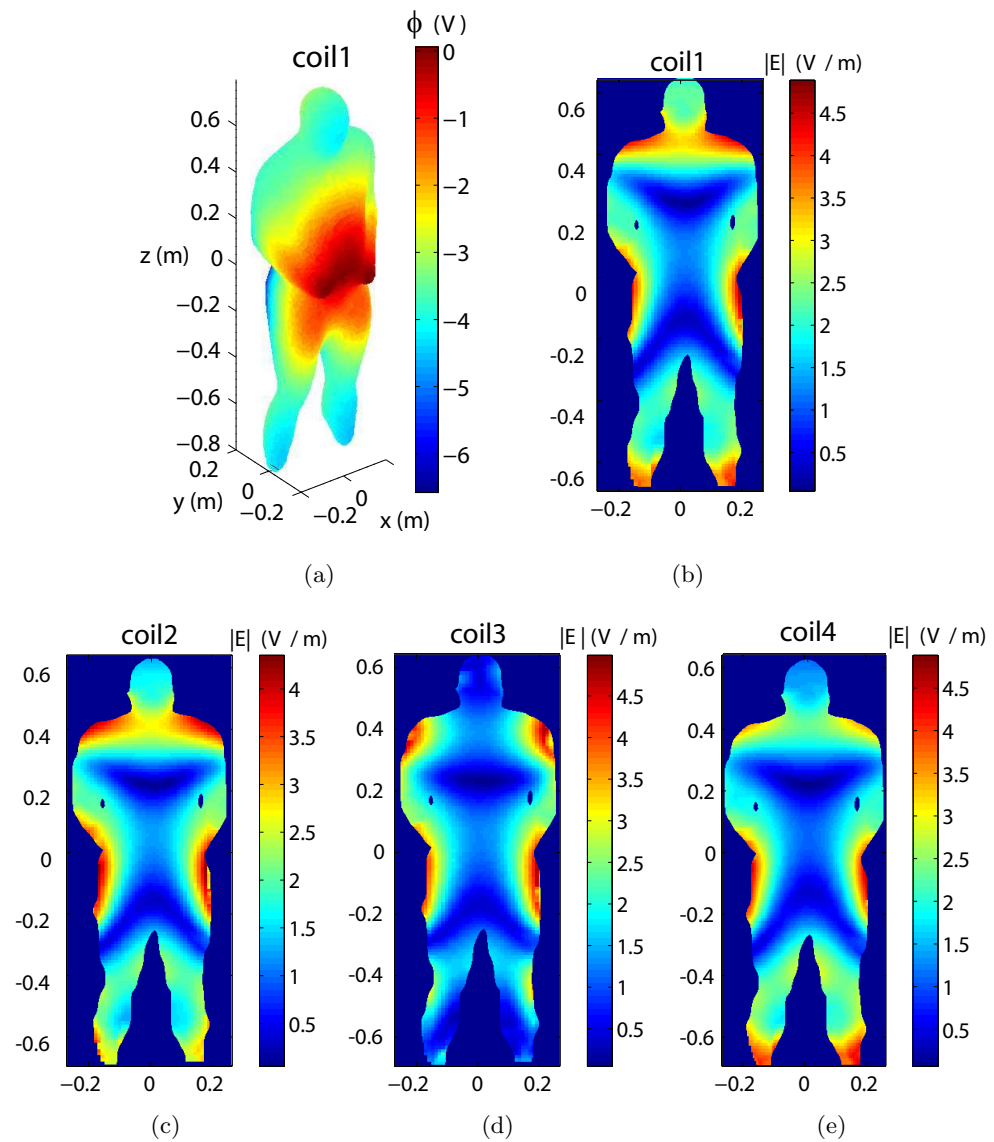
Figure 4.11: *(a) Scalar potential on surface of the human model induced during body exposure to coil1; colour-coded |E| maps for the body model exposed to time-varying x-gradients, produced by the four different coils.*

Chapter 5

Electric fields generated by magnetic fields used in MRI

5.1 Introduction

In order to investigate the electric fields that exposure to time-changing magnetic fields and natural movements in and around high field MRI systems can produce in conducting objects, a full electromagnetic theory valid for both cases is presented in this chapter. Faraday's Law for a moving system requires that the electrostatic charge associated with certain rotations is taken into account. This is demonstrated for simple geometries with known analytical solutions.

5.2 Electric field induced

MRI relies on the use of both rapidly switched magnetic field gradients and strong static magnetic fields. Understanding the interactions between these magnetic fields and the human body has become an important issue with the increasing use of high field MR scanners. In the following we focus on two of the most important safety issues in MRI:

i) Exposure to time varying magnetic fields,

ii) Movement in large static magnetic fields.

Temporally varying magnetic fields induce electric fields, **E**, by Faraday's Law and consequently electric currents in conducting tissues, which may cause PNS (peripheral nerve stimulation) in subjects [14, 15]. Although the process of nerve stimulation is not fully understood, the problem of determining the spatial distribution of the electric field induced by

gradient coils has been widely studied. Direct measurements of the induced current or electric field are not feasible inside the human body, so we are forced to use numerical analysis techniques due to the complicated structure and inhomogeneity of the electrical properties of the human body. One of the first approaches applied to simple body geometries was a finite element method used by Wang et al. [70]. Similarly a scalar-potential finite-difference (SPFD) calculation was presented by Dawson [71]; this approach was later used to compute electric fields induced in a heterogenous human model [72]. Another relevant approach is the impedance method [73], whose numerical results were compared to those produced with SPFD by Stuchly [74]. Analytical expressions for the electric field induced in a spherical conductor or an infinite conducting cylinder by switched magnetic field gradients were reported by Bencsik *et al.* and Bowtell and Bowley [75, 76] and these authors also studied the effect of using only the magnetic vector potential in evaluating the current induced [66]. Similarly Forbes and While evaluated analytical solutions for the magnetic and electric fields, where body and coil are represented as perfect cylindrical conductors [77, 78]. The finite difference time domain (FDTD) method has been the most widely used numerical technique, it was introduced by Brand [79], and modified and employed by other authors [81]-[85]. Mao et al. [86] also reported calculations of the induced E-field in an anatomically realistic body model sited within an x-gradient coil, including the effect of an RF shield. Finally we must mention other recent approaches such us the finite integration method [87, 88] which have proved to be a useful tool in the analysis of electric fields induced in the human body models by time varying magnetic field gradients.

The effect of natural movements of workers and subjects in the large static field of MR scanners is another important safety issue [89], as such movements may cause induced currents in conducting tissues and hence have potential bio-effects such as dizziness [90], metallic taste, vertigo [91] and other physiological sensations. Calculating the spatial distribution of the electric field induced by body motion in a magnetic field is a problem of similar electromagnetic nature to the case of switched gradients, but the literature relevant to this problem is much smaller. A notable exception is the work of Crozier et al. [92, 96] who used an FDTD approach to calculate the fields induced by movements in and around an MR scanner.

In the following sections an electromagnetic study of the exposure to switched gradients magnetic fields and movements in large static fields is presented, in which all the relevant processes including charge and current induction are investigated. Although these two problems share a similar electromagnetic basis, for a full understanding of the effect of movements in static fields we need to use an appropriate electromagnetic theory. There is an abundant literature on the interaction of moving conductors and magnetic fields,

which can provide a suitable electromagnetic framework including consistent expression of Maxwell's equations for this problem.

Our starting point is Faraday's Law of electromagnetic induction, one of Maxwell's equations that characterizes the interaction between magnetic and electric phenomena, whose generalization for moving systems leads to important conclusions when computing the current and charge induced. These well-known facts have unfortunately been neglected by some previous authors in their studies [92, 96], where numerical investigations of head and body motion in the magnetic field of an MR scanner have been carried out using an incomplete expression for the induced electric field.

The differences in the results obtained when using the formalism described here and other approaches is shown for some examples of moving conductors with simple geometries.

5.3   Faraday's Law

Faraday's Law is one of the most important laws of modern physics, whose relevance goes beyond electromagnetism[1].

Faraday influenced by previous investigations performed by Oersted, Arago and Ampère [98], carried out a series of experiments that culminated with the announcement of his law in 1832, which links electricity and magnetism. It states a relationship between the electromotive force (emf), $\mathcal{E}$, induced in a circuit, C of area S, and the change of the magnetic flux, Φ, through this circuit. The previous statement can be written in the following forms

$$\mathcal{E} = -\frac{d\Phi}{dt} = -\frac{d}{dt} \int_{S(t)} \mathbf{B} \, d\mathbf{S} \tag{5.1}$$

$$\mathcal{E} = \oint_{C(t)} \mathbf{E} \, d\mathbf{l} = \int_{S(t)} \nabla \times \mathbf{E} \, d\mathbf{S} \tag{5.2}$$

where $\mathbf{E}$ is the electric field measured in the system, whereas $C(\text{t})$ and $S(\text{t})$ can be functions of time, as the system may be moving.

This law explains successfully all the cases of magnetic (motional emf) and electric induction. If we consider the circuit, and hence the integration path, to be fixed (C and S are no longer functions of time) the temporal derivative operator then commutes with the integration

$$\int_{S} \nabla \times \mathbf{E} \, d\mathbf{S} = \int_{S} \frac{\partial \mathbf{B}}{\partial t} \, d\mathbf{S} \tag{5.3}$$

---

[1] For example, it was one of the key elements in the genesis of Einstein's Principle of Relativity [97].
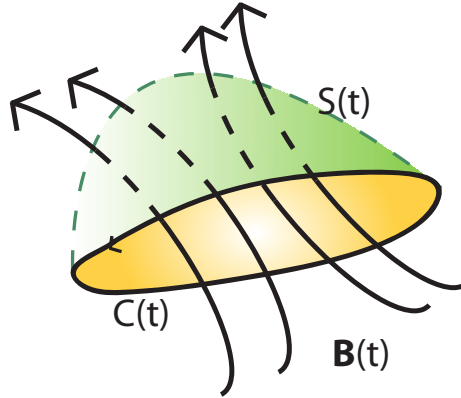
Figure 5.1: *Circuit C(t) and Surface S(t) with the flux of the magnetic induction* $\boldsymbol{B}$

where the partial derivative is equal to the time derivative of $\mathbf{B}$ because the surface is at rest [99], and since this equation is valid for any surface the integrands have to be identical

$$\nabla \times \mathbf{E} = -\frac{\partial \mathbf{B}}{\partial t}. \tag{5.4}$$

This is one of the four Maxwell's equations that Heaviside and Gibbs included in 1884 in their reformulation of electromagnetism, into the format that we use nowadays.

By applying Stokes' theorem the electric field can be written in terms of the scalar, $\phi(\mathbf{r})$, and magnetic vector, $\mathbf{A}(\mathbf{r})$, potentials

$$\mathbf{E} = -\nabla\phi - \frac{\partial \mathbf{A}}{\partial t} \tag{5.5}$$

where the vector potential defines the magnetic field via $\mathbf{B} = \nabla \times \mathbf{A}$. So there are two sources of the electric field for this case, the conservative one that is generated by a charge distribution and another contribution of magnetic origin.

In the derivation of Eq. 5.4 we imposed the condition that it can only be applied to systems at rest [2], and hence this approach would only be valid when tackling the problem of finding the electric field induced due to exposure to time-varying magnetic fields.

To obtain a generalized version of Faraday's law including the effect of motion several equivalent derivations can be performed: Appendix A details one version based on the change of flux. An alternative approach is the one given by Redžić [101] in which the convective derivative [100] (also called the substantive derivative or material derivative) is

---

[2]A restriction that was not originally in the Maxwell theory [102].

used to derive Faraday's Law via the magnetic vector potential.

Both approaches yield the same law of electromagnetic induction that is applicable to any system moving with velocity $\mathbf{v}$

$$\nabla \times \mathbf{E}' = -\frac{\partial \mathbf{B}}{\partial t} + \nabla \times (\mathbf{v} \times \mathbf{B}) \tag{5.6}$$

where $\mathbf{E}'$ is the electric field measured in a frame S′ that moves with the system.

It is quite important to emphasize the existence of two systems of reference, in which the fields' magnitudes may take different values. In the following, all primed magnitudes are measured in the moving frame, while unprimed terms relate to the laboratory frame.

The transformations of the electric and magnetic fields between the laboratory and the moving frames are described by [103]

$$\mathbf{E}' = \mathbf{E} + (\mathbf{v} \times \mathbf{B}) \tag{5.7}$$

$$\mathbf{B}' = \mathbf{B} \tag{5.8}$$

where Eq. 5.7 can easily be obtained by applying Stokes theorem to Eq. (5.6).

In general we are interested in the magnitude of the electromagnetic fields measured by the moving observer, as this is the value experienced by the subject, but it is worth noting that charge and current density are both invariant for the movements and velocities that are considered here.

So the expression for the Faraday's Law that we should use for gradient switching is

$$\mathbf{E} = -\nabla\phi - \frac{\partial \mathbf{A}}{\partial t} \tag{5.9}$$

and for movements in static fields

$$\mathbf{E}' = -\nabla\phi + (\mathbf{v} \times \mathbf{B}) = \mathbf{E} + (\mathbf{v} \times \mathbf{B}) \tag{5.10}$$

In the next sections the electric charge and current induced by movement in static magnetic fields and exposure to rapidly switched magnetic field gradients are studied using the equations stated above that characterize the interaction between magnetic and electric phenomena.

5.4 Quasi-Static Limit

Gradient switching frequencies, ω, for an MR scanner are usually below 10 kHz and the frequencies involved in natural movements of the body lie in the range 0 - 20 Hz. At these low frequencies, the electromagnetic properties of the body allow us to use a quasi-static approximation, as has been discussed in [70] and [76]. This involves the assumption that the induced current inside the conducting system does not produce a significant contribution to the magnetic field, and that the ratio of displacement to conduction current is very small

$$\frac{\omega\epsilon}{\sigma} < 10^{-3}, \tag{5.11}$$

so that the displacement current can be neglected (where ϵ is the electric permittivity and σ the conductivity of the system). The current density, $\mathbf{J} = \sigma\mathbf{E}$, can be considered to be solenoidal, such that

$$\nabla \cdot \mathbf{J} = 0. \tag{5.12}$$

Also in the case of a time-varying field we can adopt a sinusoidal variation without loss of generality as any more complex waveform can be represented in terms of a Fourier superposition of such modes.

5.5 Electrostatic Charges

5.5.1 Volume Electrostatic Charges

It is well known that conducting materials at rest do not contain any free charge and all possible charge exists as a surface density at the boundary of the system. This absence of charge can be explained as follows

$$\nabla \cdot \mathbf{D} = \rho \tag{5.13}$$

where $\mathbf{D} = \varepsilon\mathbf{E}$ is the electric displacement, ρ the charge density and ε the permittivity of the medium. Using charge conservation

$$\nabla \cdot \mathbf{J} + \frac{\partial\rho}{\partial t} = 0 \tag{5.14}$$

and the constitutive equation

$$\mathbf{J} = \sigma\mathbf{E} \tag{5.15}$$

where σ is the conductivity of the medium, we can obtain the following differential equation for the charge density

$$\frac{\sigma}{\varepsilon}\rho + \frac{\partial\rho}{\partial t} = 0 \tag{5.16}$$

whose solution is

$$\rho(t) = \rho_0 \, e^{-\frac{\sigma t}{\varepsilon}}. \tag{5.17}$$

As the relaxation time $\frac{\varepsilon}{\sigma}$ is very small for a conductor, (and also for conducting biological tissue) we can approximate

$$\rho(t) \approx 0. \tag{5.18}$$

However this expression does not hold for moving conductors in magnetic fields, since there exists a new electromotive field, $\mathbf{v} \times \mathbf{B}$, which will sweep free charge inside the conductor, leaving charged regions .

This result was already pointed out by van Bladel [104] and Lorrain [105] (with some minor corrections by Redžić [106]) and it can be proved as follows: let us consider a conductor moving in a static magnetic field, $\mathbf{B}$, where the movement is composed of a translation (characterized by a velocity $\mathbf{v}_0(t)$) plus a rotation (characterized by angular velocity $\mathbf{\Omega}(t)$) so that we can represent any type of movement[3] by

$$\mathbf{v}(\mathbf{r}, t) = \mathbf{v}_0(t) + \mathbf{\Omega}(t) \times \mathbf{r}. \tag{5.19}$$

Also the general continuity equation valid for moving media is given by

$$\nabla \cdot \mathbf{J} + \frac{D\rho}{Dt} = 0 \tag{5.20}$$

where $\frac{D}{Dt}$ is the convective derivative operator [100]. The current density in a moving ohmic conductor is given by [4]

$$\mathbf{J} = \sigma(\mathbf{E} + \mathbf{v} \times \mathbf{B}). \tag{5.21}$$

The constitutive equation for a medium in motion is

$$\mathbf{D} = \epsilon_0\mathbf{E} + \epsilon_0(\epsilon_r - 1)(\mathbf{E} + \mathbf{v} \times \mathbf{B}) = \epsilon_0\mathbf{E} + \mathbf{P} \tag{5.22}$$

where $\mathbf{P}$ is the polarization density and ϵ_r is the relative electrical permittivity of the material

$$\epsilon_r = \frac{\epsilon}{\epsilon_0}. \tag{5.23}$$

---

[3]For our problem we consider only non-relativistic velocities.
[4]A proper derivation including current density due to free charges can be found in [107].

Therefore as Eq. 5.13 holds for moving media, the space free-charge satisfies

$$\frac{\sigma}{\varepsilon}\rho + \frac{\sigma}{\varepsilon}2\varepsilon_0\boldsymbol{\Omega}\cdot\mathbf{B} + \frac{D\rho}{Dt} = 0, \tag{5.24}$$

where the source of the magnetic field, $\nabla\times\mathbf{B} = \mu_0\mathbf{J}$, is considered to lie outside the moving body. If we solve the above differential equation for a movement with a constant angular velocity we obtain

$$\rho(t) = \rho_0\ e^{-\frac{\sigma t}{\varepsilon}} - 2\varepsilon_0\boldsymbol{\Omega}\cdot\mathbf{B}\left[1 - e^{-\frac{\sigma t}{\varepsilon}}\right]. \tag{5.25}$$

This equation confirms that the approximation of zero charge can be used for translations of conductors, but not for some rotations.

For the case of rotation with constant angular frequency the equilibrium charge density becomes

$$\rho = -2\varepsilon_0\boldsymbol{\Omega}\cdot\mathbf{B} \tag{5.26}$$

The same result could have been achieved by applying the steady state conditions (section 5.4) that characterises the situations considered here. The divergence-free current condition implies that

$$\nabla\cdot\mathbf{P} = 0. \tag{5.27}$$

So if we apply the above result to Eq. 5.22, it yields

$$\rho = \varepsilon_0\nabla\cdot\mathbf{E} = -\varepsilon_0\nabla\cdot(\mathbf{v}\times\mathbf{B}) = -2\varepsilon_0\boldsymbol{\Omega}\cdot\mathbf{B}. \tag{5.28}$$

It can be noted that the induced charge is independent of the conductivity, and it is induced if the system rotates in a magnetic field that is not perpendicular to the axis of rotation.

The process of charge induction may be described with a helpful chart from Bringuier's paper [108], as follows: $\mathbf{v}\times\mathbf{B}$ produces a movement of free charges, i.e. if in a given region, $\boldsymbol{\Omega}\cdot\mathbf{B} < 0$, then there is a flux of electrons towards this area. The redistribution of charges yields a conservative electric field $\mathbf{E}$ that is opposed to the electromotive one, until eventually equilibrium is reached and both fields coexist; in some cases they may even completely cancel each other.

It is worth noting that ε_0, rather than the dielectric constant of the system, ε, appears for the expression of the induced charge. This is because the electric field in the conductor is built up by the free charges and not the polarization charges. In the case of a perfect
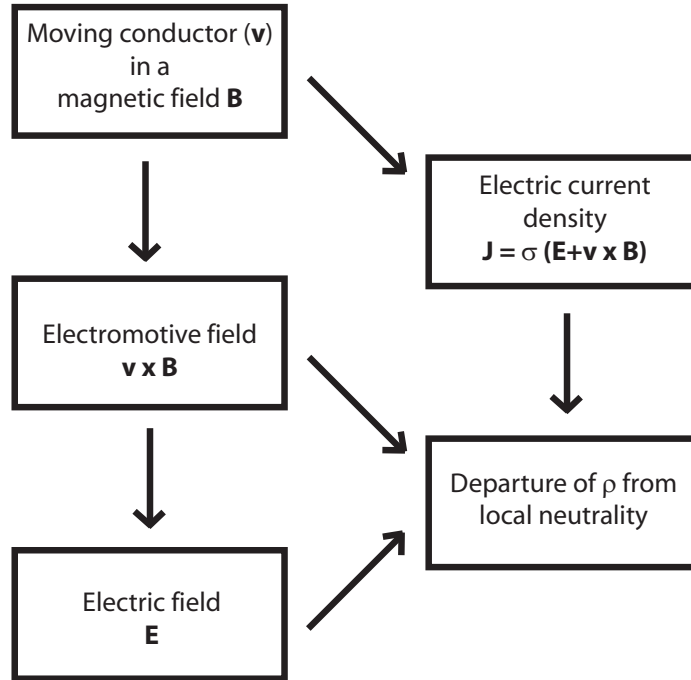
Figure 5.2: *Charge and current induced by movement at velocity, v, in a magnetic field, B.*

dielectric (this is not our case), Eq. 5.28 becomes [108]

$$\nabla \cdot \mathbf{E} = -\frac{\varepsilon - \varepsilon_0}{\varepsilon + \varepsilon_0} \, \nabla \cdot (\mathbf{v} \times \mathbf{B}) \tag{5.29}$$

5.5.2   Surface Electrostatic Charges

In the foregoing section we have seen that there is a charge redistribution in a conductor that moves in a static field, and that this charge can build up at the surfaces. This phenomenon can also happen in the case of a conductor exposed to a time-varying magnetic field as has been shown in previous work [109]; it also becomes more relevant when dealing with heterogenous systems, as in the case of the human body, since charge usually accumulates at the boundaries between media of different electrical properties. The process of surface charge induction is equivalent to the one described for the volume charge.

In general the surface charge density, ζ, is associated with a jump or discontinuity of the normal component of the electric displacement field, $\mathbf{D}$, at the surface. This condition applies even in the case of moving systems [110]

$$\zeta = (\mathbf{D}_2 - \mathbf{D}_1) \cdot \mathbf{n} = D_2^n - D_1^n, \tag{5.30}$$

where $\mathbf{n}$ is the unit vector normal to the surface directed from medium 1 to 2, and the sub-index makes reference to the side of the interface where the magnitudes are evaluated. Let's illustrate this with one example, consider an uncharged homogenous conductor moving in a static field. In this case, the correct expression for $\mathbf{D}$ is given in Eq. 5.28, so at the surface of the system

$$D_1^n = \epsilon_0 E_1^n + \epsilon_0(\epsilon_r - 1)(\mathbf{E}_1 + \mathbf{v} \times \mathbf{B}) \cdot \mathbf{n}. \tag{5.31}$$

If the conductor is moving in air

$$D_2^n = \epsilon_0 E_1^n, \tag{5.32}$$

but also to avoid unrealistic current flux out of the conductor, at the surface

$$\sigma(\mathbf{E}_1 + \mathbf{v} \times \mathbf{B}) \cdot \mathbf{n} = 0 \tag{5.33}$$

then

$$D_1^n = \epsilon_0 E_1^n \tag{5.34}$$

and

$$\zeta = \epsilon_0 E_2^n - \epsilon_0 E_1^n. \tag{5.35}$$

So the surface charge, in this particular case, is independent of the dielectric properties of the conductor.

5.6   Induced current

So far we have seen that one of the effects induced by movements in magnetic fields or exposure to time-varying magnetic fields is the induction of electrostatic charge, but the main effect responsible for the bio-effects that subjects and MRI staff may experience can be the current induced within the tissues of the body. Since we only need to consider conduction current, when a system is exposed to time-varying magnetics fields the current density is given by

$$\mathbf{J} = -\sigma\Big[\nabla\phi + \frac{\partial \mathbf{A}}{\partial t}\Big] = \sigma\mathbf{E}. \tag{5.36}$$

For conducting systems moving in a magnetic field

$$\mathbf{J} = \sigma\Big[\mathbf{E} + (\mathbf{v} \times \mathbf{B})\Big] = \sigma\mathbf{E}'. \tag{5.37}$$

In order to study this, let us examine the curl of the current density. If this vanishes for a given isolated moving system, that is, it is not connected to another circuit (and hence the current line forms a closed loop), then according to Stokes' theorem the circulation of this current will be zero for any closed path and thus $\mathbf{J}=0$, and there will be no induced current. So if we take the curl of $\mathbf{J}$ we obtain

$$\nabla \times \mathbf{J} = \sigma \big[\nabla \times \mathbf{E} + \nabla \times (\mathbf{v} \times \mathbf{B}) \big] \tag{5.38}$$

but

$$\nabla \times \mathbf{E} = -\frac{\partial \mathbf{B}}{\partial t} = 0, \tag{5.39}$$

for the case of static fields. It can also be shown that

$$\nabla \times (\mathbf{v} \times \mathbf{B}) = \mathbf{\Omega} \times \mathbf{B} - (\mathbf{v} \cdot \nabla)\mathbf{B} \tag{5.40}$$

where the relations $\nabla \cdot \mathbf{v} = 0$ and $\nabla \times \mathbf{v} = 2\mathbf{\Omega}$ have been used. Thus

$$\nabla \times \mathbf{J} = \sigma \big[\mathbf{\Omega} \times \mathbf{B} - (\mathbf{v} \cdot \nabla)\mathbf{B} \big]. \tag{5.41}$$

Suppose, for example, that the system moves in a field such that $(\mathbf{v} \cdot \nabla)\mathbf{B} = 0$, then no current will be induced for any translation. Table 5.1 summarises the current induced for this case and other simple cases involving translation and rotation.

The spatial distribution of $\mathbf{J}$, in general, depends on the shape of the object as well as the spatial variation of $\mathbf{B}$. Some interesting examples can be found in Lorrain's papers [105] and [111].

5.7 Pseudo Electromotive Term: $-(\mathbf{v} \cdot \nabla)\mathbf{A}$

Crozier et al. [92]-[96] present a complete and interesting study of the spatial distribution of the electric fields induced by body-motion around MRI magnets. They investigate multidirectional translations, bending movements and shaking of the head.
Unfortunately it seems that some of the results may have been incorrectly derived due to the use of an incomplete expression for the electromotive component of the electric field. Although these authors are aware of the electromotive term $\mathbf{v} \times \mathbf{B}$ [92], they use $-(\mathbf{v} \cdot \nabla)\mathbf{A}$ to take account of the magnetic effect, so the employed expression for the electric field is:

$$\mathbf{E}' = -\nabla\phi - (\mathbf{v} \cdot \nabla)\mathbf{A} \tag{5.42}$$

FIELD MOVEMENT	UNIFORM $\mathbf{B} \neq \mathbf{B}\,(\mathbf{r})$	NON UNIFORM $\mathbf{B} = \mathbf{B}\,(\mathbf{r})$
TRANSLATION	$\rho = 0$	$\rho = 0$
	$\mathbf{J} = 0$	$\mathbf{J} \neq 0$ if $(\mathbf{v} \cdot \nabla)\mathbf{B} \neq 0$
ROTATION	$\rho = -2\varepsilon_{\circ}\,\mathbf{\Omega} \cdot \mathbf{B}$	$\rho = -2\varepsilon_{\circ}\,\mathbf{\Omega} \cdot \mathbf{B}$
	$\mathbf{J} = 0$ if $\mathbf{\Omega} \parallel \mathbf{B}$	$\mathbf{J} = 0$ if $\nabla \times (\mathbf{v} \times \mathbf{B}) = 0$

Table 5.1: Current, $\mathbf{J}$, and charge induced, ρ in two kinds of magnetic fields, $\mathbf{B}$: uniform and non-uniform in a system under translation ($\mathbf{v}$) and rotation ($\mathbf{\Omega}$).

instead of the full form suggested here in Eq. 5.10.

Let's study the validity of this approximation; first using the vector identity

$$\nabla(\mathbf{v} \cdot \mathbf{A}) = \mathbf{A} \times (\nabla \times \mathbf{v}) + (\mathbf{A} \cdot \nabla)\mathbf{v} + \mathbf{v} \times (\nabla \times)\mathbf{A} + (\mathbf{v} \cdot \nabla)\mathbf{A}, \qquad (5.43)$$

we find that

$$\mathbf{v} \times \mathbf{B} = -(\mathbf{v} \cdot \nabla)\mathbf{A} + \nabla(\mathbf{v} \cdot \mathbf{A}) + \mathbf{\Omega} \times \mathbf{A}. \qquad (5.44)$$

So we see that by using $-(\mathbf{v} \cdot \nabla)\mathbf{A}$ as electromotive term, we are neglecting the terms $\nabla(\mathbf{v} \cdot \mathbf{A})$ and $\mathbf{\Omega} \times \mathbf{A}$. In the following we examine the importance of disregarding these terms depending on the type of movement.

5.7.1   Translation

If we consider only translations in static fields Eq. 5.44 takes the following form

$$\mathbf{v} \times \mathbf{B} = -(\mathbf{v} \cdot \nabla)\mathbf{A} + \nabla(\mathbf{v} \cdot \mathbf{A}), \qquad (5.45)$$

and by taking the curl in the above equation we obtain

$$\nabla \times (\mathbf{v} \times \mathbf{B}) = \nabla \times [-(\nabla \cdot \mathbf{v})\mathbf{A}] \tag{5.46}$$

so if the system is not connected (all the lines of current are closed loops) and the curls are the same for any line, then circulation is equal as well, and therefore the current induced is the same using $\mathbf{v} \times \mathbf{B}$ or $-(\mathbf{v} \cdot \nabla)\mathbf{A}$.

Although the two approaches predict the same current distribution, they can define different problems, as a conservative factor has to be added to the electric field to compensate the neglected term, $\nabla(\mathbf{v} \cdot \mathbf{A})$ when using the pseudo electromotive field $-(\mathbf{v} \cdot \nabla)\mathbf{A}$. Let's illustrate this with one example.

Translation in a uniform static field

Consider a uniform magnetic induction $\mathbf{B}$ applied in the direction of the velocity $\mathbf{v}$

$$\mathbf{v} = v\hat{\mathbf{k}} \tag{5.47}$$

$$\mathbf{B} = B\hat{\mathbf{k}} \tag{5.48}$$

In this case the induced current is zero, $\mathbf{J}=0$, (independent of the electromotive term used) as

$$\mathbf{v} \times \mathbf{B} = 0, \tag{5.49}$$

so that, there is no magnetic effect on the moving system. Then the conservative component of the electric field must be zero as well to maintain the zero current condition, so there is no surface charge induced.

For the second case, a plausible magnetic vector $\mathbf{A}$ which satisfies the Lorentz Gauge and generates a uniform magnetic field $\mathbf{B}$, is

$$\mathbf{A} = B[(x - y)\hat{\mathbf{i}} - z\hat{\boldsymbol{k}}]. \tag{5.50}$$

Then

$$-(\mathbf{v} \cdot \nabla)\mathbf{A} = vB\hat{\boldsymbol{k}}, \tag{5.51}$$

so that, the magnetic field affects the system producing this contribution of the electric field. However, since we know that $\mathbf{J} = 0$ there must be another electric field contribution equal to $\nabla(\mathbf{v} \cdot \mathbf{A}) = -vB\hat{\boldsymbol{k}}$, which cancels the electromotive term. This must come from the generation of a surface charge by the movement.

So we therefore see that the use of $-(\mathbf{v} \cdot \nabla)\mathbf{A}$ may lead to identification of the correct current density but with an unrealistic representation of the whole situation.

5.7.2 Rotation

When considering movements involving rotation in a static magnetic field, the differences in the results obtained by using $\mathbf{v} \times \mathbf{B}$ and $-(\mathbf{v} \cdot \nabla)\mathbf{A}$ increase. If we take the curl of Eq. 5.44 we obtain

$$\nabla \times (\mathbf{v} \times \mathbf{B}) = \nabla \times [-(\mathbf{v} \cdot \nabla)\mathbf{A}] + \nabla \times (\mathbf{\Omega} \times \mathbf{A}). \tag{5.52}$$

So only when the term $\nabla \times (\mathbf{\Omega} \times \mathbf{A})$, or equivalently $(\mathbf{\Omega} \cdot \nabla)\mathbf{A}$, vanishes we would expect to find the same spatial pattern of current density using the two different approaches.

Next, to illustrate the foregoing discussion, three conductors with simple geometries moving in static magnetic fields are studied, and the difference between the results produced by using the different approaches is described.

Rotation of a sphere in a uniform magnetic field

Let us consider a homogeneous and uncharged spherical conductor of radius a rotating about the x-axis, with angular velocity, $\mathbf{\Omega} = \Omega\,\hat{\mathbf{i}}$, in a uniform static magnetic field perpendicular to the axis of rotation, $\mathbf{B} = B\,\hat{\boldsymbol{k}}$. If the sphere is considered to be a rigid body, then

$$\mathbf{v} = \mathbf{\Omega} \times \mathbf{r} = \Omega(-z\hat{\mathbf{j}} + y\hat{\boldsymbol{k}}) \tag{5.53}$$

and the electromotive field in the sphere is

$$\mathbf{v} \times \mathbf{B} = -\Omega B z\hat{\mathbf{i}}, \tag{5.54}$$

and a suitable choice for the magnetic vector potential is

$$\mathbf{A} = \frac{B}{2}[-y\hat{\mathbf{i}} + x\hat{\mathbf{j}}] \tag{5.55}$$

since it produces the desired magnetic induction $\mathbf{B}$, then

$$-(\mathbf{v} \cdot \nabla)\mathbf{A} = -\frac{\Omega B}{2}z\hat{\mathbf{i}}. \tag{5.56}$$

In this problem, there is no volume charge induced as $(\boldsymbol{\omega} \perp \mathbf{B})$, also

$$\nabla \times (\mathbf{\Omega} \times \mathbf{A}) \neq 0 \tag{5.57}$$

so , from Eq. 5.44, it expected that the current induced by the electromotive term will be different to that obtained using the pseudo electromotive term.

Let's begin the study with the approach based on using $\mathbf{v} \times \mathbf{B}$. There must exist another field able to cancel the radial electromotive field at the surface to avoid an unrealistic flux of current out of the sphere. This new electrostatic field, $\mathbf{E}^\zeta$, has to be produced by the surface charge ζ, as for this movement no volume charge is induced (see Table 5.1), hence

$$(\mathbf{v} \times \mathbf{B}) \cdot \hat{\mathbf{r}}\big|_{r=a} = -\Omega B a \cos\theta \sin\phi \cos\theta \tag{5.58}$$

$$(\mathbf{v} \times \mathbf{B}) \cdot \hat{\mathbf{r}}\big|_{r=a} + \ E_r^\zeta\big|_{r=a} = 0 \tag{5.59}$$

so

$$E_r^\zeta\big|_{r=a} = \Omega B a \cos\theta \sin\phi \cos\theta = 2\alpha a\ Y_{21}(\theta,\phi) \tag{5.60}$$

where

$$\alpha = \Omega \frac{B}{2} \sqrt{\frac{8\pi}{15}}. \tag{5.61}$$

The scalar potential produced by the surface charge satisfies Laplace's equation, so it can be written in terms of spherical harmonics and powers of r [25], inside and outside the sphere

$$\phi^\zeta(\mathbf{r}) = \sum_{l=0}^{\infty} \sum_{m=-l}^{l} \left[A_{lm} r^l + B_{lm} r^{-(l+1)} \right] Y_{lm}(\theta,\phi) \tag{5.62}$$

using $E_r^\zeta = -\frac{\partial \phi^\zeta}{\partial r}$ and the continuity of the potential at the surface, we obtain

$$\phi^\zeta(\mathbf{r}) = \begin{cases} -\alpha r^2\ Y_{21}(\theta,\phi) & , \text{ if } r < a \\ -\frac{\alpha a^5}{r^3}\ Y_{21}(\theta,\phi) & , \text{ if } r > a \end{cases} \tag{5.63}$$

$$E_r^\zeta(\mathbf{r}) = \begin{cases} 2\alpha r\ Y_{21}(\theta,\phi) & , \text{ if } r < a \\ -\frac{3\alpha a^5}{r^4}\ Y_{21}(\theta,\phi) & , \text{ if } r > a \end{cases}. \tag{5.64}$$

Finally the surface charge from the radial component of the electrostatic field can be found as follows

$$\zeta(\theta,\phi) = \epsilon_0 E_{r,out}^\zeta\big|_{r=a} - \epsilon_0 E_{r,in}^\zeta\big|_{r=a} \tag{5.65}$$

$$\zeta(\theta,\phi) = -5\alpha a \epsilon_0\ Y_{21}(\theta,\phi). \tag{5.66}$$
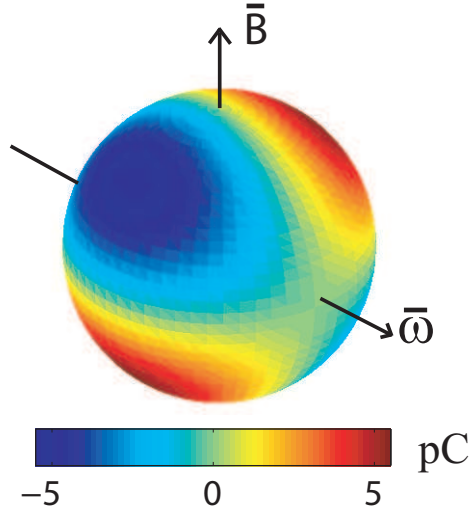
Figure 5.3: Surface charge for $\omega = 1rad/s$, a=0.5m and B= $1T$.

It is easy to check that this distribution satisfies the initial assumption of zero net charge,

$$\int_S \zeta(\mathbf{r})ds = 0. \tag{5.67}$$

The value of the electric field inside the sphere is

$$\mathbf{E}'(\mathbf{r}) = -\nabla\phi_{in}^\zeta(\mathbf{r}) + \mathbf{v} \times \mathbf{B} \tag{5.68}$$

and since from Eq. 5.63

$$\phi_{in}^\zeta(\mathbf{r}) = -\alpha r^2 \, Y_{21}(\theta, \phi) = \frac{\omega B}{2} xz \tag{5.69}$$

then

$$\mathbf{E}'(\mathbf{r}) = \frac{\Omega B}{2}[-z\hat{\mathbf{i}} + x\hat{\mathbf{k}}] \tag{5.70}$$

and

$$\mathbf{J}(\mathbf{r}) = \frac{\sigma \Omega B}{2}[-z\hat{\mathbf{i}} + x\hat{\mathbf{k}}]. \tag{5.71}$$

We now consider the effect of using the term -$(\mathbf{v}\cdot\nabla)\mathbf{A}$, instead of $\mathbf{v}\times\mathbf{B}$. By applying similar analysis to that used for the first case we find that the total electric field produced in the sphere is given by

$$\mathbf{E}'(\mathbf{r}) = \frac{\Omega B}{4}[-z\hat{\mathbf{i}} + x\hat{\mathbf{k}}]. \tag{5.72}$$

which is the half of the value computed previously, therefore also yielding half the induced current that was calculated using $\mathbf{v} \times \mathbf{B}$.

Rotation of a cylinder in a uniform field

We now apply the preceding discussion to a homogeneous infinite conducting cylinder (so end effects can be disregarded) of radius, a, with no net charge, rotating in a uniform magnetic field parallel to the axis of rotation

$$\boldsymbol{\Omega} = \Omega \, \hat{\boldsymbol{k}} \tag{5.73}$$

$$\mathbf{B} = B\hat{\boldsymbol{k}} \tag{5.74}$$

this rotation produces a negative uniform volume charge density

$$\rho(\mathbf{r}) = -2\varepsilon_0 \Omega B \tag{5.75}$$

which produces a electric field that can be computed using Gauss' law to be

$$\mathbf{E}^\rho(\mathbf{r}) = -\Omega B(x\hat{\mathbf{i}} + y\hat{\mathbf{j}}) = -\Omega B \varrho \hat{\boldsymbol{\varrho}} \tag{5.76}$$

where ϱ is the radial cylindrical coordinate.
We also find

$$\mathbf{v} = \Omega(-y\hat{\mathbf{i}} + x\hat{\mathbf{j}}) \tag{5.77}$$

$$\mathbf{v} \times \mathbf{B} = \Omega B \varrho \hat{\boldsymbol{\varrho}} \tag{5.78}$$

therefore $\mathbf{v} \times \mathbf{B} + \mathbf{E}^\rho(\mathbf{r}) = 0$, which is the expected result from Table 5.1 of zero current ($\nabla \times (\mathbf{v} \times \mathbf{B}) = 0$) inside the cylinder. Nevertheless in order to maintain the zero net charge a positive surface charge, ζ, which distributes uniformly on the surface must also exist. It is easy to check that $\zeta = \varepsilon_0 \Omega B a$. This surface charge produces no electric field inside the cylinder.

If instead of using $\mathbf{v} \times \mathbf{B}$ we use $-(\mathbf{v} \cdot \nabla)\mathbf{A}$, where a plausible choice for $\mathbf{A}$ could be

$$\mathbf{A} = \frac{B}{2}[(x - y)\hat{\mathbf{i}} + (x - y)\hat{\mathbf{j}}] \tag{5.79}$$

then

$$-(\mathbf{v} \cdot \nabla)\mathbf{A} = \frac{\Omega B}{2}[(x + y)\hat{\mathbf{i}} + (x + y)\hat{\mathbf{j}}]. \tag{5.80}$$

Zero current is predicted as $\nabla \times [-(\mathbf{v} \cdot \nabla)\mathbf{A}] = 0$ (or equivalently as $\nabla \times (\boldsymbol{\Omega} \times \mathbf{A}) = 0$).
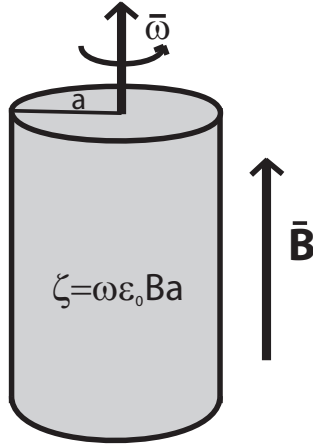
Figure 5.4: Cylinder with uniform surface charge.

If we use $-(\mathbf{v} \cdot \nabla)\mathbf{A}$ to find the volume charge density, this would be

$$\rho(\mathbf{r}) = \varepsilon_0 \nabla \cdot [(\mathbf{v} \cdot \nabla)\mathbf{A}] = -\varepsilon_0 \Omega B \tag{5.81}$$

which is half as large as the value calculated when using $\mathbf{v} \times \mathbf{B}$ as the driving term. It can now be seen how the electric field produced by the volume charge does not cancel completely the $-(\mathbf{v} \cdot \nabla)\mathbf{A}$ term, so in order to get zero current inside the cylinder a non uniform distribution of surface charge is needed. Obviously this assumption is not realistic, as it breaks the symmetry of the problem.

Rotation of a sphere in a longitudinal gradient field

A homogeneous uncharged conducting sphere of radius a rotates with angular velocity, $\boldsymbol{\Omega} = \Omega \hat{\boldsymbol{k}}$, in an ideal longitudinal field gradient

$$\mathbf{B} = G[-\frac{x}{2}\hat{\mathbf{i}} - \frac{y}{2}\hat{\mathbf{j}} + z\hat{\boldsymbol{k}}] \tag{5.82}$$

where the vector potential may be written as

$$\mathbf{A} = \frac{G}{2}[-yz\hat{\mathbf{i}} + xz\hat{\mathbf{j}}] \tag{5.83}$$

and since we are considering a rigid system

$$\mathbf{v} = \boldsymbol{\Omega} \times \mathbf{r} = \Omega[-y\hat{\mathbf{i}} + x\hat{\mathbf{j}}]. \tag{5.84}$$

The electromotive field is straightforwardly found to be

$$\mathbf{v} \times \mathbf{B} = \Omega G \left[xz\hat{\mathbf{i}} + yz\hat{\mathbf{j}} + \left(\frac{x^2 + y^2}{2} \right) \hat{\mathbf{k}} \right] \tag{5.85}$$

so there is no induction of current as:

$$\nabla \times (\mathbf{v} \times \mathbf{B}) = 0. \tag{5.86}$$

It follows from Table (5.1) that the induced volume charge is

$$\rho(\mathbf{r}) = -2\varepsilon_0 \mathbf{\Omega}\mathbf{B} = -2\varepsilon_0 \Omega G z, \tag{5.87}$$

and the pseudo electromotive term is

$$-(\mathbf{v} \cdot \nabla)\mathbf{A} = \frac{\Omega G}{2}(xz\hat{\mathbf{i}} + yz\hat{\mathbf{j}}) \tag{5.88}$$

but

$$\nabla \times (\mathbf{\Omega} \times \mathbf{A}) \neq 0 \tag{5.89}$$

so this predicts the existence of induced current.

The potential corresponding to the inhomogeneous volume charge distribution is given by

$$\phi^\rho(\mathbf{r}) = \frac{1}{4\pi\varepsilon_0} \int_V d^3 r' \frac{\rho(\mathbf{r}')}{|\mathbf{r} - \mathbf{r}'|} \tag{5.90}$$

here we have assumed that $\epsilon_r = 1$ for the sphere for sake of simplicity. The Green's function can be expanded in terms of spherical harmonics [25]

$$\frac{1}{|\mathbf{r} - \mathbf{r}'|} = 4\pi \sum_{l=0}^{\infty} \sum_{m=-l}^{l} \frac{1}{2l+1} \frac{r_<^l}{r_>^{l+1}} Y_{lm}^*(\theta', \phi') \, Y_{lm}(\theta, \phi) \tag{5.91}$$

where $r_<(r_>)$ is the smaller (larger) of $\mathbf{r}$ and $\mathbf{r}'$. Since $\rho(\mathbf{r}) \propto Y_{10}(\theta, \phi)$, when we perform the integral and use the orthogonality of the spherical harmonics, we find that the scalar potential due to the volume charges is

$$\phi^\rho(\mathbf{r}) = \Omega G \cos\theta \left[\frac{r^3}{5} - \frac{a^2 r}{3} \right] = \Omega G \left[\frac{z(x^2 + y^2 + z^2)}{5} - \frac{a^2 z}{3} \right] \tag{5.92}$$

and hence the electric field

$$\mathbf{E}^{\rho}(\mathbf{r}) = -\nabla\phi^{\rho}(\mathbf{r}) = -\Omega G\left[\frac{2}{5}xz\hat{\mathbf{i}} + \frac{2}{5}yz\hat{\mathbf{j}} + \left(\frac{x^2+y^2+3z^2}{5} - \frac{a^2}{3}\right)\hat{\mathbf{k}}\right] \tag{5.93}$$

whose radial component is

$$E_r^{\rho}(\mathbf{r}) = \Omega G\cos\theta\left[\frac{a^2}{3} - \frac{3r^2}{5}\right]. \tag{5.94}$$

The electric field due to the space charge does not completely cancel the electromotive one, but the zero current condition still applies, as we have to take into account the electrostatic field due to surface charges. Here to compute $\mathbf{E}^{\zeta}$ we apply the boundary condition on the radial component of the current, which has to vanish at $r = a$ so that

$$E_r^{\zeta}\big|_{r=a} = -\mathbf{v}\times\mathbf{B}\cdot\hat{\mathbf{r}}\big|_{r=a} - E_r^{\rho}\big|_{r=a} \tag{5.95}$$

and

$$E_r^{\zeta}\big|_{r=a} = -\alpha Y_{10}(\theta,\phi) - 3\beta a^2\, Y_{30}(\theta,\phi) \tag{5.96}$$

where

$$\begin{aligned}
\alpha &= \sqrt{\frac{4\pi}{3}}\,\frac{\Omega G a^2}{3} \\
\beta &= -\sqrt{\frac{16\pi}{7}}\,\frac{\Omega G}{10}
\end{aligned} \tag{5.97}$$

also since $E_r^{\zeta} = \frac{\partial\Phi^{\zeta}}{\partial r}$, and the corresponding scalar potential must have the form of the general solution for the Laplace's case Eq.(5.62), then

$$\phi^{\zeta}(\mathbf{r}) = \begin{cases} \alpha r\, Y_{10}(\theta,\phi) + \beta r^3\, Y_{30}(\theta,\phi) & \text{, if } r < a \\ \alpha\frac{a^3}{r^2}\, Y_{10}(\theta,\phi) + \beta\frac{a^7}{r^4}\, Y_{30}(\theta,\phi) & \text{, if } r > a \end{cases} \tag{5.98}$$

which yields the following electric field

$$\mathbf{E}^{\zeta}(\mathbf{r}) = -\frac{3}{5}\Omega G\left[xz\hat{\mathbf{i}} + yz\hat{\mathbf{j}} + \left(\frac{x^2+y^2+2z^2}{2} - \frac{5a^2}{9}\right)\hat{\mathbf{k}}\right] \tag{5.99}$$

and after some calculations it is easy to show that adding the contribution of this field, a zero current in the sphere is obtained.

$$\mathbf{E}^{\rho}(\mathbf{r}) + \mathbf{E}^{\zeta}(\mathbf{r}) + \mathbf{v}\times\mathbf{B} = 0, \quad\Longrightarrow \mathbf{J} = 0. \tag{5.100}$$

Now a simple analysis using the radial component of the electric field inside and outside the sphere gives the surface charge density

$$\zeta(\theta, \phi) = 3\epsilon_0 \alpha \, Y_{10}(\theta, \phi) + 5\beta a^2 \epsilon_0 Y_{30}(\theta, \phi) \tag{5.101}$$

The net surface charge is zero, which is an expected result to maintain the electric neutrality of the sphere, since the net volume charge is null as well.

Let us now investigate the use of the pseudo electromotive term, it produces a different volume charge density

$$\nabla \cdot \mathbf{E} = -\nabla[(\mathbf{v} \cdot \nabla)\mathbf{A}] = -\varepsilon_0 \Omega G z \tag{5.102}$$

which is half the size of the value calculated previously using $\mathbf{v} \times \mathbf{B}$. Consequently the associated electric field is

$$\mathbf{E}^\rho(\mathbf{r}) = -\frac{\Omega G}{2} \left[\frac{2}{5} xz\hat{\mathbf{i}} + \frac{2}{5} yz\hat{\mathbf{j}} + \left(\frac{x^2 + y^2 + 3z^2}{5} - \frac{a^2}{3} \right)\hat{\boldsymbol{k}} \right] \tag{5.103}$$

Following analogous analysis to that used before and after imposing the zero radial flux of current at the surface we obtain the following scalar potential due to the surface charges for points in the sphere

$$\phi^\zeta(\mathbf{r}) = \tilde{\alpha} r \, Y_{10}(\theta, \phi) + \tilde{\beta} r^3 \, Y_{30}(\theta, \phi) \tag{5.104}$$

where

$$\begin{aligned} \tilde{\alpha} &= \sqrt{\frac{4\pi}{3}} \frac{\Omega G a^2}{15} \\ \tilde{\beta} &= -\sqrt{\frac{16\pi}{7}} \frac{\Omega G}{30}. \end{aligned} \tag{5.105}$$

However it is easy to show that the electric field produced by this surface charge density does not cancel the other two contributions

$$\mathbf{E}^\zeta(\mathbf{r}) \neq (\mathbf{v} \cdot \nabla)\mathbf{A} - \mathbf{E}^\rho(\mathbf{r}) \implies \mathbf{J} \neq 0. \tag{5.106}$$

and hence the zero current condition does not hold in the sphere. This current is

$$\mathbf{J}(\mathbf{r}) = -\frac{\Omega G \sigma}{10} \left[xz\hat{\mathbf{i}} + yz\hat{\mathbf{j}} + \left(a^2 - 2x^2 - 2y^2 - z^2 \right)\hat{\boldsymbol{k}} \right], \tag{5.107}$$

although its normal component vanishes at the surface

$$\mathbf{J}(\mathbf{r} = a) \cdot \mathbf{n} = 0 \tag{5.108}$$

this a situation completely contrary to that obtained using $\mathbf{v} \times \mathbf{B}$.
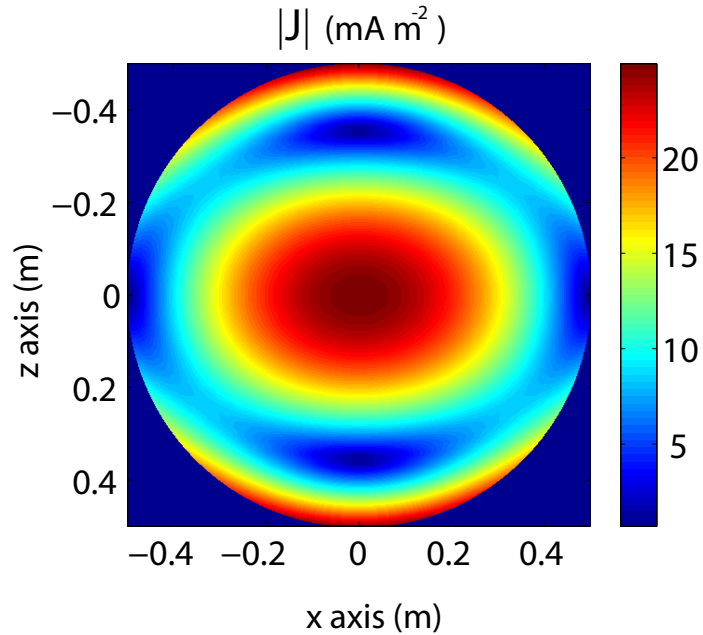
Figure 5.5: *Modulus of the induced current density predicted by the pseudo electromotive term for a sphere of 1 m diameter, rotating at velocity 1 rads/s in an ideal longitudinal field gradient of strength 1 Tm^{-1}.*

5.8   Laplace's and Poisson's Equations

We recall that the electric field, for the two problems we considered here, can be written in terms of the scalar, $\phi(\mathbf{r})$, and magnetic vector, $\mathbf{A}(\mathbf{r})$, potentials

$$\mathbf{E} = -\nabla\phi - i\omega\mathbf{A} \tag{5.109}$$

for exposure to time-varying magnetic fields, and where a sinusoidal variation has been assumed. Whereas for movements in static fields we use

$$\mathbf{E} = -\nabla\phi + \mathbf{v} \times \mathbf{B}. \tag{5.110}$$

We can generalize both equation and re-express the electric field for both as

$$\mathbf{E} = -\nabla\phi + \vec{\mathbb{A}}, \qquad (5.111)$$

such that it can be seen that there are two sources of $\mathbf{E}$. By defining $\vec{\mathbb{A}}$ we obtain a general magnetic contribution to the electric field that allows us to pose both problems studied here using the same equation: $\vec{\mathbb{A}}$ becomes $-i\omega\mathbf{A}$ for exposure to time varying magnetic fields and $\mathbf{v} \times \mathbf{B}$ for movement at velocity $\mathbf{v}$ in a static field, $\mathbf{B}$.

The computation of the second magnetic term is straightforward as $\vec{\mathbb{A}}$ is produced by current flowing in coils (main magnet or gradient) whose wirepaths are generally known; whereas the conservative term (generated by electric charges) can not be simply evaluated, and its calculation is the goal of our approach.

Using the approximation described in Eq. (5.12), it can be shown that the scalar potential can be found by solving

$$\nabla \cdot \left(\sigma\nabla\phi\right) = \nabla \cdot (\sigma\vec{\mathbb{A}}). \qquad (5.112)$$

For regions with uniform conductivity this equation reduces to Laplace's equation for the case of time-varying magnetic field gradients

$$\nabla^2\phi = 0, \qquad (5.113)$$

since the magnetic vector potential is a divergence-free field, and to Poisson's equation

$$\nabla^2\phi = \nabla \cdot (\mathbf{v} \times \mathbf{B}) = -\frac{\rho}{\varepsilon_0} \qquad (5.114)$$

for movements in static magnetic fields, where ε_0 is the electric permittivity of vacuum. In the latter case the source term can be identified as an electrostatic space charge, which is expected to be present only when certain rotations (Section 5.5.1) are considered

$$\rho = -2\varepsilon_0\mathbf{\Omega} \cdot \mathbf{B}. \qquad (5.115)$$

Chapter 6

Forward BEM for Laplace's and Poisson Equations

6.1 Introduction

We have shown the need of to take account of the electric field produced by the electro-static charges built up on the interface between media (or volume charge) when calculating the electric field produced by exposure of a conducting body to changing magnetic fields or movements in large magnetic fields. This can be posed as a boundary value problem governed by Laplace's or Poisson's equation.

These partial differential equations (PDE) are common in physics, they are found in electrostatics, magnetostatics, fluid dynamics and heat transfer; areas where boundary element methods (BEM) have proved to be an ideally suited approach for solving this type of problem.

An integral formulation of the problem and its subsequent solution using a constant BEM is described in this chapter. We first prescribe the boundary conditions that our problem is subjected to. Later by using Green's functions formalism we derive an integral formulation of the potential from the PDE. The integral equation obtained is a Fredholm equation of the second kind, similar to that presented by Geselowitz [112], which has been widely used in EEG studies [113, 114].

In the next step of the BEM approach, we construct integral formulations for the gradient of the potential, which then provide the values of the electric field.

Finally, by using this integral equation, a constant BEM approach is developed, the boundaries are discretized and approximations relating to the variation of the potential are made so as to produce numerical solutions. The validity of this approach is demonstrated for

simple geometries with known analytical solutions and it is also applied to the evaluation of the induced fields in more complicated meshed models of the human body.

For the sake of clarity a representation is formulated first for Laplace's and Poisson's equations for a single domain and next in a straightforward fashion it is extended to the multi-domain integral description, which is needed to describe objects with more than one compartment.
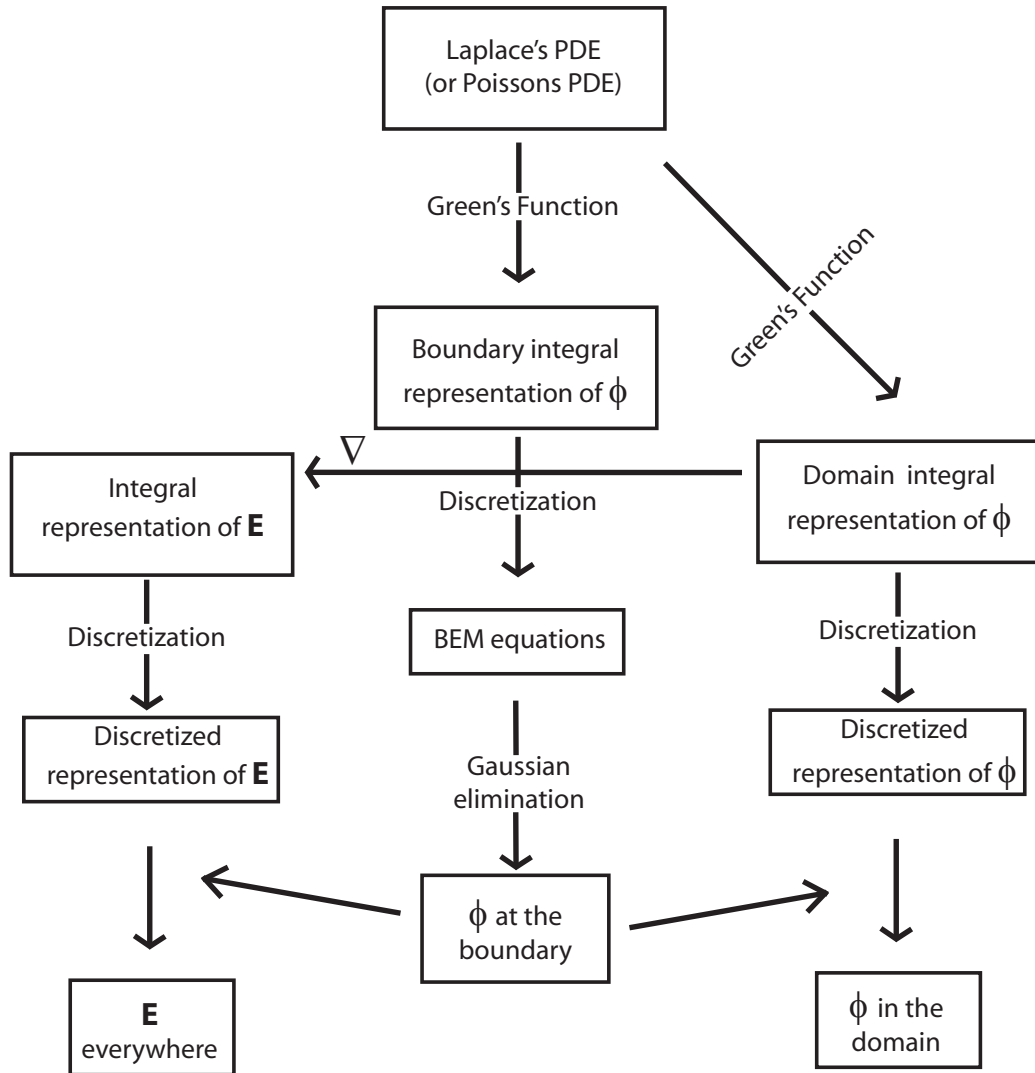
Figure 6.1: *Scheme of the BEM for Laplace's (Poisson's) equation.*

6.2 Boundary Conditions

Let us consider a system composed of a set of homogenous regions $D_1, ..., D_M$ with constant conductivities $\sigma_1, ..., \sigma_M$, separated by interfaces $S_1, ..., S_M$ with outward normal vectors to the surfaces $\mathbf{n}, ..., \mathbf{n}_M$ and which is surrounded by air ($\sigma_{air} = 0$), see Fig. 6.2.

In order to obtain realistic solutions for our problem we use the continuity of the current flowing at every surface between regions as a boundary condition between domains. This is a *natural or Neumann* condition since the normal derivative of the potential is specified. This common requirement has been used previously in Finite-Element simulations [115] (although as will be seen, we do not consider the electric field to be continuous at the interface).
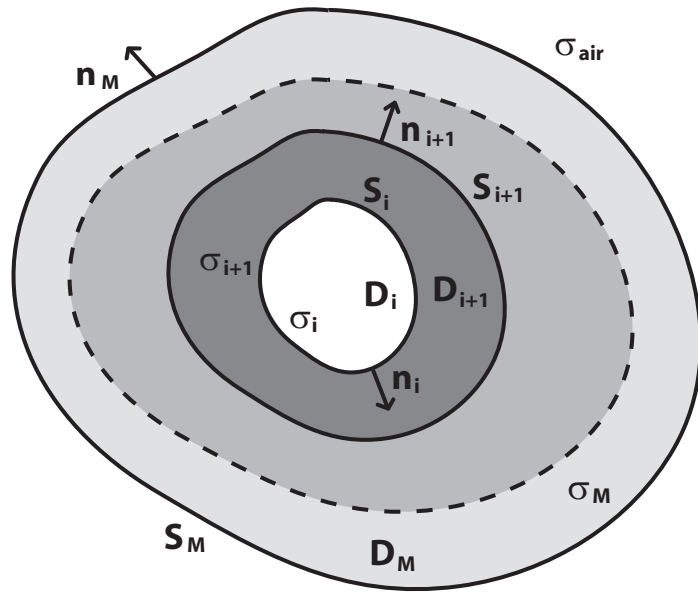
Figure 6.2: *System composed of M homogeneous domains.*

When imposing the conservation of the current density, $\mathbf{J}$, between two different domains, we find at the separation surface that

$$\mathbf{J}_i \cdot \mathbf{n}_i = \mathbf{J}_{i+1} \cdot \mathbf{n}_i \Rightarrow \sigma_i E_i^n = \sigma_{i+1} E_{i+1}^n \tag{6.1}$$

where the subindex makes reference to the domain where the magnitudes are evaluated and $E_i^n = \mathbf{E}_i \cdot \mathbf{n}_i$, is the normal component of the generalized electric field. Then at the ith-surface

$$\sigma_i(-\nabla\phi^i + \vec{\mathbb{A}}^i) \cdot \mathbf{n} = \sigma_{i+1}(-\nabla\phi^{i+1} + \vec{\mathbb{A}}^{i+1}) \cdot \mathbf{n}. \tag{6.2}$$

The normal component of the gradient of the potential is not continuous, and in fact, a discontinuity results from the existence of charges accumulated at the boundaries. This can be represented as

$$\nabla \phi^j \cdot \mathbf{n} = \frac{\partial \phi^j}{\partial n} = q^j \tag{6.3}$$

since $\vec{\mathbb{A}}$ is continuous at the surface, we can write

$$\vec{\mathbb{A}}^i \cdot \mathbf{n} = \vec{\mathbb{A}}^{i+1} \cdot \mathbf{n} = \mathbb{A}^n, \tag{6.4}$$

so that the matching condition becomes

$$\mathbb{A}^n(\sigma_{i+1} - \sigma_i) = \sigma_{i+1}q^{i+1} - \sigma_i q^i$$
$$i = 1, ..., M \tag{6.5}$$

where the index $M + 1$ is used for the magnitudes of the conductivity outside the system. As shown in the following sections, this constraint at the surface can be used to define the problem. For example for a single domain ($M = 1$ and $\sigma_2 = 0$), this condition implies that there is no current flow out of the system and we find

$$q^i = \mathbb{A}^n \tag{6.6}$$

a result which is independent of the conductivity in the domain (provided it is non-zero).

6.3 Integral formulation for Laplace's equation. Single Domain.

Let ϕ be the scalar potential that obeys Laplace's equation in a volume domain D bounded by a surface S and surrounded by air.

Also Green's second identity [7] states

$$\int_D \left(\phi(\mathbf{y})\nabla^2\psi(\mathbf{y}) - \psi(\mathbf{y})\nabla^2\phi(\mathbf{y}) \right) d^3y = \int_S \left[\phi(\mathbf{y})\frac{\partial\psi}{\partial n}(\mathbf{y}) - \psi(\mathbf{y})\frac{\partial\phi(\mathbf{y})}{\partial n} \right] ds(\mathbf{y})$$
$$\mathbf{y} \in S \tag{6.7}$$

where ψ is an arbitrary scalar function that is continuous and differentiable in D. If we choose this auxiliary function as the free-space Green's function, or fundamental solution,
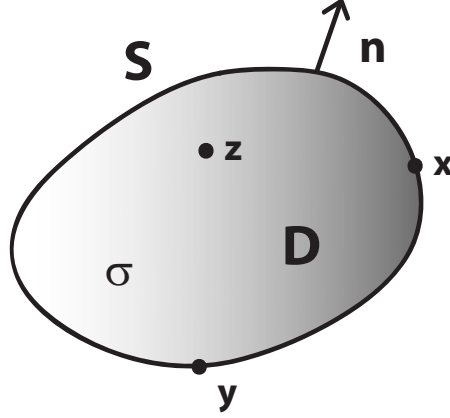
Figure 6.3: *Homogeneous single domain D of conductivity σ and bounding surface S with the outward normal,* **n**.

of the Laplace equation

$$\phi^* = \frac{1}{4\pi|\mathbf{z} - \mathbf{y}|} = \frac{1}{4\pi r},\tag{6.8}$$

and q^* is its normal derivative

$$q^* = \frac{\partial\phi^*}{\partial n} = \frac{z_j - y_j}{4\pi r^3}\,n_j,\tag{6.9}$$

here, we have used the tensor summation definition of the double index, then we obtain

$$\int_D \Big(\phi(\mathbf{y})\nabla^2\phi^*(\mathbf{z}, \mathbf{y}) - \phi^*(\mathbf{z}, \mathbf{y})\nabla^2\phi(\mathbf{y})\Big)d^3y$$
$$= \int_S \Big[\phi(\mathbf{y})\,q^*(\mathbf{z}, \mathbf{y}) - \phi^*(\mathbf{z}, \mathbf{y})\,q(\mathbf{y})\Big]ds(\mathbf{y})\tag{6.10}$$
$$\mathbf{z} \in D,\ \mathbf{y} \in S.$$

This expression is the basis of our BEM approach for solving Laplace's and Poisson's equations, and all the following integral representations are derived from it.

We can now make use of the fact that the potential and the Green's function are both harmonic functions

$$\nabla^2\phi(\mathbf{z}) = 0\tag{6.11}$$

$$\nabla^2\phi^*(\mathbf{x}, \mathbf{y}) = -\delta(\mathbf{z}, \mathbf{y})\tag{6.12}$$

then

$$c(\mathbf{z})\phi(\mathbf{z}) = \int_S \left[\phi^*(\mathbf{z}, \mathbf{y}) \, q(\mathbf{y}) - \phi(\mathbf{y}) \, q^*(\mathbf{z}, \mathbf{y}) \right] ds(\mathbf{y})$$

$$\mathbf{z} \in D \bigcup S, \ \mathbf{y} \in S \tag{6.13}$$

where $c(\mathbf{z})$ is function of the local geometry of $\mathbf{z}$

$$c(\mathbf{z}) = \begin{cases} 1, & if \quad \mathbf{z} \in D \\ \frac{1}{2}, & if \quad \mathbf{z} \in S \\ 0, & if \quad \mathbf{z} \notin D \bigcup S. \end{cases} \tag{6.14}$$

The derivation of equation (6.13) is not trivial due to the singular behaviour of $\phi^*(\mathbf{z}, \mathbf{y})$ and $q^*(\mathbf{z}, \mathbf{y})$. It is obtained in a rigorous way [63] by isolating the singular point $\mathbf{z}$ in a small sphere and performing a limit process.

The boundary condition for a single domain (Section 6.2) specifies the surface distribution of the normal derivative of the potential

$$\mathbb{A}^n(\mathbf{y}) = q(\mathbf{y}) \tag{6.15}$$

so that equation (6.13) yields

$$c(\mathbf{z})\phi(\mathbf{z}) = \int_S \phi^*(\mathbf{z}, \mathbf{y}) \, \mathbb{A}^n(\mathbf{y}) \, ds(\mathbf{y}) - \int_S \phi(\mathbf{y}) \, q^*(\mathbf{z}, \mathbf{y}) \, ds(\mathbf{y}). \tag{6.16}$$

The first and second integrals of the right-hand side of the equation are referred to as the *single layer potential* and *double layer potential* respectively.

The importance of this equation relies on the fact that the unknown potential at one point is completely defined by its values on the surface (since the normal component of $\vec{\mathbb{A}}$ is a known quantity).

Next we illustrate the integral representation of ϕ in the domain and at the boundary and show how the numerical values of the potential at the surface can be obtained from the latter.

Domain Integral Representation of the Potential

If $\mathbf{z}$ belongs to the interior of the domain ($\mathbf{z} \in D$), ϕ^* and q^* are well-behaved and the integrals are consequently not singular. Equation (6.13) therefore becomes

$$\phi(\mathbf{z}) = \int_S \phi^*(\mathbf{z}, \mathbf{y}) \, \mathbb{A}^n(\mathbf{y}) \, ds(\mathbf{y}) - \int_S \phi(\mathbf{y}) \, q^*(\mathbf{z}, \mathbf{y}) \, ds(\mathbf{y}). \tag{6.17}$$

Boundary Integral Representation of the Potential

Considering the jump property of the double layer potential when the collocation point tends to the surface [63], $\mathbf{z} \to \mathbf{x} \in S$, we can derive the boundary integral representation

$$\frac{1}{2}\phi(\mathbf{x}) + \int_S \phi(\mathbf{y}) \, q^*(\mathbf{x}, \mathbf{y}) \, ds(\mathbf{y}) = \int_S \phi^*(\mathbf{x}, \mathbf{y}) \, \mathbb{A}^n(\mathbf{y}) \, ds(\mathbf{y}) \tag{6.18}$$

again it is worth stressing this result, which shows that the values of ϕ at the boundary are linked. We also note that this equation is completely independent of the conductivity.

In integral equation theory this type of expression is known as a Fredholm [116] equation of the second kind, as the unknown function appears inside and outside the integral.

Domain Integral Representation of the Electric Field

The final aim of our scheme is to find the electric field, which requires the evaluation of the gradient of the scalar potential. We can find this gradient by differentiating Eq. 6.17 with respect to the coordinates of $\mathbf{z} = (z_1, z_2, z_3)$. This step is allowed since all the functions involved are continuous inside the domain, and we obtain

$$\frac{\partial \phi}{\partial z_j}(\mathbf{z}) = \int_S \left[\frac{\partial \phi^*}{\partial z_j}(\mathbf{z}, \mathbf{y}) \mathbb{A}^n(\mathbf{y}) - \frac{\partial q^*}{\partial z_j}(\mathbf{z}, \mathbf{y}) \, \phi(\mathbf{y}) \right] ds(\mathbf{y})$$
$$\mathbf{z} \in D. \tag{6.19}$$

where the Green's function dipole is given by

$$\frac{\partial \phi^*}{\partial x_j} = -\frac{z_j - y_j}{4\pi r^3}, \qquad j = 1, 2, 3 \tag{6.20}$$

and the quadrupole is

$$\frac{\partial q^*}{\partial z_j} = -\frac{1}{4\pi} \left[\frac{\delta_{j,k}}{r^3} - 3\frac{(z_j - y_j)(z_k - y_k)}{r^5} \right] n_k, \qquad j = 1, 2, 3. \tag{6.21}$$

Finally, to find the electric field we have to add the contribution of the magnetic component

$$E_j(\mathbf{z}) = \mathbb{A}_j(\mathbf{z}) - \int_S \left[\frac{\partial \phi^*}{\partial z_j}(\mathbf{z}, \mathbf{y}) \mathbb{A}^n(\mathbf{y}) - \frac{\partial q^*}{\partial z_j}(\mathbf{z}, \mathbf{y}) \ \phi(\mathbf{y}) \right] ds(\mathbf{y})$$

$$\mathbf{z} \in D.$$

(6.22)

Boundary Integral Representation of the Electric Field

In order to derive an expression for the gradient of ϕ which is valid at the boundary, we cannot proceed by differentiating Eq. 6.18 because the directional derivatives of the single and double layer potentials are not continuous across their charge density carrying surface. For a rigorous derivation we can use Eq. 6.19 and take the limit where the interior point $\mathbf{z} \in D$ tends to the surface, $\mathbf{z} \to \mathbf{x} \in S$, so as to take account of the jump properties of the directional derivative of the surface potentials [116]

$$\lim_{\mathbf{z} \to \mathbf{x}} \left[\frac{\partial}{\partial z_j} \int_S \phi^*(\mathbf{z}, \mathbf{y}) \mathbb{A}^n(\mathbf{y}) ds(\mathbf{y}) \right] = \frac{1}{2} \mathbb{A}^n(\mathbf{x}) \ n_j(\mathbf{x}) + \int_S \frac{\partial \phi^*}{\partial z_j}(\mathbf{x}, \mathbf{y}) \mathbb{A}^n(\mathbf{y}) ds(\mathbf{y})$$

$$\mathbf{z} \in D, \qquad \mathbf{x} \in S,$$

(6.23)

and

$$\lim_{\mathbf{z} \to \mathbf{x}} \left[\frac{\partial}{\partial z_j} \int_S q^*(\mathbf{z}, \mathbf{y}) \ \phi(\mathbf{y}) ds(\mathbf{y}) \right] = -\frac{1}{2} \left[\frac{\partial \phi}{\partial x_j}(\mathbf{x}) - q(\mathbf{x}) \ n_j(\mathbf{x}) \right]$$

$$+ \int_{S_p} \frac{\partial q^*}{\partial x_j}(\mathbf{x}, \mathbf{y}) \ \phi(\mathbf{y}) ds(\mathbf{y})$$

$$\mathbf{z} \in D, \qquad \mathbf{x} \in S.$$

(6.24)

After performing the limit process and applying the boundary conditions (Section 6.2), Eq. 6.19 becomes

$$\frac{1}{2} \frac{\partial \phi}{\partial x_j}(\mathbf{x}) = \int_S \left[\frac{\partial \phi^*}{\partial x_j}(\mathbf{x}, \mathbf{y}) \mathbb{A}^n(\mathbf{y}) - \frac{\partial q^*}{\partial x_j}(\mathbf{x}, \mathbf{y}) \ \phi(\mathbf{y}) \right] ds(\mathbf{y})$$

$$\mathbf{x} \in S, \qquad j = 1, 2, 3.$$

(6.25)

The electric field at the boundary is then given by

$$E_j(\mathbf{x}) = \mathbb{A}_j(\mathbf{x}) - 2 \int_S \left[\frac{\partial \phi^*}{\partial x_j}(\mathbf{x}, \mathbf{y}) \mathbb{A}^n(\mathbf{y}) - \frac{\partial q^*}{\partial x_j}(\mathbf{x}, \mathbf{y}) \ \phi(\mathbf{y}) \right] ds(\mathbf{y})$$

$$\mathbf{x} \in S, \qquad j = 1, 2, 3.$$

(6.26)

6.4 Constant BEM for Laplace's equation. Single Domain

By solving equation (6.18) we can obtain ϕ at the boundary, but the solution of this integral equation is not trivial, and analytical solutions are only available for simple geometries, whereas BEM provides a numerical solution valid for any closed geometry [1].

The first step of the BEM approach is the discretization of the boundary, which is divided into simple geometrical forms S_k, here we will use flat triangular elements, whose vertices will be referred to as nodes

$$S \simeq \bigcup_{k=1}^{n} S_k \tag{6.27}$$

where n is the number of elements and the mesh (union of elements) does not usually coincide with S. Equation (6.18) then takes the form

$$\frac{1}{2}\phi(\mathbf{x}) + \sum_{k=1}^{n} \int_{S_k} \phi(\mathbf{y}) \, q^*(\mathbf{x}, \mathbf{y}) \, ds(\mathbf{y}) = \sum_{k=1}^{n} \int_{S_k} \phi^*(\mathbf{x}, \mathbf{y}) \, \mathbb{A}^n(\mathbf{y}) \, ds(\mathbf{y}). \tag{6.28}$$

(a) *Original boundary.*   (b) *Meshed boundary.*

Figure 6.4: *Discretization of the boundary*

A second approximation is considered now on the variation of the potential, a constant BEM will be used, such that ϕ is the same over the whole element

$$\phi(\mathbf{y}) = \phi_k \qquad \forall \mathbf{y} \in S_k. \tag{6.29}$$

A similar estimation can be applied to the derivatives of the potential and the value taken

---

[1] Symmetric BEM formulations have been proved able to handle topologies with openings in EEG simulations [114].

for every element is that evaluated at its centre, although this is not strictly necessary since the derivative is generally known over the element

$$\mathbb{A}^n(\mathbf{y}) = \mathbb{A}_k^n \qquad \forall \mathbf{y} \in S_k. \tag{6.30}$$

Hence if the collocation point belongs to the lth-element, $\mathbf{x} \in S_l$, it follows that

$$\frac{1}{2}\phi_l + \sum_{k=1}^n \phi_k \int_{S_k} q^*(\mathbf{x}, \mathbf{y})\, ds(\mathbf{y}) = \sum_{k=1}^n \mathbb{A}_k^n \int_{S_k} \phi^*(\mathbf{x}, \mathbf{y})\; ds(\mathbf{y}). \tag{6.31}$$
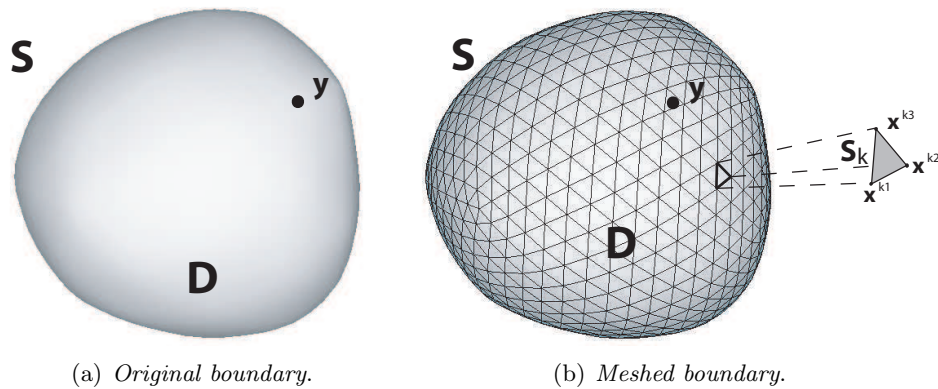
By taking the collocation point at every element (it is placed at the barycentre of the triangle) we can generate the following system of equations

$$\mathcal{H}\mathbf{\Phi} = \mathcal{G}\mathcal{A} \tag{6.32}$$

or equivalently

$$\sum_{k=1}^n \mathcal{H}(l, k)\phi_k = \sum_{k=1}^n \mathcal{G}(l, k)\mathbb{A}_k^n \tag{6.33}$$

$$l = 1, ..., n$$

where

$$\mathcal{H}(l, k) = \frac{1}{2}\, \delta_{l,k} + \int_{S_k} q^*(\boldsymbol{x}_l, \mathbf{y})ds(\mathbf{y}) \tag{6.34}$$

$$\mathcal{G}(l, k) = \int_{S_k} \phi^*(\boldsymbol{x}_l, \mathbf{y})ds(\mathbf{y}) \tag{6.35}$$

also $\mathcal{A}$ and $\mathbf{\Phi}$ are n-dimensional vectors containing $\mathbb{A}^n$ and the unknown potential at every element. It is interesting to point out that the coefficients $\mathcal{H}(l, k)$ and $\mathcal{G}(l, k)$ do not depend on the boundary conditions, and their values are defined completely by the geometry of the element.

By solving this system of equations we find the values of the potential at the surface, but first the $\mathcal{H}$ and $\mathcal{G}$ matrices must be computed. The difficulty in the calculation of the matrix coefficients depends, in general, on whether the collocation point belongs ($l = k$) or not ($l \neq k$) to the element where the integral is evaluated.

Off diagonal coefficients of the BEM matrices

When $l \neq k$ the collocation point does not belong to the element where the integration is performed, $\boldsymbol{x}_l \notin S_k$, and therefore we avoid the singular behaviour of the integral kernels (ϕ^* and q^*).

Although an analytical approach could be used for simple geometries the standard approach to evaluating the integrals of both, $\mathcal{H}(l, k)$ and $\mathcal{G}(l, k)$, is Gauss quadrature over a triangle.

Diagonal coefficients of the BEM matrices

When the collocation point lies on the element ($\boldsymbol{x}_l \in S_k \Rightarrow l = k$), the presence of singularities due to the functions ϕ^* and q^* necessitates the use of higher integration techniques. Next we therefore propose numerical approaches for each coefficient.

Singular double layer: $\mathcal{H}(l, l)$

In this case fortunately we do not have to deal with numerical integrations, because the double layer kernel vanishes

$$q^* = \nabla\phi^* \cdot \mathbf{n} = \frac{1}{4\pi r^3}(\mathbf{x} - \mathbf{y}) \cdot \mathbf{n} = 0 \tag{6.36}$$

since $(\mathbf{x} - \mathbf{y})$ and $\mathbf{n}$ are perpendicular in a flat triangle.

Hence the diagonal elements of the matrix $\mathcal{H}$ are

$$\mathcal{H}(l, l) = \frac{1}{2} \qquad l = 1, ..., n \tag{6.37}$$

Singular single layer: $\mathcal{G}(l, l)$

The integrand becomes unbounded as $\mathbf{y} \to \mathbf{x}$ because the integral exhibits a weak singularity [63] that can be handled with special numerical quadratures [117][118] or analytical integration [119]. The latter approach has been preferred here followed by a standard Gauss quadrature.

By using the singular point $\mathbf{x}$ placed at the centre of the element and the vertices, $\mathbf{x}^{ka}, \mathbf{x}^{kb}$ and $\mathbf{x}^{kc}$, we divide the triangle, S_l, into three smaller flat triangles, $S_l = \bigcup_{\alpha=1}^3 S_l^\alpha$, as shown in Fig.6.5.

The single layer coefficient is then given by the sum of the integrals over three sub-triangles, each having a singular vertex

$$\mathcal{G}(l, l) = \sum_{\alpha=1}^3 \mathcal{I}_l^\alpha \tag{6.38}$$
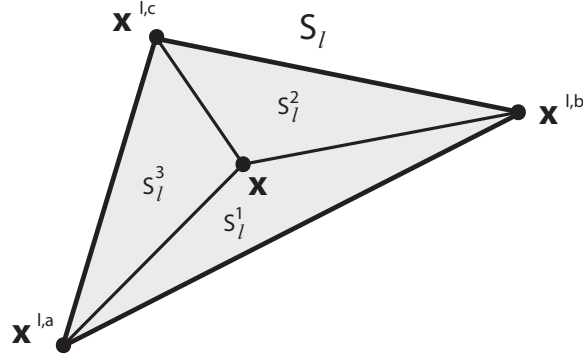
Figure 6.5: *Division of a singular element through its barycentre.*

where

$$\mathcal{I}_l^\alpha = \int_{S_l^\alpha} \phi^*(\boldsymbol{x}_l, \mathbf{y}) \, ds(\mathbf{y}) = \frac{1}{4\pi} \int_{S_l^\alpha} \frac{1}{|\mathbf{x} - \mathbf{y}|} \, ds(\mathbf{y})$$

$$\alpha = 1, 2, 3.$$

(6.39)

A common approach can be used to evaluate those integrals. It is illustrated in the following for the case where the first vertex of the sub-triangle is the singular point, we note $\mathbf{x}_1 = \mathbf{x}$. We begin by performing a coordinate transformation to map the triangle into the 2-D parametric space, where the singular point is placed at the origin of the parametric or oblique coordinates as schematically shown in Fig. 6.6. The required coordinate change is described by the following expressions

$$\mathbf{y} = \mathbf{x}_1(1 - \xi - \eta) + \mathbf{x}_2\xi + \mathbf{x}_3\eta$$

(6.40)

where $\mathbf{y}$ is a point in the triangle, the coordinates of the vertices are $\mathbf{x}_i$ with $i = 1, 2, 3$ and $\xi, \eta \in [0, 1]$.

By using this parametrization Eq. 6.39 can be expressed as

$$\mathcal{I}_l^\alpha = \frac{J(\xi, \eta)}{4\pi |\mathbf{x}_2 - \mathbf{x}_1|} \int_0^1 \int_0^{1-\xi} \frac{d\xi \, d\eta}{\sqrt{\xi^2 + 2B\xi\eta + C\eta^2}}$$

(6.41)

where $J(\xi, \eta)$ is the surface metric or Jacobian (for a flat triangle it is equal to the area of the element) and

$$B = \frac{(\mathbf{x}_3 - \mathbf{x}_1) \cdot (\mathbf{x}_2 - \mathbf{x}_1)}{|\mathbf{x}_2 - \mathbf{x}_1|^2}, \qquad C = \frac{|\mathbf{x}_3 - \mathbf{x}_1|^2}{|\mathbf{x}_2 - \mathbf{x}_1|^2}.$$

(6.42)
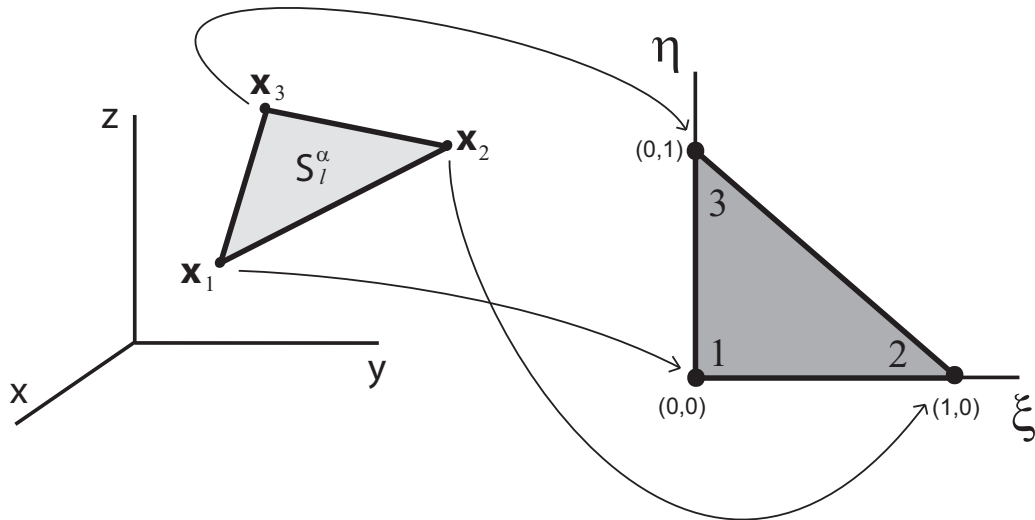
Figure 6.6: *Parametric transformation.*

Next we adopt polar coordinates

$$\xi = \rho \cos(\chi)$$
$$\eta = \rho \sin(\chi)$$

(6.43)

and the weakly singular integral then becomes regular [120]

$$\mathcal{I}_l^\alpha = \frac{J(\xi, \eta)}{4\pi |\mathbf{x}_2 - \mathbf{x}_1|} \int_0^{\frac{\pi}{2}} \frac{R(\chi)}{\sqrt{\cos^2(\chi) + B \sin(2\chi) + C \sin^2(\chi)}} \, d\chi$$

(6.44)

where

$$R(\chi) = \frac{1}{\cos(\chi) + \sin(\chi)}$$

(6.45)

and the resulting integral can be easily calculated using Gauss-Legendre quadrature.

6.4.1   Potential in the Domain

We have just seen how to compute the matrices in Eq. 6.32. The solution of this system of equations which can be found by simple Gauss elimination is the potential at the boundary (ϕ_k) which, as was previously stated, is enough information to find the potential at any point inside the domain.

If we discretize the integral representation Eq. 6.17, and adopt a constant BEM approxi-
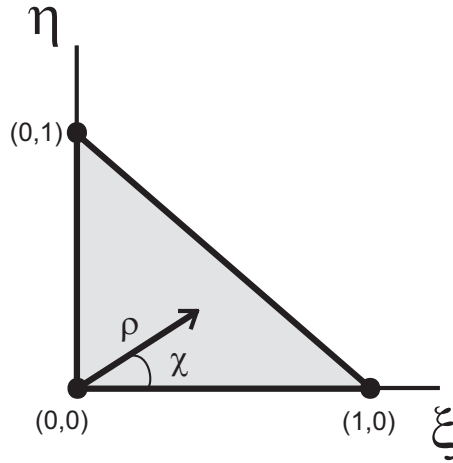
Figure 6.7: *Plane polar coordinates in the parametric space.*

mation we find by simple manipulations

$$\phi(\mathbf{z}) = \sum_{k=1}^{n} \mathbb{A}_k^n \int_{S_k} \phi^*(\mathbf{z}, \mathbf{y}) \, ds(\mathbf{y}) - \sum_{k=1}^{n} \phi_k \int_{S_k} q^*(\mathbf{z}, \mathbf{y}) \, ds(\mathbf{y}) \tag{6.46}$$

$$\mathbf{z} \in D.$$

This expression can be written in the following form

$$\phi(\mathbf{z}) = \sum_{k=1}^{n} \mathbb{A}_k^n \mathcal{G}_k^*(\mathbf{z}) - \sum_{k=1}^{n} \phi_k \mathcal{H}_k^*(\mathbf{z}) \tag{6.47}$$

where

$$\mathcal{H}_k^*(\mathbf{z}) = \int_{S_k} q^*(\mathbf{z}, \mathbf{y}) \, ds(\mathbf{y}) \tag{6.48}$$

$$\mathcal{G}_k^*(\mathbf{z}) = \int_{S_k} \phi^*(\mathbf{z}, \mathbf{y}) \, ds(\mathbf{y}). \tag{6.49}$$

The integrals in these coefficients are well-behaved since $\mathbf{z}$ falls inside the domain and $\mathbf{y}$ at the surface, and they can therefore be evaluated with a standard Gauss technique. Hence the potential at the point $\mathbf{z}$ can be easily found since $\mathbb{A}_k^n$ and ϕ_k are known.

A known disadvantage in BEM is the precision drop when $\mathbf{z}$ is close to the boundary. More precisely our domain approach yields erroneous information when the distance from $\mathbf{z}$ to any point at the boundary is comparable to the size of the element. To illustrate this

fact, let us consider a constant potential then Eq. 6.47 becomes[2]

$$\sum_{k=1}^{n} \mathcal{H}_k^*(\mathbf{z}) = -1 \tag{6.50}$$

where $\mathbf{z} \in D$. Figure 6.8 shows $\sum_{k=1}^{n} \mathcal{H}_k^*(\mathbf{z})$ for points on the z-axis in a sphere of unit radius which was meshed with 224 elements of a characteristic size d
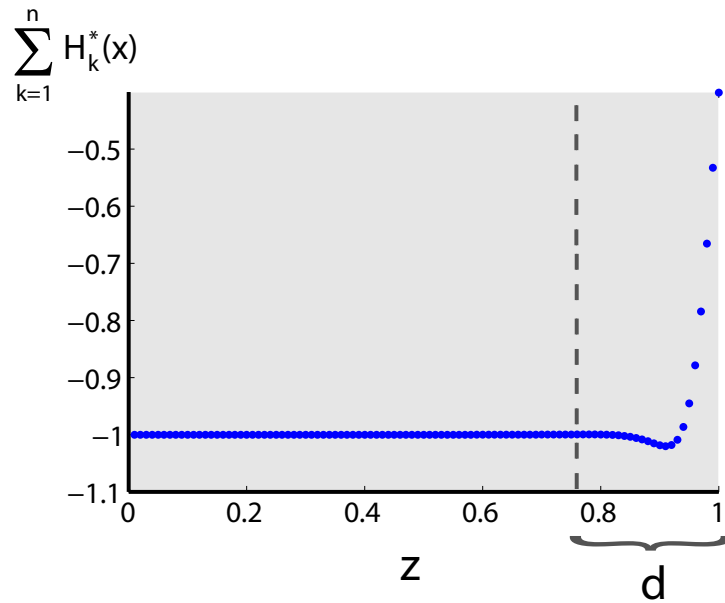
Figure 6.8: *Values of $\sum_{k=1}^{n} \mathcal{H}_k^*$ for points lying on the radius with direction OZ for a sphere of 224 elements.*

It can be appreciated how the accuracy starts to decrease when the distance to the surface is the order of d. Precisely, for this case of spherical domain we can get information till a distance a bit more than half of the characteristic size d, and $\sum_{k=1}^{n} \mathcal{H}_k^*$ deviates more than a 20% from its ideal value a distance to the boundary of $0.25d$.

To improve the evaluation of the potential at a point close to the boundary a domain subdivision or an algorithm to evaluate near singular integrals can be used.

---

[2] This identity is independent of the choice of potential and is satisfied for all constant approaches.

6.4.2 Electric field in the Domain

We can find the gradient of the scalar potential by discretization of Eq. 6.19, and obtain

$$\frac{\partial \phi}{\partial z_i}(\mathbf{z}) = \sum_{k=1}^{n} \mathbb{A}_k^n \int_{S_k} \frac{\partial \phi^*}{\partial x_i}(\mathbf{z}, \mathbf{y}) \ ds(\mathbf{y}) - \sum_{k=1}^{n} \phi_k \int_{S_k} \frac{\partial q^*}{\partial x_i}(\mathbf{z}, \mathbf{y}) \ ds(\mathbf{y})$$

$$\mathbf{z} \in D, \qquad i = 1, 2, 3. \tag{6.51}$$

which we can rewrite as

$$\frac{\partial \phi}{\partial x_i}(\mathbf{z}) = \sum_{k=1}^{n} \mathbb{A}_k^n \mathcal{C}_k^{*,i}(\mathbf{z}) - \sum_{k=1}^{n} \phi_k \mathcal{D}_k^{*,i}(\mathbf{z})$$

$$\mathbf{z} \in D, \qquad i = 1, 2, 3. \tag{6.52}$$

where

$$\mathcal{C}_k^{*,i}(\mathbf{z}) = \int_{S_k} \frac{\partial \phi^*}{\partial z_i}(\mathbf{z}, \mathbf{y}) \ ds(\mathbf{y}) \tag{6.53}$$

$$\mathcal{D}_k^{*,i}(\mathbf{z}) = \int_{S_k} \frac{\partial q^*}{\partial z_i}(\mathbf{z}, \mathbf{y}) \ ds(\mathbf{y}). \tag{6.54}$$

Following the same reasoning from the foregoing section, the value of the gradient of the scalar potential can be evaluated in a straightforward fashion since all the integrals are regular and can be computed with Gauss quadrature. The accuracy of this equation drops near to the surface.

Finally, to find the electric field we have to add the contribution of the magnetic component

$$E_i(\mathbf{z}) = \mathbb{A}_i(\mathbf{z}) - \sum_{k=1}^{n} \left[\mathbb{A}_k^n \mathcal{C}_k^{*,i}(\mathbf{z}) + \phi_k \mathcal{D}_k^{*,i}(\mathbf{z}) \right]$$

$$\mathbf{z} \in D, \qquad i = 1, 2, 3. \tag{6.55}$$

6.4.3 Electric field at the boundary

In a similar way an expression for the gradient of ϕ that is valid at the boundary can be derived by discretization of Eq. 6.25 . The resulting expression is

$$\frac{1}{2} \frac{\partial \phi}{\partial x_i}(\mathbf{x}) = \sum_{k=1}^{n} \mathbb{A}_k^n \int_{S_k} \frac{\partial \phi^*}{\partial x_i}(\mathbf{x}, \mathbf{y}) \ ds(\mathbf{y}) - \sum_{k=1}^{n} \phi_k \int_{S_k} \frac{\partial q^*}{\partial x_i}(\mathbf{x}, \mathbf{y}) \ ds(\mathbf{y})$$

$$\mathbf{x} \in S_l, \qquad i = 1, 2, 3. \tag{6.56}$$

which can be written as

$$\frac{1}{2}\frac{\partial \phi}{\partial x_i}(\mathbf{x}) = \sum_{k=1}^{n} \mathbb{A}_k^n \mathcal{C}_k^i(\mathbf{x}) - \sum_{k=1}^{n} \phi_k \mathcal{D}_k^i(\mathbf{x}) \tag{6.57}$$

$$\mathbf{x} \in S_l, \qquad i = 1, 2, 3.$$

where

$$\mathcal{C}_k^i(\mathbf{x}) = \int_{S_k} \frac{\partial \phi^*}{\partial x_i}(\mathbf{x}, \mathbf{y}) \, ds(\mathbf{y}) \tag{6.58}$$

$$\mathcal{D}_k^i(\mathbf{x}) = \int_{S_k} \frac{\partial q^*}{\partial x_i}(\mathbf{x}, \mathbf{y}) \, ds(\mathbf{y}), \tag{6.59}$$

note that since $\mathbf{x} \in S_l$ we could have used $\frac{\partial \phi}{\partial x_i}(\mathbf{x}) = \frac{\partial \phi_l}{\partial x_i}$ since it is considered constant over the element.

The calculation of these integrals is not trivial whenever the source point falls on the element since, $\mathcal{C}_k^i$ has a strong singularity (of order $1/r$), whereas a hyper-singularity exists in $\mathcal{D}_k^i$ (of order $1/r^2$). Methods for the direct evaluation of these integrals are presented in the following subsections.

If $\mathbf{x} \notin S_k$ the integral is regular and can be performed by standard techniques.

Hyper-singular integral $\mathcal{D}_k^i$

Although semi-analytical methods are available [121], we choose what is called a *rigid body motion* argument,i.e., if we consider the collocation point localized at the pth-element and a constant potential over the boundary in Eq. 6.57 then

$$\sum_{k=1}^{n} \mathcal{D}_k^i(\mathbf{x}_p) = 0 \tag{6.60}$$

$$\mathbf{x} \in S_p$$

this identity is purely geometric since the coefficients do not depend on the potential, and it is satisfied in all the cases. Therefore the hyper-singular coefficient can be found by computing the remaining coefficients

$$\mathcal{D}_p^i(\mathbf{x}_p) = -\sum_{\substack{k=1 \\ k \neq p}}^{n} \mathcal{D}_k^i(\mathbf{x}_p). \tag{6.61}$$

It should be pointed out that this result is independent of the evolution of the potential in the element, and is satisfied for any flat triangle.

Strong singular integral $\mathcal{C}_k^i$

The method used here to deal with the coefficient $\mathcal{C}_k^i$ has been taken from Guiggiani's paper [122].

First we operate as in Section 6.4 by using the singular point $\mathbf{x}$ placed at the barycentre of the element to divide it into three sub triangles as is shown in Fig. 6.5. Then[3]

$$\mathcal{C}_k^i(\mathbf{x}) = \sum_{\alpha=1}^{3} \int_{S_k^\alpha} \frac{\partial \phi^*}{\partial x_i}(\mathbf{x}, \mathbf{y}) \, ds(\mathbf{y}) = -\frac{1}{4\pi} \sum_{\alpha=1}^{3} \int_{S_k^\alpha} \frac{x_i - y_i}{r^3} \, ds(\mathbf{y}) = -\frac{1}{4\pi} \sum_{\alpha=1}^{3} \mathcal{I}_i^\alpha \qquad (6.62)$$

$$\mathbf{x} \in S_k$$

The integration technique over these triangles, S_k^α, is equivalent, as each of them have a singularity at one of their vertices, so we will analyze as an example only the case where the singular point lies at the first vertex ($\mathbf{x} = \mathbf{x}_1$).

Next it is convenient to introduce a suitable parametric representation (see Fig. 6.6)

$$\mathbf{y} = \mathbf{x}_1(1 - \xi - \eta) + \mathbf{x}_2\xi + \mathbf{x}_3\eta \qquad (6.63)$$

it then follows that

$$\mathcal{I}_i^\alpha = \int_{S_k^\alpha} \frac{x_i - y_i}{r^3} \, ds(\mathbf{y}) = J(\xi, \eta) \int_0^1 \int_0^{1-\xi} \frac{x_i - y_i(\xi, \eta)}{r^3(\xi, \eta)} \, d\xi \, d\eta. \qquad (6.64)$$

Let us now perform another transformation to polar coordinates centered at the image of the singular point, $\xi = \rho \cos(\chi)$ and $\eta = \rho \sin(\chi)$, as can be seen in Fig. 6.7. Thus

$$\mathcal{I}_i^\alpha = \int_0^{\frac{\pi}{2}} \int_0^{R(\chi)} F_i(\rho, \chi) \, d\rho \, d\chi \qquad (6.65)$$

where

$$R(\chi) = \frac{1}{\cos(\chi) + \sin(\chi)} \qquad (6.66)$$

and

$$F_i(\rho, \chi) = J(\xi, \eta) \frac{x_i - y_i(\rho, \chi)}{r^3(\rho, \chi)} \rho. \qquad (6.67)$$

---

[3]In most texts this type of integral is noted as $\fint$ to indicate that it should be taken in the Cauchy principal value sense [63].

Since $\mathbf{x}_1 = \mathbf{x}$ we also know that

$$x_i^1 - y_i = \rho \Big[\cos(\chi)(x_i^1 - x_i^2) + \sin(\chi)(x_i^1 - x_i^3) \Big] = \rho A_i(\chi) \tag{6.68}$$

so we can define

$$A(\chi) = [\sum_{i=1}^{3} A_i^2(\chi)]^{\frac{1}{2}} \tag{6.69}$$

then for flat elements

$$F_i(\rho, \chi) = \frac{J(\xi, \eta)}{\rho} \frac{A_i(\chi)}{A^3(\chi)} \tag{6.70}$$

and finally by asymptotic study it can be demonstrated that

$$\mathcal{I}_i^\alpha = J(\xi, \eta) \int_0^{\frac{\pi}{2}} \frac{A_i(\chi)}{A^3(\chi)} \ln \Big[R(\chi) A(\chi) \Big] \, d\chi \tag{6.71}$$

which can be more conveniently computed using standard one-dimensional, logarithmic Gaussian quadrature formulae [123].

6.5 Integral formulation for Poisson's Equation. Single Domain

Poisson's equation governs some of the problems we want to study as described in Chapter 5. In this chapter we illustrate a constant BEM for this differential equation which presents similarities with regard to the solution of Laplace's equation. So as to avoid extensive duplication we focus mainly on the differences between the approaches.

Let ϕ be the scalar potential that obeys Poisson's equation in a homogeneous, bounded volume domain, D

$$\nabla^2 \phi(\mathbf{z}) = b(\mathbf{z}) \tag{6.72}$$

By using Green's second identity we obtain

$$\int_D \left(\phi(\mathbf{y}) \nabla^2 \phi^*(\mathbf{z}, \mathbf{y}) - \phi^*(\mathbf{z}, \mathbf{y}) \nabla^2 \phi(\mathbf{y}) \right) d^3 y$$
$$= \int_S \left[\phi(\mathbf{y}) \, q^*(\mathbf{z}, \mathbf{y}) - \phi^*(\mathbf{z}, \mathbf{y}) \, q(\mathbf{y}) \right] ds(\mathbf{y}) \tag{6.73}$$
$$\mathbf{z} \in D \bigcup S, \ \mathbf{y} \in S.$$

Making use of Eq. 6.72 and performing a suitable limit process, it follows that

$$c(\mathbf{z})\phi(\mathbf{z}) = \int_S \left[\phi^*(\mathbf{z}, \mathbf{y}) \, q(\mathbf{y}) - \phi(\mathbf{y}) \, q^*(\mathbf{z}, \mathbf{y}) \right] ds(\mathbf{y}) - \int_D \phi^*(\mathbf{z}, \mathbf{y}) b(\mathbf{y}) \, d^3 y$$
$$\mathbf{z} \in D, \ \mathbf{y} \in S \tag{6.74}$$

where the geometric coefficient $c(\mathbf{x})$ has the usual meaning (Eq. 6.14). The structure of this equation is analogous to that obtained when considering Laplace's equation. However Eq. 6.74 differs through the presence of an inconvenient domain integral, resulting from the source term, $b(\mathbf{x})$. As we need all the integrals in the equation to be defined over the boundary to perform the BEM derivation we must express the domain integral as an equivalent surface integral to overcome this drawback.

Let us study the source term $b(\mathbf{z})$, which is related to the free charge density which occurs for rotation of the system with certain field arrangements

$$b(\mathbf{z}) = -\frac{\rho(\mathbf{z})}{\epsilon_0}. \tag{6.75}$$

An important property of $b(\mathbf{z})$ is that it is a harmonic function, as can be seen by expressing the charge density in terms of the magnetic induction and the angular velocity

$$b(\mathbf{z}) = 2\boldsymbol{\omega} \cdot \mathbf{B}(\mathbf{z}) \tag{6.76}$$

then

$$\nabla^2[\rho(\mathbf{z})] = 2\nabla^2[\boldsymbol{\omega} \cdot \mathbf{B}(\mathbf{z})] = 0 \tag{6.77}$$

as all the components of $\mathbf{B}$ are harmonic as well. Therefore $b(\mathbf{z})$ satisfies Laplace's equation, a fact that will allow us to transform the volume integral. It can be proved by a convenient

use once again of Green's theorem that

$$
\begin{aligned}
&\int_D \left(b(\mathbf{y})\nabla^2\omega^*(\mathbf{z},\mathbf{y}) - \omega^*(\mathbf{z},\mathbf{y})\nabla^2 b(\mathbf{y}) \right) d^3 y \\
&= \int_S \left[b(\mathbf{y})\frac{\partial\omega^*}{\partial n}(\mathbf{z},\mathbf{y}) - \omega^*(\mathbf{z},\mathbf{y})\frac{\partial b(\mathbf{y})}{\partial n} \right] ds(\mathbf{y}) \\
&\qquad\qquad\qquad \mathbf{z} \in D,\ \mathbf{y} \in S
\end{aligned}
\tag{6.78}
$$

where

$$
\omega^*(\mathbf{z},\mathbf{y}) = \frac{1}{8\pi}\ r, \qquad \frac{\partial\omega^*}{\partial n}(\mathbf{z},\mathbf{y}) = -\sum_{j=1}^{3} \frac{z_j - y_j}{8\pi r}\ n_j
\tag{6.79}
$$

and the main advantage of using $\omega^*(\mathbf{z},\mathbf{y})$ is that

$$
\nabla^2\omega^*(\mathbf{z},\mathbf{y}) = \phi^*(\mathbf{z},\mathbf{y})
\tag{6.80}
$$

applying this equality in Eq. 6.78 gives

$$
\int_D \phi^*(\mathbf{z},\mathbf{y}) b(\mathbf{y})\ d^3 y = \int_S \left[b(\mathbf{y})\frac{\partial\omega^*}{\partial n}(\mathbf{z},\mathbf{y}) - \omega^*(\mathbf{z},\mathbf{y})\frac{\partial b(\mathbf{y})}{\partial n} \right] ds(\mathbf{y})
\tag{6.81}
$$

which is the desired result that expresses the domain integral in terms of two surface integrals. This idea establishes the basis of the so-called dual reciprocity method in BEM [124]. It is worth stressing that the last equation is valid even for the case that $\mathbf{z}$ lies on the boundary $(\mathbf{z}{\to}\mathbf{x})$, because ω^* is a continuous function and $\frac{\partial\omega^*}{\partial n}$ is also well-behaved on the surface.

If we make use of this last result and apply the boundary conditions, Eq. 6.74 now takes the form

$$
\begin{aligned}
c(\mathbf{z})\ \phi(\mathbf{z}) = {}&\int_S \phi^*(\mathbf{z},\mathbf{y})\ \mathbb{A}^n(\mathbf{y}\ ds(\mathbf{y}) - \int_S \phi(\mathbf{y})\ q^*(\mathbf{z},\mathbf{y})\ ds(\mathbf{y}) \\
&-\int_S b(\mathbf{y})\ \frac{\partial\omega^*}{\partial n}(\mathbf{z},\mathbf{y})\ ds(\mathbf{y}) + \int_S \omega^*(\mathbf{z},\mathbf{y})\ \frac{\partial b(\mathbf{y})}{\partial n}\ ds(\mathbf{y}).
\end{aligned}
\tag{6.82}
$$

Domain Integral Representation of the Potential

Let us study the case where $\mathbf{z}$ belongs to the interior of the domain. Equation 6.82 then becomes

$$
\begin{aligned}
\phi(\mathbf{z}) = & \int_S \phi^*(\mathbf{z}, \mathbf{y}) \, \mathbb{A}^n(\mathbf{y}) \, ds(\mathbf{y}) - \int_S \phi(\mathbf{y}) \, q^*(\mathbf{z}, \mathbf{y}) \, ds(\mathbf{y}) \\
& - \int_S b(\mathbf{y}) \, \frac{\partial \omega^*}{\partial n}(\mathbf{z}, \mathbf{y}) \, ds(\mathbf{y}) + \int_S \omega^*(\mathbf{z}, \mathbf{y}) \, \frac{\partial b(\mathbf{y})}{\partial n} \, ds(\mathbf{y})
\end{aligned}
\tag{6.83}
$$

Again we must to solve a Fredholm integral equation of the second kind, which involves similar single layer and double layer potentials to those found in solving Laplace's equation, plus two integrals with known kernels.

Boundary Integral Representation of the Potential

If the collocation point lies on the boundary $(\mathbf{z} \to \mathbf{x} \in S)$, we obtain

$$
\begin{aligned}
\frac{1}{2} \, \phi(\mathbf{x}) = & \int_S \phi^*(\mathbf{x}, \mathbf{y}) \, \mathbb{A}^n(\mathbf{y}) \, ds(\mathbf{y}) - \int_S \phi(\mathbf{y}) \, q^*(\mathbf{x}, \mathbf{y}) \, ds(\mathbf{y}) \\
& - \int_S b(\mathbf{y}) \, \frac{\partial \omega^*}{\partial n}(\mathbf{x}, \mathbf{y}) \, ds(\mathbf{y}) + \int_S \omega^*(\mathbf{x}, \mathbf{y}) \, \frac{\partial b(\mathbf{y})}{\partial n} \, ds(\mathbf{y}).
\end{aligned}
\tag{6.84}
$$

Domain Integral Representation of the Electric Field

The gradient of the scalar potential is found by differentiating Eq. 6.83 with respect to the coordinates of $\mathbf{z} = (z_1, z_2, z_3)$.

$$
\begin{aligned}
\frac{\partial \phi}{\partial z_j}(\mathbf{z}) = & \int_S \left[\frac{\partial \phi^*}{\partial z_j}(\mathbf{z}, \mathbf{y}) \mathbb{A}^n(\mathbf{y}) - \frac{\partial q^*}{\partial z_j}(\mathbf{z}, \mathbf{y}) \, \phi(\mathbf{y}) \right] ds(\mathbf{y}) \\
& - \int_S b(\mathbf{y}) \frac{\partial^2 \omega^*}{\partial n \, \partial z_i}(\mathbf{z}, \mathbf{y}) \, ds(\mathbf{y}) + \int_S \frac{\partial \omega^*}{\partial z_i}(\mathbf{z}, \mathbf{y}) \frac{\partial b(\mathbf{y})}{\partial n} \, ds(\mathbf{y})
\end{aligned}
\tag{6.85}
$$

$$
\mathbf{z} \in D.
$$

So the electric field is given by

$$E_j(\mathbf{z}) = \mathbb{A}_j(\mathbf{z}) - \int_S \left[\frac{\partial \phi^*}{\partial z_j}(\mathbf{z}, \mathbf{y}) \mathbb{A}^n(\mathbf{y}) - \frac{\partial q^*}{\partial z_j}(\mathbf{z}, \mathbf{y}) \; \phi(\mathbf{y}) \right] ds(\mathbf{y})$$

$$- \int_S b(\mathbf{y}) \frac{\partial^2 \omega^*}{\partial n \; \partial z_i}(\mathbf{z}, \mathbf{y}) \; ds(\mathbf{y}) - \int_S \frac{\partial \omega^*}{\partial z_i}(\mathbf{z}, \mathbf{y}) \frac{\partial b(\mathbf{y})}{\partial n} \; ds(\mathbf{y})$$

$$\mathbf{z} \in D. \tag{6.86}$$

where

$$\frac{\partial^2 \omega^*}{\partial n \; \partial x_i}(\mathbf{z}, \mathbf{y}) = -\frac{1}{8\pi} \left[\frac{\delta_{i,j}}{r} - \frac{(z_j - y_j)(z_i - y_i)}{r^3} \right] n_j \tag{6.87}$$

and

$$\frac{\partial \omega^*}{\partial z_i}(\mathbf{z}, \mathbf{y}) = \frac{1}{8\pi} \frac{(z_i - y_i)}{r}. \tag{6.88}$$

Boundary Integral Representation of the Electric Field

For a rigorous derivation of the gradient of the scalar potential we again make the interior point $\mathbf{z} \in D$ tend to the surface, $\mathbf{z} \to \mathbf{x} \in S$, and take into account the jump properties of the directional derivative of the surface potentials

$$\frac{1}{2} \frac{\partial \phi}{\partial z_j}(\mathbf{z}) = \int_S \left[\frac{\partial \phi^*}{\partial z_j}(\mathbf{z}, \mathbf{y}) \mathbb{A}^n(\mathbf{y}) - \frac{\partial q^*}{\partial z_j}(\mathbf{z}, \mathbf{y}) \; \phi(\mathbf{y}) \right] ds(\mathbf{y})$$

$$- \int_S b(\mathbf{y}) \frac{\partial^2 \omega^*}{\partial n \; \partial z_i}(\mathbf{z}, \mathbf{y}) \; ds(\mathbf{y}) + \int_S \frac{\partial \omega^*}{\partial z_i}(\mathbf{z}, \mathbf{y}) \frac{\partial b(\mathbf{y})}{\partial n} \; ds(\mathbf{y})$$

$$\mathbf{z} \in D. \tag{6.89}$$

So the electric field is given by

$$E_j(\mathbf{z}) = \mathbb{A}_j(\mathbf{z}) - 2 \int_S \left[\frac{\partial \phi^*}{\partial z_j}(\mathbf{z}, \mathbf{y}) \mathbb{A}^n(\mathbf{y}) - \frac{\partial q^*}{\partial z_j}(\mathbf{z}, \mathbf{y}) \; \phi(\mathbf{y}) \right] ds(\mathbf{y})$$

$$+ 2 \int_S \left[b(\mathbf{y}) \frac{\partial^2 \omega^*}{\partial n \; \partial z_i}(\mathbf{z}, \mathbf{y}) - \frac{\partial \omega^*}{\partial z_i}(\mathbf{z}, \mathbf{y}) \frac{\partial b(\mathbf{y})}{\partial n} \right] ds(\mathbf{y})$$

$$\mathbf{z} \in D. \tag{6.90}$$

6.6 Constant BEM for Poisson's equation. Single Domain

Once we have derived the boundary integral representation, we proceed to the discretization of the integrals by triangulation of the surface into flat elements, followed by the approximation of constant potentials over the triangle. Equation 6.84 then becomes

$$
\begin{aligned}
\frac{1}{2}\phi(\mathbf{x}) + \sum_{k=1}^{n} \phi_k \int_{S_k} q^*(\mathbf{x}, \mathbf{y})\ ds(\mathbf{y}) &= \sum_{k=1}^{n} \mathbb{A}_k^n \int_{S_k} \phi^*(\mathbf{x}, \mathbf{y}) \\
- \sum_{k=1}^{n} b_k \int_{S_k} \frac{\partial \omega^*}{\partial n}(\mathbf{x}, \mathbf{y})\ ds(\mathbf{y}) &+ \sum_{k=1}^{n} \frac{\partial b_k}{\partial n} \int_{S_k} \omega^*(\mathbf{x}, \mathbf{y})\ ds(\mathbf{y})
\end{aligned}
\tag{6.91}
$$

where b_k and $\frac{\partial b_k}{\partial n}$ are the values of the source function and its normal derivatives at the centre of the element.

If the collocation point is taken at every element and the notation and coefficients defined in section 6.4 are used, Eq. 6.84 yields

$$
\sum_{k=1}^{n} \mathcal{H}(l, k)\phi(k) = \sum_{k=1}^{n} \left[\mathcal{G}(l, k)\mathbb{A}_k^n - \mathcal{R}^1(l, k)b_k + \mathcal{R}^2(l, k)\frac{\partial b_k}{\partial n} \right]
\tag{6.92}
$$

$$
l = 1, ..., n
$$

where

$$
\mathcal{R}^1(l, k) = \int_{S_k} \frac{\partial \omega^*}{\partial n}(\mathbf{x}_l, \mathbf{y})\ ds(\mathbf{y})
\tag{6.93}
$$

$$
\mathcal{R}^2(l, k) = \int_{S_k} \omega^*(\mathbf{x}_l, \mathbf{y})\ ds(\mathbf{y}).
\tag{6.94}
$$

The evaluation of single and double layer potential coefficients has already been described, and the new coefficients can be easily found by Gauss quadrature. We can then produce a system of equations that yields the value of ϕ at every element.

6.6.1 Potential in the Domain

An expression that describes the potential in the domain can be produced by simple discretization of the domain representation

$$
\phi(\mathbf{z}) = \sum_{k=1}^{n} \left[\mathbb{A}_k^n \mathcal{G}_k^*(\mathbf{z}) - \phi_k \mathcal{H}_k^*(\mathbf{z}) - \mathcal{R}_k^{*,1}(\mathbf{z})b_k + \mathcal{R}_k^{*,2}(\mathbf{z})\frac{\partial b_k}{\partial n} \right]
\tag{6.95}
$$

$$
\mathbf{z} \in D
$$

where

$$\mathcal{R}_k^{*,1}(\mathbf{z}) = \int_{S_k} \frac{\partial \omega^*}{\partial n}(\mathbf{z}, \mathbf{y}) \, ds(\mathbf{y}) \tag{6.96}$$

$$\mathcal{R}_k^{*,2}(\mathbf{z}) = \int_{S_k} \omega^*(\mathbf{z}, \mathbf{y}) \, ds(\mathbf{y}). \tag{6.97}$$

6.6.2 Electric field in the Domain

The value of the gradient of the potential can be found by differentiating Eq. 6.95

$$\frac{\partial \phi}{\partial x_i}(\mathbf{z}) = \sum_{k=1}^{n} \left[\mathbb{A}_k^n \mathcal{C}_k^i(\mathbf{z}) - \phi_k \mathcal{D}_k^i(\mathbf{z}) - \mathcal{P}_{k,i}^{*,1}(\mathbf{z}) b_k + \mathcal{P}_{k,i}^{*,2}(\mathbf{z}) \frac{\partial b_k}{\partial n} \right] \tag{6.98}$$

$$\mathbf{z} \in D, \qquad i = 1, 2, 3.$$

where

$$\mathcal{P}_{k,i}^{*,1}(\mathbf{z}) = \int_{S_k} \frac{\partial^2 \omega^*}{\partial n \, \partial z_i}(\mathbf{z}, \mathbf{y}) \, ds(\mathbf{y}), \tag{6.99}$$

$$\mathcal{P}_{k,i}^{*,2}(\mathbf{z}) = \int_{S_k} \frac{\partial \omega^*}{\partial z_i}(\mathbf{z}, \mathbf{y}) \, ds(\mathbf{y}). \tag{6.100}$$

For all the integrals that have to be computed the coefficients are regular and can be found by using Gauss quadrature. As a domain representation the validity of this equation drops near to the surface, as described in Section 6.4.1.

6.6.3 Electric field at the boundary

Following the parallelism with the Laplace's equation, we can produce an expression for the gradient of ϕ at the boundary

$$\frac{1}{2} \frac{\partial \phi}{\partial x_i}(\mathbf{x}) = \sum_{k=1}^{n} \left[\mathbb{A}_k^n \mathcal{C}_k^i(\mathbf{x}) - \phi_k \mathcal{D}_k^i(\mathbf{x}) - \mathcal{P}_{k,i}^1(\mathbf{x}) b_k + \mathcal{P}_{k,i}^2(\mathbf{x}) \frac{\partial b_k}{\partial n} \right] \tag{6.101}$$

$$\mathbf{x} \in S_l, \qquad i = 1, 2, 3.$$

where

$$\mathcal{P}_{k,i}^1(\mathbf{x}) = \int_{S_k} \frac{\partial^2 \omega^*}{\partial n \, \partial x_i}(\mathbf{x}, \mathbf{y}) \, ds(\mathbf{y}), \tag{6.102}$$

$$\mathcal{P}_{k,i}^2(\mathbf{x}) = \int_{S_k} \frac{\partial \omega^*}{\partial x_i}(\mathbf{x}, \mathbf{y}) \, ds(\mathbf{y}). \tag{6.103}$$

6.7 Integral formulation for Laplace's Equation. Multi Domain

The formalism established so far is valid for simple homogeneous connected regions, but in general the systems that we are interested in have a higher complexity. This section presents an extended formulation for a multi-compartment volume conductor (D) made of different homogeneous sub-domains (D_i) as a representation of a heterogeneous system. We shall only consider in the following formulation nested regions, although BEM can be used for more general topologies [114].
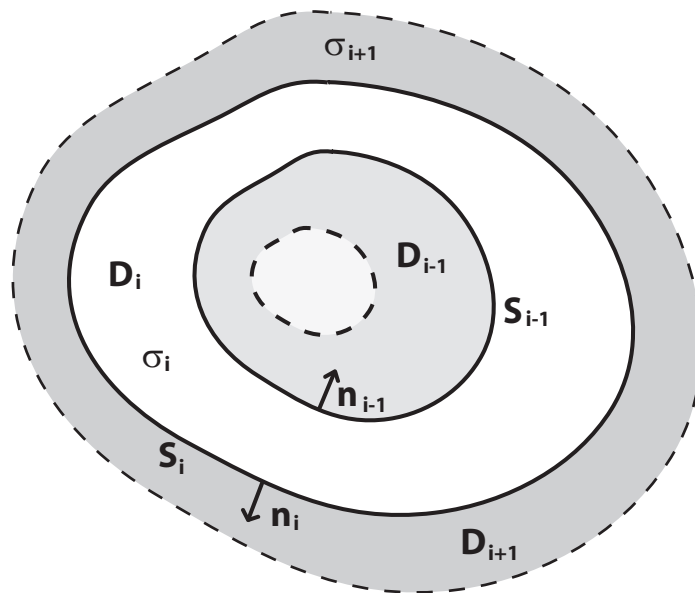
Figure 6.9: *System composed of M homogeneous domains.*

Consider a domain made of M sub-domains $D = \bigcup_k^M D_i$ inside any of which the potential satisfies Laplace equation. If Green's theorem is applied in the sub-domain D_i, it holds

$$
\begin{aligned}
c(\mathbf{z})\phi^i(\mathbf{z}) =& \int_{S_i} \Big[\phi^*(\mathbf{z},\mathbf{y})\ q^i(\mathbf{y}) - \phi^i(\mathbf{y})\ q^*(\mathbf{z},\mathbf{y})\Big] ds(\mathbf{y}) \\
&- \int_{S_{i-1}} \Big[\phi^*(\mathbf{z},\mathbf{y})\ q^i(\mathbf{y}) - \phi^i(\mathbf{y})\ q^*(\mathbf{z},\mathbf{y})\Big] ds(\mathbf{y})
\end{aligned}
\tag{6.104}
$$

where c($\mathbf{z}$) is function of the local geometry of $\mathbf{x}$, and its values away from the surfaces are easily found, whereas if the collocation point is placed at the boundary a suitable limit

process has to be applied

$$c(\mathbf{z}) = \begin{cases} 1, & if \quad \mathbf{z} \in D_i \\ \frac{1}{2}, & if \quad \mathbf{z} \in S_i \bigcup S_{i-1} \\ 0, & if \quad \mathbf{z} \notin D_i \bigcup S_i \bigcup S_{i-1} \end{cases} \tag{6.105}$$

The super-index in the potential and its derivative denotes the domain which it is evaluated in.

Note that we are dealing with nested regions bounded by two surfaces (except the first domain) where the normal vector is always outward (see Fig.6.9).

Equation 6.104 is going to be the base to derive the integrals representation, it is valid for $i = 1, ..., M$ and when $i = 1$ the integral over S_0 should be regarded as null.

Domain Integral Representation of the Potential

Let us evaluate Eq. 6.104 for every sub-domain, with the collocation point situated inside the pth-domain, $\mathbf{z} \in D_p$, and multiply by the conductivity in this region

$$\delta_{p,i} \ \sigma_i \phi^p(\mathbf{z}) = \int_{S_i} \sigma_i \Big[\phi^*(\mathbf{z},\mathbf{y}) \ q^i(\mathbf{y}) - \phi^i(\mathbf{y}) \ q^*(\mathbf{z},\mathbf{y})\Big] ds(\mathbf{y})$$
$$- \int_{S_{i-1}} \sigma_i \Big[\phi^*(\mathbf{z},\mathbf{y}) \ q^i(\mathbf{y}) - \phi^i(\mathbf{y}) \ q^*(\mathbf{z},\mathbf{y})\Big] ds(\mathbf{y}) \tag{6.106}$$
$$i = 1, ..., M.$$

Two unknown magnitudes, the potential and its derivative, are found in these expressions which are going to be used to derive an alternative and more appropriate equation for the application of the boundary conditions. If we combine Eq. 6.106 for every sub-domain, from $i = 1...M$, it yields

$$\sigma_p \ \phi^p(\mathbf{z}) = \sum_{i=0}^{M} \int_{S_i} \phi^*(\mathbf{z},\mathbf{y}) \Big[\sigma_i \ q^i(\mathbf{y}) - \sigma_{i+1} \ q^{i+1}(\mathbf{y})\Big] ds(\mathbf{y})$$
$$- \sum_{i=0}^{M} \int_{S_i} q^*(\mathbf{z},\mathbf{y}) \Big[\sigma_i \ \phi^i(\mathbf{y}) - \sigma_{i+1} \ \phi^{i+1}(\mathbf{y})\Big] ds(\mathbf{y}). \tag{6.107}$$

Again we must point out that all the variables with indexes zero must vanish, and indexes equal to $M + 1$ make reference to the surrounding air, therefore $\sigma_{M+1} = 0$.

We continue by applying boundary conditions (section 6.2)

$$(\sigma_{i+1} - \sigma_i)\mathbb{A}^n(\mathbf{y}) = \sigma_{i+1}q^{i+1}(\mathbf{y}) - \sigma_i q^i(\mathbf{y})$$
$$i = 1, ..., M \tag{6.108}$$

then Eq. 6.107 leads to

$$\sigma_p \, \phi^p(\mathbf{z}) = \sum_{i=0}^{M} \int_{S_i} \phi^*(\mathbf{z}, \mathbf{y}) \Big[(\sigma_i - \sigma_{i+1})\mathbb{A}^n(\mathbf{y}) \Big] ds(\mathbf{y})$$
$$- \sum_{i=0}^{M} \int_{S_i} q^*(\mathbf{z}, \mathbf{y}) \Big[\sigma_i \, \phi^i(\mathbf{y}) - \sigma_{i+1} \, \phi^{i+1}(\mathbf{y}) \Big] ds(\mathbf{y}) \tag{6.109}$$

but the scalar potential is continuous across the surface between media, that is

$$\phi^i(\mathbf{y}) = \phi^{i+1}(\mathbf{y}) = \phi(\mathbf{y}), \qquad \mathbf{y} \in S_i \tag{6.110}$$

so the domain integral representation takes the final form

$$\phi^p(\mathbf{z}) = \sum_{i=0}^{M} \frac{(\sigma_i - \sigma_{i+1})}{\sigma_p} \int_{S_i} \Big[\phi^*(\mathbf{z}, \mathbf{y})\mathbb{A}^n(\mathbf{y}) - q^*(\mathbf{z}, \mathbf{y}) \, \phi(\mathbf{y}) \Big] ds(\mathbf{y})$$
$$\mathbf{z} \in D_p, \qquad p = 1, ..., M. \tag{6.111}$$

Boundary Integral Representation of the Potential

By analogy with Eq. 6.104 and considering the collocation point placed on the pth-boundary we can derive the boundary integral representation

$$\phi^p(\mathbf{x}) = 2 \sum_{i=0}^{M} \frac{(\sigma_i - \sigma_{i+1})}{(\sigma_p + \sigma_{p+1})} \int_{S_i} \Big[\phi^*(\mathbf{x}, \mathbf{y})\mathbb{A}^n(\mathbf{y}) - q^*(\mathbf{x}, \mathbf{y}) \, \phi(\mathbf{y}) \Big] ds(\mathbf{y})$$
$$\mathbf{x} \in S_p, \qquad p = 1, ..., M. \tag{6.112}$$

It can be seen that the value of the potential at a given point on one of the surfaces is linked to its form over the other boundaries.
Once more we have to solve an integral equation of the second kind for the surface potential.

Domain Integral Representation of the Electric Field

The final aim of our scheme is to find the electric field, which requires evaluation of the gradient of the scalar potential. We can find this gradient by differentiating Eq. 6.111 with

respect to the coordinates of $\mathbf{z} = (z_1, z_2, z_3)$. This step is allowed since all the functions involved are continuous inside the domain, and we obtain

$$\frac{\partial \phi^p}{\partial x_j}(\mathbf{z}) = \sum_{i=0}^{M} \frac{(\sigma_i - \sigma_{i+1})}{\sigma_p} \int_{S_i} \left[\frac{\partial \phi^*}{\partial z_j}(\mathbf{z}, \mathbf{y}) \mathbb{A}^n(\mathbf{y}) - \frac{\partial q^*}{\partial z_j}(\mathbf{z}, \mathbf{y}) \, \phi^i(\mathbf{y}) \right] ds(\mathbf{y})_. \tag{6.113}$$

$$\mathbf{z} \in D_p, \qquad p = 1, ..., M.$$

Finally, to find the electric field we have to add the contribution of the magnetic component

$$E_j^i(\mathbf{z}) = \mathbb{A}_j(\mathbf{z}) - \sum_{i=0}^{M} \frac{(\sigma_i - \sigma_{i+1})}{\sigma_p} \int_{S_i} \left[\frac{\partial \phi^*}{\partial z_j}(\mathbf{z}, \mathbf{y}) \mathbb{A}^n(\mathbf{y}) - \frac{\partial q^*}{\partial z_j}(\mathbf{z}, \mathbf{y}) \, \phi^i(\mathbf{y}) \right] ds(\mathbf{y}) \tag{6.114}$$

$$\mathbf{z} \in D_p, \qquad j = 1, 2, 3.$$

Boundary Integral Representation of the Electric Field

In order to derive an expression for the gradient of ϕ which is valid at the boundary, we cannot proceed by differentiating Eq. 6.112 because the directional derivatives of the single and double layer potentials are not continuous across the boundary. For a rigorous derivation we can use Eq. 6.113 and take the limit where the interior point $\mathbf{z} \in D_p$ tends to the surface, $\mathbf{z} \to \mathbf{x} \in S_p$, so as to take account of the jump properties of the directional derivative of the surface potentials [116]

$$\lim_{\mathbf{z} \to \mathbf{x}} \left[\frac{\partial}{\partial z_j} \int_{S_p} \phi^*(\mathbf{z}, \mathbf{y}) \mathbb{A}^n(\mathbf{y}) ds(\mathbf{y}) \right] = \frac{1}{2} \mathbb{A}^n(\mathbf{x}) \, n_j(\mathbf{x}) + \int_{S_p} \frac{\partial \phi^*}{\partial z_j}(\mathbf{x}, \mathbf{y}) \mathbb{A}^n(\mathbf{y}) ds(\mathbf{y}) \tag{6.115}$$

$$\mathbf{z} \in D_p, \qquad \mathbf{x} \in S_p, \qquad p = 1, ..., M$$

and

$$\lim_{\mathbf{z} \to \mathbf{x}} \left[\frac{\partial}{\partial z_j} \int_{S_p} q^*(\mathbf{z}, \mathbf{y}) \, \phi^p(\mathbf{y}) ds(\mathbf{y}) \right] = -\frac{1}{2} \left[\frac{\partial \phi^p}{\partial z_j}(\mathbf{x}) - q^p(\mathbf{x}) \, n_j(\mathbf{x}) \right]$$

$$+ \int_{S_p} \frac{\partial q^*}{\partial x_j}(\mathbf{x}, \mathbf{y}) \, \phi^p(\mathbf{y}) ds(\mathbf{y}) \tag{6.116}$$

$$\mathbf{z} \in D_p, \qquad \mathbf{x} \in S_p, \qquad p = 1, ..., M.$$

After performing the limit process and applying the boundary conditions, Eq. 6.113 becomes

$$
\begin{aligned}
\frac{\partial \phi^p}{\partial x_j}(\mathbf{x}) = 2 \sum_{i=0}^{M} & \frac{(\sigma_i - \sigma_{i+1})}{(\sigma_p + \sigma_{p+1})} \int_{S_i} \left[\frac{\partial \phi^*}{\partial x_j}(\mathbf{x}, \mathbf{y}) \mathbb{A}^n(\mathbf{y}) - \frac{\partial q^*}{\partial x_j}(\mathbf{x}, \mathbf{y}) \ \phi^i(\mathbf{y}) \right] ds(\mathbf{y}) \\
& + \frac{(\sigma_{p+1})}{(\sigma_p + \sigma_{p+1})} \left[q^p(\mathbf{x}) - q^{p+1}(\mathbf{x}) \right] \ n_j(\mathbf{x}) \\
& \mathbf{x} \in S_p, \qquad p = 1, ..., M.
\end{aligned}
\tag{6.117}
$$

Therefore the electric field at the pth-boundary when approaching from the pth-domain is given by

$$
\begin{aligned}
E_j^p(\mathbf{x}) = \mathbb{A}_j(\mathbf{x}) - 2 \sum_{i=0}^{M} & \frac{(\sigma_i - \sigma_{i+1})}{(\sigma_p + \sigma_{p+1})} \int_{S_i} \left[\frac{\partial \phi^*}{\partial x_j}(\mathbf{x}, \mathbf{y}) \mathbb{A}^n(\mathbf{y}) - \frac{\partial q^*}{\partial x_j}(\mathbf{x}, \mathbf{y}) \ \phi^i(\mathbf{y}) \right] ds(\mathbf{y}) \\
& - \frac{(\sigma_{p+1})}{(\sigma_p + \sigma_{p+1})} \left[q^p(\mathbf{x}) - q^{p+1}(\mathbf{x}) \right] \ n_j(\mathbf{x}) \\
& \mathbf{x} \in S_p, \qquad j = 1, 2, 3.
\end{aligned}
\tag{6.118}
$$

Where $q^p(\mathbf{x})$ and $q^{p+1}(\mathbf{x})$ are the unknown values of the normal component of the gradient of the scalar potential at both sides of the interface, S_p, which can be found by considering the product of Eq. 6.117 times the normal vector, $\mathbf{n}$

$$
\begin{aligned}
\frac{1}{2}(\sigma_p q^p(\mathbf{x}) + \sigma_{p+1} q^{p+1}(\mathbf{x})) = \sum_{i=0}^{M} (\sigma_i - \sigma_{i+1}) \int_{S_i} & \left[q^*(\mathbf{x}, \mathbf{y}) \mathbb{A}^n(\mathbf{y}) \right. \\
& \left. - \frac{\partial q^*}{\partial n}(\mathbf{x}, \mathbf{y}) \ \phi^i(\mathbf{y}) \right] ds(\mathbf{y})
\end{aligned}
\tag{6.119}
$$

and applying the matching condition once more. The above flux integral representation can be directly obtained by considering the limiting value of the normal derivative of Eq. 6.104, taking into account the jump property of the single layer normal derivative. The local values of $q^p(\mathbf{z})$ and $q^{p+1}(\mathbf{z})$ are found by the solution of the algebraic system of equations given by the above flux integral representation using the conservation of the current density matching condition, Eq. 6.5.

6.8 Constant BEM for Laplace's Equation. Multi-Domain

We now proceed to the discretization of the boundary integral representation by dividing the surfaces into flat triangular elements, i.e., every surface, S_i is meshed into n_i triangles

$$s_\alpha^i$$

$$S_i = \bigcup_{\alpha=1}^{n_i} s_\alpha^i, \qquad i = 1, ..., M \tag{6.120}$$

We take the potentials to have a constant evolution over the triangle, then
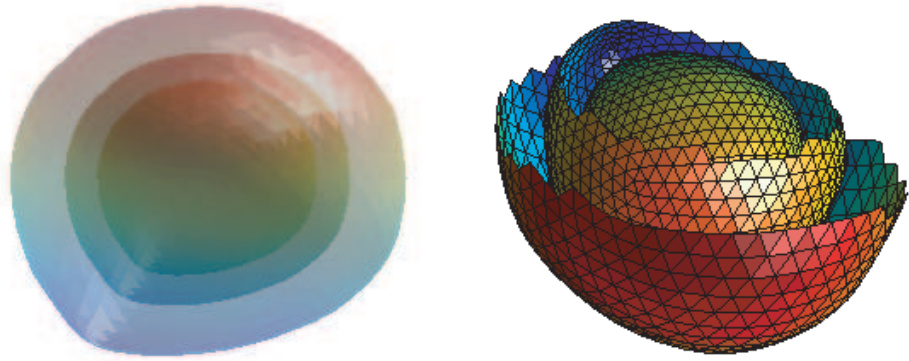
$$\phi^p(\mathbf{x}) = 2 \sum_{i=0}^{M} \sum_{\alpha=1}^{n_i} \frac{(\sigma_i - \sigma_{i+1})}{(\sigma_p + \sigma_{p+1})} \int_{S_\alpha} \left[\phi^*(\mathbf{x}, \mathbf{y}) \mathbb{A}^n(\mathbf{y}) - q^*(\mathbf{x}, \mathbf{y}) \ \phi(\mathbf{y}) \right] ds(\mathbf{y}) \tag{6.121}$$

$$\mathbf{x} \in S_p, \qquad p = 1, ..., M.$$

We can define the set of the all boundaries, $S = \bigcup_{i=1}^{M} S_i$, as the union of all the elements (s_k) of all the boundaries

$$S = \bigcup_{k=1}^{N} s_k \tag{6.122}$$

where the total number of elements is $N = \sum_{i}^{M} n_i$.

(a) *Original multi-domain .*   (b) *Partial   multi-domain   showing   meshed boundaries.*

Figure 6.10: *Discretization of the boundaries*

Evaluating Eq. 6.121 for every element,s_l we can generate the following system of equations

$$\sum_{k=1}^{N} \mathcal{H}(l, k) \ \phi_k = \sum_{k=1}^{N} \mathcal{G}(l, k) \ \mathbb{A}_k^n \tag{6.123}$$

$$l = 1, ..., N$$

where

$$\mathcal{H}(l,k) = \frac{1}{2}\,\delta_{l,k} + \frac{(\sigma_i - \sigma_{i+1})}{(\sigma_p + \sigma_{p+1})}\int_{s_k} q^*(\boldsymbol{x}_l, \mathbf{y})ds(\mathbf{y}) \tag{6.124}$$

$$\mathcal{G}(l,k) = \frac{(\sigma_i - \sigma_{i+1})}{(\sigma_p + \sigma_{p+1})}\int_{s_k} \phi^*(\boldsymbol{x}_l, \mathbf{y})ds(\mathbf{y}) \tag{6.125}$$

and $\mathbf{x}_l$ is the barycentre of the element s_l which is in the pth-domain, $s_l \in S_p$; likewise s_k belongs to the ith-domain, that is, $s_k \in S_i$.[4]

These coefficients can be easily found by applying the techniques described for the single domain case.

The solution of this system of equations will produce the values of the scalar potential at every element.

6.8.1   Potential in the Domains

A parallel process can be developed for the domain integral representation (Eq. 6.111), and after an appropriate discretization we can find an expression to evaluate the potential at any point inside the domain, for example, let us take $\mathbf{z} \in D_p$

$$\phi(\mathbf{z}) = \sum_{k=1}^{N} \mathbb{A}_k^n \mathcal{G}_k^*(\mathbf{z}) - \sum_{k=1}^{N} \phi_k \mathcal{H}_k^*(\mathbf{z}) \tag{6.126}$$

where

$$\mathcal{H}_k^*(\mathbf{z}) = \frac{(\sigma_i - \sigma_{i+1})}{\sigma_p}\int_{s_k} q^*(\mathbf{z}, \mathbf{y})\ ds(\mathbf{y}) \tag{6.127}$$

$$\mathcal{G}_k^*(\mathbf{z}) = \frac{(\sigma_i - \sigma_{i+1})}{\sigma_p}\int_{s_k} \phi^*(\mathbf{z}, \mathbf{y})\ ds(\mathbf{y}) \tag{6.128}$$

$$s_k \in S_i.$$

The integrals can be computed by Gauss quadrature.

---

[4]Please note that the index of the conductivity is given by the index of the sub-domain to which the element belongs .

6.8.2 Electric field in the Domains

By differentiation of Eq. 6.126 an expression for the gradient of the potential can be identified

$$\frac{\partial \phi}{\partial x_j}(\mathbf{z}) = \sum_{k=1}^{n} \mathbb{A}_k^n \mathcal{C}_k^{*,j}(\mathbf{z}) - \sum_{k=1}^{n} \phi_k \mathcal{D}_k^{*,j}(\mathbf{x}) \tag{6.129}$$

$$\mathbf{z} \in D_p, \qquad j = 1, 2, 3.$$

where

$$\mathcal{C}_k^{*,j}(\mathbf{z}) = \frac{(\sigma_i - \sigma_{i+1})}{\sigma_p} \int_{s_k} \frac{\partial \phi^*}{\partial x_j}(\mathbf{z}, \mathbf{y}) \, ds(\mathbf{y}) \tag{6.130}$$

$$\mathcal{D}_k^{*,j}(\mathbf{z}) = \frac{(\sigma_i - \sigma_{i+1})}{\sigma_p} \int_{s_k} \frac{\partial q^*}{\partial z_j}(\mathbf{z}, \mathbf{y}) \, ds(\mathbf{y}) \tag{6.131}$$

$$s_k \in S_i.$$

As in the case of the single domain representation, care must be taken when $\mathbf{z}$ approaches the surface, and when the distance is comparable to the size of the element we have to resort to the corresponding boundary description.

Unlike the single domain case, the different conductivity values in the multiple domains play an important role in these equations. Actually it can be seen that if we set all the conductivities to be equal and different to zero, we obtain the single domain representation.

6.8.3 Electric field at the boundaries

To complete the analysis of the multi-domain Laplace's equation, we have to evaluate the electric field. This can be done by discretization of Eq. 6.117 and assuming constant evolution of the magnitudes involved, we then obtain

$$\frac{1}{2}\frac{\partial \phi^p}{\partial x_j}(\mathbf{x}) = \sum_{k=1}^{N} \mathbb{A}_k^n \mathcal{C}_k^j(\mathbf{x}) - \sum_{k=1}^{N} \phi_k \mathcal{D}_k^j(\mathbf{x}) + \frac{(\sigma_{p+1})}{(\sigma_p + \sigma_{p+1})} \left[q^p(\mathbf{x}) - q^{p+1}(\mathbf{x}) \right] n_j(\mathbf{x}) \tag{6.132}$$

$$\mathbf{x} \in s_l \subset S_p, \qquad j = 1, 2, 3.$$

where

$$\mathcal{C}_k^j(\mathbf{x}) = \frac{(\sigma_i - \sigma_{i+1})}{(\sigma_p + \sigma_{p+1})} \int_{s_k} \frac{\partial \phi^*}{\partial x_j}(\mathbf{x}, \mathbf{y}) \, ds(\mathbf{y}) \tag{6.133}$$

$$\mathcal{D}_k^j(\mathbf{x}) = \frac{(\sigma_i - \sigma_{i+1})}{(\sigma_p + \sigma_{p+1})} \int_{s_k} \frac{\partial q^*}{\partial x_j}(\mathbf{x}, \mathbf{y}) \, ds(\mathbf{y}) \tag{6.134}$$

$$s_k \in S_i.$$

These coefficients show a singular behaviour, so they have to be computed using the techniques described in Section 6.4.3.

6.9 Integral formulation for Poisson's Equation. Multi Domain

The final step in our BEM description is the solution of Poisson's equation in a heterogenous system made of homogenous sub-domains, $D = \bigcup_k^M D_i$. First let us derive the integral representation of the PDE, by application of Green's theorem to any sub-domain where the potential satisfies $\nabla^2 \phi(\mathbf{z}) = b(\mathbf{z})$. Doing this, we find

$$
\begin{aligned}
c(\mathbf{z})\phi^i(\mathbf{z}) = & \int_{S_i} \left[\phi^*(\mathbf{z}, \mathbf{y})\ q^i(\mathbf{y}) - \phi^i(\mathbf{y})\ q^*(\mathbf{z}, \mathbf{y}) \right] ds(\mathbf{y}) \\
& - \int_{S_{i-1}} \left[\phi^*(\mathbf{z}, \mathbf{y})\ q^i(\mathbf{y}) - \phi^i(\mathbf{y})\ q^*(\mathbf{x}, \mathbf{y}) \right] ds(\mathbf{y}) \\
& \qquad\qquad - \int_{D_i} \phi^*(\mathbf{z}, \mathbf{y})b(\mathbf{y})\ d^3 y
\end{aligned}
\tag{6.135}
$$

where the coefficient $c(\mathbf{z})$ has the usual meaning (Eq. 6.105). The volume integral can be transformed by using the function ω^*

$$
\begin{aligned}
\int_{D_i} \phi^*(\mathbf{z}, \mathbf{y})b(\mathbf{y})\ d^3 y = & \int_{S_i} \left[b(\mathbf{y}) \frac{\partial \omega^*}{\partial n}(\mathbf{z}, \mathbf{y}) - \omega^*(\mathbf{z}, \mathbf{y}) \frac{\partial b(\mathbf{y})}{\partial n} \right] ds(\mathbf{y}) \\
& - \int_{S_{i-1}} \left[b(\mathbf{y}) \frac{\partial \omega^*}{\partial n}(\mathbf{x}, \mathbf{y}) - \omega^*(\mathbf{z}, \mathbf{y}) \frac{\partial b(\mathbf{y})}{\partial n} \right] ds(\mathbf{y}).
\end{aligned}
\tag{6.136}
$$

Domain Integral Representation of the Potential

As for the single domain there exist a parallelism between the approaches to solving Laplace's and Poisson's equations, so to obtain the domain integral formulation we perform an equivalent process to the one described in Section 6.7, finding

$$
\begin{aligned}
\phi^p(\mathbf{z}) = & \sum_{i=0}^{M} \frac{(\sigma_i - \sigma_{i+1})}{\sigma_p} \int_{S_i} \left[\phi^*(\mathbf{z}, \mathbf{y})\mathbb{A}^n(\mathbf{y}) - q^*(\mathbf{z}, \mathbf{y})\ \phi(\mathbf{y}) \right] ds(\mathbf{y}) \\
& - \sum_{i=0}^{M} \frac{(\sigma_i - \sigma_{i+1})}{\sigma_p} \int_{S_i} \left[b(\mathbf{y}) \frac{\partial \omega^*}{\partial n}(\mathbf{z}, \mathbf{y}) - \omega^*(\mathbf{z}, \mathbf{y}) \frac{\partial b(\mathbf{y})}{\partial n} \right] ds(\mathbf{y}) \\
& \qquad\qquad\qquad\qquad \mathbf{z} \in D_p, \qquad p = 1, ..., M.
\end{aligned}
\tag{6.137}
$$

where the indices 0 and $M + 1$ have the usual meaning.

Boundary Integral Representation of the Potential

For a point localized on the p-boundary it can be shown that

$$
\begin{aligned}
\frac{1}{2}\phi^p(\mathbf{x}) = &\sum_{i=0}^{M} \frac{(\sigma_i - \sigma_{i+1})}{(\sigma_p + \sigma_{p+1})} \int_{S_i} \left[\phi^*(\mathbf{x}, \mathbf{y}) \mathbb{A}^n(\mathbf{y}) - q^*(\mathbf{x}, \mathbf{y})\ \phi(\mathbf{y}) \right] ds(\mathbf{y}) \\
&- \sum_{i=0}^{M} \frac{(\sigma_i - \sigma_{i+1})}{(\sigma_p + \sigma_{p+1})} \int_{S_i} \left[b(\mathbf{y}) \frac{\partial \omega^*}{\partial n}(\mathbf{x}, \mathbf{y}) - \omega^*(\mathbf{x}, \mathbf{y}) \frac{\partial b(\mathbf{y})}{\partial n} \right] ds(\mathbf{y})
\end{aligned}
\tag{6.138}
$$

$$
\mathbf{x} \in S_p, \qquad p = 1, ..., M.
$$

This expression is an integral equation of the second kind for the unknown potential.

Domain Integral Representation of the Electric field

The integral formulation for the gradient of the potential can be found by differentiating $\phi^p(\mathbf{z})$ in Eq. 6.137

$$
\begin{aligned}
\frac{\partial \phi^p}{\partial z_j}(\mathbf{z}) = &\sum_{i=0}^{M} \frac{(\sigma_i - \sigma_{i+1})}{\sigma_p} \int_{S_i} \left[\frac{\partial \phi^*}{\partial z_j}(\mathbf{z}, \mathbf{y}) \mathbb{A}^n(\mathbf{y}) - \frac{\partial q^*}{\partial x_j}(\mathbf{z}, \mathbf{y})\ \phi^i(\mathbf{y}) \right] ds(\mathbf{y}) \\
&- \sum_{i=0}^{M} \frac{(\sigma_i - \sigma_{i+1})}{\sigma_p} \int_{S_i} \left[b(\mathbf{y}) \frac{\partial^2 \omega^*}{\partial n \partial z_j}(\mathbf{z}, \mathbf{y}) - \frac{\partial \omega^*}{\partial z_j}(\mathbf{z}, \mathbf{y}) \frac{\partial b(\mathbf{y})}{\partial n} \right] ds(\mathbf{y})
\end{aligned}
\tag{6.139}
$$

$$
\mathbf{z} \in D_p, \qquad p = 1, ..., M, \qquad j = 1, 2, 3.
$$

To yield a final expression for the total electric field, the magnetic contribution must be added to Eq. 6.140.

Boundary Integral Representation of the Electric Field

Following the parallelism with the analysis used when considering Laplace's equations, to produce an expression for the gradient of ϕ at the boundary in a rigorous way, a limit

process must be taken in the domain representation, $\mathbf{z} \to \mathbf{x} \in S_p$. This yields

$$
\begin{aligned}
\frac{1}{2}\frac{\partial \phi^p}{\partial x_j}(\mathbf{x}) = &\sum_{i=0}^{M} \frac{(\sigma_i - \sigma_{i+1})}{(\sigma_p + \sigma_{p+1})} \int_{S_i} \left[\frac{\partial \phi^*}{\partial x_j}(\mathbf{x},\mathbf{y}) \mathbb{A}^n(\mathbf{y}) - \frac{\partial q^*}{\partial z_j}(\mathbf{x},\mathbf{y})\,\phi^i(\mathbf{y}) \right] ds(\mathbf{y}) \\
&- \sum_{i=0}^{M} \frac{(\sigma_i - \sigma_{i+1})}{(\sigma_p + \sigma_{p+1})} \int_{S_i} \left[b(\mathbf{y}) \frac{\partial^2 \omega^*}{\partial n \partial x_j}(\mathbf{x},\mathbf{y}) - \frac{\partial \omega^*}{\partial x_j}(\mathbf{x},\mathbf{y}) \frac{\partial b(\mathbf{y})}{\partial n} \right] ds(\mathbf{y}) \qquad (6.140) \\
&+ \frac{(\sigma_{p+1})}{(\sigma_p + \sigma_{p+1})} \left[q^p(\mathbf{x}) - q^{p+1}(\mathbf{x}) \right] n_j(\mathbf{x}) \\
&\mathbf{x} \in S_p, \qquad p = 1, ..., M, \qquad j = 1, 2, 3.
\end{aligned}
$$

6.10 Constant BEM for Poisson's Equation. Multi Domain

As for the foregoing sections we perform a triangulation on the boundaries to discretize the boundary integral formulation, then

$$
\sum_{k=1}^{N} \mathcal{H}(l,k)\phi(k) = \sum_{k=1}^{N} \left[\mathcal{G}(l,k)\mathbb{A}_k^n - \mathcal{R}^1(l,k)b_k + \mathcal{R}^2(l,k)\frac{\partial b_k}{\partial n} \right] \qquad (6.141)
$$

$$
l = 1, ..., N
$$

where

$$
\mathcal{H}(l,k) = \frac{1}{2}\delta_{l,k} + \frac{(\sigma_i - \sigma_{i+1})}{(\sigma_p + \sigma_{p+1})} \int_{s_k} q^*(\boldsymbol{x}_l, \mathbf{y})ds(\mathbf{y}) \qquad (6.142)
$$

$$
\mathcal{G}(l,k) = \frac{(\sigma_i - \sigma_{i+1})}{(\sigma_p + \sigma_{p+1})} \int_{s_k} \phi^*(\boldsymbol{x}_l, \mathbf{y})ds(\mathbf{y}) \qquad (6.143)
$$

$$
\mathcal{R}^1(l,k) = \frac{(\sigma_i - \sigma_{i+1})}{(\sigma_p + \sigma_{p+1})} \int_{s_k} \frac{\partial \omega^*}{\partial n}(\mathbf{x}_l, \mathbf{y})\,ds(\mathbf{y}) \qquad (6.144)
$$

$$
\mathcal{R}^2(l,k) = \frac{(\sigma_i - \sigma_{i+1})}{(\sigma_p + \sigma_{p+1})} \int_{s_k} \omega^*(\mathbf{x}_l, \mathbf{y})\,ds(\mathbf{y}) \qquad (6.145)
$$

and $\mathbf{x}_l$ is found in the s_l, element which is in the pth-domain, $s_l \in S_p$; likewise s_k belongs to the ith-domain, that is, $s_k \in S_i$.

6.10.1 Potential in the Domains

The potential is given by

$$\phi(\mathbf{z}) = \sum_{k=1}^{N} \left[\mathbb{A}_k^n \mathcal{G}_k^*(\mathbf{z}) - \phi_k \mathcal{H}_k^*(\mathbf{z}) - \mathcal{R}_k^{*,1}(\mathbf{z}) b_k + \mathcal{R}_k^{*,2}(\mathbf{z}) \frac{\partial b_k}{\partial n} \right]$$

$$\mathbf{x} \in D_p$$

(6.146)

where

$$\mathcal{H}_k^*(\mathbf{z}) = \frac{(\sigma_i - \sigma_{i+1})}{\sigma_p} \int_{s_k} q^*(\mathbf{z}, \mathbf{y}) \, ds(\mathbf{y})$$

(6.147)

$$\mathcal{G}_k^*(\mathbf{z}) = \frac{(\sigma_i - \sigma_{i+1})}{\sigma_p} \int_{s_k} \phi^*(\mathbf{z}, \mathbf{y}) \, ds(\mathbf{y})$$

(6.148)

$$\mathcal{R}_k^{*,1}(\mathbf{z}) = \frac{(\sigma_i - \sigma_{i+1})}{\sigma_p} \int_{s_k} \frac{\partial \omega^*}{\partial n}(\mathbf{x}, \mathbf{y}) \, ds(\mathbf{y})$$

(6.149)

$$\mathcal{R}_k^{*,2}(\mathbf{z}) = \frac{(\sigma_i - \sigma_{i+1})}{\sigma_p} \int_{s_k} \omega^*(\mathbf{z}, \mathbf{y}) \, ds(\mathbf{y}).$$

(6.150)

6.10.2 Electric field in the Domains

Differentiation of Eq. 6.146 yields

$$\frac{\partial \phi}{\partial z_j}(\mathbf{z}) = \sum_{k=1}^{N} \left[\mathbb{A}_k^n \mathcal{C}_k^{*,j}(\mathbf{z}) - \phi_k \mathcal{D}_k^{*,j}(\mathbf{z}) - \mathcal{P}_{k,j}^{*1}(\mathbf{z}) b_k + \mathcal{P}_{k,j}^{*2}(\mathbf{z}) \frac{\partial b_k}{\partial n} \right]$$

$$\mathbf{z} \in D_p, \qquad j = 1, 2, 3.$$

(6.151)

where

$$\mathcal{C}_k^{*,j}(\mathbf{z}) = \frac{(\sigma_i - \sigma_{i+1})}{\sigma_p} \int_{s_k} \frac{\partial \phi^*}{\partial x_j}(\mathbf{z}, \mathbf{y}) \, ds(\mathbf{y})$$

(6.152)

$$\mathcal{D}_k^{*,j}(\mathbf{z}) = \frac{(\sigma_i - \sigma_{i+1})}{\sigma_p} \int_{s_k} \frac{\partial q^*}{\partial z_j}(\mathbf{z}, \mathbf{y}) \, ds(\mathbf{y})$$

$$s_k \in S_i.$$

(6.153)

$$\mathcal{P}_{k,j}^{*1}(\mathbf{z}) = \frac{(\sigma_i - \sigma_{i+1})}{\sigma_p} \int_{s_k} \frac{\partial^2 \omega^*}{\partial n \, \partial x_j}(\mathbf{z}, \mathbf{y}) \, ds(\mathbf{y}),$$

(6.154)

$$\mathcal{P}_{k,j}^{*2}(\mathbf{z}) = \frac{(\sigma_i - \sigma_{i+1})}{\sigma_p} \int_{s_k} \frac{\partial \omega^*}{\partial x_j}(\mathbf{z}, \mathbf{y}) \, ds(\mathbf{y})$$

(6.155)

6.10.3 Electric field at the boundaries

By applying a suitable limit process to Eq. 6.151 the scalar gradient of the potential is given by

$$\frac{1}{2}\frac{\partial \phi}{\partial x_j}(\mathbf{x}) = \sum_{k=1}^{N}\left[\mathbb{A}_k^n \mathcal{C}_k^j(\mathbf{x}) - \phi_k \mathcal{D}_k^j(\mathbf{x}) - \mathcal{P}_{k,j}^1(\mathbf{x})b_k + \mathcal{P}_{k,j}^2(\mathbf{x})\frac{\partial b_k}{\partial n}\right]$$
$$+\frac{(\sigma_{p+1})}{(\sigma_p + \sigma_{p+1})}\left[q^p(\mathbf{x}) - q^{p+1}(\mathbf{x})\right]\,n_j(\mathbf{x}) \qquad (6.156)$$
$$\mathbf{x} \in s_l, \qquad j = 1, 2, 3.$$

where

$$\mathcal{C}_k^j(\mathbf{x}) = \frac{(\sigma_i - \sigma_{i+1})}{(\sigma_p + \sigma_{p+1})}\int_{s_k}\frac{\partial \phi^*}{\partial x_j}(\mathbf{x}, \mathbf{y})\,ds(\mathbf{y}) \qquad (6.157)$$

$$\mathcal{D}_k^j(\mathbf{x}) = \frac{(\sigma_i - \sigma_{i+1})}{(\sigma_p + \sigma_{p+1})}\int_{s_k}\frac{\partial q^*}{\partial x_j}(\mathbf{x}, \mathbf{y})\,ds(\mathbf{y}) \qquad (6.158)$$

$$\mathcal{P}_{k,j}^1(\mathbf{x}) = \frac{(\sigma_i - \sigma_{i+1})}{(\sigma_p + \sigma_{p+1})}\int_{s_k}\frac{\partial^2 \omega^*}{\partial n\,\partial x_j}(\mathbf{x}, \mathbf{y})\,ds(\mathbf{y}), \qquad (6.159)$$

$$\mathcal{P}_{k,j}^2(\mathbf{x}) = \frac{(\sigma_i - \sigma_{i+1})}{(\sigma_p + \sigma_{p+1})}\int_{s_k}\frac{\partial \omega^*}{\partial x_j}(\mathbf{x}, \mathbf{y})\,ds(\mathbf{y}) \qquad (6.160)$$

6.11   A BEM application to EEG

To demonstrate the versatility of the formulation presented here, we also describe its application to the forward problem in electro encephalography (EEG) (although this technique is not a primary aim of this thesis).

In EEG we record a set of electric potential differences at the surface of the scalp, which are produced by current sources in the brain, which can be represented as dipole elements. Given a nested heterogenous multidomain, the scalar potential satisfies Poisson's equation in every sub-domain

$$\nabla^2 \phi(\mathbf{x}) = \nabla \cdot \mathbf{J}^p(\mathbf{x}) \tag{6.161}$$

where $\mathbf{J}^p$ is the primary current which can be approximated by current dipoles [125]

$$\mathbf{J}^p(\mathbf{x}) = \sum_{\alpha=1}^{N_d} \mathbf{p}_\alpha \delta(\mathbf{x} - \mathbf{x}_\alpha) \tag{6.162}$$

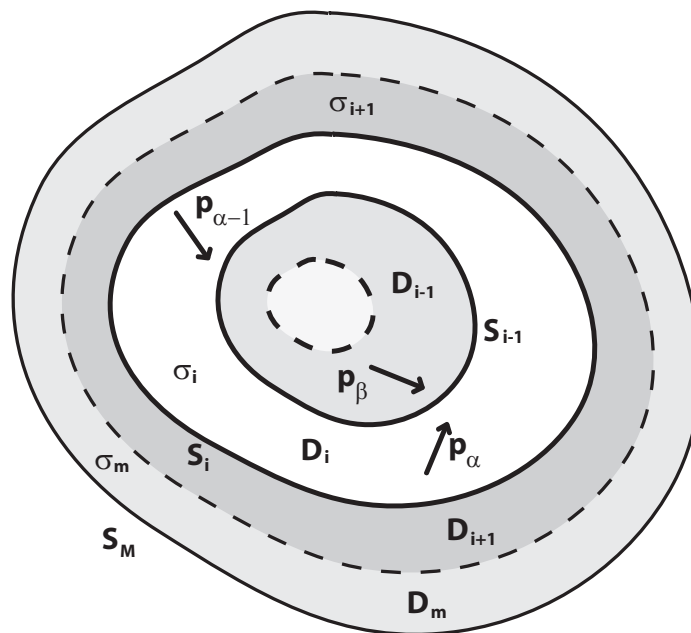where $\mathbf{p}_\alpha$ is dipole strength and $\mathbf{x}_\alpha$ are the positions of the N_d sources.

Figure 6.11:   *Current dipoles $\boldsymbol{p}_\alpha$ in a heterogeneous multi-domain made of homogenous sub-domains D_i of conductivity σ_i and bounding surface S_i.*

If we apply Green's second identity to the ith-surface, we obtain

$$
\frac{1}{2} \phi^i(\mathbf{x}) = \int_{S_i} \left[\phi^*(\mathbf{x}, \mathbf{y}) \, q^i(\mathbf{y}) - \phi^i(\mathbf{y}) \, q^*(\mathbf{x}, \mathbf{y}) \right] ds(\mathbf{y})
$$
$$
- \int_{S_{i-1}} \left[\phi^*(\mathbf{x}, \mathbf{y}) \, q^i(\mathbf{y}) - \phi^i(\mathbf{y}) \, q^*(\mathbf{x}, \mathbf{y}) \right] ds(\mathbf{y}) \qquad (6.163)
$$
$$
- \int_{D_i} \phi^*(\mathbf{x}, \mathbf{y}) \nabla \cdot \mathbf{J}^p(\mathbf{y}) \, d^3y
$$

where this time there is no need to calculate domain representations since our aim is to compute the potential at the outer surface.

Also since we can neglect the magnetic effect, the boundary conditions for this problem become

$$
\sigma_{i+1} q^{i+1} = \sigma_i q^i
$$
$$
i = 1, ..., M \qquad (6.164)
$$

Let us now transform the volume integrals into surface integrals using the properties of the sources

$$
\int_{D_i} \phi^*(\mathbf{x}, \mathbf{y}) \nabla \cdot \mathbf{J}^p(\mathbf{y}) \, d^3y = \int_{D_i} \nabla \cdot \left[\phi^*(\mathbf{x}, \mathbf{y}) \mathbf{J}^p(\mathbf{y}) \right] d^3y -
$$
$$
\int_{D_i} \nabla \phi^*(\mathbf{x}, \mathbf{y}) \cdot \mathbf{J}^p(\mathbf{y}) \, d^3y \qquad (6.165)
$$

but

$$
\int_{D_i} \nabla \cdot \left[\phi^*(\mathbf{x}, \mathbf{y}) \mathbf{J}^p(\mathbf{y}) \right] d^3y = \int_{S_i} \phi^*(\mathbf{x}, \mathbf{y}) \mathbf{J}^p(\mathbf{y}) d\vec{s}(\mathbf{y}) - \int_{S_{i-1}} \phi^*(\mathbf{x}, \mathbf{y}) \mathbf{J}^p(\mathbf{y}) d\vec{s}(\mathbf{y})
$$
$$
= \sum_{\alpha=1}^{N_d} \mathbf{p}_\alpha \left[\int_{S_i} \phi^*(\mathbf{x}, \mathbf{y}) \delta(\mathbf{y} - \mathbf{x}_\alpha) d\vec{s}(\mathbf{y}) - \int_{S_{i-1}} \phi^*(\mathbf{x}, \mathbf{y}) \delta(\mathbf{y} - \mathbf{x}_\alpha) d\vec{s}(\mathbf{y}) \right] = 0 \qquad (6.166)
$$

because we suppose that there are no current dipole sources at the boundaries. Also

$$
\int_{D_i} \nabla \phi^*(\mathbf{x}, \mathbf{y}) \mathbf{J}^p(\mathbf{y}) \, d^3y = \sum_{\alpha=1}^{N_d} \mathbf{p}_\alpha \int_{D_i} \nabla \phi^*(\mathbf{x}, \mathbf{y}) \delta(\mathbf{y} - \mathbf{x}_\alpha) d^3y = \sum_{\alpha=1}^{N_{d_i}} \mathbf{p}_\alpha \nabla \phi^*(\mathbf{x}, \mathbf{x}_\alpha) \quad (6.167)
$$

where now α runs only for the N_{d_i} sources placed in D_i.

By performing a parallel analysis to the previous multi-domain sections, we obtain the following integral representation

$$\frac{1}{2} \phi^p(\mathbf{x}) = \sum_{i=0}^{M} \frac{(\sigma_i - \sigma_{i+1})}{(\sigma_p + \sigma_{p+1})} \int_{S_i} \left[\phi^*(\mathbf{x}, \mathbf{y}) \mathbb{A}^n(\mathbf{y}) - q^*(\mathbf{x}, \mathbf{y}) \ \phi(\mathbf{y}) \right] ds(\mathbf{y})$$

$$- \sum_{i=1}^{M} \frac{\sigma_i}{(\sigma_p + \sigma_{p+1})} \sum_{\alpha=1}^{N_{d_i}} \mathbf{p}_\alpha \nabla \phi^*(\mathbf{x}, \mathbf{x}_\alpha) \tag{6.168}$$

$$\mathbf{x} \in S_p, \qquad p = 1, ..., M,$$

and by discretization of boundaries and a constant approximation of the potential, we can generate the following system of equations

$$\sum_{k=1}^{N} \mathcal{H}(l, k) \phi(k) = \mathcal{J}(l) \tag{6.169}$$

$$l = 1, ..., N$$

where

$$\mathcal{H}(l, k) = \frac{1}{2} \delta_{l,k} + \frac{(\sigma_i - \sigma_{i+1})}{(\sigma_p + \sigma_{p+1})} \int_{s_k} q^*(\boldsymbol{x}_l, \mathbf{y}) ds(\mathbf{y}) \tag{6.170}$$

and

$$\mathcal{J}(l) = - \sum_{\alpha=1}^{N_d} \frac{\sigma_\alpha}{(\sigma_p + \sigma_{p+1})} \ \mathbf{p}_\alpha \nabla \phi^*(\mathbf{x}, \mathbf{x}_\alpha) \tag{6.171}$$

the collocation point $\mathbf{x}$ is the barycentre of the element s_l which is in the p-domain, $s_l \in S_p$; likewise s_k belongs to the ith-domain, that is, $s_k \in S_i$. And σ_α is the conductivity of the domain where the α-source is placed.

The solution of this set of equations yields the values of the electric potential, precisely, at the outer surface, that is, the scalp.

This result is equivalent to that produced in a similar BEM approach used for EEG modelling [113],[126].

6.12 Mesh Generation

A simple mesh generator was developed in Matlab (Mathworks Inc.) to create models of anatomical structures. It takes a magnetic resonance image file as input to generate a scalp mesh and brain mask files from BET2 (fMRIB, Oxford) to produce brain meshes, as shown in Fig. 6.12.

For more complex surfaces such as other human organs or full body meshes, data from the HUGO human body model (Medical VR Studio, GmbH, Lorrach, Germany) was used.
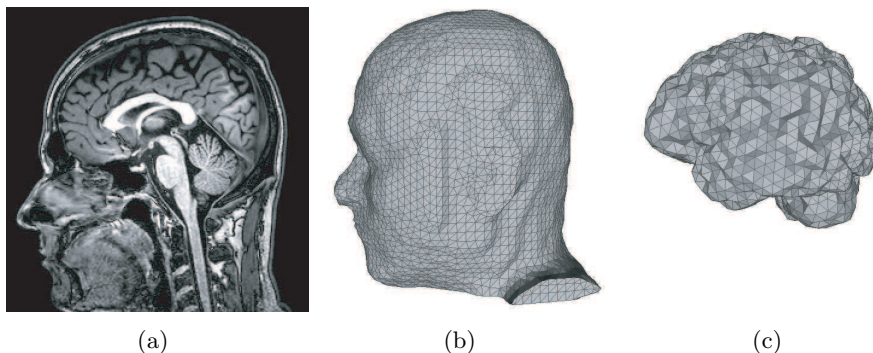

(a) (b) (c)

Figure 6.12: *Mesh generation: (a) original MRI image file; (b) scalp mesh of 9000 elements created by the mesh generator; (c) brain mesh of 5000 elements created by the mesh generator.*

If in Eq. 6.33 a constant potential over the whole surface is chosen we obtain

$$\sum_{k=1}^{n} \mathcal{H}(l, k) = 0, \qquad l = 1, ..., n \tag{6.172}$$

this condition is purely geometric and in the process of mesh generation it is imposed to achieved suitable meshes with the desired smoothness.

Figure 6.13 shows the values of $\sum_{k=1}^{n} \mathcal{H}(l, k)$ for the mesh shown in Fig. 6.12(b)

The mesh generation algorithm relies on the *isosurface* function of Matlab, which for a given three dimensional volume data constructed from an MP-RAGE scan, computes isosurface data. That is, the isosurface connects points that have the specified value in much the same way as contour lines connect points of equal elevation.
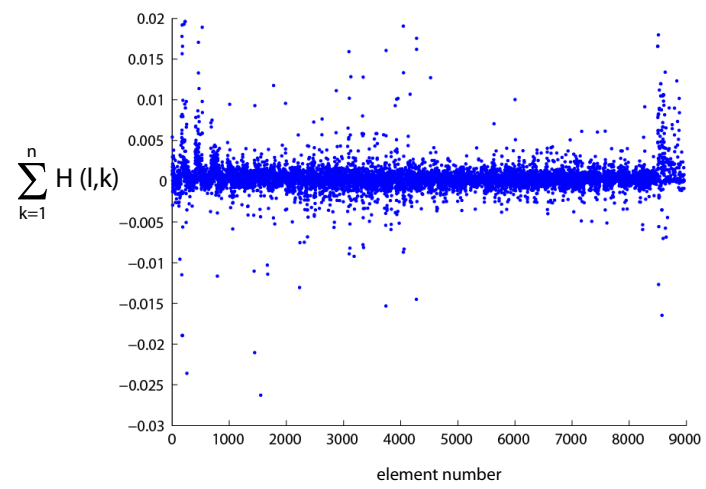
Figure 6.13: *Value of $\sum_{k=1}^{n} \mathcal{H}(l,k)$ for every element in the mesh shown in Fig. 6.12(b).*

Chapter 7

Electric field Calculations: Numerical Results

7.1 Introduction

The constant BEM approach described in the previous chapter has been tested by comparison with analytic solutions for basic-shaped objects forming a single domain exposed to switched gradients or moving in simple static fields. Emphasis is placed on spherical objects since these form the most elemental model for representing the human head. The BEM approach has also been used to evaluate the scalar potential, the induced electric fields and the current densities in more complex models.

The algorithm used to mesh each spherical surface starts at the top of the sphere where the polar angle $\theta = \arccos(z/r)$ is zero and ends at the bottom of the sphere where $\theta = \pi$. At each value of θ, elements are spread over the azimuthal angle ($\varphi = \arctan(y/x)$). Figure 7.1 shows how θ and φ vary with the element number for a spherical surface divided into 360 elements. In general, the number of elements, N, is given by $N = 2[n_\theta(n_\varphi - 1)]$, where n_θ and n_φ are the number of steps in θ and ϕ respectively.
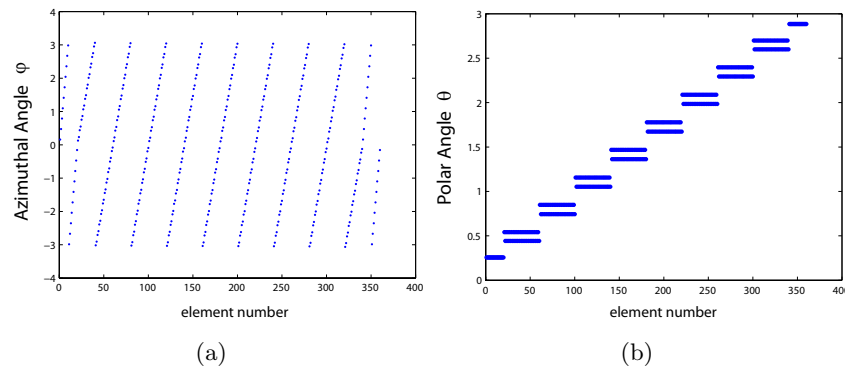
Figure 7.1: *Angular position of the elements on the surface of a sphere meshed with 360 elements: (a) azimuthal angle at each mesh element ; (b) polar angle at each mesh element.*

7.2 Sphere in a time-varying longitudinal gradient

We initially considered a homogeneous conducting sphere of 0.08 m radius placed in an ideal longitudinal field gradient of 30 mTm^{-1} strength ($\omega = 1$ kHz) and compared the constant BEM calculations to the analytical results described in Bencsik's paper [75]. Numerical calculation produced a null scalar potential which is in agreement with theory. Figure 7.2(a) shows the electric field produced at the surface of the sphere meshed into 1520 elements. This follows the magnetic vector potential.

If the sphere is now placed 0.13 m from the origin in the x-direction we obtain a different problem. Figure 7.2(b) shows how the theoretical scalar potential, ϕ_t, and the scalar potential obtained with the constant BEM calculation, ϕ, vary over the surface when the sphere is divided into 360 elements. From this graphic it can be seen that the two potentials behave in a very similar fashion. The analytically and numerically calculated values of the electric fields at each mesh element for the same case are shown in Fig. 7.3(a). This comparison again demonstrates the similarity of the theoretical and the numerical values. A three-dimensional plot of $|\mathbf{E}|$ is presented in Fig. 7.3(b) for a sphere placed in the same position in a longitudinal field gradient, but this time meshed into 1520 elements.
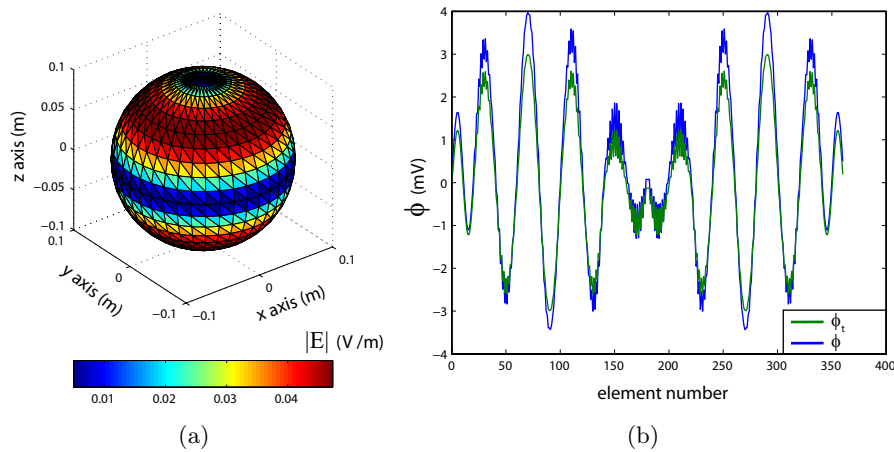
(a)   (b)

Figure 7.2: *(a) Three-dimensional plot of $|\mathbf{E}|$ for a single spherical conductor discretized into 1520 elements. The sphere is centred in a longitudinal field gradient of 30 mTm^{-1} strength varying at 1 kHz; (b) calculated values of ϕ for a spherical mesh of 360 elements and analytically calculated scalar potential, ϕ_t at each mesh element. The 0.08 m radius sphere is shifted by 0.13 m in the x-direction in a longitudinal field gradient. The relationship between element number and position on the surface of the sphere is shown in Fig. 7.1.*

(a)   (b)

Figure 7.3: *(a) Calculated values of $|\mathbf{E}|$ for a spherical mesh of 360 elements and analytically calculated electric field, $|\mathbf{E}_t|$. The sphere is shifted by 0.13 m in the x-direction in a longitudinal field gradient. The relationship between element number and posit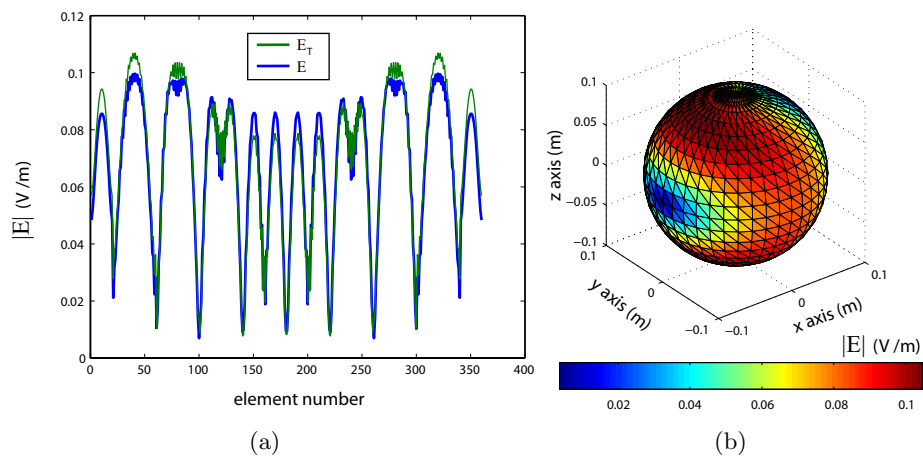ion on the surface of the sphere is shown in Fig. 7.1. (b) Three-dimensional plot of $|\mathbf{E}|$ for a single spherical conductor discretized into 1520 elements. The sphere is shifted by 0.13 m in the x-direction in a longitudinal field gradient.*

7.2.1   Convergence of the numerical method

For this numerical approach, it easy to see that the difference between the computed and the theoretical values becomes smaller when the number of elements in the mesh is increased. This convergence of the numerical results to the theoretical ones can be shown with the use of the L^2-norm

$$L = \sum_{k}^{N} \frac{[E(\mathbf{r}_n) - E(\mathbf{r}_n)_t]^2}{N} \tag{7.1}$$

where E is the actual field and E_t is the analytical field and N the number of elements in the mesh.

Figure 7.4 depicts this convergence for the problem of a sphere shifted by 0.13m in the x-direction in a longitudinal field gradient, it is evident how the larger number of elements in the mesh the better the approximation is.
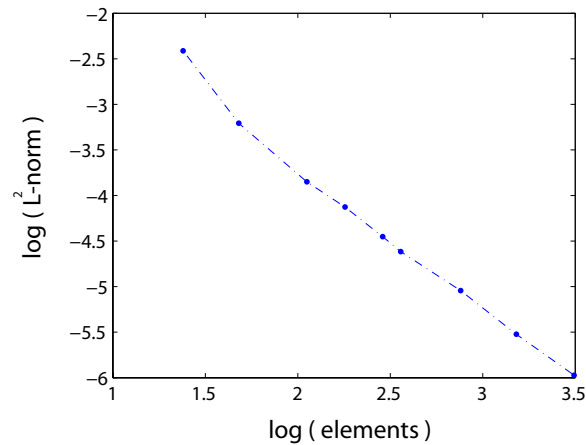

Figure 7.4: *Convergence for the problem of a sphere shifted by 0.13m in the x-direction in a longitudinal field gradient in terms of the logarithm of the L^2 norm.*

7.3   Longitudinally shifted sphere in a time-varying transverse gradient

Figure 7.5(a) shows the theoretical and numerical values of the modulus of the electric field at each mesh element, for a sphere of radius 0.08 m exposed to an x-gradient of 30 mTm^{-1} amplitude varying sinusoidally at 1 kHz. In Figure 7.5(b) the centre of the sphere was shifted 0.13 m in the z-direction from the origin of the gradient. In both cases a mesh of
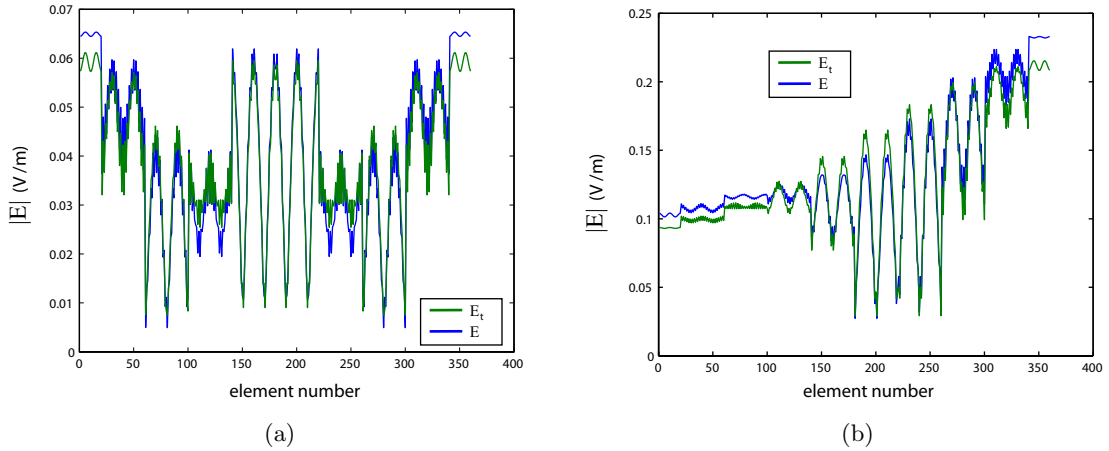
360 elements was used.

Figure 7.5: *(a) Calculated values of* $|\mathbf{E}|$ *and* $|\mathbf{E}_t|$ *for a spherical mesh of 360 elements. The sphere is centred in a transverse field gradient; (b) calculated values of* $|\mathbf{E}|$ *and* $|\mathbf{E}_t|$ *for spherical mesh of 360 elements. The sphere is shifted by 0.13 m in the z-direction in a transverse field gradient. The relationship between element number and position on the surface of the sphere is shown in Fig. 7.1.*

$|\mathbf{E}|$ and $|\mathbf{E}_t|$ are in a good agreement in both cases.

7.4 Rotation of a sphere in a uniform magnetic field

We now consider a homogeneous and uncharged spherical conductor of radius 0.2 m rotating about the x-axis, $\boldsymbol{\Omega} = 1\ \hat{\mathbf{i}}$ (rad s $^{-1}$), in a uniform static magnetic field perpendicular to the axis of rotation, $\mathbf{B} = 1\ \hat{\boldsymbol{k}}$ (T). The scalar potential (produced by the electrostatic surface charge distribution) satisfies Laplace's equation, and so can be written in terms of spherical harmonics and appropriate powers of r [25], inside and outside the sphere. The analytical solutions for this potential and the total electric field are then

$$\phi(\mathbf{r}) = -\alpha r^2\ Y_{21}(\theta, \phi) = \frac{\Omega B}{2} xz \qquad (7.2)$$

$$\mathbf{E}(\mathbf{r}) = \frac{\Omega B}{2}[-z\hat{\mathbf{i}} + x\hat{\boldsymbol{k}}]. \qquad (7.3)$$

where $Y_{lm}(\theta, \phi)$ represents the spherical harmonics of order l and degree m, and

$$\alpha = \Omega \frac{B}{2} \sqrt{\frac{8\pi}{15}}. \tag{7.4}$$

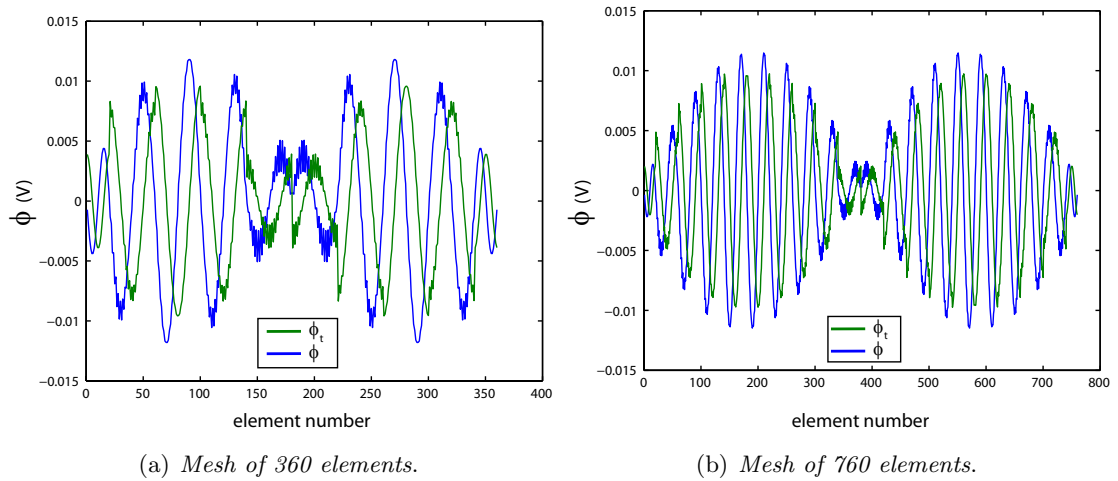(a) *Mesh of 360 elements.*　　　　　　　(b) *Mesh of 760 elements.*

Figure 7.6: *(a) Calculation of ϕ and analytical scalar potential, ϕ_t at each mesh element for a sphere described using a mesh of 360 elements rotating in a uniform magnetic field $(\Omega \perp B)$; (b) calculation of ϕ and analytical scalar potential, ϕ_t at each mesh element for a sphere described using a mesh of 760 elements rotating in a uniform magnetic field $(\Omega \perp \boldsymbol{B})$.*

Figure 7.6 shows the analytical and numerically calculated values of the potential for a mesh of 360 elements. The difference between the computed and the theoretical values becomes smaller when increasing the number of elements in the mesh. This is evident from Fig. 7.6(b) which shows values calculated for a discretization of the sphere with 760 elements, as a larger number of elements in the mesh provides a closer representation of a perfect sphere.

7.5 Rotation of an infinite cylinder in a uniform magnetic field

We now consider a homogeneous conducting cylinder of height 10 m and radius 0.1 m (this can be considered to be an approximation to an infinite cylinder where end effects may be disregarded) with no net charge, rotating ($\Omega = 1$ rad s^{-1}) about the axis of the cylinder

(z-direction) in a uniform magnetic field parallel to the z-axis of $B{=}1$ T. This rotation produces a negative uniform volume charge density which generates a scalar potential that can be computed using Gauss' law and which is constant at the cylinder's surface

$$\phi(\mathbf{r}) = \omega B \, \frac{x^2 + y^2}{2}. \tag{7.5}$$

Figure 7.7(a) shows the numerically calculated and theoretical values of the potential. They correspond to two different lines of constant potential. In further calculations we noted that the numerical line approaches the analytical one when the number of mesh elements is increased. The difference between the analytical and numerical solution is due to the non-uniqueness of the solution of this kind of boundary problem, i.e. the solution admits the addition of an arbitrary constant value.

It can be appreciated from Fig. 7.7(a) that the numerical value of the potential is not constant at the elements placed at extremes of the cylinder. This is an expected result since we are using an approximation to an infinite cylinder. A color map of the numerically calculated scalar potential on a square of 0.05 m side on the xy-plane positioned inside the cylinder is displayed in Fig. 7.7(b). Numerically computed results are in good agreement with the analytically calculated values.

7.6 Rotation of a sphere in a longitudinal field gradient

The situation where a homogeneous uncharged conducting sphere of radius 1.0 m rotates, $\mathbf{\Omega} = \omega \hat{\boldsymbol{k}}$, in an ideal longitudinal field gradient

$$\mathbf{B} = G[-\frac{x}{2}\hat{\mathbf{i}} - \frac{y}{2}\hat{\mathbf{j}} + z\hat{\boldsymbol{k}}] \tag{7.6}$$

where $G{=}1$ T m^{-1} and $\omega = 1$ rad s^{-1} is now considered. In this situation the scalar potential is found by solving Poisson's equation, and is given by

$$\phi = \Omega G(\frac{x^2 + y^2}{2})z. \tag{7.7}$$

In Fig. 7.8(a) the theoretical values of the potential at the surface of the sphere is compared to the numerically calculated values for a mesh of 1520 elements. As can be observed from Eq.7.7, at the surface of the sphere the potential is a function of the z-position only, and is largest when $z = \frac{1}{\sqrt{3}}$ m ($\theta = \arccos(\frac{1}{\sqrt{3}})$). The obtained numerical result exactly predicts the location of this maximum value, as shown by Fig. 7.8(b).
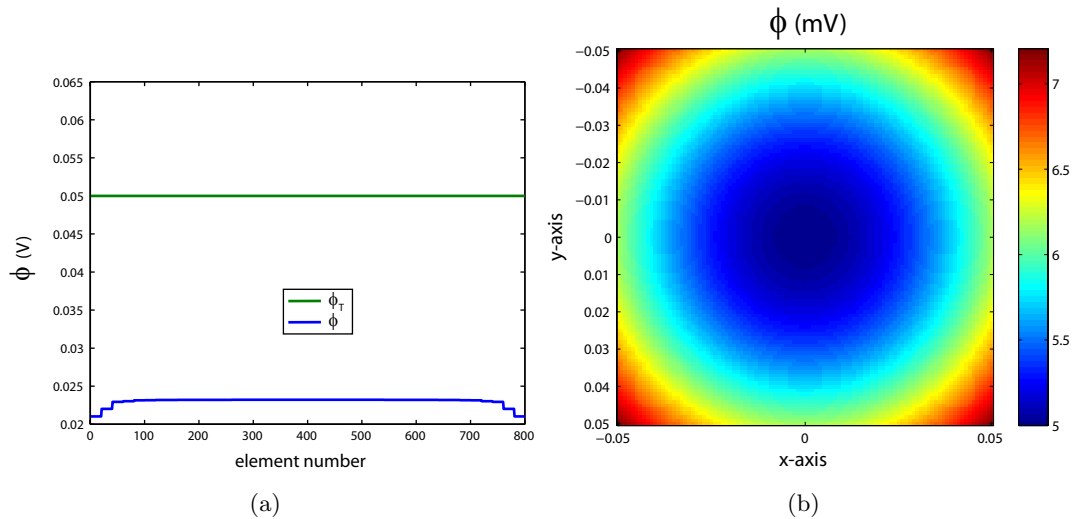
Figure 7.7: *(a)Numerical ϕ and theoretical, ϕ_t values of the scalar potential at each mesh element for a cylinder rotating in a uniform magnetic field ($\Omega \parallel B$). Elements were sequentially ordered along the length of the cylinder with 20 elements used to span the circumference at each of the 40 z-positions; (b) scalar potential in a central xy-plane inside the cylinder, rotating in a uniform magnetic field of 1T at a rate of $1 \ rad \ s^{-1}$*

Summary

We can thus summarize that the constant BEM approach produces results that agree with analytical solutions for basic-shaped objects exposed to switched gradients or moving in simple static fields.

7.7 Simple human body model exposed to a temporally varying longitudinal gradient

We now increase the modeling precision by considering a homogeneous (the whole system has the same conductivity) human body model based on data from the HUGO human body model (Medical VR Studio, GmbH, Lorrach, Germany).

The model is made of a mesh of 9000 elements, placed in the centre of an ideal longitudinal field gradient (4.21 mTm^{-1} amplitude varying sinusoidally at 500 Hz). The obtained numerical results for the potential and the corresponding magnitude of the electric field are shown in Fig. 7.9(a) and 7.9(b). For a rate of change of gradient of 100 Tm^{-1}s^{-1}, values typically used in MRI, the peak of the E-field for the same homogeneous human body model

(a)   (b)

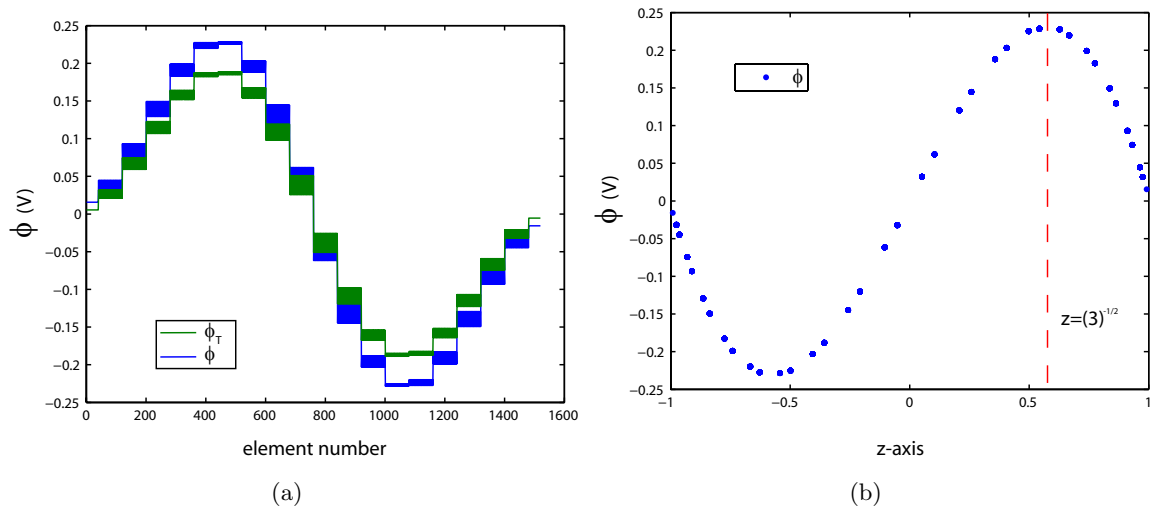Figure 7.8: *(a) Variation of the potential at the surface of a sphere meshed using 1520 elements rotating about the z-axis in a z-gradient; (b) variation of the numerically computed potential, ϕ, with the z coordinate of the element for a sphere meshed using 1520 elements rotating about the z-axis in a z-gradient.*

used would correspond to 0.46 Vm^{-1}.

7.8 Multi-domain head model exposed to a temporally varying transverse gradient

More biologically relevant models that represent the heterogeneity of the electric properties of the human body require consideration of systems composed of more than one homogeneous sub-domain. As a first step in testing the application of the BEM approach to such multi-compartmental systems, a two-compartment head-brain model (see Fig. 6.12) of conductivities 0.0125 and 1 Sm^{-1} is placed shifted 0.05 m along the z-direction from the centre of an ideal x-gradient of strength 3.0 mT m^{-1} varying at a frequency of 1 kHz. Figures 7.10(a) and 7.10(b) show the scalar potential found at the surface of the head and brain of the simple two compartment head-model using the BEM approach (the differences in the scalar potential at the head surface are slightly smaller to those found in EEG, higher than mV).
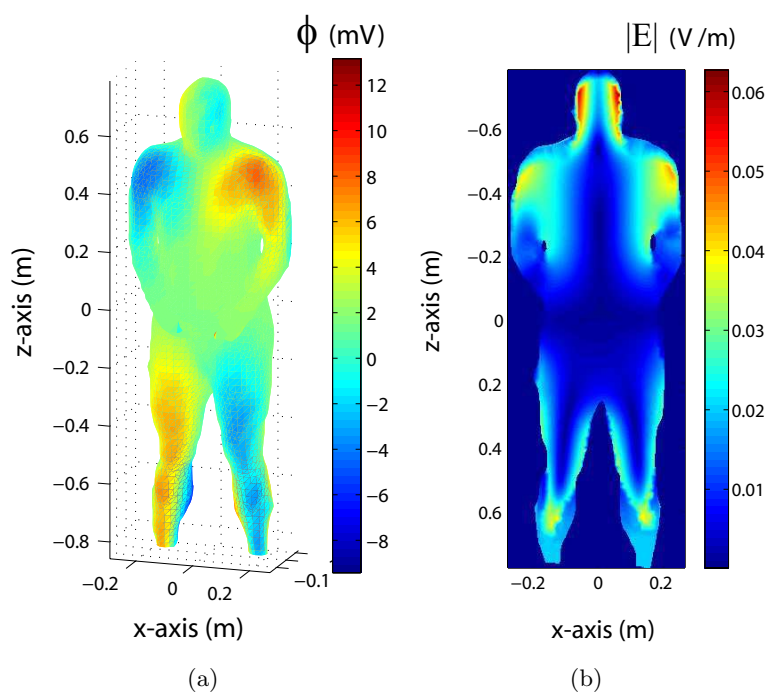
Figure 7.9: *A human body model placed in a longitudinal field gradient of strength 4.21 mTm^{-1} varying at 500 Hz: (a) calculated values of ϕ ; (b) calculated values of the electric field modulus in a central xz-plane in the body model.*

Figure 7.10: *Two domain system head-brain in a transverse gradient field (of 3.0 mT m^{-1} strength varying at frequency of 1 kHz), the scalar potential at: (a) the surface of the brain and the surface of the head (b). Current density modulus in the xy-plane for : (c) the two-compartment head-brain model and (d) the two concentric spheres model.*

The result obtained is compared to that produced using two concentric spheres of radii 0.07 m and 0.10 m (conductivities 1, 0.0125 Sm^{-1} respectively). The two spheres are shifted 0.05 m along the z-direction from the origi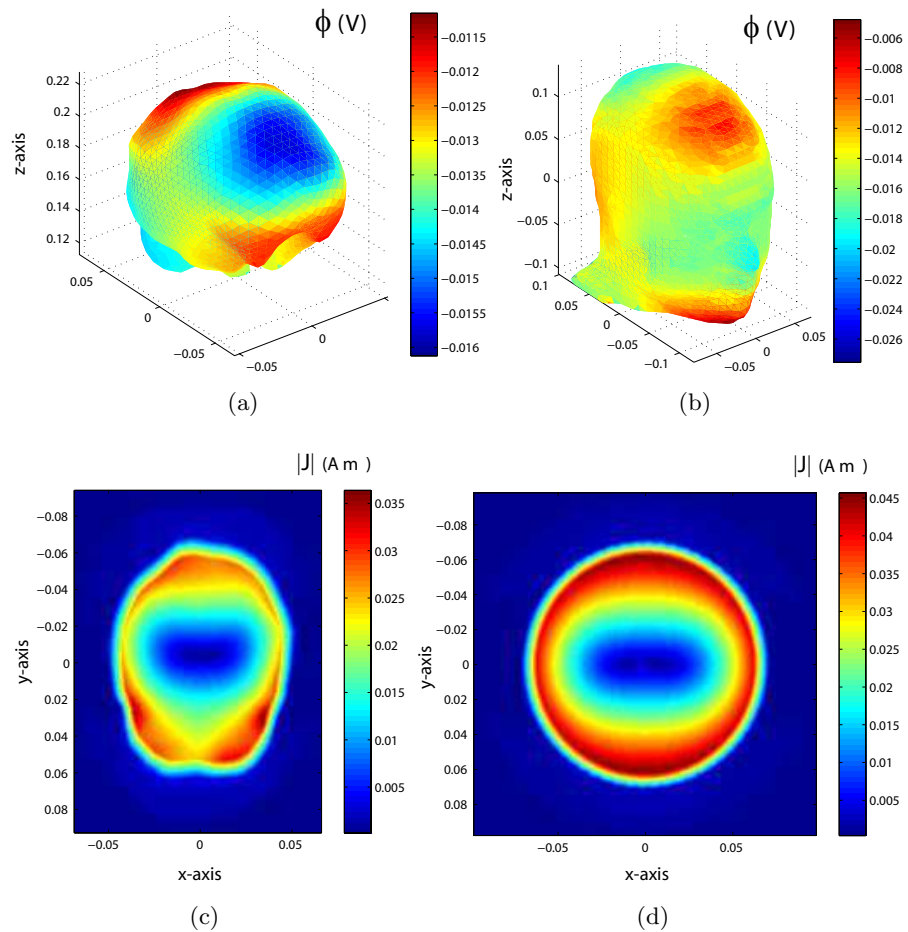n of the gradient field and form a simple model of the brain and scalp. Figures 7.10(c) and 7.10(d) provide the current distribution for the two-compartment head-brain model and the model consisting of two concentric spheres. It can be appreciated that although the two spatial current distributions span similar values, the irregular geometry of the head-brain system produces a different pattern.
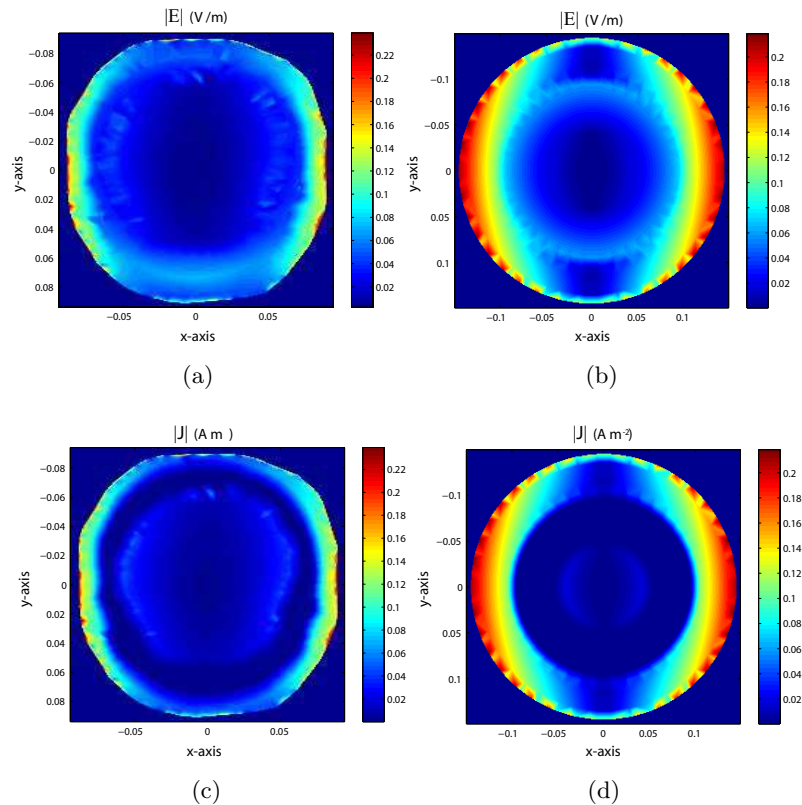
Figure 7.11: *Three domain models in a transverse field gradient: (a) electric field modulus in the xy-plane for the system scalp-skull-brain; (b) electric field modulus in the xy-plane for a 3 concentric spheres system; (c) current density modulus in the xy-plane for the system scalp-skull-brain; (d) current density modulus in the xy-plane for a 3 concentric spheres system.*

To provide a more realistic human head model, we can include a third sub-domain representing the scalp [114]. Simulations were carried out on a three-compartment scalp-skull-brain system (Fig. 6.12) of conductivities 1, 0.0125, and 1 Sm^{-1} when it is exposed to

the same transverse gradient, and the results are again compared to a three concentric sphere model centred at the origin of the field gradient with the same conductivity distribution and radii 0.05 , 0.10 and 0.15 m. Figure 7.11(a) and 7.11(b) show the modulus of the electric field induced in the central xy-plane; Fig. 7.11(c) and 7.11(d) the current density modulus and direction produced by the electric field in the same xy-plane. In both cases, the highest electric fields can be found in the outer sub-domain, and the current is negligible in the regions with the lowest conductivity.

Although the field patterns are not identical, the three concentric sphere model centred at the origin mimics reasonably well the E-field produced in a scalp-skull-brain human head model.

7.9   Three-domain rotating in a uniform field

Rotation of the three-compartment head model scalp-skull-brain model (Fig.6.12) (of conductivities 1, 0.0125 and 1 Sm^{-1}) about the x-axis, $\mathbf{\Omega} = 1$ (rad s $^{-1}$), in a uniform static magnetic field perpendicular to the axis of rotation and directed at $45°$ to the y-axis and z-axis $\mathbf{B} = 7(\hat{\boldsymbol{i}} + \hat{\boldsymbol{j}})$ (T) was also considered. The results were compared to those produced by a set of concentric spheres of radii 0.05 m, 0.10 and 0.15 m forming a simple model of the brain, skull and scalp.

Figures 7.12(a) and 7.12(b) show the modulus of the electric field induced in the central yz-plane; Fig. 7.12(c) and 7.12(d) the current density modulus produced by the electric field in the same yz-plane for the two models.

As expected the highest values of the current density are found in areas of higher conductivity, and electric field and current density patterns and peak values are quite similar for both models, so the three concentric model provides very valuable insight in understanding the distribution of the E-field inside a simple scalp-skull-brain human head model of the human head.
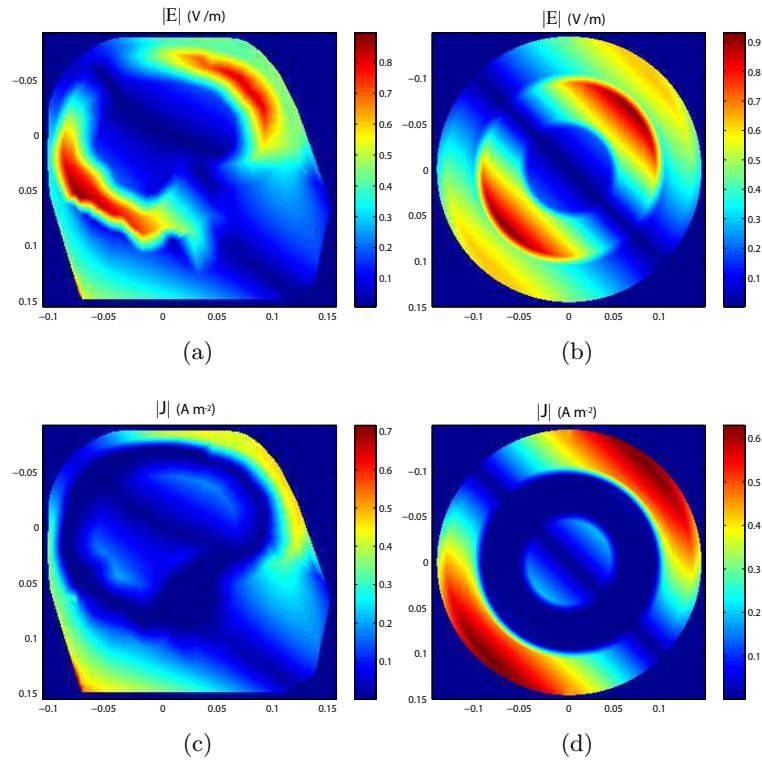
Figure 7.12: *Three domain model rotating ($\Omega = 1$ rad s^{-1}) in a uniform magnetic field ($\mathbf{B} = 7(\hat{\boldsymbol{i}}+\hat{\boldsymbol{j}})$) : (a) electric field modulus in the yz-plane for the system scalp-skull-brain; (b) electric field modulus in the yz-plane for a 3 concentric spheres system; (c) current density modulus in the yz-plane for the system scalp-skull-brain; (d) current density modulus in the yz-plane for a 3 concentric spheres system.*

7.10   Multi-domain head model moving in a field gradient

Translation of the three-compartment scalp-skull-brain model (conductivities 1, 0.0125 and 1 Sm^{-1}) with velocity $v = 1$ ms^{-1} in an ideal longitudinal field gradient (4.21 mTm^{-1}) was also studied. This can be related to real movements of workers or subjects close to the scanner where the main static field is not uniform.

Figures 7.13(a) and 7.13(b) show the electric field and current induced in a central xz-plane when the system is 0.1 m away from the origin in the negative z-direction.

(a)   (b)

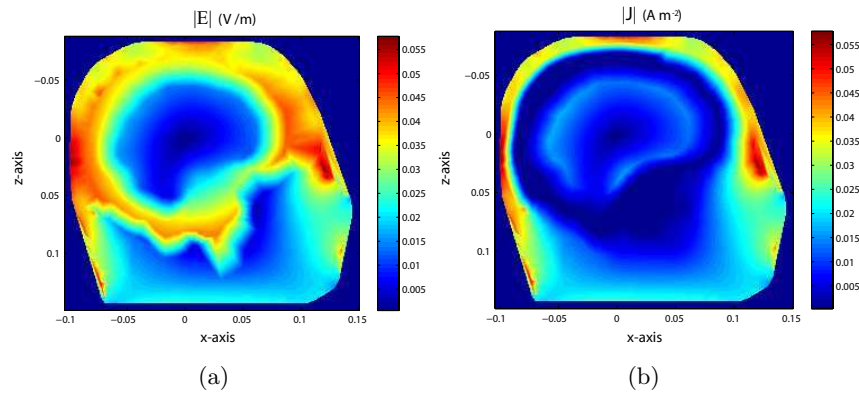Figure 7.13: *Three-compartment head model head-skull-brain model moving in a field gradient (4.21 mTm^{-1} amplitude varying sinusoidally at 500 Hz): (a) electric field modulus in the central xz-plane, (b) current density modulus in the central xz-plane .*

It can be seen how the biggest values of the electric field can be found in the region between scalp and skull.

7.11   Electric potential produced by a dipole in a homogeneous sphere

The formulation presented here was also applied to a direct EEG problem to find the potential produced by a dipole of components

$$(p_x, p_y, p_z) = (10^{-8}, 10^{-8}, 10^{-8})C \ m, \tag{7.8}$$

sited in a homogeneous sphere of radius 0.2 m. We compared the results of constant BEM calculations to analytical results described in Yao's paper [127] when the position of the dipole is shifted 0.1 m from the origin of the sphere along the positive y-axis.
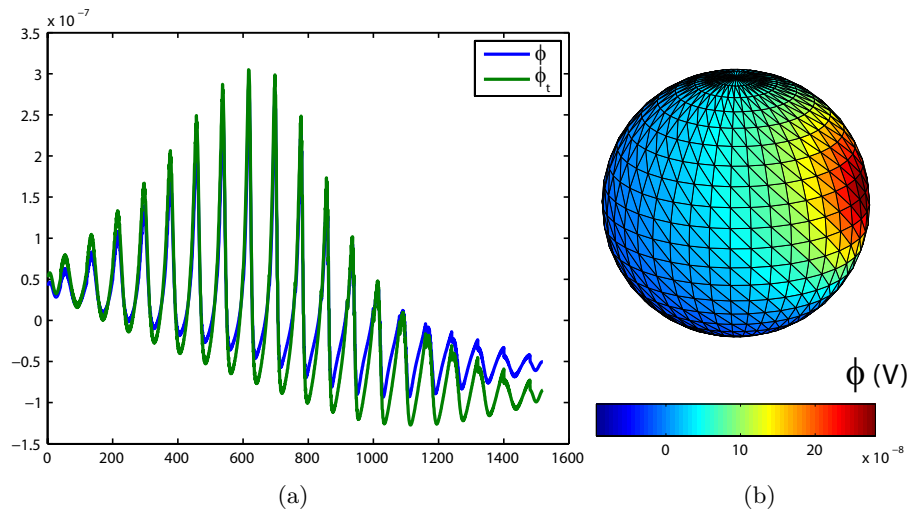
Figure 7.14: *(a) Calculated values of ϕ for a spherical mesh of 1520 elements and analytically calculated scalar potential, ϕ_t at each mesh element; (b) colour coded variation of the calculated potential at the surface of the meshed sphere.*

Figure 7.14(a) shows the good agreement of the numerically computed and analytical values. BEM is also well suited to the forward problem solution is brain electromagnetic source imaging as in EEG.

7.12 Pseudo Electromotive Term

Finally, we used the BEM code to investigate the importance of using $\mathbf{v} \times \mathbf{B}$ instead of $-(\mathbf{v} \cdot \nabla)\mathbf{A}$ as the electromotive term in some simple examples, as discussed in Chapter 5.

7.12.1 Rotation of a sphere in a uniform magnetic field

First we considered the homogeneous conducting sphere described in Section 7.4 rotating in a uniform static magnetic field applied perpendicular to the axis of rotation. A suitable choice for the magnetic vector potential is

$$\mathbf{A} = \frac{B}{2}[-y\hat{\mathbf{i}} + x\hat{\mathbf{j}}] \tag{7.9}$$

Figure 7.15 shows the corresponding three-dimensional plot of the field at the periphery of the conductor calculated using a constant BEM when $\mathbf{v} \times \mathbf{B}$ (Fig. 7.15(a)) or $-(\mathbf{v} \cdot \nabla)\mathbf{A}$ (Fig. 7.15(b)) are used as the electromotive term. The field strength for the second case is half that obtained using $\mathbf{v} \times \mathbf{B}$. The field obtained using $\mathbf{v} \times \mathbf{B}$ as a driving term is in agreement with the theoretical predictions discussed in Section 5.7.
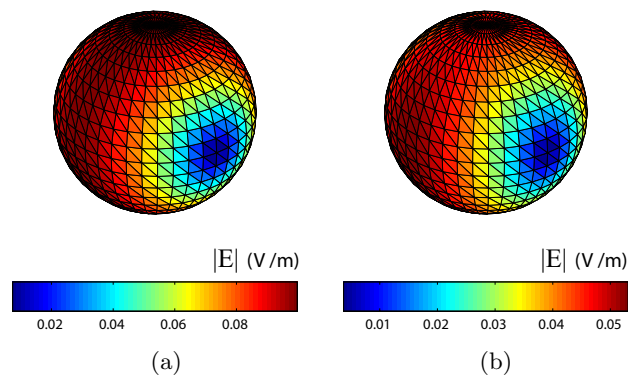
Figure 7.15: *Three-dimensional plot of* $|\boldsymbol{E}|$ *for a single spherical conductor discretized into 1520 elements computed by employing a BEM and (a) using* $\boldsymbol{v} \times \boldsymbol{B}$*, or (b)* $-(\boldsymbol{v} \cdot \nabla)\boldsymbol{A}$*.*

Clearly, both driving terms produce similar patterns of the spatial distributions of induced E-field. However, the calculated peak values of the electric field differs significantly from one case to another. Therefore for simulation of rotations the use of the pseudo electromotive term may lead to incorrect values for the electric field induced.

7.12.2   Rotation of an infinite cylinder in a uniform magnetic field

We then considered a homogeneous conducting cylinder of height 10 m and radius 0.05 m (this can be considered to be an approximation to an infinite cylinder where end effects may be disregarded) with no net charge, rotating ($\Omega = 1\ rad\ s^{-1}$) about the axis of the cylinder (z-direction) in a uniform magnetic field parallel to the z-axis of B=1 T. A plausible choice for **A** is again

$$\mathbf{A} = \frac{B}{2}[(x-y)\hat{\mathbf{i}} + (x-y)\hat{\mathbf{j}}]. \tag{7.10}$$

This rotation produces a negative uniform volume charge density which generates an electric field that, in the case of $\mathbf{v} \times \mathbf{B}$, cancels out completely with the electromotive term so there is no net current flowing in the cylinder.

The colour-coded map of the field produced in a central xy-plane by the volume charge calculated using a constant BEM is shown in Fig. 7.16(a) when $\mathbf{v} \times \mathbf{B}$ or in Fig. 7.16(b) when $-(\mathbf{v} \cdot \nabla)\mathbf{A}$ are considered as electromotive terms.

(a)   (b)
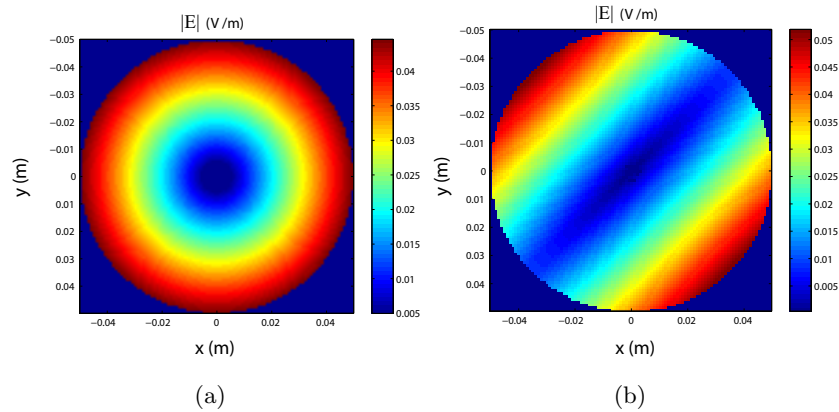
Figure 7.16: *Electrostatic $|\boldsymbol{E}|$ produced by the volume charges in an xy-plane inside the cylinder discretized into 1600 elements, rotating in a uniform magnetic field of 1T at a rate of $1\ rad\ s^{-1}$ (a) BEM computed electric field modulus produced by the charges using $\boldsymbol{v} \times \boldsymbol{B}$, (b) BEM computed electric field modulus produced by the charges using $-(\boldsymbol{v} \cdot \nabla)\boldsymbol{A}$.*

7.12.3   Three-domain rotating in a uniform field

Finally the rotation of the three-compartment scalp-skull-brain model (Fig.6.12) of conductivities 1, 0.0125 and 1 Sm^{-1}, about the x-axis, $\boldsymbol{\Omega} = 1$ (rad s $^{-1}$), in a uniform static magnetic field applied perpendicular to the axis of rotation and directed along the z-axis

$\mathbf{B} = 10(\hat{\boldsymbol{k}})$ (T) was also considered. A plausible choice for $\mathbf{A}$ is again

$$\mathbf{A} = \frac{10}{2}[-y\hat{\mathbf{i}} + x\hat{\mathbf{j}}]. \tag{7.11}$$

(a) (b)
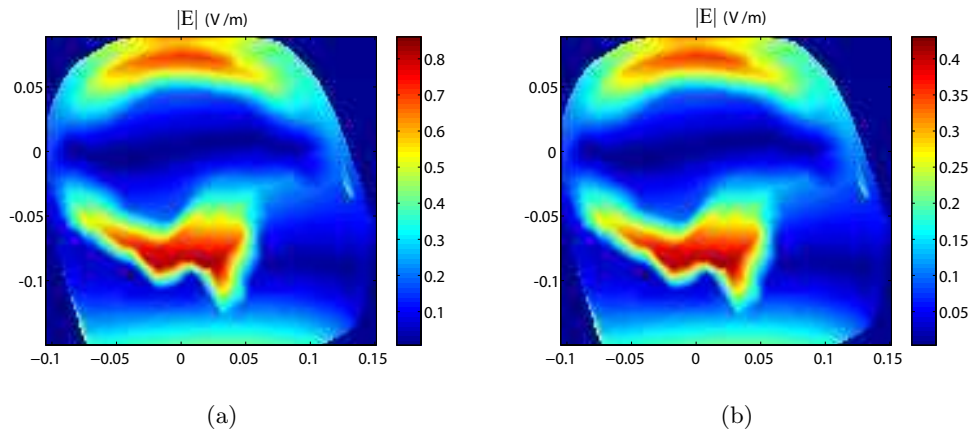
Figure 7.17: *Electric field modulus in the* xz-*plane for the scalp-skull-brain system rotating in a uniform static magnetic field perpendicular to the axis of rotation computed using (a)* $\boldsymbol{v} \times \boldsymbol{B}$ *and (b)* $-(\boldsymbol{v} \cdot \nabla)\boldsymbol{A}$.

Figure 7.17(b) shows the electric field produced in xz-plane by this rotation using the pseudo-electromotive term $-(\mathbf{v} \cdot \nabla)\mathbf{A}$, these values of this calculation are half of those produced using correct $\mathbf{v} \times \mathbf{B}$ electromotive term Fig. 7.17(a).

The current density patterns and peak values are quite different for both cases. So once again, it is clear that for simulation of rotations the use of the pseudo electromotive term may lead to incorrect values for the electric field induced.

Summary

It is clear then that when simulating the effect of translation and rotation in static magnetic fields it is necessary to use $\boldsymbol{v} \times \boldsymbol{B}$ *rather* $-(\boldsymbol{v} \cdot \nabla)\boldsymbol{A}$ *as the driving term.*

7.13 Numerical implementation

Software was written in Fortran 90 to implement the constant BEM approach for the calculation of the electric fields induced in the human body by temporally varying magnetic field gradients and by motion in the strong static fields.

The results of the simulations have been tested by comparison with analytic solutions for basic-shaped objects (spheres or cylinder) forming a single domain exposed to switched gradients or moving in simple static fields. This comparison demonstrates the similarity of the theoretical and the numerical values.

For a spherical surface meshed using 1520 elements, the calculations took 2 minutes to run on a PC dual Pentium III motherboard 2x850 MHz, whereas for 360 elements the computation time was less than 5 seconds. In this case the solution of the system of equations is the most time demanding process, as the computation time taken for this step grows approximately as n^3.

7.14 Number of Mesh Elements and Precision

A known disadvantage of BEM is the precision drop when the distance of the field point to the boundary is comparable to the size of the element. So, in general, a finer mesh typically results in a more accurate solution. However, as a mesh is made finer, the computation time increases. Let us illustrate this fact by considering a head model which is made up of a multilayered concentric spheres [81], where the radius of sphere representing the skin is, R=100 mm.

If all the N triangular mesh elements have similar size, we can define a characteristic element area, a, as

$$a = \frac{4\pi R^2}{N}.$$ (7.12)

which also reflects the distance from a mesh element at which the calculated fields deviate significantly from expected values.

If we define l as a characteristic element size then

$$\frac{l^2}{2} = \frac{4\pi R^2}{N}$$ (7.13)

so

$$N = 8\pi \left(\frac{R}{l}\right)^2.$$ (7.14)

So, for example, if the distance between two of the tissue layers of the model is 5 mm

we may need more than 10^4 elements in the spherical meshes, which is approximately the maximum number of elements used in this thesis.

The number of element in the mesh increases (and hence the computation time which is proportional to N^3) dramatically when there is an increment in the required precision.

For large numbers of mesh elements it is then suitable to consider the use of techniques such the domain decomposition method (DDM) or the fast multi-pole method (FMM), which could reduce the computational time [130].

Chapter 8

Conclusions

8.1 Summary

The work presented in this thesis has involved investigation of problems in electromagnetism of relevance to MRI. A mathematical formalism has been established that allows the numerical solution of both forward and inverse electromagnetic problems, via boundary element method (BEM); and computer software capable of efficiently carrying out BEM calculations has been developed.

The numerical technique has been applied to two main areas corresponding to different frequencies of field variation

(A) An inverse BEM approach which has been developed to solve the magneto-static problem.

(B) A forward BEM approach which has been developed to solve the quasi-static problem.

The Boundary Element Stream Function Method (BESFM) is the inverse approach which has been used to design novel gradient coils for MRI. An extension of the BESFM has also been developed and employed to design gradient coils potentially allowing higher rates of change of gradient to be achieved without causing peripheral nerve stimulation. BESFM relies on the use of a general technique created to obtain current density over a given surface which satisfies the continuity equation.

The forward BEM suitable for the quasi-static regime has been developed and used to calculate the electric fields induced in the human body by temporally varying magnetic field gradients employed in MRI and by motion in the strong static fields produced around MR scanners. This approach is based on an integral formulation of the Laplace's and Poisson's equations and an appropriate electromagnetic description of the problem.

In this work, the experimental results confirm a significant number of advantages of the proposed BEM compare to previous methods such us FDTD, as it provides a new framework for solving both forward and inverse electromagnetic problems.

The BESFM provides a solid mathematical framework for gradient coil design, allowing the production of torque-balanced coils of minimum inductance with a wide variety of shapes and geometries.

The incorporation of the window is an advantage compared with conventional coils as it facilitates interaction with the subject.

Flat and quadratic curved elements used in BESFM both produce effective solutions, although the particular BEM approximation for which convergence occurs at the smallest number of elements will depend on the particular geometry of the coil design. The best choice of element type for very large number of mesh elements seems to be the linear isoparametric approximation, which produces effective solutions with a computational time that is significantly shorter than for other approximations.

The extension of the BESFM to coil designs where the vector potential is minimized over a prescribed region can significantly reduce the electric field induced and hence the peripheral nerve stimulation, as the numerical simulations presented using BEM have shown.

The forward BEM techniques reported here can be applied to modeling of the currents induced in tissue at low frequencies and should be valuable in the study of bio-effects due to high static field and rapidly switched magnetic field. For the examples analysed, the accuracy of the proposed method has been demonstrated by comparison with analytic solutions for basic-shaped objects forming a single domain exposed to switched gradients or moving in simple static fields.

In addition, the need to employ an appropriate electromagnetic theory (Faraday's Law for a moving system) for understanding the interactions between strong static magnetic fields and the human body has been demonstrated. In particular, it has been shown that when simulating the effect of translation and rotation in static magnetic fields it is necessary to use $\mathbf{v} \times \mathbf{B}$ rather than $-(\mathbf{v} \cdot \nabla)\mathbf{A}$ as the driving term.

8.2 Future Work

Future work will include

- Investigating new current distributions based on different type of elements. The particular symmetry of some coil geometries can be incorporated in the choice of the element to improve the IBEM.

- The general technique created to obtain divergence-free current density over a given surface can be exported for other applications outside of the area of MRI. Many areas in industrial engineering such as the design of multi-poles used in particle accelerators.

- For large numbers of mesh elements the computational time could be reduced by employing either the domain decomposition method (DDM) or the fast multi-pole method (FMM).

- Applying the mathematical formalism developed for the magneto- static forward problem to higher orders of element.

- By incorporating BESFM into the integral formulation developed for the quasi-static problem, we can achieve an inverse BEM suitable for the quasi-static regime, which could be used to design gradient coils in which the induced electric field rather than rate of change of vector potential is minimized, thus reducing the likelihood of peripheral nerve stimulation.

Appendix A

Generalized Faraday's law.

The following derivation is based on the demonstration developed by Lorrain [103]. To deduce Eq. 5.6 the surface is fixed in space and the only change of flux results from the variation of $\mathbf{B}$. If the system now moves with velocity $\mathbf{v}$ there is a new variation of flux resulting from the movement of the path of integration, and the time derivative and the integral do not commute

$$\frac{d\Phi}{dt} = \frac{\int_{S(t+dt)} \mathbf{B}(t+dt) \ d\mathbf{S} - \int_{S(t)} \mathbf{B}(t) \ d\mathbf{S}}{dt} \tag{A.1}$$

if we consider only the first order expansion

$$\mathbf{B}(t+dt) \approx \mathbf{B}(t) + \frac{\partial \mathbf{B}(t)}{\partial t} dt \tag{A.2}$$

then

$$\frac{d\Phi}{dt} = \frac{\int_{S(t+dt)} \mathbf{B}(t) \ d\mathbf{S} - \int_{S(t)} \mathbf{B}(t) \ d\mathbf{S}}{dt} \\ + \frac{\int_{S(t)} \frac{\partial \mathbf{B}(t)}{\partial t} \ dt \ d\mathbf{S}}{dt} \tag{A.3}$$

But since $\nabla \cdot \mathbf{B} = 0$ the flux through the volume defined by the displacement of the integration path C is

$$\oint_{Surface} \mathbf{B} \ d\mathbf{S} = \int_{S(t+dt)} \mathbf{B} \ d\mathbf{S} - \int_{S(t)} \mathbf{B} \ d\mathbf{S} \\ + \int_{side} \mathbf{B} \ d\mathbf{S} = 0 \tag{A.4}$$
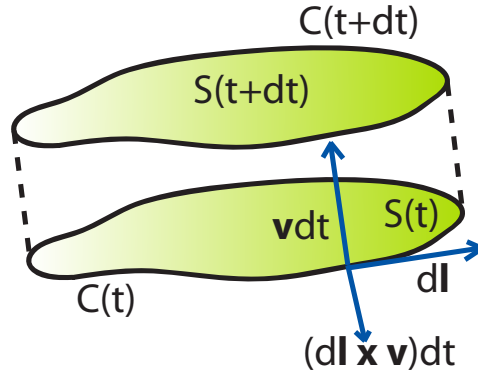
Figure A.1: *Volume defined by the displacement of the integration path C in a time t to t+dt with a velocity v.*

and

$$\int_{side} \mathbf{B} \; d\mathbf{S} = \oint_C \mathbf{B} \; d\mathbf{l} \times (\mathbf{v}dt) = -dt \oint_C (\mathbf{v} \times \mathbf{B}) \; d\mathbf{l} \tag{A.5}$$

substituting

$$\frac{d\Phi}{dt} = \oint_C (\mathbf{v} \times \mathbf{B}) \; d\mathbf{l} - \int_{S(t)} \frac{\partial \mathbf{B}}{\partial t} \; d\mathbf{S} \tag{A.6}$$

$$\int_S \nabla \times \mathbf{E'} \; d\mathbf{S} = \int_S \left[-\frac{\partial \mathbf{B}}{\partial t} + \nabla \times (\mathbf{v} \times \mathbf{B}) \right] d\mathbf{S} \tag{A.7}$$

and since S may be any surface bounded by C finally

$$\nabla \times \mathbf{E'} = -\frac{\partial \mathbf{B}}{\partial t} + \nabla \times (\mathbf{v} \times \mathbf{B}) \tag{A.8}$$

Note that in this derivation it has been assumed that the loop is rigid, but this result holds for any other circuit.

Appendix B

Publications

The following publications have arisen from the work described in this thesis

Journal Papers

1 L. Marin, H. Power, R.W. Bowtell, C. Cobos Sanchez, A.A. Becker, P. Glover and I.A. Jones, *Numerical solution for an inverse MRI problem using a regularized boundary element method*, (Special Issue) Engineering Analysis with Boundary Elements 2007.

2 L. Marin, H. Power, R.W. Bowtell, C. Cobos Sanchez, A.A. Becker, P. Glover and I.A. Jones, *Boundary element method for an inverse problem in magnetic resonance imaging gradient coils*, Computer Methods in Engineering & Sciences, CMES 2007.

3 C. Cobos Sanchez, P. Glover, H. Power, L. Marin, A.A. Becker, I.A. Jones and R.W. Bowtell, *Forward electric field calculation using BEM for time-varying magnetic field gradients and motion in strong static fields*, submitted (Engineering Analysis with Boundary Elements).

4 C. Cobos Sanchez, H. Power, P. Glover, L. Marin, A.A. Becker, I.A. Jones and R.W. Bowtell, *Electromagnetic formalism for calculation of electric fields generated by magnetic fields used in MRI.*, in progress.

5 C. Cobos Sanchez, H. Power, P. Glover, L. Marin, A.A. Becker, I.A. Jones and R.W. Bowtell, *Coil design using a quasi-static IBEM*, in progress.

Conference Abstracts

1 C. Cobos Sanchez, L. Marin, H. Power, R.W. Bowtell, A.A. Becker, P. Glover and I.A. Jones, Application of higher-order boundary element method to gradient coil design,

British Chapter of the International Society for Magnetic Resonance in Medicine (ISMRM 2006), 12th Annual Meeting, University of Surrey, Guildford, UK, 23-25 August 2006. (Poster)

2 C. Cobos Sanchez, L. Marin, H. Power, R.W. Bowtell, A.A. Becker, P. Glover and I.A. Jones, Application of high-order boundary element method to gradient coil design, Paper 737, 23rd Annual Scientific Meeting of the European Society for Magnetic Resonance in Medicine and Biology (ESMRMB 2006), Warsaw, Poland, 21-23 September 2006. (Talk)

3 C. Cobos Sanchez, P. Glover, H. Power, L. Marin, A.A. Becker, I.A. Jones and R.W. Bowtell, Boundary element method for calculation of induced electric fields in quasi-static regime , ISMRM Workshop on Advances in High Field MR, 25-28 March 2007 at Asilomar in Pacific Grove, California, USA. (Poster)

4 C. Cobos Sanchez, P. Glover, H. Power, L. Marin, A.A. Becker, I.A. Jones and R.W. Bowtell, Boundary element method for induced electric fields due to switched magnetic field gradients and movement in strong static fields, International Society for Magnetic Resonance in Medicine (ISMRM 2007), 16th Annual Meeting, Berlin, Germany, 19-25 May 2007. (Poster)

Bibliography

[1] E. M. Purcell, H. C. Torrey, and R. V. Pound. *Resonance absorption by nuclear magnetic moments in a solid.* Physical Review, 69:37−38, 1946.

[2] F. Bloch. Nuclear induction. Physical Review, 70:460−474, 1946.

[3] P. Mansfield and P. K. Grannell. *NMR diffraction in solids?.* Journal of Physics C: Solid State Physics, 6:L422−426, 1973.

[4] P. C. Lauterbur. *Image formation by induced local interactions: Examples employing nuclear magnetic resonance.* Nature, 242:190−191, 1973.

[5] M. A. Jaswon, and A. R Ponter,: *An integral equation solution of the torsion problem,* Proc. Roy. Soc. Series A 273−237 (1963)

[6] G. T. Symm: *Integral equation methods in potential theory 2,* Proc. Roy. Soc. Series A 275−33 (1963).

[7] Morse P M and Feshbach H (1953). *Methods of Theoretical Physics*, Part I. *New York: McGraw-Hill*

[8] R. Turner. *Gradient coil design: A review of methods, Magn.Reson.Imaging* , (1993) **11**, 903 − 920.

[9] J.M. Jin. *Electromagnetic Analysis and Design in Magnetic Resonance Imaging.* CRC Press LLC, (1998).

[10] F. Romeo, D.I. Hoult . *Magnetic field profiling: analysis and correcting coil design.* Magn.Reson.Med, (1984) **1**, 44 − 65.

[11] R. Turner, R. M. Bowley. *Passive screening of switched magnetic field gradients.* *J.Phys.E,*(1986) **19**, 876 − 879.

[12] P. Mansfield, B. Chapman. *Multishield active magnetic screening of coil structures in NMR*, Journal of marnetic resonance 72 (1987), 211−223.

[13] R. Bowtell and P. Mansfield. *Gradient coil design using active magnetic screening.* Magnetic Resonance in Medicine 17 (1998), 15−21.

[14] D. J. Schaefer, J. D. Bourland, and J. A. Nyenhuis, *Review of patient safety in time-varying gradient fields*, J. Magn. Reson. Imag., vol. 12, pp. 20−29, 2000.

[15] J. A. Nyenhuis, J. D. Bourland,A. V. Kildishev, and D. J. Schaefer, *Health effects and safety of intense MRI gradient fields*, Magnetic Resonance Procedures: Health Effects and Safety, 1 ed, F. G. Shellock, Ed. Cleveland, OH: CRC, 2001, pp. 31−52.

[16] P. R. Harvey and E. Katznelson, *Modular gradient coil: A new concept in high-performance whole-body gradient coil design.* Magn. Reson. Med. (1999) 42: 561−570.

[17] D. L. Parker ans J. R. Hadley. *Multiple-region gradient arrays for extended field of view, Increased performance, and reduced nerve stimulation in magnetic resonance imaging.* Magnetic Resonance in Medicine, 56, 1251−1260, (2006).

[18] R.A. Hedeen, W. A. Edelstein. *Characterization and prediction of gradient acoustic noise in MR imagers.* Magn Reson Med 1997; 37: 7−10.

[19] P. Mansfield, P.M. Glover and J. Beaumont . *Sound generation in gradient coil structures for MRI.* Magn Reson Med 1998; 39:539−550.

[20] M. E. Quirk, A. J. Letendre, R. A. Ciottone and J. F. Lingley. *Anxiety in patients undergoing MR imaging.* Radiology 1989; 170:463−466.

[21] P. Mansfield, B. Haywood. *Principles of active acoustic control in gradient coil design.* MAGMA 2000; 10:147−151.

[22] R. Bowtell and P. Mansfield. *Quiet Transverse Gradient Coils: Lorentz Force Balanced Designs Using Geometrical Similitude.* Magn Reson Med. 1995 Sep; 34(3):494−7.

[23] P. Mansfield, B. Haywood and R. Coxon. *Active acoustic control in gradient coils for MRI.* Magn Reson Med 2001; 46:807−818.

[24] D.L. Price, J.P. De Wilde, J.A. Williams, I. Delakis, C. Renaud, Proc. ISMRM Safety Workshop, Munich, Germany 2003.

[25] J.D. Jackson, *Classical Electrodynamics, Wiley*, New York, 1962

[26] M. J. Golay (1957). Magnetic field control apparatus. *U.S.patent 3, 515, 979*

[27] B. H. Suits and D.E. J Wilken, *Improving magnetic field gradient couls for NMR imagin*, Phys E: Sci. Instrum, 22:565−573; 1989.

[28] H. Siebold, *Design optimization of main gradient and RF field coils for MR imagin*, IEEE Trans. Magn 26:897−900; 1990.

[29] D. I. Hoult and R. Deslauriers. *Accurate Shim-Coil Design And Magnet-Field Profiling By A Power-Minimization-Matrix Method*. Journal of Magnetic Resonance Series A, 108(1), 9−20, (1994).

[30] M. A. Brideson, L. K. Forbes, and S. Crozier. *Determining Complicated Winding Patterns for Shim Coils Using Stream Functions and the Target-Field Method*. Concepts in Magnetic Resonance, 14(1), 9−18, (2002).

[31] J. F. Schenck, M. A. Hussein and W. Eldestein *Transverse gradient field coils for nuclear magnetic imagin*. (1987), U.S. Patent 4, 646,024.

[32] R. Turner. *A Target Field Approach To Optimal Coil Design*. Journal of Physics D: Applied Physics, 19(8), L147−L151, (1986).

[33] M. Engelsberg, R. E. D. Souza and C. M. D. Pazos. *The Limitations Of A Target Field Approach To Coil Design*. Journal of Physics D: Applied Physics, 21(7), 1062−1066, (1988).

[34] Bracewell R N (1986). *The fourier transform and its applications*. New York: McGraw-Hill

[35] R. Turner. *Minimum Inductance Coils*. Journal of Physics E: Scientific Instruments, 21(10), 948−952, (1988).

[36] R. Bowtell, P. Mansfield . *Minimum power flat gradient gradients pair for NMR microscopy*. (1989), Design and evaluation of shielded gradient coils, 977 − 990.

[37] J. W. Carlson, K. A. Derby, K. C. Hawryszko, and M. Weideman. *Design And Evaluation Of Shielded Gradient Coils*. Magnetic Resonance in Medicine, 26(2), 191−206, (1992).

[38] M. Poole and R. Bowtell. Short, *Low Inductance Insert Shim Coils Designed Using the Slack Method*. Proceedings of the International Society for Magnetic Resonance in Medicine, 13, 775, (2005).

[39] S. Crozier and M. Doddrell. *Gradient Coil Design by Simulated Annealing* . Journal of Magnetic Resonance Series A, 103, 354−357, (1993).

[40] S. Crozier. *Design of shielded quadrupolar gradient coils for magnetic resonance microscopy by simulated annealing.* IEEE Transactions on Magnetics, 30(6), 4311−4313, (1994).

[41] K. Adamiak, A. J. Czaja, and B. K. Rutt. *Optimizing Strategy For MR-Imaging Gradient Coils.* IEEE Transactions on Magnetics, 30(6), 4311−4313, (1994).

[42] H. Liu and L. S. Petropoulos. *Spherical Gradient Coil For Ultrafast Imaging.* The 41st Annual Conference On Magnetism And Magnetic Materials, 81(8), 3853−3855, (1997).

[43] D. Green, J. Leggett, and R. Bowtell. *Hemispherical Gradient Coils For Magnetic Resonance Imaging.* Magnetic Resonance in Medicine, 54(3), 656−668, (2005).

[44] J. Leggett, D. Green, and R. Bowtell. Insert Dome Gradient Coils for Brain Imaging. Proceedings of the International Society for Magnetic Resonance in Medicine, 14, 779, (2006).

[45] K. Yoda. Analytical *Design Method of Self-Shielded Planar Coils.* Journal of Applied Physics, 67(9), 4349−4353, (1990).

[46] R. Bowtell and P. Mansfield. *Gradient Coil Design Using Active Magnetic Screening.* Magnetic Resonance in Medicine, 17(1), 15−9; (1991).

[47] M. A. Martens, L. S. Petropoulos, R. W. Brown, J. H. Andrews, M. A. Morich, and J. L. Patrick. *Insertable Biplanar Gradient Coils For Magnetic Resonance Imaging.* Review of Scientific Instruments, 62(11), 2639−2645, (1991).

[48] H. Liu. *Finite Size Bi-Planar Gradient Coil for MRI.* IEEE Transactions on Magnetics, 34(4), 2162−2164, (1998).

[49] H. Liu and C. Truwit. *True Energy-Minimal and Finite-Size Biplanar Gradient Coil Design for MRI.* IEEE Transactions on Medical Imaging, 17(5), 826−830, (1998).

[50] L. Forbes and S. Crozier. *Novel Target-Field Method For Designing Shielded Biplanar Shim And Gradient Coils.* IEEE Transactions on Magnetics, 40(4), 1929−1938, (2004).

[51] L. Forbes, M. Brideson, and S. Crozier. *A Target-Field Method To Design Circular Biplanar Coils For Asymmetric Shim And Gradient Fields.* IEEE Transactions on Magnetics, 41(6), 2134−2144, (2005).

[52] V. Vegh, H. Sanchez, I. M. Brereton, and S. Crozier. *Toward Designing Asymmetric Head Gradient Coils for High-Resolution Imaging.* Concepts in Magnetic Resonance Part B: Magnetic Resonance Engineering, 31B(1), 1−11, (2007).

[53] V. Vegh, H. W. Zhao, I. M. Brereton, G. J. Galloway, and D. M. Doddrell. *A Wave Equation Technique for Designing Compact Gradient Coils.* Concepts in Magnetic Resonance Part B: Magnetic Resonance Engineering, 29B(2), 62−74, (2006).

[54] D. Tomasi, *Stream function optimization for gradient coil design*, Magnetic Resonance in Medicine 45 (1986) 505−512.

[55] S. Pissanetzky. *Minimum energy MRI gradient coil of general geometry*, Measurement of Science Technology 3 (1992).

[56] R. A. Lemdiasov and R. Ludwig. *A Stream Function Method For Gradient Coil Design.* Concepts in Magnetic Resonance Part B: Magnetic Resonance Engineering, 26B(1), 67−80, (2005).

[57] T. F. Eibert and V. Hansen. *On The Calculation Of Potential Integrals For Linear Source Distributions On Triangular Domains.* IEEE Transactions On Antennas And Propagation, 43(12), 1499−1502, (1995).

[58] G. N. Peeren. *Stream Function Approach For Determining Optimal Surface Currents.* Journal of Computational Physics, 191(1), 305−321, (2003).

[59] M. Poole. *Improved Equipment and Techniques for Dynamic Shimming in High Field MRI.* PhD thesis, University of Nottingham, (2007).

[60] M. Poole and R. Bowtell. Novel Gradient Coils Designed Using a Boundary Element Method. Concepts in Magnetic Resonance Part B: Magnetic Resonance Engineering, (2007).

[61] C. H. Moon, H. W. Park, M. H. Cho, and S. Y. Lee. Design of Convex-Surface Gradient Coils for a Vertical-Field Open MRI System. Measurement Science and Technology, 11(8), N89−N94, (2000).

[62] C. Cobos Sanchez, L. Marin, R. W. Bowtell, H. Power, P. Glover, A. A. Becker, and I. A. Jones. Application of Higher-Order Boundary Element Method to Gradient Coil Design. Proceedings of the British Chapter of the International Society for Magnetic Resonance in Medicine, 12, P23, (2006).

[63] F. París and J. Cañas , *Boundary Element Method: Fundamentals and Applications*. Oxford Science Publications, 1997.

[64] C.A. Brebbia, J.F.C. Telles and L.C. Wrobel (1984), *Boundary Element Techniques*. Springer-Verlag, 1984.

[65] A. N. Tiknonov and V. Y. Arsenin. *Methods for solving ill-posed problems*. Moscow: Nauka; 1986.

[66] M. Bencsik, R. Bowtell and R.M. Bowley, *Using the vector potential in evaluating the likelihood of peripheral nerve stimulation due to switched magnetic field gradients*, Magn. Reson. Med.50 405−410, 2003

[67] L. Marin, H. Power, R.W. Bowtell, C. Cobos Sanchez, A.A. Becker, P. Glover and I.A. Jones, *Numerical solution for an inverse MRI problem using a regularized boundary element method*, (Special Issue) Engineering Analysis with Boundary Elements 2007.

[68] M. Kamon, M. J. Tsuk, and J. K. White. FASTHENRY: A Multipole-Accelerated 3-D Inductance Extraction Program. IEEE Transactions on Microwave Theory and Techniques, 42, 1750−1758, (1994).

[69] S. Hidalgo-Toobon, M. Bencsik, R. W. Bowtell. *Reduction of peripheral nerve stimulation via the use of combined gradient and uniform field coils*. Proceedings of the International Society for Magnetic Resonance in Medicine, 659, (2004).

[70] W. Wang and S. R. Eisenberg, *A three-dimensional finite element method for computing magnetically induced currents in tissues*, IEEE Trans. Magnetics, 30 5015−5023, 1994

[71] TW Dawson and MA Stuchly, *Analytic validation of a three-dimensional scalar-potential finite-difference code for low frequency magnetic induction*, Applied Computational Electromagnetics Society, 1996:11:72−81.

[72] P. M. Poman, M. A. Stuchly and J. A. Nyenhuis, *Peripheral Nerve Stimulation by Gradient Switching Fields in Magnetic Resonance Imaging*, IEEE Trans. Biomed. Eng. 51, 1907−1914, 2004

[73] N. Orcutt and O. P. Gandhi (1988), *A 3D impedance method to calculate power depo-sition in biological bodies subjected to time-varying magnetic fields*, IEEE Transactions on Biomedical Engineering 35, (1988), 577−583.

[74] MA. Stuchly and OP. Gandhi, *Inter-laboratory comparison of numerical dosime-try for human exposure to 60 Hz electric and magnetic fields.* Bioelectromagnetics 2000;21:167−174.

[75] M. Bencsik, R. Bowtell and R.M. Bowley, *Electric fields induced in a spherical vol-ume conductor by temporally varying magnetic field gradients*, Phys. Med. Biol .47, 557−576, 2002

[76] R. Bowtell and R.M. Bowley *Analytic calculations of the E-fields induced by time-varying magnetic fields generated by cylindrical gradient coils*, Magn. Reson. Med.44 782−90, 2000

[77] Forbes LK, Crozier S, *On a possible mechanism for peripheral nerve stimulation during magnetic resonance imaging scans*, Phys Med Biol 2001;46:591−608.

[78] P.T. While and L.K. Forbes, *Electromagnetic fields in the human body due to switched transverse gradient coils in MRI*, Phys Med Biol 49 (2004) 2779−2798.

[79] Brand M, Heid O, *Induction of electric fields due to gradient switching: a numerical approach*, Magn Reson Med 2002;48:731−734.

[80] O.P. Gandhi and X.B:Chen, *Specific absorption rates and induced current densities for an anatomy-based model of the human for exposure to time-varying magnetic fields of MRI*, Magn. Reson. Med. 41 816−23,1999.

[81] F. Liu and S. Crozier, *A distributed equivalent magnetic current based FDTD method for the calculation of the E-fields induced by gradient coils*, J. Magn. Reson. 169 323−7, 2004

[82] F. Liu, H. Zhao and S. Crozier, *On the induced electric field gradients in the human body for magnetic stimulation by gradient coils in MRI*, IEEE Trans. Biomed. Eng. 50 804−15, 2003

[83] F. Liu, S. Crozier, H. Zhao and B. Lawrence *Finite-difference time-domain-based studies of MRI pulsed field gradient-induced eddy currents inside the human body*, Concepts Magn. Reson. 15 26−36,2002

[84] F. Liu, S. Crozier, H. Zhao and B. Lawrence *An improved quasi-static finete-difference scheme for induced field evaluation in MRI based on the bincojugate gradient method*, Proceedings of the 29th conference of the IEEE EMBS. 487−490, 2007

[85] S. Crozier, H. Wang, A. Trakic and F. Liu , *Exposure of Workers to Pulsed Gradients in MRI*, Journal of Magnetic Resonace, 26:1236−1254 (2007).

[86] W. Mao , B.A. Chronik ,R.E. Feldman ,M.B. Smith and C.M. Collins , *Consideration of magnetically-induced and conservative electric fields within a loaded gradient coil*, Magn Reson Med 2006;55:1424−1432. 25.

[87] M. Bencsik, R. Bowtell and R. Bowley *Electric fields induced in the human body by time-varying magnetic field gradients in MRI: numerical calculations and correlation analysis*, Physics in Medicine and Biology. 52 2337−2353, 2007

[88] Y. Li, J.W. Hand and T. Wills, *Numerically-simulated induced electric field and current density within a human model located close to a z-gradient*, J. Magn. Reson. 26 1286−1295, 2007.

[89] J.P. De Wilde, D. Grainger, D.L. Price and C. Renaud , *Magnetic resonance imaging safety issues including an analysis of recorded incidents within the UK*, Progress in Nuclear Magnetic Resonance Spectroscopy, 51, (1):37−48, 2007

[90] Kornhuber HH, editor. 1974a. Vestibular System Part 1: Basic Mechanisms. Berlin: *Springer-Verlag*

[91] P. M. Glover, I. Cavin, W. Quian, R. Bowtell and P.A. Gowland "Magnetic-Field-Induced Vertigo: A Theoretical and Experimental Investigation", *Bioelectromagnetics*, 28(5), 349−361. 2007

[92] F. Liu, H. Zhao and S. Crozier, *Calculation of electric fields induced by body and head motion in high field MRI*, Journal of Magnetic Resonace, 2003 Mar; 161(1):99−107.

[93] S. Crozier and F. Liu , *Numerical evaluation of the fields induced by body motion in or near high-field MRI scanners*, Progress in Biophysics and Molecular Biology 87, 2−3, 2005, 267−278

[94] S. Crozier, ,A. Trakic, H. Wang and F. Liu, *Numerical study of currents in workers induced by body-motion around high-ultrahigh field MRI magnets*, Magn Reson Med 2008; 59 (2): 410−422.

[95] H. Wang ,A. Trakic , and S. Crozier, *Numerical field evaluation of healthcare workers when bending towards high-field MRI magnets*, Magn Reson Med 2008; 59 (2): 410−422.

[96] S. Crozier, H. Wang, A. Trakic and F. Liu , *Numerical Study of Currents in Workers Induced by Body-Motion Around High-Ultrahigh Field MRI Magnets*, Journal of Magnetic Resonace, 26:1261−1277 (2007).

[97] A. Einstein *"Electrodynamics of Moving Systems"* Ann. Phys., 1905, (17)891−921.

[98] P. Marazzini et al *"The physical meaning of Faraday's law from an historical point of view"*, *Eur. J. Phys.*1983, 4 170−179.

[99] D.R. Corson *"Electromagnetic Induction in Moving Systems"*, *American Journal of Physics*, Bioelectromagnetics, 1956.(24), 126−130.

[100] Panofsky W. and Phillips M. "Classical Electricity and Magnetism", 1955 ,(Addison-Wesley)

[101] D. V. Redžić "Farday's Law via the magnetic vector potential", *European Journal of Physics*, 2007,28(5),7−10.

[102] J.C.Maxwell, *"A Dynamical Theory of the Electromagnetic Field "*, 1864.

[103] Lorrain P., Corson D. R. and Lorrain F. *" Electromagnetic Fields and Waves"*, 1988 , 3rd edn (New York: Freeman)

[104] van Bladel J. *"Relativity and Engineering"*, *Berlin: Springer.*, 1984.

[105] Lorrain P. *"Electrostatic charges in $v \times B$ fields: the Faraday disk and the rotating sphere"*, *Eur. J. Phys.*, 11, 94−98.

[106] D. V. Redžić ''*Comments on Electrostatic charges in $v \times B$ fields "*, *Eur. J. Phys.*, 2001, 22, L1−2.

[107] D. V. Redžić *"Conductors moving in magnetic fields: approach to the equilibrium"*, Eur. J. Phys., 2004, 25, 623−632.

[108] E. Bringuier *"Electrostatic chargues in $v \times B$ fields and the phenomenon of induction"*, Eur. J. Phys., 24(2003), 21−29.

[109] J. Mathis, U. Seemann, T. Weyh, C. Jakoband A. Struppler " *The boundary effect in magnetic stimulation. Analysis at the peripheral nerve"*, Motor Contr. Electroenc. Clin. Neurophys. 97, 238−45, 1995.

[110] R.C. Costen and D. Adamson, *"Three-dimensional derivation of the electrodynamic jump conditions and momentum-energy laws at a moving boundary"*, Proceedings of the IEEE. 9, 1181−1196, 1965.

[111] P. Lorrain , J. McTavish and F. Lorrain "Magnetic fields in moving conductors: four simple examples", *Eur. J. Phys.*, 19(1998), 451−457.

[112] D. B.Geselowitz, *On bioelectric potentials in an homogeneous volume conductor.* Biophys. J. 7 1−11, 1967.

[113] N. G. Gençer and I. O. Tanzer , *Forward problem solution of electromagnetic source imaging using a new BEM formulation with high-order elements.* Phys. Med. Biol. 44 2275−87, 1999.

[114] J. Kybic et al, *Generalized head models for MEG/EEG: boundary element method beyond nested volumes.* Phys. Med. Biol. 51 1333−1346, 2006.

[115] P.C. Miranda, M.Hallett, P.J Basser, *The electric field induced in the brain by magnetic stimulation: a 3-D finite-element analysis of the effect of tissue heterogeneity and anisotropy.* Biomedical Engineering. 50(9) 1074− 1085, 2003.

[116] H. Power and L.C. Wrobel, *Boundary Integral Method in Mechanics.* Computational Mechanics Publications, 1995.

[117] H. Pina, J. Fernandes, and C. Brebbia, *Some Numerical Integration Formulae over Triangles and Squares with a 1/r Singularity.* Applied Mathematical Modelling, 5 (1981) 209−211.

[118] H. Pina, *Numerical quadrature over triangles with weak singularities.* Int. J. Numer. Meth. Engng, 45 (1999) 1871−1885.

[119] C. Pozrikidis (1984), *A Practical Guide to Boundary Element Methods.* Chapman and Hall, 2002.

[120] Q. Huang, T. A. Cruse, *Some notes on singular integral techniques in boundary element analysis.* Int. J. Numer. Meth. Engng, 36 (1993) 2643−2659.

[121] M. Guiggiani, G. Krishnashamy, T.J. Rudolphi and F.J.Rizzo, *A General Algorithm for the Numerical Solution of Hypersingular Boundary Integral Equations.* Journal of Applied Mechanics, Vol.159, (1992), pp.604−614.

[122] M. Guiggiani, A. Gigante, *A general algorithm for multidimensional Cauchy principal value integrals in the boundary element method.* Journal of Applied Mechanics, Vol. 57, pp. 906−915, 1990.

[123] A. M. Stroud, D. Secrest, *Gaussian Quadrature Formulas.* Prentice-Hall, New York, 1966.

[124] P.W. Partridge, C.A. Brebbia, and L.C. Wrobel, *The Dual Reciprocity Boundary Element Method.* CMP/Elsevier, 1992.

[125] R.Plonsey, *Biomagnetic Phenomena.* McGraw-Hill, New York (1969).

[126] Z. Akalin-Acar and N. G. Gençer, *An advanced boundary element method (BEM) implementation for the forward problem of electromagnetic source imaging.* Phys. Med. Biol.,49 5011−5028, 2004.

[127] D. Yao, *Electric potential produced by a dipole in a homogeneous conductingsphere,* Biomedical Engineering. 47(7) 964 −966, 2000.

[128] N. Metropolis, A. W. Rosenbluth, M. Rosenbluth,A. H. Teller, and E. Teller. *Equation of State Calculations by Fast Computing Machines,* J. Chem. Phys. 21, 1087−1092, 1953.

[129] P.E. Gill, W. Murray and M.H. Wright, *Practical Optimization,* Academic Press, London, (1981).

[130] J. Kybic, M. Clerc, O. Faugeras, R. Keriven and T. Papadopoulo, *Fast multipole acceleration of the MEG/EEG boundary element method.* Phys. Med. Biol. 50 (2005) 4695−4710